Etude des propriétés élastiques de la croûte : analyse numérique et applications au bruit de fond sismique

Anne-Christine Obermann

UNIVERSITÉ DE GRENOBLE

THÈSE

Pour obtenir le grade de

DOCTEUR DE L'UNIVERSITÉ DE GRENOBLE

Spécialité : **Sciences de la Terre, de l'Univers et de l'Environnement**

Arrêté ministériel : 7 Août 2006

Présentée par

Anne Obermann

Thèse dirigée par **Éric Larose et Michel Campillo**

préparée au sein **de l'ISTerre (Institut des Sciences de la Terre)**
et de **l'école doctorale Terre, Univers, Environnement**

Monitoring the elastic properties of the crust: numerical analysis and applications using ambient seismic noise

4 Novembre 2013 ,
devant le jury composé de :

Prof. Dr. Michel Campillo
ISTerre, Grenoble, France, Directeur de thèse
Dr. Eric Larose
ISTerre, Grenoble, France, Co-Directeur de thèse
Prof. Dr. Torsten Dahm
GFZ, Potsdam, Germany, Rapporteur
Prof. Dr. Haruo Sato
Tohoku University, Tohoku, Japan, Rapporteur
Dr. Valérie Cayol
Observatoire de Physique du Globe, Clermont-Ferrand, France, Examinateur
Dr. Olivier Coutant
ISTerre, Grenoble, France, Président

Remerciements

I am very grateful for the three years that I spent in Grenoble working on this PhD thesis!

- **THANKS to** my jury members: Haruo Sato and Torsten Dahm who attentively read my manuscript and read my manuscript and travelled quite a distance to attend my defense, and ValÃ©rie Cayol and Olivier Coutant who were also part of my jury.
- **THANKS to** my advisors Eric Larose and Michel Campillo who made this PhD possible. They gave me the unique opportunity to work on a very interesting topic in a very inspiring environment at ISTerre. During my thesis they provided me with essential help, and were available when I needed their advice.
  I also wish to thank them for the many occasions that I had to participate in international scientific conferences. I actively took advantage of this and met many interesting other researchers and had many very stimulating discussions.
- **THANKS to** Thomas Planès, Bérénice Froment, Christoph Sens-Schönfelder and Bernard Valette with whom I collaborated during my thesis.
- **THANKS to** my family and friends for the organization of the buffet after my defense and for supporting me during my thesis :)
- **THANKS to** the great friends that I made during my time in Grenoble!!. We spent a marvelous time hiking, skiing, climbing, canyoning... and not to forget the numerous memorable "soirées"!! And a special thanks to Thomas for having been by my side!

Résumé

Durant mes trois années de thèse, j'ai été amenée à travailler sur différents aspects de la surveillance des propriétés élastiques de la croûte, à la fois par analyses numériques, mais aussi par des applications d'utilisation du bruit ambiant. Ma thèse s'articule autour de deux parties principales:

1. **Les propriétés des ondes de la coda**
   Le libre parcours moyen est un paramètre crucial rencontré continuellement dans les différentes parties de mon travail. Dans cette partie, je présente une nouvelle façon de déterminer ce libre parcours moyen à partir des statistiques de phase. Cette méthode a été testée avec succès dans l'étude d'un volcan situé en Auvergne (France).
   Je présente ensuite une analyse numérique de la sensibilité que les ondes de la coda manifestent en fonction de la profondeur. Ce travail nous a permis de relier cette sensibilité à la profondeur observée dans les ondes de la coda, à une combinaison de la sensibilité des ondes de volume et de celle des ondes de surface. En effet, cette sensibilité des ondes de volume et de surface dépend directement du temps considéré dans la coda et du libre parcours moyen du milieu étudié. Nous avons été capable de montrer que le changement de vitesse relatif dans la coda était lié à une dépendance en temps. Cette importante observation nous permet de pouvoir établir une distinction entre un changement qui se produit en surface et un changement ayant lieu en profondeur.

2. **Localisation des changements dans un milieu diffusif**
   Nous avons développé une méthode d'inversion basée sur des approches probabilistes de la propagation des ondes, afin de pouvoir localiser les changements dans le milieu. Nous avons également étudié la décohérence de la forme d'onde, ce qui constitue un aspect additionnel des techniques de surveillance du bruit sismique, qui traditionnellement sont basés sur l'évaluation du temps de retard dans la coda. Au cours de cette thèse, nous avons affiné notre méthode d'inversion en l'appliquant à trois cas d'études. Dans un premier cas, nous avons étudié les changements ayant eu lieu avant et pendant l'éruption du volcan du Piton de la Fournaise situé sur l'Ile de la Réunion. Le challenge ici est de parvenir à localiser correctement la

prochaine éruption. La seconde application a concerné le séisme de Mw7,9 de Wenchuan (Chine), sur lequel nous avons obtenu de nombreuses données. Dans ce cas, nous avons pris en compte l'évolution de la coda au cours du temps et nous avons conjointement inversé les données à différents temps dans la coda pour étudier les changements induits dans la croûte, avant et pendant le séisme. A partir de ces résultats, nous avons pu clairement voir que la décohérence de la forme d'onde et les variations de vitesse n'étaient pas sensibles aux mêmes propriétés physiques. Dans le troisième cas d'étude, nous avons testé la procédure d'inversion avec un noyau 3D pour étudier la fracturation dans un bloc de béton soumis à une contrainte croissante.

Abstract

During my thesis, I worked on different aspects of monitoring the elastic properties of the crust, with both numerical analysis and applications with ambient noise. The main body of my thesis consists of two main parts:

1. **Properties of coda waves**
   A very important parameter that we continuously encounter in the different parts of my thesis work is the scattering mean free path ℓ. I present an original way to determine the scattering mean free path from phase statistics that was successfully tested on a volcano in Auvergne.
   Then I discuss an intensive numerical analysis of the depth sensitivity of coda waves. This work allowed us to relate the depth sensitivity of coda waves to a combination of bulk wave sensitivity and surface wave sensitivity that depends on the time in the coda and on the scattering mean free path of the medium. We were able to show a time dependence of the relative velocity change in the coda that allows us to discriminate a change that occurs at the surface from a change that occurs at depth.

2. **Locating changes in multiply scattering media**
   We developed an inversion method based on probabilistic approaches of the wave propagation to locate changes in the medium. As an additional aspect to seismic noise monitoring techniques that are based on the evaluation of time delays in the coda, we also study the waveform decoherence. Within this thesis, we apply and refine the inversion method with three case studies. We study pre-and co-eruptive changes at Piton de la Fournaise volcano in La Réunion Island. The challenge here is to correctly locate forthcoming eruptions. A second data set comes from the Mw7.9 Wenchuan earthquake in China. In this study, we take the time evolution of the coda into account and jointly invert the data at different times in the coda to study changes in the crust during and after the earthquake. From the results, we can clearly see that waveform decoherence and velocity variations are not sensitive to the same physical properties. In the third study, we test the inversion procedure with a 3D sensitivity kernel to study the fracturing of concrete blocks under increased tension.

Contents

Chapter 1

Introduction

Contents

1.1 General context

Imaging Earth's subsurface is the main purpose of most geophysical methods. For these studies, the record of the passage of elastic waves through the Earth is one of the most powerful methods available. The Earth's lithosphere is hereby often assumed to be a simple stratified medium. The properties of the subsurface can then be estimated from classical experiments with reflected and refracted seismic waves. In reality though, the Earth is heterogeneous at different scales (Fig.1.1) and wave propagation quickly becomes very complex. In very heterogeneous media, waves are multiply scattered by medium heterogeneities, so that no conclusion about the traveled distance can be drawn. This renders classical imaging processes impossible.

Fortunately, scattering does not only cause nuisance. The scattering processes result in long-lasting wave tails in seismograms, the **seismic coda**. It is only since the pioneering work of Aki (1969); Aki and Chouet (1975), who discovered that coda waves contain decisive information about regional scattering and attenuation properties, that coda waves have received increasing attention. Today it is widely accepted that coda waves are deterministic, reproducible signals. Due to the scattering processes, they sample large areas of the subsurface very densely, and become very sensitive to weak changes in the medium, which may have no detectable influence on the first arrivals. If there was not the limited spatial and temporal distribution of earthquakes, coda waves would be a good candidate for the continuous **monitoring** of geological structures. But, where can we find a continuous source of seismic energy, that is available everywhere on Earth?

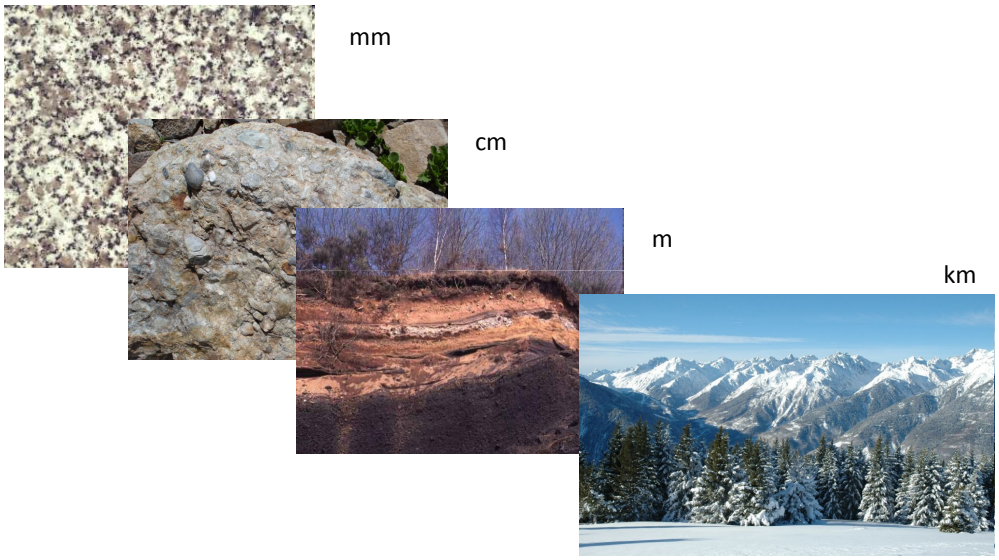

Figure 1.1: Heterogeneities of the Earth at different scales.

Luckily, Earth itself provides us the solution in form of the so-called **ambient seismic noise**. Oceanic and atmospheric interactions cause a permanent vibration of the Earth's surface, that can be continuously recorded at any place. Shapiro and Campillo (2004) were the first to show that by cross-correlating this seismic noise, the Earth's impulse response (Green's function) between two points can be reconstructed. These virtual seismograms yield all the characteristics of seismograms produced with earthquakes or active experiments, including coda waves. While there are strong theoretical requirements to reconstruct the Green's function from a noise field regarding a uniform source distribution, in practice, numerous recent application in surface-wave (e.g. Shapiro et al. (2005)) and body-wave tomography (Boué et al., 2013) and monitoring of volcanoes (e.g. Sens-Schönfelder and Wegler (2006); Brenguier et al. (2008b)) or fault zones (Brenguier et al., 2008a) have shown that the cross-correlations can be used efficiently even though the strong requirements are not perfectly met.

1.2 Context and outline of the thesis

Within the three years of my thesis work, one large aspect was to use the coda of seismic noise correlations to monitor temporal changes of rock properties. While published studies in this domain only investigate the temporal changes in seismic velocities that are related to changes in stress, temperature, water saturation etc., we also investigated

the changes in waveform coherence due to structural changes in the medium. We then developed an imaging technique based on probabilistic approaches in multiple scattering media (Larose et al., 2010; Froment, 2011; Planès, 2013) to locate these changes in space. With this least-square inversion technique, we could successfully image pre-and co-eruptive changes at Piton de la Fournaise volcano, La Réunion Island. We then refined the technique by using different times in the coda and studied co-and postseismic changes in the lower and middle crust associated with the 2008 Mw7.9 Wenchuan earthquake. In these studies we used two-dimensional sensitivity kernels. In a recent project, we implemented a three-dimensional kernel (Planès, 2013) in the inversion scheme to detect the 3D-crack extension in concrete samples under tension in a laboratory environment.

A very important aspect for these imaging techniques, but also for other applications, is a better understanding of the nature of the waves that compose the coda. Under this more theoretical perspective, we investigated the possibility to determine the scattering mean free path from spatial phase decoherence. And with extensive numerical simulations of wave-field propagations in heterogeneous media, we studied the depth sensitivity of coda waves to velocity perturbations and obtained among others, interesting insights in the partition of surface and body waves at different times in the coda.

According to these different aspects, my thesis manuscript is organized in three main parts:

In Part I, I specify important ideas and concepts of the wave propagation in complex media (Chapter 2), the concepts of ambient seismic noise and how we can use the noise correlations for monitoring purposes (Chapter 3).

Part II deals with properties of coda waves. First, I present a study to determine the scattering mean free path from spatial phase decoherence (Chapter 4). And then I show the numerical simulations that we did in 2D heterogeneous media to study the sensitivity of coda waves to velocity perturbations at depth (Chapter 5). I also briefly show the first results that we recently obtained with wave-field simulations in 3D heterogeneous media.

Part III is dedicated to the least-square inversion method to locate structural and mechanical changes in multiply scattering media. This technique is applied: to locate pre- and co-eruptive changes at Piton de la Fournaise (Chapter 6; to locate changes in the crust associated with the Wenchuan M8 earthquake in China (Chapter 7); and to a laboratory experiment with concrete blocks that are exposed to increasing tension. We locate and size the cracks (Chapter 8). For each chapter I give a short introduction to the particular objectives, before I present our study and results.

I then conclude my thesis work and outline some avenues for future studies.

1.3 List of publications

My thesis contains a collection of articles that we published in or submitted to scientific peer-reviewed journals:

- Chapter 4: Measuring the scattering mean free path of Rayleigh waves on a volcano from spatial phase decoherence, accepted at Geophysical Journal International, by Anne Obermann, Eric Larose, Ludovic Margerin and Vincent Rossetto.
- Chapter 5: Depth sensitivity of seismic coda waves to velocity perturbations in an elastic heterogeneous medium, Geophysical Journal International, 2013, 194(1), 372-382, by Anne Obermann, Thomas Planès, Eric Larose, Christoph Sens-Schönfelder and Michel Campillo.
- Chapter 6: Imaging pre- and co-eruptive structural and mechanical changes of a volcano with ambient seismic noise, Journal of Geophysical Research, 2013, 118, 1-10, by Anne Obermann, Thomas Planès, Eric Larose and Michel Campillo.
- Chapter 7: Seismic noise correlations to image structural and mechanical changes associated with the Mw7.9 2008 Wenchuan earthquake, submitted to Journal of Geophysical Research, by Anne Obermann, Bérénice Froment, Michel Campillo, Eric Larose, Thomas Planès, Bernard Valette, Jiuhui Chen and Qiyuan Liu.

Currently, we are working on a publication about the content of Chapter 8: Locating and sizing a crack in concrete. The publication will most likely be intended for JASA.

Part I

Methods and Concepts

Chapter 2

Wave propagation in complex media

Contents

2.1 Waves in homogeneous media

In this section, I give a brief introduction (that follows Shearer (2010)) for non-specialists to the wave equation and the Green's function as a particular solution of this equation for an impulse source. Then, I briefly discuss the different types of seismic waves.

2.1.1 Seismic wave equation and Green's function

A wave is a disturbance that propagates through space and time and is governed by local physical properties. If we apply Newton's second law of motion ($\boldsymbol{F} = m\boldsymbol{a}$, where $\boldsymbol{F}$ is the applied force, m the mass and a the acceleration) to continuous medium, the equation yields:

$$\rho \frac{\partial^2 u_i}{\partial t^2} = \partial_j \tau_{ij} + f_i, \tag{2.1}$$

where ρ is the density, $\boldsymbol{u}$ is the displacement and $\boldsymbol{\tau}$ is the stress tensor. i and j range from 1 to 3 for the x, y and z directions. f is the body force term and can generally be neglected for body- and surface-wave calculations if we are not in a seismic source region. The homogeneous equation of motion then reads:

$$\rho \frac{\partial^2 u_i}{\partial t^2} = \partial_j \tau_{ij}, \tag{2.2}$$

As the passage of seismic waves is generally associated with little strain, we can assume a linear stress-strain relationship to solve 2.2 and express the stress tensor $\boldsymbol{\tau}$ with the displacement $\boldsymbol{u}$. For isotropic media this linear relationship is defined by Hooke's law:

$$\tau_{ij} = \lambda \delta_{ij} \epsilon_{kk} + 2\mu \epsilon_{ij}, \tag{2.3}$$

where λ and μ are the Lamé parameters and ϵ_{ij} is the strain tensor. We now define $\epsilon_{ij} = \frac{1}{2}(\partial_i u_j + \partial_j u_i)$ and substitute the stress-tensor (Eq.2.3) into Eq.2.2. When we neglect the terms that involve gradients in the Lamé parameters, we obtain the standard form of the seismic wave equation in a homogeneous medium:

$$\rho \frac{\partial^2 u}{\partial t^2} = (\lambda + 2\mu) \nabla \nabla \bullet u - \mu \nabla \times \nabla \times u. \tag{2.4}$$

This equation can be separated into solutions for P-waves and S-waves[1] by taking the divergence and curl, respectively. The corresponding P-wave equation is

$$\nabla^2 (\nabla \bullet u) - \frac{1}{\alpha^2} \frac{\partial^2 (\nabla \bullet u)}{\partial t^2} = 0, \tag{2.5}$$

where the P-wave velocity, α, is given by

$$\alpha = \sqrt{\frac{\lambda + 2\mu}{\rho}}. \tag{2.6}$$

The resulting S-wave equation is

$$\nabla^2 (\nabla \times u) - \frac{1}{\beta^2} \frac{\partial^2 (\nabla \times u)}{\partial t^2} = 0, \tag{2.7}$$

where the S-wave velocity, β, is given by

$$\beta = \sqrt{\frac{\mu}{\rho}}. \tag{2.8}$$

We now introduce a particular solution $g_0(r, t)$ of the wave equation for an impulse source under the following boundary conditions:

[1] P- and S-waves are explained in section 2.1.2 for the non-specialist.

$$\begin{cases} g_0(\boldsymbol{r} \to \infty) & = 0. \\ g_0(t = 0) & = 0. \\ \frac{\partial g_0}{\partial t}(t = 0) & = 0. \end{cases} \tag{2.9}$$

This solution $g_0(r, t)$ is referred to as Green's function and is described by the mathematical definition:

$$\left[\Delta - \frac{1}{c^2}\frac{\partial^2}{\partial t^2}\right] g_0(\boldsymbol{r}, t) = \delta(\boldsymbol{r})\,\delta(t)\,, \tag{2.10}$$

where the physical dimensions can represent, among others, a displacement, a wave speed or an acceleration. The Green's function in a medium between two points represents a signal emitted in one of the points and recorded in the other. The Green's function hence describes the wave propagation between these two points and contains all the information about the different propagation modes of the waves in the medium.

2.1.2 Types of seismic waves

With help of Fig. 2.1 we explain the main types of seismic waves propagating in the Earth. Firstly, we can differentiate **body waves**, that penetrate and traverse the Earth and **surface waves**, whose motion is confined to the surface of the crust.
The fastest body wave is the P-wave, also termed primary wave or compressional wave. The displacement of P-waves only occurs in the direction of motion (longitudinal polarization) (Fig. 2.1a). Hence, P-waves introduce shear and volume changes in the medium ($\nabla \bullet u \neq 0$) (Eq.2.5 and 2.6).
S-waves, also termed secondary waves or shear waves, mark the second arrivals on seismograms (Fig. 2.4). Their motion is perpendicular to the propagation direction (transverse polarization) (Fig. 2.1b). We can differentiate S-waves with a particle motion in the vertical plane (SV-waves) and S-waves with a particle motion in the horizontal plane (SH-waves). The motion in both planes is pure shear without any volume change (Eq. 2.8). As a consequence, S-waves can only travel in solid materials and not in liquids.
There are also two types of surface waves. The faster propagating Love waves, whose motion is essentially that of S-waves, except that there is no vertical displacement (Fig. 2.1c); and Rayleigh waves. Rayleigh waves show longitudinal and transverse motions that exponentially decrease in amplitude with increasing distance from the surface (Fig. 2.1d). Surface wave propagation is slower than that of body waves (Fig. 2.4), nevertheless they are almost entirely responsible for the damage and destruction associated with earthquakes.

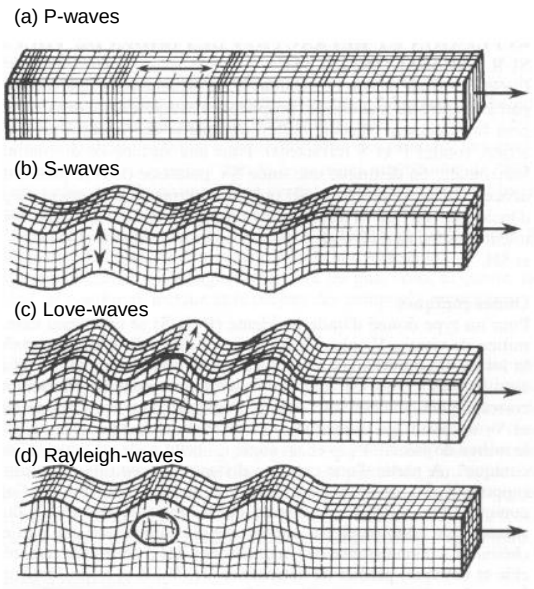

Figure 2.1: Different types of seismic wave.

2.2 Waves in heterogeneous media

In this section, we have a look at wave propagation in heterogeneous media. I introduce the different propagation regimes according to the degree of disorder in the medium. Then I discuss some characteristic parameters that intervene in multiple scattering media, before discussing seismic coda waves in more detail. At the end, I discuss the partitioning of energy in the seismic coda that is an indicator of multiple scattering.

2.2.1 Different propagation regimes

Wave propagation in heterogeneous media is governed by the degree of disorder, that determines the nature of the physical phenomena that are observed. According to the degree of disorder in the medium, we can distinguish at least three different propagation regimes: single scattering, multiple scattering and Anderson localization (Fig. 2.2). To have a closer look at the three regimes, let us consider an energy source and a receiver at distance L (depicted as an eye in Fig. 2.2) in a medium that contains several scatterers:

- **Single scattering**: (Fig. 2.2a): In this regime, the scatterers are far apart compared to the wavelength and the observation distance. The wave interacts only with a single scatterer on its way from the source to the receiver. We can hence trace the path of the wave and use classical imaging techniques to establish a relationship between the travel-time and the position of the scatterer.

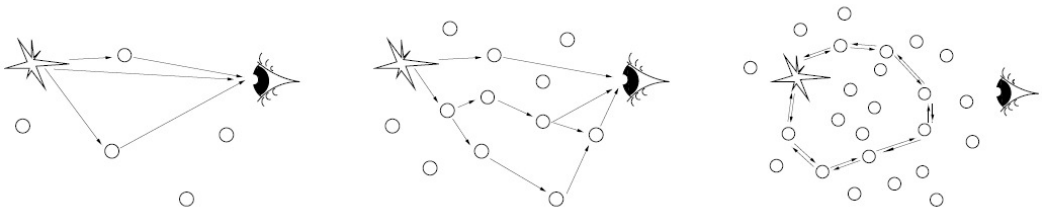

Figure 2.2: From left to right: Single scattering, multiple scattering, Anderson localisation (Source: Anache-Ménier et al. (2009)).

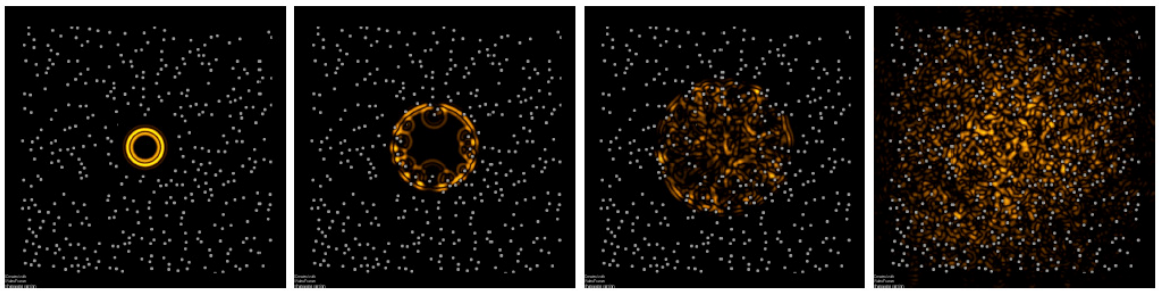

Figure 2.3: Finite difference simulation of the scattering of a spherical accoustic wave in a 2D diffusive medium. The scatterers represented by the white points have a diameter of $\lambda/2$. Source: M.Tanter, ACEL,LOA-ESPCI

- **Multiple scattering**: (Fig. 2.2b): In this regime, there are either many more scatterers in the medium or the distance between source and receiver is very large, so that the waves are reflected several times before being recorded and "forget" their origin. In this case the equivalence between time and distance is not valid, which makes classical imaging techniques inapplicable. Multiple scattering is also illustrated in Fig. 2.3 in form of a finite difference simulation of the diffusion of a spherical acoustic wave in a 2D diffusive medium.

- **Anderson localization**: (Fig. 2.2): A third regime is the strong localization, also referred to as Anderson localization. In this regime the wave energy is caught by the ambient disorder and there is a total absence of diffusion. The phenomenon results from the wave interference between the different scattering paths. In the strong scattering limit no signal will reach the receiver as the strong interferences completely halt the waves inside the disordered medium (Anderson, 1958). However, this regime is unlikely in seismology because of absorption.

Within this thesis we are interested in the multiple scattering regime.

2.2.2 Characteristic lengths in multiply scattering media

Besides the wavelength λ and the medium dimension L, there are three characteristic lengths that intervene in wave propagation in disordered media: the scattering mean free path ℓ, the transport mean free path $\ell^\star$ and the absorption length ℓ_a (van Rossum and Nieuwenhuizen, 1999).

- **The scattering mean free path** ℓ corresponds to the average distance between successive scattering events. The magnitude of the scattering mean free path depends on the characteristics of the system containing the particles and is defined via the total cross-section of interaction σ as:

$$\ell = \frac{1}{n\sigma} \tag{2.11}$$

  with

$$\sigma = \int \frac{d\sigma(\Omega)}{d\Omega} d\Omega \tag{2.12}$$

  where n is the number of scatterers per unit volume, $d\sigma$ is the differential cross-section and $d\Omega = \sin(\theta) d\theta d\phi$. Note that in a 3D medium the effective cross-section is a surface, while it is a length in a 2D medium. The medium is in "weak" disorder as long as $\ell > \lambda$.

- **The transport mean free path** $\ell^\star$ is the characteristic distance along which a wave keeps memory of its incident propagation direction. $\ell^\star$ is closely related to ℓ:

$$\ell^\star = \frac{\ell}{1 - \langle \cos(\theta) \rangle} \tag{2.13}$$

  where θ is the angle between the vector of the incident wave and the vector of the scattered wave. $\langle \cos(\theta) \rangle$ is the anisotropy of diffusion and the brackets denote averaging over all solid angles. The physics are subtly different: while ℓ is determined by superposition of the different paths, $\ell^\star$ is also sensitive to interference. Hence, if the differential effective section is isotropic, $\langle \cos(\theta) \rangle = 0$ and $\ell^\star = \ell$.

- **The absorption length** ℓ_a for a system of size $L > \ell_a$ indicates that the waves are significantly absorbed and damped. The expression for ℓ_a is given by:

$$I \propto \exp(-\frac{t}{\tau_a}) = \exp(-\frac{\ell}{\ell_a}) \Rightarrow \ell_a = c\tau_a \tag{2.14}$$

  where τ_a is the characteristic absorption time and c is the propagation velocity.

In highly heterogeneous media, wave propagation can be described by the diffusion approximation. The diffusive regime is formulated in three inequalities (Kaveh, 1991):

$$\lambda << \ell, \ell^\star << L << \ell_a \tag{2.15}$$

The first inequality that the wavelength is significantly smaller than the transport mean free path, $\lambda << \ell^\star$, implies that two consecutive scattering events of the wave are independent. The second inequality states that the transport mean free path is significantly smaller than the medium dimension, $\ell^\star << L$. This is the condition for being in the multiple scattering regime. With the third inequality, that the medium dimension is significantly smaller than the absorption length, $L << \ell_a$, we neglect absorption. In practice, in an open infinite space, we find: $\lambda << \ell^\star \leq \ell_a$.

As ℓ and $\ell^\star$ are of great importance for the inversion procedure based on probabilistic approaches that we use in part III of this thesis, we discuss a possibility to determine the scattering mean free path from seismic data in more detail in section 4.

2.2.3 Seismic coda waves

When studying a regional seismogram (Fig. 2.4), we often observe that the P-, S-, and surface wave arrivals are followed by a long-lasting wave train in the tail portion of the seismogram. This wave train is named "coda", which literally means tail. Coda waves can last more than 10 times the travel time of direct waves, before reaching the level of seismic noise (Aki, 1969). As it is impossible to forecast the coda waveform a priori, coda waves are useless for classical imaging techniques and for a long time it was thought that it was not possible to obtain any useful information from them.

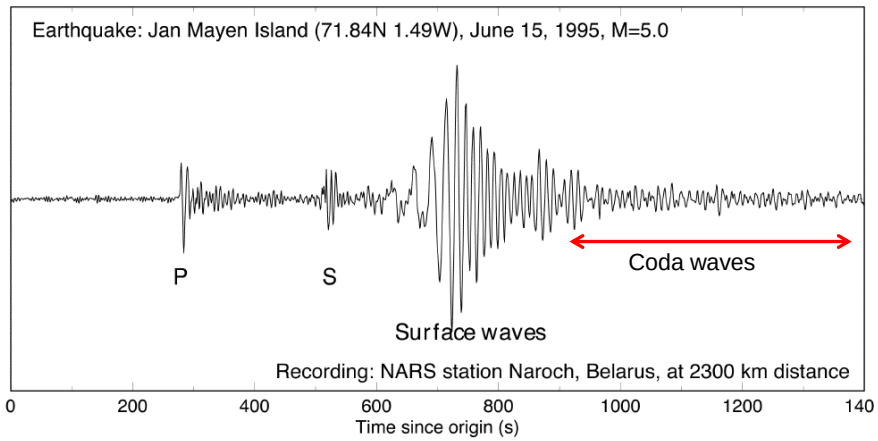

Figure 2.4: Seismogram of an earthquake showing P-waves, S-waves, surface waves and long-lasting coda waves.

Keiiti Aki was one of the pioneers in the analysis of coda waves (Aki, 1969; Aki and Chouet, 1975). Aki and Chouet (1975) could show that the energy decay of coda waves with time is a local characteristic parameter, independent of the magnitude and

localization of the source. In a frequency band of 1 to 10 Hz they could show that the energy envelope of the coda decay is well described by:

$$E_\omega(t) \approx \frac{1}{t^\gamma} \exp\left(-\frac{\omega t}{Q_c(\omega)}\right), \tag{2.16}$$

where $1/t^\gamma$ is a geometrical factor with γ varying between 1 and 2. ω is the pulsation and Q_c is called coda quality factor. Q_c is an empirical parameter that depends on the local characteristics of the crust and on frequency. Q_c is given by a combination of intrinsic (Q_i) and scattering (Q_s) attenuation:

$$\frac{1}{Q_c} = \frac{1}{Q_i} + \frac{1}{Q_s}. \tag{2.17}$$

$Q_i = \omega\tau_a$ where τ_a is the characteristic time for energy absorption and $Q_s = \omega H^2/D$, where $D = \frac{v\ell^\star}{2}$ is the diffusion constant and H a characteristic length for the thickness of the crust. Since these discoveries, measurements of Q_c have been widely explored to study attenuation properties of the crust throughout the world. Typical Q_c values vary between 50 and 1000 (e.g. Singh and Hermann (1983); Jin and Aki (1988)). It still remains very difficult to measure Q_s and Q_i separately (Del Pezzo et al., 2001) and hence to determine $\ell^\star$ from attenuation measurements on seismic waves.

Aki (1969), followed by others (Aki and Chouet, 1975; Sato, 1977; Herraiz and Espinoza, 1997), suggested that the coda was composed of a sum of incoherent waves that are singly scattered from heterogeneities in the Earth's crust. Hoshiba (1997) showed that a combination of single scattering and attenuation can account for some aspects of the seismic coda. However, the Earth is not a simple homogeneous medium with a few scattering points, but on the contrary, heterogeneous at different scales. As we have seen, the scattering of a wave depends on the difference in constitutive parameters between scatterers and propagating medium, such as the wave velocity, and the shape and size of the scatterers compared to the wavelength. It may hence not be negligible to include higher scattering orders to describe seismic coda waves. Margerin et al. (1999) studied the decay of Q_c with earthquake data acquired in Mexico. They could explain the decay of Q_c with a model of guided waves in the crust and scattering. Hennino et al. (2001) resolved the controversy "single or multiple scattering in the seismic coda". They measured the equipartitioning of the energy of seismic coda waves over the different elastic modes from earthquake data in Mexico (Fig. 2.5). Equipartitioning is a clear evidence of multiple scattering in elastic heterogeneous media, as we will see in more detail in section 2.2.4. In continuation of these works, Larose et al. (2004b) observed the interference of multiply scattered waves by measuring the weak localization of seismic waves.

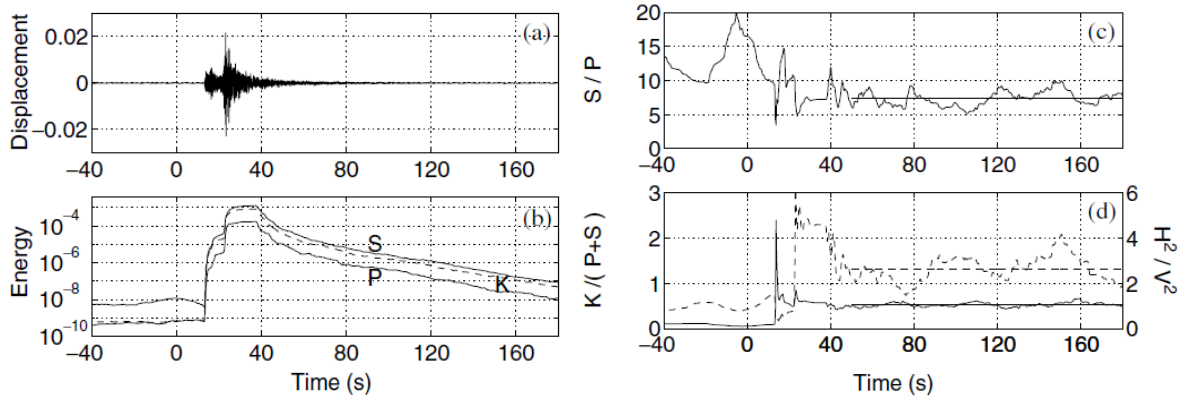

Figure 2.5: Equipartition of seismic coda waves. (a) Displacements of a magnitude 4 earthquake as a function of time. (b) Semilogarithmic plot of the energy density. As distinction is made between kinetic energy (K), shear energy (S) and compressional energy (P). (c) Linear plot of the energy ratio S/P. (d) Linear plot of the energy ratios K/(S+P) (solid line) and H^2/V^2 (dashed line). The horizontal lines denote the estimated time average. Source: Hennino et al. (2001).

Besides studying the temporal decay of the amplitude of coda waves as a measure of the scattering properties of the transversed medium, what other information can we obtain from coda waves? As random as the signal might seem, coda waves are deterministic. If the medium and the source remain unchanged, the waveform also remains the same from one record to the other. Thanks to the multiple scattering, coda waves spend a lot of time in the medium, sampling it repeatedly. This repeated sampling amplifies weak medium perturbations. So even if the changes are not detectable in the first arrivals, they may become detectable in the coda in form of small phase shifts. In recent years this sensitivity has been increasingly used for monitoring purposes based on the Coda Wave Interferometry technique (Poupinet et al., 1984; Snieder et al., 2002; Snieder, 2006), that measure time-lapse changes based on the phase and amplitude information of coda waves.

One question that has not been clearly answered yet, concerns the constitution of coda waves. Do we more accurately describe coda waves as body waves or surface waves, or a mixture of both of them? The answer to this question will have strong implications for the depth sensitivity of coda waves and also for an accurate construction of sensitivity kernels that describe the wave propagation between two points in multiply scattering media. In chapter 5, we investigate the partition ratio between surface and bulk waves in the coda in more detail with extensive numerical simulations of wave propagation in heterogeneous media. Among others, we study the dependence of the partition ratio on the degree of heterogeneity in the medium and on the time in the coda.

2.2.4 Energy equipartitioning

As a consequence of the multiple scattering, seismic waves are converted from P- to S-waves and vice-versa at each scatterer. After several diffusion processes, the modes have been "mixed" and a stationary regime is reached with a constant amount of P- and S-waves. Please note, that this principle only applies when we are in the multiple scattering regime.
Let us have a closer look at the mode density of P- and S-waves: for plane waves in an infinite medium in 3D, there exist one polarization direction for P-waves and two polarizations directions for S-waves (SH and SV). We can thus calculate the density of P- and S-wave state around a given frequency ω in the phase space as:

$$\rho_{P,S} = \frac{\omega^2}{v_{P,S}^3} \tag{2.18}$$

The equipartition ratio is the ratio between these two densities. If all modes are excited in the same way, the theoretical ratio between the potential shear and compressional energy is constant and given as (Weaver, 1982; Shapiro et al., 2000; Tregourès and van Tiggelen, 2002):

$$\frac{E_S}{E_P} = \frac{2v_P^3}{v_S^3} \approx 10.4 \tag{2.19}$$

In a single scattering regime, the E_S/E_P ratio depends on the source. The measure of the equipartition ratio can thus be seen as a proof of multiple scattering.

Shapiro et al. (2000) determined the equipartition ratio in the seismic coda from an experimental setup in Mexico as 7.30±0.72. This value is in disagreement with the theoretical ratio mentioned in EQ. 2.19. The explanation for this discrepancy is that when we consider the free surface that is present on the Earth, the phase space is modified. The equipartition value will hence be different. Hennino et al. (2001) calculated the theoretical equipartition value considering a free surface and Tregourès and van Tiggelen (2002) confirmed it numerically as:

$$\left.\frac{E_S}{E_P}\right|_{\text{freesurface}} \approx 7.19, \tag{2.20}$$

which is in good agreement with the value observed by Shapiro et al. (2000).

Chapter 3

Ambient seismic noise and coda wave interferometry

Contents

In classical seismology earthquake signals are used to study the Earth's interior. As pointed out in the introduction, a major disadvantage of earthquake signals is their inhomogeneous and limited distribution in space and time. So what can we do, if we want to continuously monitor an aseismic region/location on Earth?

The solution comes from the observation that the Earth's surface is under permanent vibration that produces a continuous wave excitation, the so-called ambient seismic noise (Fig. 3.3). This seismic noise can be permanently recorded everywhere on Earth. In the following, I discuss the origin of this noise, describe how we can reconstruct the Earth's response (Green's function) between two points by cross-correlating continuous noise records, and I point out different applications in seismology. Then I discuss the effect of global and local velocity and structural changes on the coda and the possibilities that emerge for monitoring purposes.

3.1 Origins of ambient seismic noise

Several studies made the attempt to characterize ambient seismic noise (Friedrich et al., 1998; Nishida et al., 2002; Stehly et al., 2006). Since Gutenberg (1936) we know that the noise intensity evolves with the meteorological activity and the motion of the sea. Friedrich et al. (1998) discovered that the biggest part of the noise energy is hold by surface waves. These observations suggest that the noise is generated at the Earth surface, or more precisely, in the oceans.

The origin of the noise depends strongly on the frequency range under consideration (Bonnefoy-Claudet et al., 2006). The seismic noise spectra contains two prominent peaks: the primary microseism at 0.05-1 Hz and the secondary microseism 0.1-0.3 Hz. The frequency of the primary microseism corresponds to the dominant frequency of ocean waves and originates from direct forcing of oceanic waves. The secondary microseism is characterized by stronger amplitudes and is produced at double frequency by a nonlinear interaction of these waves (Longuet-Higgins, 1950). At frequencies above 1 Hz, seismic noise essentially results from anthropogenic sources (circulation, factories, etc.) and should be studied with care (Campillo et al., 2011).
Both microseismic peaks are dominated by fundamental mode surface waves, whose origin is still under debate (Landès et al., 2010). Different works propose that they are generated along coastlines (e.g., Friedrich et al. (1998); Bromirski and Duennebier (2002); Yang and Ritzwoller (2008)) or in deep sea areas (e.g., Cessaro (1994); Stehly et al. (2006); Chevrot et al. (2007)). At the same time, dense seismic arrays have shown that teleseismic body waves are also present in the secondary microseism (e.g., Backus et al. (1964); Iyer and Healy (1972)) and can often be associated with specific storms (e.g., Gerstoft et al. (2006, 2008)). As oceanic and atmospheric processes modulate the generation of seismic noise, it is not surprising, that ambient noise sources show clear seasonal and non-random pattern (Stehly et al., 2006; Landès et al., 2010) (Fig. 3.1).

3.2 Reconstruction of the Green's function

In this section we outline the basic principles for the reconstruction of the Green's function from coda waves with the help of an analogy between cross-correlations and time reversal (Derode et al., 2003a,b). This analogy is based on the spatial reciprocity theorem and the invariance towards time reversal (Fink, 1992) and applies equally to the coda of ambient noise correlations and earthquakes. The way to present the analogies here was inspired by the thesis works of Gouédard (2008); Hadziioannou (2011); Rivet (2008).

To understand the **source receiver reciprocity**, we consider a signal emitted by a source in point A and received in point B. It seems intuitive that for any complexity of the medium this signal is identical to a signal emitted by a source in point B and received in point A. This implies that inter changing the position of source and receiver

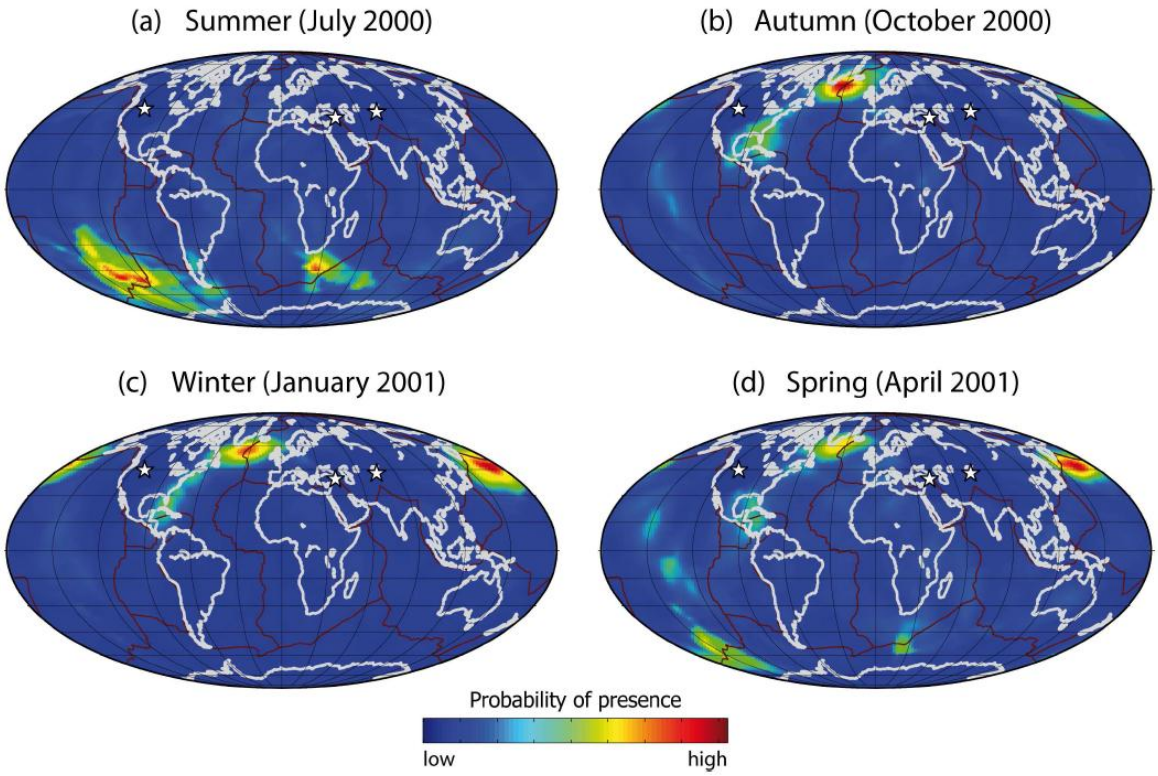

Figure 3.1: Seasonal variation of the location of P-wave seismic noise sources in the secondary microseismic band (0.1-0.3 Hz). (Source: Landès et al. (2010)).

does not change the shape of the received signal.

The **time invariance** results directly from the time symmetry of the wave equation. Let us consider the acoustic case of the wave equation:

$$\frac{\partial^2 \phi}{\partial t^2} = c^2 \Delta \phi, \tag{3.1}$$

where c is the celerity of the acoustic waves in the medium, ϕ the wave field and Δ the Laplace-operator. Let $\phi_{sol}(t)$ be a solution of the equation, than $\phi_{sol}(-t)$ is a solution as well, as $\partial(.)/\partial t^2 = \partial(.)/\partial(-t)^2$. Following this symmetry, the backwards propagation of waves will result in a concentration in the original source.

Now, to understand the analogy between cross-correlations and time reversal, we consider the following experiment (Fig. 3.2): two receivers A and B and a source C are placed in a medium. The source C emits a signal $S_C(t) = e(t)$. The displacement registered in A and B corresponds to a convolution of the signal emitted at the source C with the impulse response of the medium (Green's function) between A and C ($h_{AC}(t)$)

Figure 3.2: Illustration of the principle of time reversal. a) C emits a signal that is registered by A and B. b) B emits a signal that is received by C. C inverses the signal and re-emits it. A records the signal.

and B and C ($h_{BC}(t)$):

$$\begin{aligned} S_A(t) &= e(t) * h_{AC}(t), \\ S_B(t) &= e(t) * h_{BC}(t), \end{aligned} \tag{3.2}$$

where the asterisk stands for the convolution. The correlation between the signals registered in A and B is given by:

$$\begin{aligned} C_{AB}(\tau) &= S_A(t) * S_B(-t) \\ &= h_{AC}(t) * h_{BC}(-t) * f(t) \\ &= h_{AC}(t) * h_{CB}(-t) * f(t), \end{aligned} \tag{3.3}$$

where τ is the time of correlation and $f(t) = e(t) * e(-t)$. As we have seen, the wave propagation is reciprocal in space, and hence $h_{BC}(t) = h_{CB}(t)$. Let us now consider an experiment of time reversal. The source is placed in point B and point C plays the role of a mirror point. B emits an impulse that is registered in C ($h_{CB}(t)$). C then inverts the signal and re-emits ($h_{CB}(-t)$). At the end A will record:

$$S_A(t) = h_{BC}(-t) * h_{AC}(t). \tag{3.4}$$

The correlation formulation (3.3) is identical to the time reversal (3.4). Nevertheless we still have a dependence of C in the formulations. We are looking for an explicit formulation of h_{AB}.

If we now consider a similar experiment to the time reversal, but instead of a unique mirror point C, we have a series of points C_i that surround A and B. A emits an impulse that is diffused in all directions. B will register the signal $h_{AB}(t)$, that corresponds to the Green's function that we are looking for. All the points C_i register the signal $h_{AC_i}(t)$ and re-emit the time reversed signal $h_{AC_i}(-t)$. If the number of mirror points C_i is sufficiently large and without any loss of information, there exists a time-reversed wave that propagates back to the source in point A and is registered in point B as $h_{AB}(-t)$.

In other words, the time reversal experiment corresponds to the sum of the Green's functions between A and B in negative and positive times. As the time reversal is analogous to the cross-correlation, we can write:

$$\sum_{C_i} h_{AC}(t) * h_{C_iB}(-t) = h_{AB}(t) + h_{AB}(-t). \tag{3.5}$$

It can be shown, that this analogy is also valid in the case of few sources, but a very heterogeneous medium. In this case the scatterers act as secondary sources (Derode et al., 2003a,b).

We retain that the Green's function between two arbitrary points A and B in a medium can be reconstructed if one of the following conditions is fulfilled:

- The noise sources are distributed evenly around the receivers.
- The medium is highly heterogeneous, so that the scatterers act as secondary sources.

As we have seen, the noise sources are not distributed symmetrically, and the correlations of ambient seismic noise often result in anisotropic functions (Fig. 3.3). We can hence conclude that the cross-correlations have not converged to the Green's function. However, as Hadziioannou et al. (2009) have shown, a complete convergence is not necessary for seismic monitoring.

3.3 Use of ambient seismic noise cross-correlations in seismology

In seismology Campillo and Paul (2003) were the first to show the emergence of surface waves from cross-correlations of earthquake coda waves. One year later, Shapiro and Campillo (2004) used ambient seismic noise for the Green's function reconstruction, opening the way to numerous applications in seismology. Shapiro et al. (2005) and Sabra et al. (2005) used passive seismic imaging in California, and demonstrated the high spatial accuracy of the method that largely exceeds the resolution of active techniques for regional tomographies. Since then, surface waves from ambient seismic noise correlations are widely used for high-resolution imaging of the Earth's lithosphere. Ritzwoller et al. (2011) assort publications in this domain from all around the globe; e.g. US: Moschetti et al. (2007); Bensen et al. (2008); Ekström et al. (2009); Asia: Kang and Shin (2006); Zheng et al. (2008); Li et al. (2009); Europe: Villaseñor et al. (2007); Yang et al. (2007); New Zealand and Australia: Lin et al. (2007); Saygin and Kennett (2010); Arroucau et al. (2010); Ocean bottom and islands: Gudmundsson et al. (2007). However, surface waves are not sufficient to explore the deep structure of the Earth as they have limited

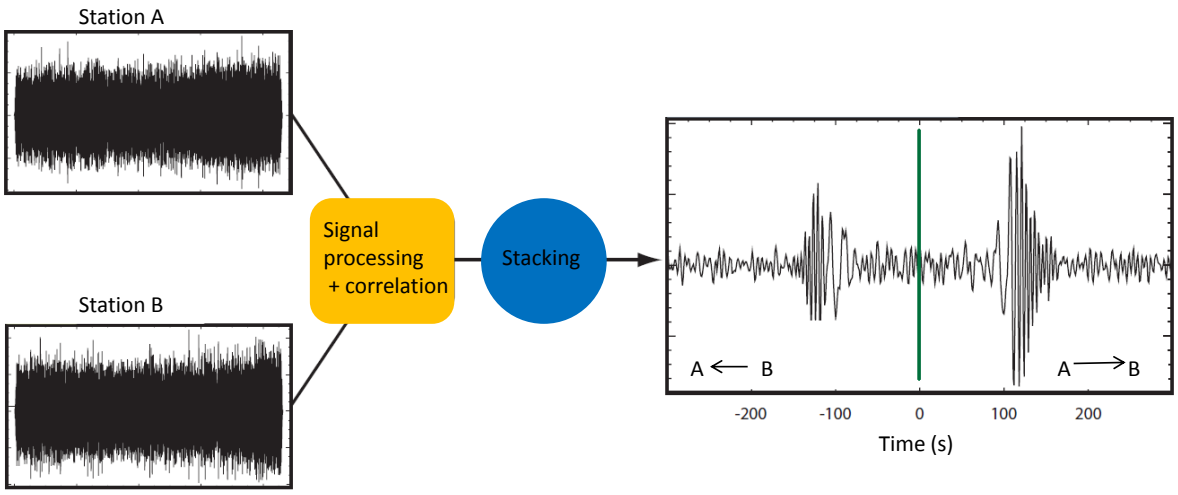

Figure 3.3: Illustration of the Green's function reconstruction from seismic noise recorded at station A and B. After data specific processing steps, the records are correlated and in general stacked to obtain the correlation shown on the right handside. We can see the causal (right) and anti-causal (left) part of the fundamental Rayleigh waves. The positiv times correspond to a wave that propagated from station A to station B, and vice-versa for the negative times. (modified after Landès (2009)).

depth resolution. By merging noise correlations and earthquake records the frequency band could be extended, and hence the depth of investigation (Yao et al., 2006; Yang et al., 2008a,b). Roux et al. (2005) have shown that P-waves are contained in the noise correlation and that they can be extracted at local scale. Recently, crustal high-frequency body wave reflections have been detected within noise correlations from dense regional arrays (Zhan et al., 2010; Ruigrok et al., 2011; Poli et al., 2012b; Lin et al., 2013), as well as reflections from the mantle transition zone (Poli et al., 2012a) and the core (Lin et al., 2013). Boué et al. (2013) have shown that also at global distances between seismic stations, body waves that propagated through the entire Earth can be extracted and used for high-resolution imaging techniques.

In the last years, the feasibility to use noise cross-correlations to monitor continuous changes in medium properties within volcanoes and active faults was demonstrated (e.g., Sens-Schönfelder and Wegler (2006); Wegler and Sens-Schönfelder (2007); Brenguier et al. (2008b,a)). In an attempt to locate the medium changes in space, a couple of works applied a geometrical regionalization procedure (Brenguier et al., 2008b; Duputel et al., 2009; Chen et al., 2010; Takagi et al., 2012; Froment et al., 2013), which however has a very limited resolution. We present in part III an inversion procedure, based on probabilistic approaches, that allows to image medium changes with a much higher spatial resolution.

The success of both noise based seismic imaging and monitoring depends on spatio-temporal properties of the available noise wave-field. It is hence logical, that there are extensive studies to better characterize the distribution of noise sources and to evaluate the effects of this distribution for tomography and monitoring (Tsai, 2009; Yao and van der Hilst, 2009; Froment et al., 2010). In many cases knowledge of the distribution of the noise sources can bring important information about the coupling between the solid Earth, the ocean and the atmosphere.

To summarize, we can identify three main types of seismological applications related to noise correlations:

1. studies of spatio-temporal distribution of seismic noise sources.
2. noise-based tomographic imaging at different scales.
3. noise based seismic monitoring.

In the following, we will have a closer look at noise based monitoring.

3.4 Monitoring global velocity changes

Let us imagine a global (spatially homogeneous) velocity change in a medium. This change in the medium will show its signature in the coda in form of a time shift δt in the arriving waves. The time shift, in the case of a global velocity change, grows proportionally with the time t that the waves spent in the medium. This effect is illustrated in Fig. 3.4 for a homogeneous velocity diminution of 1%. If the velocity variation is the same everywhere in the medium, the relation between δt and t is linear: $\delta t/t = const$. If the distance remains constant, $\delta v/v + \delta t/t = const$. The relative velocity variation is then given by:

$$\delta v/v = -\delta t/t. \tag{3.6}$$

To quantify the temporal change in the diffuse coda, we discuss in the following in further detail the doublet technique (also referred to as moving-window cross-spectrum technique (MWCST)) that has been developed in the eighties (Poupinet et al., 1984), and the more recent stretching technique (Sens-Schönfelder and Wegler, 2006).

3.4.1 Doublet technique

Poupinet et al. (1984) developed a method to measure velocity changes in the crust from the coda of repetitive earthquakes that have almost identical wave-forms. These repetitive earthquakes are commonly referred to as *doublets* or *multiplets*. Hence the name doublet technique. The technique is also known in literature as moving-window cross-spectrum technique (MWCST) and has been widely used for monitoring velocity changes

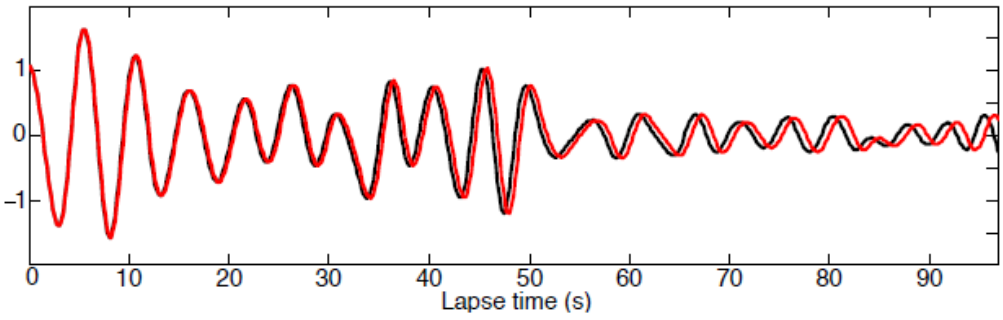

Figure 3.4: Illustration of the effect of a velocity diminution of 1% on the coda. In black, the signal prior and in red after the velocity change. (Source: Froment (2011))

(Ratdomopurbo and Poupinet, 1995; Schaff and Beroza, 2004; Brenguier et al., 2008b,a).

The idea of the seismic doublet technique is to measure a time-shift δt_i between a reference signal φ_{Ref} that corresponds to the initial state, and a current signal φ_{Ref} that has encountered a global velocity change in the medium (Fig. 3.5a). The time-shift is measured in short time windows centered around various lapse times t_i (Fig. 3.5b). The relative time shift $\delta t/t$ is then estimated by a linear regression passing through zero (Fig. 3.5d). $\delta v/v$ can be obtained according to equation 3.6.

In the time domain the time delay between the windows may be measured as the peak in correlation between the two signals, but it is generally more precise to measure the delay in the frequency domain. To measure δt in the frequency domain, the windowed segments are Fourier transformed and the cross-spectrum $X(f)$ between the two Fourier-transformed windowed time series ($\mathcal{F}_{\text{Ref}}$ and $\mathcal{F}_{\text{Curr}}$) is calculated as follows:

$$X(f) = \mathcal{F}_{\text{Ref}}(f)\mathcal{F}^*_{\text{Curr}}(f), \tag{3.7}$$

where the asterisk denotes the complex conjugation and f is the frequency. The complex cross-spectrum can also be represented by its amplitude $|X(f)|$ and phase $\phi(f)$:

$$X(f) = |X(f)|\, e^{i\phi(f)}. \tag{3.8}$$

Assuming that the time-shift is constant in each window, ϕ is linearly proportional to the frequency f:

$$\phi(f) = 2\pi\delta t_i f. \tag{3.9}$$

From a linear regression we can estimate δt_i (Fig. 3.5c). The error can be determined as the squared misfit of the data to the modeled slope. Clarke et al. (2011) refined the analysis and incorporated a weight during the regression which depends on the cross-coherence at each sampled frequency and that is assigned to each cross-phase value. But this aspect is not relevant for this thesis and hence we will not discuss it in greater detail.

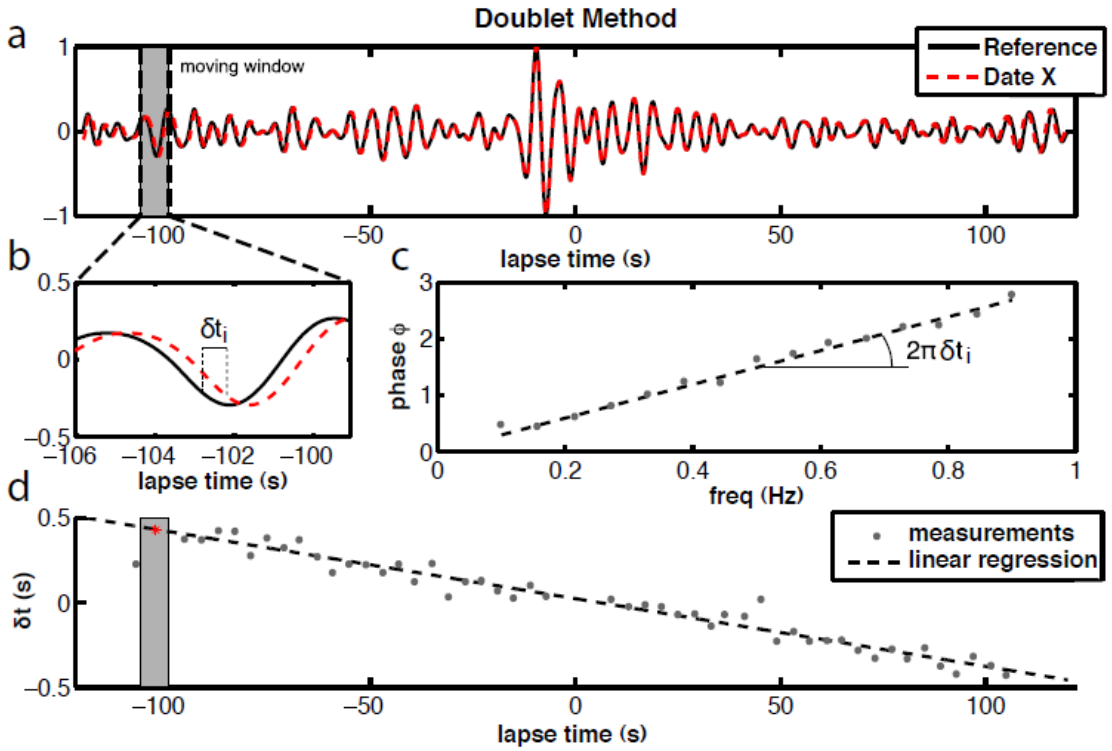

Figure 3.5: Illustration of the doublet technique. (a) Reference signal φ_{Ref} (black) and time delayed signal φ_{Curr} (red). (b) Zoom into the windowed cross-correlations functions, marked with the shaded grey area in Fig. 3.5a. (c) The phase of the cross-spectrum of the windowed cross-correlations. The slope is equal to $2\pi\delta t$. (d) Estimation of $\delta t/t$ via linear regression of the delay measurements in all time windows. (Source: Hadziioannou (2011)).

3.4.2 Stretching technique

Another more recent method to quantify the temporal evolution of the seismic velocity is the stretching technique (Lobkis and Weaver (2003), Sens-Schönfelder and Wegler (2006)). This method builds on the fact that a small global velocity change introduces a relative time-shift between φ_{Curr} and φ_{Ref} which is proportional to the traveltime. The current waveform φ_{Curr} is stretched or compressed in time by a factor $t \rightarrow t(1 \pm \varepsilon)$, depending on an eventual increase or decrease in the medium velocity. Then, the stretched waveform is correlated with the reference waveform in the time domain:

$$CC(\varepsilon) = \frac{\int_{t_1}^{t_2} \varphi_{\mathrm{Curr}}\left[t(1-\varepsilon)\right] \varphi_{\mathrm{Ref}}\left[t\right] dt}{\sqrt{\int_{t_1}^{t_2} \varphi_{\mathrm{Curr}}^2\left[t(1-\varepsilon)\right] dt \int_{t_1}^{t_2} \varphi_{\mathrm{Ref}}^2\left[t\right] dt}}, \tag{3.10}$$

where t_1 and t_2 are the beginning and the end of the time window used. The value of ε, that maximizes the cross-correlation coefficient CC between φ_{Curr} and φ_{Ref} corresponds

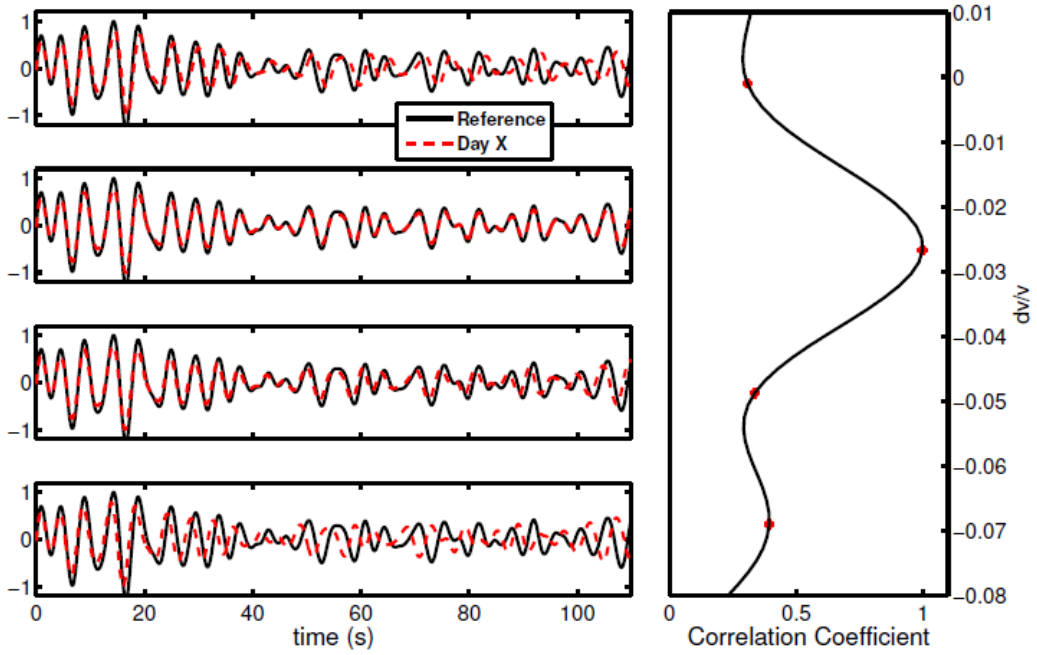

Figure 3.6: Stretching method. Left: the red signal has been stretched for different values of ε. Right: the calculated correlation coefficient between the stretched and the reference trace (black) for the different values of ε. (following Hadziioannou (2011))

to the relative velocity change in the medium $\varepsilon = \frac{dv}{v}$. An illustration of this method is found in Fig 3.6.

3.4.3 Comparison of the methods

Hadziioannou et al. (2009) compared the two techniques quantitatively on a controlled laboratory data-set. They came to the conclusion that: A strong point of the Doublet technique is that it does not suffer from amplitude changes of the waveform and manages clock errors in the origin time without further processing. Besides the processing is very fast. On the other hand, the main advantage of the stretching technique is its increased stability in presence of residual noise in the correlations and its increased sensitivity to detect weak changes. This copes with the disadvantages of a more time consuming processing and the not entirely correct assumption of a linear stretching of the waveform that underlies this technique. For the present work, an essential point in favor of the stretching technique is that we measure not only the stretching of the waveform in time, but also its coherence. We use the waveform decoherence to obtain an additional, independent information about structural changes in the medium (section 3.6).

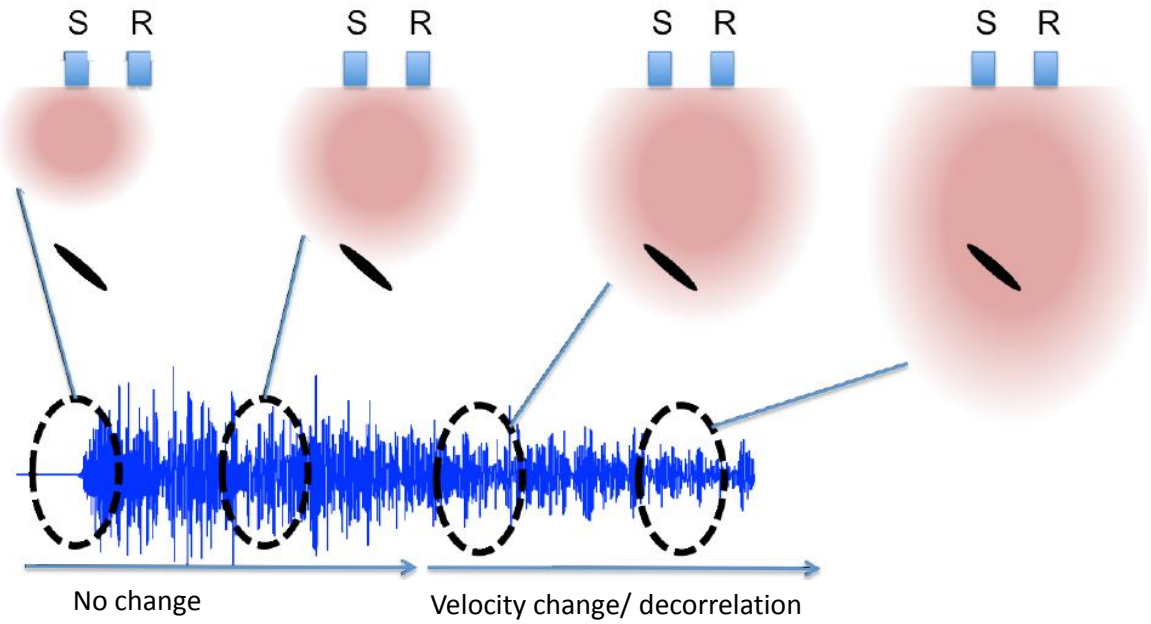

Figure 3.7: Schematic view of the spatio-temporal sensitivity of coda waves to a local change (black oval). The diffusive halo of waves propagating in the medium is represented in brown. Its characteristic size is governed by $\sqrt{Dt}$, where D is the diffusion constant in the medium and t the time in the coda. At early times in the coda (first two snapshots on the left), the waves propagating from the source S to the receiver R have hardly felt the change. Later on (two snapshot on the right), the waves have likely encountered the change and the coda is partially delayed/decorrelated. Modified after Planès et al. (2012).

3.5 Monitoring local velocity changes

In most cases, the assumption that $\varepsilon_{app} = \frac{dv}{v}$ is not totally true because the relative velocity changes are restricted to limited regions and are not spatially homogeneous. In these cases, the apparent velocity changes ε^i_{app} depend on the time in the coda, on the position of the change relative to the couple of receivers i and on the intensity of the local change $\frac{dv}{v}(x)$. As a result $\varepsilon^i_{app} < \frac{dv}{v}(x)$.

So instead of using the stretching technique on the entire coda, we use it in limited time windows (at least two periods long) which allows us to study the evolution of the temporal changes with time in the coda (Obermann et al., 2013b).

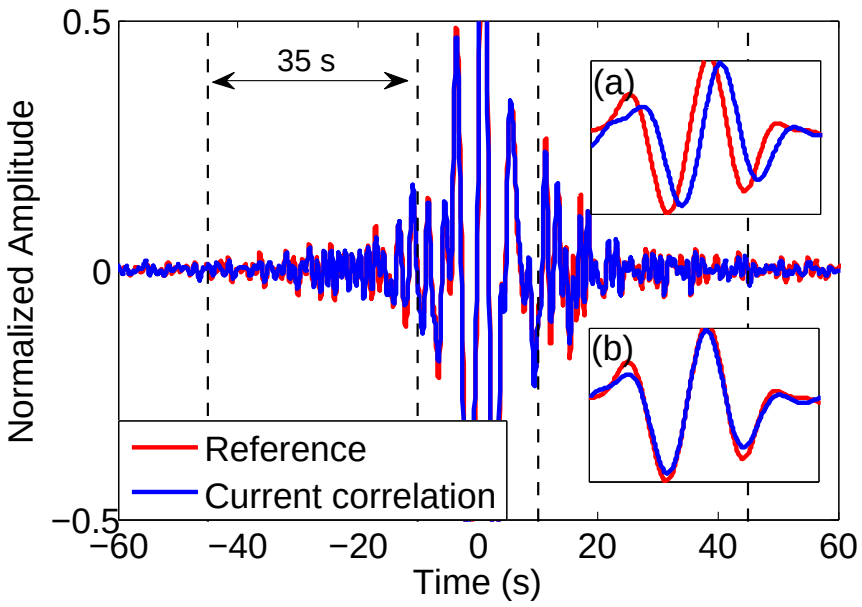

Figure 3.8: Reference correlation function (blue) and "current" correlation function (red). Inset (a) shows the time delay of the "current" correlation function in the coda. Inset (b): the "current" correlation function has been corrected for its time delay. We observe waveform decoherence.

3.6 Monitoring structural changes

We now focus on the monitoring of the waveform decoherence (Fig. 3.8). We consider again a wave that encounters a local velocity perturbation. The change will show its signature on the "current" record (blue) in form of a time shift of the later arriving waves when compared to a reference (initial state in red) (Fig. 3.8, Inset a). We quantify the temporal change with the stretching technique and correct for it by multiplying the "current" record with ε^i_{app}. After the correction of the time shift in the coda, we often observe a small change remaining in the waveform (Fig. 3.8, Inset b). This signature results from local structural changes in the medium that are responsible for residual distortion or decorrelation of the coda waveforms. In experiments with active sources, the waveform coherence can be directly measured by correlating the signals at different states of the experiment.

This waveform decoherence has been used in acoustics on laboratory experiments with aluminum plates (Michaels and Michaels, 2005) and on concrete (Larose et al., 2010; Rossetto et al., 2011; Planès et al., 2013) to quantify defects in materials that are much smaller than one wavelength. We use the decoherence in Chapter 6 and Chapter 7 successfully in seismology.

Part II

Simulation and analysis of coda waves

Chapter 4

Measuring the scattering mean free path of Rayleigh waves on a volcano from spatial phase decoherence

Contents

Numerically it is relatively easy to determine the scattering mean free path ℓ and the transport mean free path $\ell^\star$ from the coherent and incoherent part of the signals respectively (section 5.2.2). With seismic data there are attempts to separate the intrinsic and scattering attenuation (Del Pezzo et al., 2001), which theoretically gives access to $\ell^\star$. However, this remains very challenging if not unfeasible in most regions. Here, we propose an alternative way to determine the scattering mean free path by using the phase information of coda waves instead of the amplitude. For this purpose, during the dissertation project of my master thesis prior to my PhD, we designed a field experiment on a volcano in the French Auvergne, that would enable us to measure the scattering

mean free path from spatial phase decoherence.

Measuring the scattering mean free path of Rayleigh waves on a volcano from spatial phase decoherence

Anne Obermann, Eric Larose, Ludovic Margerin, Vincent Rossetto.

Article accepted at *Geophysical Journal International* 2013.

Abstract: We analyze the statistics of phase fluctuations of seismic signals obtained from a temporary small aperture array deployed on a volcano in the French Auvergne. We demonstrate that the phase field satisfies Circular Gaussian statistics. We then determine the scattering mean free path of Rayleigh waves from the spatial phase decoherence. This phenomenon, observed for diffuse wavefields, is found to yield a good approximation of the scattering mean free path. Contrary to the amplitude, spatial phase decoherence is free from absorption effects and provides direct access to the scattering mean free path.

4.1 Introduction

In heterogeneous media, after a sufficient amount of time of propagation, waves enter the multiple scattering regime. In this regime waves bounce on several heterogeneities before reaching the receivers. The characteristic length (resp. time) after which such a regime can be observed is the scattering mean free path ℓ (resp. time), defined as the distance (resp. time) between two successive scattering events. This distance also refers to the characteristic distance of attenuation of the coherent wavefront. The coherent wave, rigorously defined as the wave that resists ensemble averaging, roughly corresponds to the direct (or ballistic) wave. The scattering mean free path ℓ reflects the degree of heterogeneity of the medium: the longer the scattering mean free path, the weaker the scattering. ℓ depends on two features: the intensity of the fluctuations of the mechanical properties in the medium, and the spatial extension of the fluctuations. In nature, ℓ is found to vary over several orders of magnitude, depending on the frequency, and also on the nature of the material at test.

The multiple scattering regime can be observed in many fields of wave physics. It was for instance demonstrated in optics and in acoustics with the observation of the coherent backscattering effect (or weak localization) (van Albada and Lagendijk, 1985; Wolf and Maret, 1985; Tourin et al., 1997). Seismic waves are also known to exhibit long lasting wave-trains that follow ballistic P- or S-waves: the so-called seismic coda. Since the pioneering works of Aki (1969), the coda is known to be reproducible and has been recognized to possibly originate from multiple scattering effects. Among other

applications, scattering parameters are excellent candidates for remotely characterizing geological media at depth, which is a key challenge in geosciences (Margerin and Nolet, 2003). Nevertheless, in most practical cases it is very hard to discriminate scattering effects from intrinsic absorption effects. For instance, the Spatial Auto-Correlation (SPAC) technique, widely used in near-surface geophysics (Aki, 1957), consists in fitting the seismic wave spatial-correlation by the product of a Bessel function and an exponential decay whose physical interpretation remains debated (Prieto et al., 2009; Tsai, 2011; Nakahara, 2012). At longer distance from the source, it is also possible to study the envelope of the diffusive coda, which in principle allows one to evaluate the scattering and intrinsic attenuation (Hoshiba, 1993; Carcolé and Sato, 2010). In continental areas however, an unbiased estimation of these two parameters may become difficult when the leakage of scattered waves is dominant (Margerin et al., 1999). Although a possible remedy has been recently proposed (Del Pezzo and Bianco, 2010), evaluating the scattering mean free path of a complex material without the bias of intrinsic absorption remains a challenging issue.

Recently, Anache-Ménier et al. (2009) studied the phase fluctuations in the coda of earthquakes recorded during a temporary experiment at the Pinyon Flats Observatory in California. They proved that seismic coda waves obey Gaussian statistics in certain frequency bands, and suggested to use the correlation of the spatial phase derivative measured in the coda to estimate the scattering mean free path. The key point of their approach is that the phase fluctuations are caused by random phase shifts acquired at each scattering event, and are therefore independent of the absorption structure. Note that the quantity of physical interest is the spatial phase difference (or derivative) and not the phase itself, because the latter is dominated by a trivial ωt dependence, with ω the circular frequency. The determination of the scattering mean free path at Pinyon Flats was not completely conclusive because the aperture of the experimental network was less than one wavelength.

In this article, we pursue the work of Anache-Ménier et al. (2009) and communicate the results of a temporary field experiment that was specially designed to measure the scattering mean free path from spatial phase decoherence. The field experiment was set up at the foot of a recent (late pleistocene & holocene) but inactive volcano in the French Auvergne in 2010. A volcanic area is particularly convenient for the study, as areas with tectonic and/or volcanic activity are highly heterogeneous and known to produce long lasting coda waves (Abubakirov and Gusev, 1990; Aki and Chouet, 1975; Aki and Ferrazzini, 2000; Goodman, 1985). Larose et al. (2004a) studied the weak localization of seismic waves at this site and found an estimate of 200 m for the mean-free path for seismic waves around 20 Hz. This gives us a typical order of magnitude of the scattering mean free path that we can expect in our experiment.

In section 4.2 we first give an overview of the theoretical aspects that underlie our study. Then, in section 4.3 we describe the field experiment; prove that our signal obeys

circular Gaussian statistics, the requirement to determine the scattering mean free path ℓ from spatial phase decoherence; and show the good estimate of ℓ that we obtain with our experiment (section 4.3.5).

4.2 Theoretical aspects

4.2.1 Definition of the phase

To define unambiguously the phase of the seismic wavefield $u(t, \mathbf{r})$ recorded at position $\mathbf{r}$ and time t, we introduce the associated analytic signal as follows:

$$\Psi(t, \mathbf{r}) = u(t, \mathbf{r}) + i\mathrm{H}u(t, \mathbf{r}), \tag{4.1}$$

where i is the imaginary unit and $\mathrm{H}u(t) = \mathrm{P.V.} \int \frac{u(t')dt'}{t-t'}$ denotes the Hilbert transform of the field $u(t)$. Using the polar representation of complex numbers, the field Ψ can be expressed as:

$$\Psi(t, \boldsymbol{r}) = A(t, \boldsymbol{r})\exp(i\Phi(t, \boldsymbol{r})) \tag{4.2}$$

where $\Phi(t, \mathbf{r})$ is the wrapped phase of the field which takes values in $(-\pi : \pi]$. By correcting the phase Φ for the 2π jumps that occur at $\pm\pi$, one obtains the unwrapped phase Φ_u, which is a continuous function taking values in $\mathcal{R}$. The unwrapping operation can be performed either in the time or in the spatial domain. In this work, the field is analyzed on a linear array of seismic stations, which calls for the spatial unwrapping of the phase. In general, the unwrapping operation is not topologically invariant, i.e., it depends on the path from the initial to the final point. In our experiment, the path is dictated by the linear geometry of the array. Note that the phase of narrowly band-passed signals is dominated by the term ωt -ω the central frequency-, which does not convey any interesting information on the medium. By evaluating the *phase difference* between two nearby stations, this trivial ωt dependence is removed and the interesting fluctuations of the phase caused by the presence of heterogeneities in the medium become accessible. Motivated by this observation, we introduce two possible definitions of the phase difference. The first one, denoted by $\Delta\Phi \in (-2\pi, 2\pi]$, is obtained by subtracting the wrapped phases measured at two adjacent stations. The second one, denoted by $\Delta\Phi_u$, is obtained by unwrapping the phase spatially at each time step. Due to the finite separation between stations, it is impossible to distinguish between a large physical jump of the phase from an artefact caused by its mathematical definition. To circumvent this cycle skipping problem, we impose that the absolute value of a phase jump between two nearby stations cannot exceed π, i.e. $\Delta\Phi_u$ takes values in $(-\pi, \pi]$. Using this convention, the following relations between the two definitions of the phase difference can be established:

$$\begin{aligned} \Delta\Phi_u &= \Delta\Phi, && \Delta\Phi \in (-\pi, \pi] \\ \Delta\Phi_u &= \Delta\Phi - 2\pi, && \Delta\Phi \in (\pi, 2\pi] \\ \Delta\Phi_u &= \Delta\Phi + 2\pi, && \Delta\Phi \in (2\pi, -\pi] \end{aligned} \tag{4.3}$$

4.2.2 Circular Gaussian Statistics

Although Gaussianity is a standard hypothesis in statistical wave propagation problems, we give some heuristic arguments in support of this assumption. In the multiple scattering regime, the field u measured at a point can be considered as a superposition of a large number of partial waves ψ_α that propagated along independent paths:

$$u = \mathrm{Re}\sum_\alpha \psi_\alpha = \mathrm{Re}\sum_\alpha a_\alpha \exp(i\phi_\alpha), \tag{4.4}$$

where the subscript α labels the different trajectories. The hypothesis that the partial waves follow independent paths is valid when the average distance between two scattering events, i.e. the mean free path ℓ, is much larger than the wavelength λ. Due to the phase shift that occurs at each scattering event, after a few scattering mean free paths, the phases of the partial waves become random and uniform in the interval $(-\pi : \pi]$. In these conditions, we may apply the central limit theorem, which stipulates that the arithmetic mean of a large number of identically distributed and independent random variables will be approximately normally distributed. Hence, we conclude that the seismic coda wavefield $u(t)$ recorded at an arbitrary point of the medium can be modeled as a centered Gaussian random variable with variance $\sigma^2(t) = I(t)$, where $I(t)$ is the intensity of the coda. Because the Hilbert transform is a linear operator, it can be demonstrated that the imaginary part of the associated analytic signal obeys the same Gaussian distribution and is independent from the real part(Goodman, 1985). A complex random variable which verifies the properties just enunciated is known as gaussian circular. Based on this observation, we now *assume* that the complex analytic signals recorded at an arbitrary number of points at time t in the coda are jointly gaussian circular:

$$P(u_1, v_1, \ldots, u_N, v_N) = P(\Psi_1, \ldots, \Psi_N) = \frac{1}{\pi^N \det(\boldsymbol{C})} \exp\left[-(\Psi_1^* \ldots \Psi_N^*) \boldsymbol{C}^{-1} \begin{pmatrix} \Psi_1 \\ \vdots \\ \Psi_N \end{pmatrix} \right], \tag{4.5}$$

where P denotes the probability density, $u_1 = \mathrm{Re}\Psi_1$, $v_1 = \mathrm{Im}\Psi_1$, and $\boldsymbol{C} = \left\langle \Psi_i \Psi_j^* \right\rangle$ is the covariance matrix. $(\Psi_i \ldots \Psi_N)$ are N different measurements of the field after application of a normalization procedure to be detailed below. In this work, we do not test the validity of Eq. (4.5) in its full extent. Instead, we will derive marginal distributions for the phase and its derivative based on assumption (4.5), and compare the experimental measurements with the theoretical predictions to obtain estimates of the wavenumber and mean free path under the array. We also assume that different times in the coda correspond to different realizations of the underlying random process and that temporal and statistical averaging are equivalent (ergodic hypothesis).

To complete our definition of the statistical properties of the wavefield, the covariance matrix $\boldsymbol{C}$ must be specified. Each element of the matrix depends on the two-point correlation function of the recorded wavefield u, narrowly band-passed around circular frequency ω. In the multiple-scattering regime, the field-field correlation function in the

coda may be approximated as follows:

$$\langle u(\mathbf{R}+\mathbf{x}/2,t)u(\mathbf{R}-\mathbf{x}/2,t)\rangle = \frac{S(\omega)e^{-R^2/4Dt-t/t_a}}{(4\pi Dt)^{d/2}}\mathrm{Im}G_d(\omega,|\mathbf{x}|), \tag{4.6}$$

where $S(\omega)$ is proportional to the source spectrum, $\mathbf{R}$ is the position vector connecting the source to the midpoint of the two receivers, D is the diffusion constant of the waves, t_a is their absorption time, and G_d is the average Green's function of the multiple-scattering medium. The subscript d represents the space dimension and $|\cdot|$ the corresponding Euclidean distance. In our experiment u represents the vertical component of the ground displacement. Formula (4.6) has been demonstrated for scalar waves by (Barabanenkov and Ozrin, 1991) based on an eigenfunction expansion of the Bethe-Salpeter equation. Extensions to vectorial fields such as electromagnetic waves or coupled P and S waves have also been published (Barabanenkov and Orzin, 1995; Margerin, 2013). Physically, Eq. (4.6) expresses the diffusive transport of the energy from the source to the array, and displays explicitly the proportionality between field-field correlations and the imaginary part of the Green's function. In seismology, the successful extraction of the surface wave part of Green's function between two stations from coda waves has been previously reported by (Campillo and Paul, 2003; Paul et al., 2005). A very important point to be noted is that the Green's function which appears in Eq. (4.6) depends solely on the mean free path, at least for sufficiently weak absorption. We must now determine the correct form of G_d to be inserted in Eq. (4.6). From our previous coherent back-scattering experiment in the same area (Larose et al., 2004a), we concluded on the dominance of Rayleigh waves in the coda. In particular, by measuring the lateral extension of the backscattering enhancement spot as a function of frequency, we were able to estimate the dispersion law of Rayleigh waves, in excellent agreement with independent estimates based on classical seismic techniques. After normalization of the two-point correlation function by the intensity received in the coda, we can write the elements of the covariance matrix as:

$$\langle \Psi_i \Psi_j^* \rangle = \bar{C}(|\mathbf{x}_j - \mathbf{x}_i|) = J_0(k|\mathbf{x}_j - \mathbf{x}_i|)e^{-|\mathbf{x}_j-\mathbf{x}_i|/2l}, \tag{4.7}$$

where k and ℓ denote the wavenumber and mean free path of the Rayleigh waves under the array, respectively. The function $\bar{C}$ is recognized as the normalized two-point correlation function of the wavefield. The underlying 2-D character of the propagation is apparent in Eq. (4.7). Note that the details of the intensity normalization are unimportant because the distribution of energy in the coda is spatially homogeneous at the scale of the linear array. While relation (4.7) gives in principle access to the mean free path ℓ, the oscillatory character of the Bessel function J_0 makes it difficult to extract the rate of decay of the exponential term in practice. The key of the method proposed by Anache-Ménier et al. (2009) is to remove the oscillatory term by considering the correlation of the phase derivative. The main properties of the phase and of its derivative are therefore outlined in the next paragraph.

4.2.3 Statistical properties of the phase

We first discuss briefly the one-point statistics ($N = 1$). We remind the reader that the real and imaginary part of the field are independent and normally distributed with zero mean and equal variance $\sigma^2 = I(t)$, which depends on the time in the coda. Although our paper focuses on the properties of the phase, it is worth recalling the marginal probability densities of other quantities derived from the complex field Ψ, as they are readily measured experimentally:

- The amplitude A follows a Rayleigh distribution:

$$P(A) = \frac{2A}{\langle I \rangle} \exp\left(-\frac{A^2}{\langle I \rangle}\right), \tag{4.8}$$

  where $\langle I \rangle = \langle A^2 \rangle$ is the average intensity. Using a large dataset from northern Japan, Nakahara and Carcolé (2010) have demonstrated that the amplitude of coda waves is described by Rayleigh statistics with very good accuracy.

- The distribution of intensity is described by a decaying exponential law:

$$P(I) = \frac{1}{\langle I \rangle} \exp\left(-\frac{I}{\langle I \rangle}\right). \tag{4.9}$$

  which follows straightforwardly from Eq. (4.8) after introduction of the new variable $I = A^2$.

- Finally, as previously remarked, the phase Φ exhibits a uniform probability distribution:

$$P(\Phi) = \frac{1}{2\pi}. \tag{4.10}$$

As any oscillating signal shows a uniform phase distribution, the last property does not constitute a conclusive test of Gaussianity. In addition, we wish to point out that a wavefield obeying one-point circular Gaussian statistics does not necessarily result from multiple scattering. On the one hand, in a single scattering medium with low-contrast inclusions, the phase of the waves is not significantly modified upon scattering, and remains essentially equal to ωt, which annihilates the independent and random character of the phase. On the other hand, in a dilute scattering medium containing high-contrast inclusions, each scattering event introduces a possibly large phase shift which depends on the scattering angle, the geometry, and the physical properties of the obstacle; since the phase of the singly- or doubly- scattered partial waves may also be considered as random, the resulting wavefield may obey Gaussian statistics and exhibit fluctuations similar to those observed in the high-order multiple scattering regime.

We now explore in more details the two-point statistics ($N = 2$). Consider two wavefields ($\Psi_1 = A_1 e^{i\Phi_1}$, $\Psi_2 = A_2 e^{i\Phi_2}$), recorded at geophones separated by a distance δ. Our objective is to derive the statistical properties of the phase difference $\Delta\Phi = \Phi_2 - \Phi_1$,

of the unwrapped phase difference $\Delta\Phi_u$, and of the phase derivative Φ'. The correlation matrix has the following simple form:

$$\boldsymbol{C} = \begin{pmatrix} 1 & g \\ g & 1 \end{pmatrix}, \tag{4.11}$$

where $0 < g = \bar{C}(\delta) < 1$. The determinant and inverse of this matrix are readily calculated. Inserting these results into Eq. (4.5), one obtains the joined distribution of the two fields:

$$P(\Psi_1, \Psi_2) = \frac{e^{-|\Psi_1|^2 - |\Psi_2|^2 + 2g\mathrm{Re}\Psi_1\Psi_2^*}}{\pi^2(1-g^2)}. \tag{4.12}$$

Introducing the new variables $(A_1, A_2, \Phi_1, \Phi_2)$ and integrating out the phase Φ_1 yields:

$$P(A_1, A_2, \Delta\Phi) = \frac{A_1 A_2 (2\pi - |\Delta\Phi|)}{\pi^2(1-g^2)} e^{\dfrac{-A_1^2 - A_2^2 + 2A_1A_2 g\cos\Delta\Phi}{1-g^2}}, \tag{4.13}$$

where $\Delta\Phi \in (-2\pi, 2\pi]$. To eliminate the remaining variables A_1 and A_2, it is convenient to introduce polar coordinates $A_1 = r\cos\theta$, $A_2 = r\sin\theta$ with $\theta \in [0, \pi/2]$. The integration over (r, θ) is a straightforward computational exercise and the final result is:

$$P(\Delta\Phi) = \frac{N(1-g^2)}{1-f^2}\left(1 + \frac{f\arccos -f}{\sqrt{1-f^2}}\right), \tag{4.14}$$

where $N = (2\pi - |\Delta\Phi|)/4\pi^2$. Note that the distribution of the unwrapped phase difference $\Delta\Phi_u$ is easily obtained using relations (4.3), and is formally identical to that of $\Delta\Phi$ with $N = 1/2\pi$. In the limit $\delta \to 0$, we may expand the phase difference $\Delta\Phi \approx \Phi'\delta$ and the correlation coefficient $g \approx 1 - Q\delta^2/2$, where Φ' represents the first spatial derivative of the phase and $Q = -\bar{C}''(0)$. Note that since the correlation function $\bar{C}$ is even, the correlation coefficient g must be expanded to second-order in the small parameter δ. Upon reporting these approximations into Eq. (13), and applying a Taylor series expansion around $\delta = 0$, we obtain the statistics of the first phase derivative:

$$P(\Phi') = \frac{Q}{2(Q + \Phi'^2)^{3/2}} \tag{4.15}$$

Remarkably, the first spatial derivative of the phase depends on only one parameter Q. Using the expression (4.7) for $\bar{C}$, we obtain $Q = k^2/2(1 - 2/(kl)^2) \approx k^2/2$. The last approximation is valid because the mean free path is in general much larger than the wavelength. This means that within the experimental accuracy, the measurement of Q does not put constraints on the mean free path. For sufficiently large values of the phase derivative, the probability density (4.15) is independent of the parameter Q and follows a power law decay $P(\Phi') \sim \Phi'^{-3/2}$, characteristic of circular gaussian statistics.

We now outline the derivation of the correlation function of the spatial phase derivative along the array. The method is analogous to the one employed to derive Eq. (4.14)

but the calculations are far more complex. We provide the key ingredients and refer the interested reader to the work of van Tiggelen et al. (1999) for more details. The first step is the calculation of the correlation matrix of four fields Ψ_i $(i = 1, 2, 3, 4)$ acquired at four positions: x_1, $x_1 + \delta$, x_3, $x_3 + \delta$. Using expression (4.7), we obtain:

$$\boldsymbol{C}(x,\delta) = \begin{pmatrix} 1 & \bar{C}(\delta) & \bar{C}(x) & \bar{C}(x+\delta) \\ -\bar{C}(\delta) & 1 & \bar{C}(x-\delta) & \bar{C}(x) \\ -\bar{C}(x) & -\bar{C}(x-\delta) & 1 & \bar{C}(\delta) \\ -\bar{C}(x+\delta) & -\bar{C}(x) & -\bar{C}(\delta) & 1 \end{pmatrix}, \tag{4.16}$$

where $x = x_3 - x_1$. Using a perturbation approach, the eigenvectors and associated eigenvalues of the matrix (4.16) are calculated to first and second order in the small parameter δ, respectively. In this way, the joint probability distribution of the fields and of their spatial derivatives ($\Psi(x_1)$,$\Psi(x_3)$,$\Psi'(x_1)$,$\Psi'(x_3)$) can be calculated. Introducing the polar representation $\Psi(x_i) = A(x_i)e^{i\Phi(x_i)}$, the joint probability distribution $P(A_1, A_1', A_3, A_3', \Phi_1, \Phi_1', \Phi_3, \Phi_3')$ of the amplitude and phase at x_1 and x_3 together with their spatial derivatives is obtained. Note that this probability density depends on $x = x_3 - x_1$ only. After integration over the amplitudes, amplitude derivatives and phases, the correlation function of the phase derivative may be expressed as (van Tiggelen et al., 2006):

$$\begin{aligned} C_{\Phi'}(x) =& \iint_{-\infty}^{+\infty} P(\Phi_1', \Phi_3')\Phi_1'\Phi_3' d\Phi_1' d\Phi_3' \\ =& \frac{1}{2}\log(\bar{C}(x))''(\log(1-\bar{C}(x)^2)) \end{aligned} \tag{4.17}$$

For sufficiently large x, the exact expression (4.17) can be approximated as follows:

$$C_{\Phi'}(x) \approx \frac{e^{-|x|/l}}{2|x|} \tag{4.18}$$

As anticipated, the oscillatory term $J_0(k|x|)$ does not show up in equation (4.18). Using numerical simulations, Anache-Ménier et al. (2009) have demonstrated that the convenient formula (4.18) applies for $x > \lambda/5$. Hence, correlations of the spatial derivative of the phase provide direct access to the mean free path. Two very important remarks must be made at this point. To derive Eq. (4.18), we have implicitly assumed that translational invariance applies. If the statistical properties vary under the array, the result (4.18) may well be invalid. The second point pertains to the evaluation of the spatial derivative of the field. Throughout the derivation of Eq. (4.18), we have assumed that the derivatives are evaluated in the direction of the array. The correlation function of the *directional* derivative of the phase at an angle α with respect to the array direction gives a quite different result. In particular the undesirable oscillations of the correlation $\bar{C}$ are not suppressed in this case (Ghysels, 2005).

4.3 Experiment and results

4.3.1 Experiment setup and data acquisition

We work at the foot of the neighboring volcanic craters "Grand Sarcoui" and "Puy des Goules" in the French Auvergne. Larose et al. (2004a) could show the evidence ofthe weak localization of seismic waves in this area (at 20Hz) and gave hence a proof of multiple scattering. To measure the scattering mean free path from phase decoherence, we set up an experiment that simultaneously fulfills two conditions: (1) The intergeophone spacing must be sufficiently small to ensure a good correlation of the signals at neighboring geophones; (2) The total aperture of the array should not be too small compared to the mean free path. From numerical simulations with a finite difference code (Derode et al., 2003b), we observed that the intergeophone spacing δ should be $\delta \leq \lambda/10$, where λ is the Rayleigh-wavelength, and that an increasing number of geophones significantly increases the precision of the determination of ℓ.
We see that it is essential to know the Rayleigh-wavelength in the area of interest. Therefore, in a preliminary study, we shot 20 refraction seismic profiles (hammer source) in the area of interest. We then computed the dispersion curves: once by determining the wavenumbers from the field correlation (Eq. 4.7) at different central frequencies, and once from a frequency-wavenumber analysis. From these analysis, we could determine an approximated wavelength of 24 m at 10 Hz, 11 m at 20 Hz and 7.5 m at 30 Hz.
We hence decided to work at high-frequencies (30 Hz) and set up a linear array of 48 geophones along an unpaved road at the foot of the volcanoes with an inter-geophone-spacing of δ =60 cm ($\approx \lambda/10$). The total length of the array is 28.8 m, which is approximately 4 times the dominant wavelength at 30 Hz. To decrease the ambient noise, we buried the geophones at 20 cm depth. We placed 18 explosives on unpaved roads around the receiver array to excite energy from all directions. The experimental setup is shown in Figure 4.1. The acquired data show long lasting coda waves with a high signal to noise ratio for the first 20 s in the coda (Fig. 4.2).
For our analysis we assume a 2D medium. This approach is valid as long as the vertical component of our signals is largely dominated by Rayleigh-waves (Larose et al., 2004a).

4.3.2 Test of one-point Circular Gaussian Statistics

To begin with, we test that the seismic coda waves that we acquired obey Circular Gaussian Statistics. Therefore, we filter the data with a narrow second-order bandpass filter of 5% around a central frequency of 30 Hz.

We selected a short time window of 1.5 s starting after the surface wave arrivals. We compute the imaginary part (Hilbert transform) of the recorded signals $u(t, \mathbf{r})$ that gives us access to the phase from the complex analytical signals (Eq. 4.4). We can define:

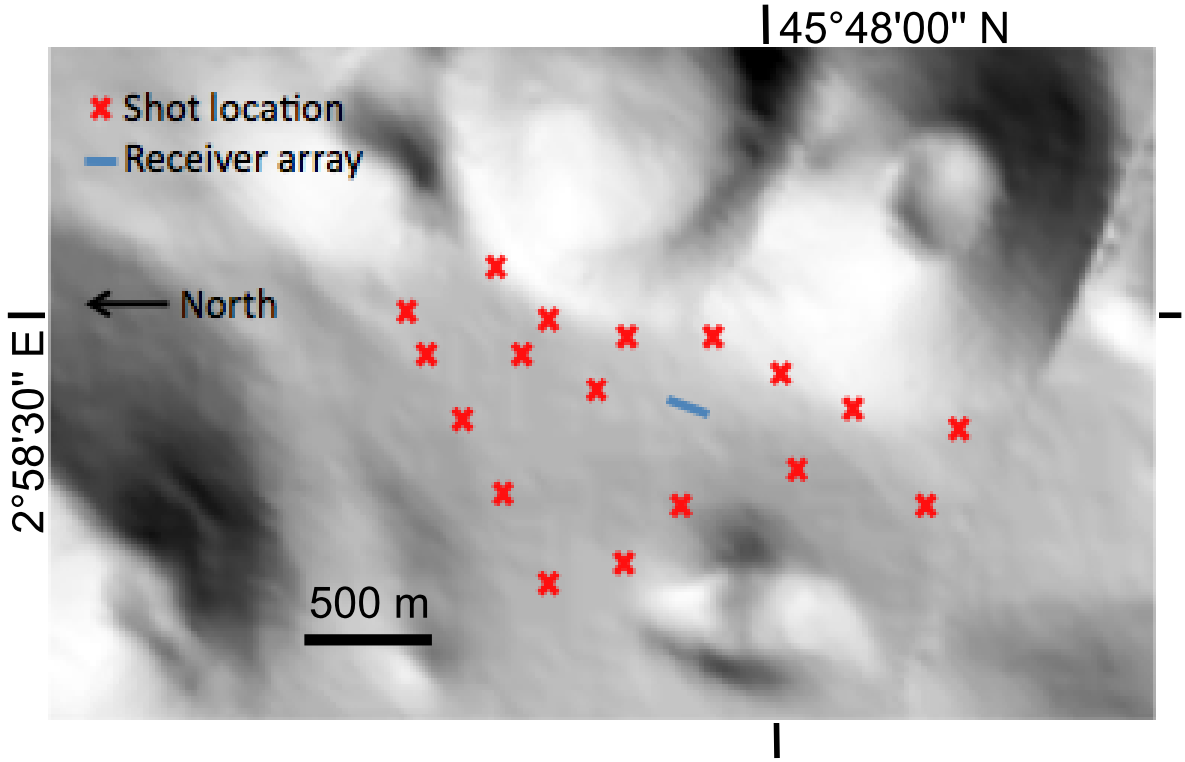

Figure 4.1: Area of interest in Auvergne. The blue line marks the array of 48 geophones with 0.6 m spacing. The red stars mark the positions of the 18 explosive sources placed around the geophones.

1. The wrapped phase Φ, which is the argument of the complex field u in the range $(-\pi, \pi]$.

2. The unwrapped phase Φ_u, that is obtained by correcting for the 2π jumps that occur when Φ goes through $\pm\pi$. The result is a continuous function.

We then test the criteria for Circular Gaussian Statistics, as mentioned in section 4.2.2. The results for the different tests are shown in Fig. 4.3 together with the theoretical predictions. We can see that:

- The real and imaginary part of the field follow a Gaussian distribution (Fig. 4.3a,b) and are independent (Fig. 4.3c).

- The amplitude presents a Rayleigh distribution (Fig. 4.3d). There are only small discrepancies for larger amplitudes that result from superimposed noise.

- The intensity is calculated as the squared amplitude of the Hilbert transformed signal. Its distribution clearly follows a decaying exponential probability function (Fig. 4.3e).

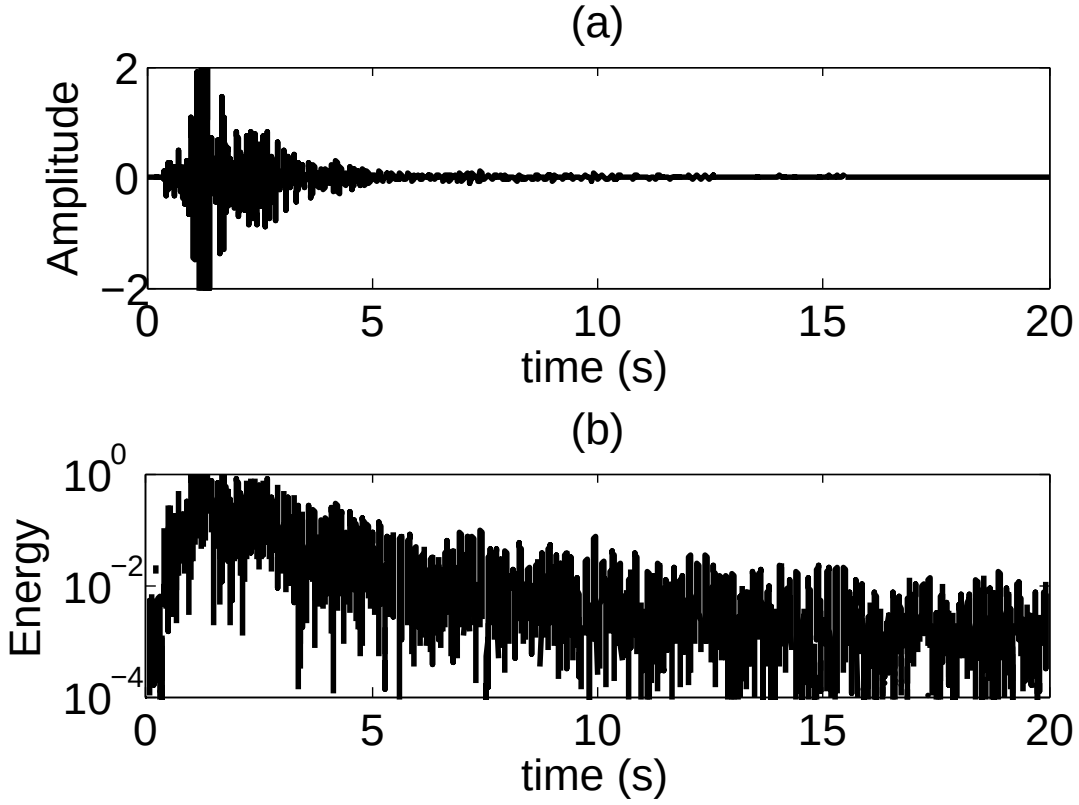

Figure 4.2: (a) Raw data from an explosive source, showing a coda of 20 s. The square indicates the chosen time window in the coda. (b) Dimensionless energy of the signal.

- The probability distribution of the phase is uniform with a value of $1/2\pi$ (Fig. 4.3f).

We mentioned in section 4.2.2 that the phase distribution is an ambiguous test for the Gaussian character of a signal, as every oscillating signal shows a uniform phase distribution. We will hence also test the phase derivative distribution to verify that the seismic coda obeys Circular Gaussian Statistics.

4.3.3 Field correlation

We compute the field correlation (Eq. 4.7) for all possible receiver combinations. As the length of our whole array is only four wavelengths, this might not be enough to average over the heterogeneities, and result in a lack of translation symmetry. In Fig. 4.4 we display the field correlation averaged over 3 shots that showed similar behavior. From the zero passage of the wave we can determine a wavelength of 8 m, which is in good agreement with the results from the preliminary analysis. From Fig. 4.4 we can also determine the correlation coefficient $C(\delta) = \langle \Psi(r - \delta/2)\Psi^*(r + \delta/2) \rangle$ between adjacent

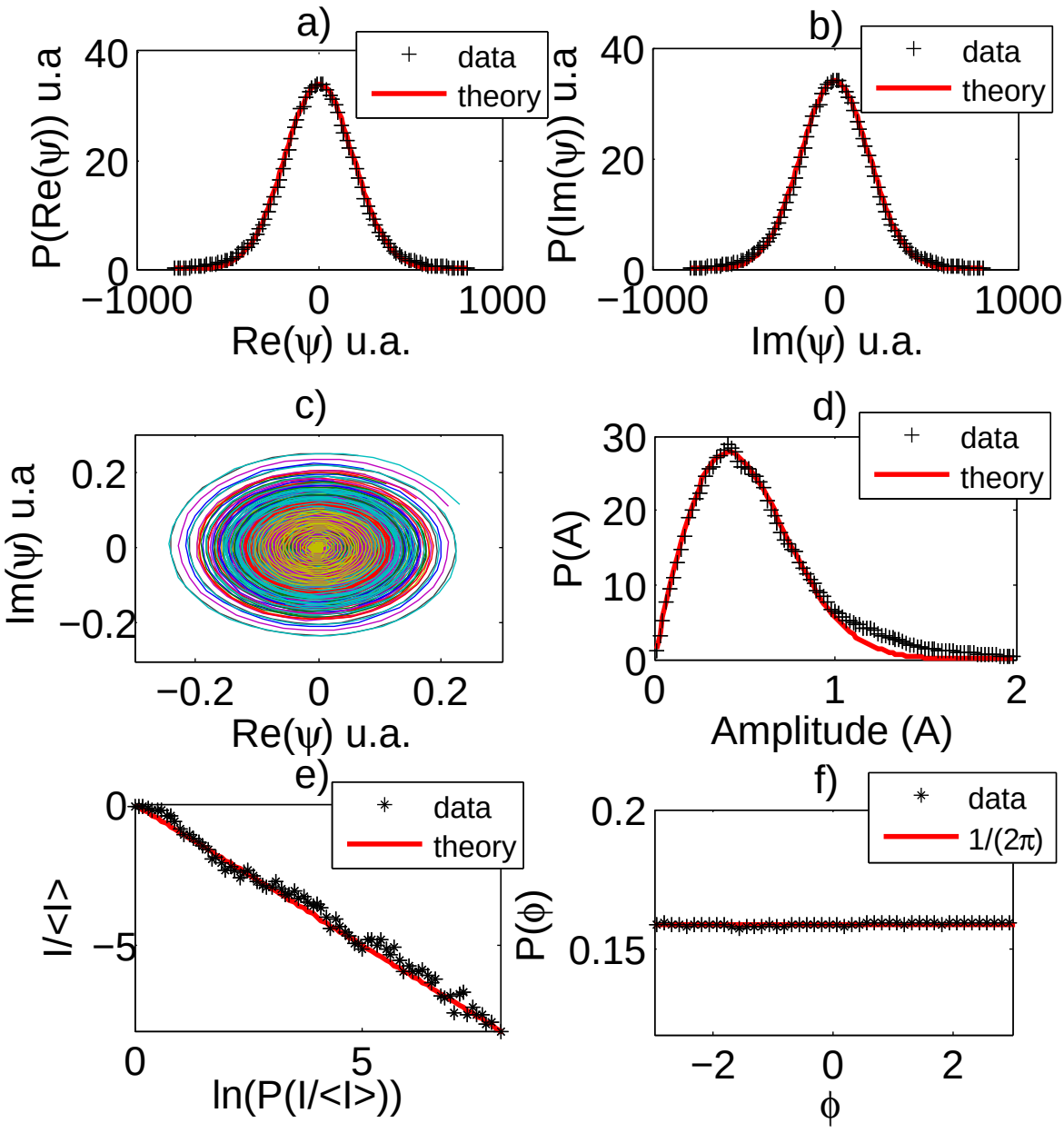

Figure 4.3: Criteria for a signal that obeys circular gaussian statistics a) Gaussianity of the real part b) Gaussianity of the imaginary part c) circular dependence of real and imaginary part d) Rayleigh distribution of the amplitude e) intensity follows a decaying exponential probability function f) uniform phase distribution.

receivers (δ=0.6 m) as $C(\delta = 0.6\ m)$=0.93=g (at 30 Hz). We will use this parameter g now as fitting parameter for the finite difference calculation of the phase derivative.

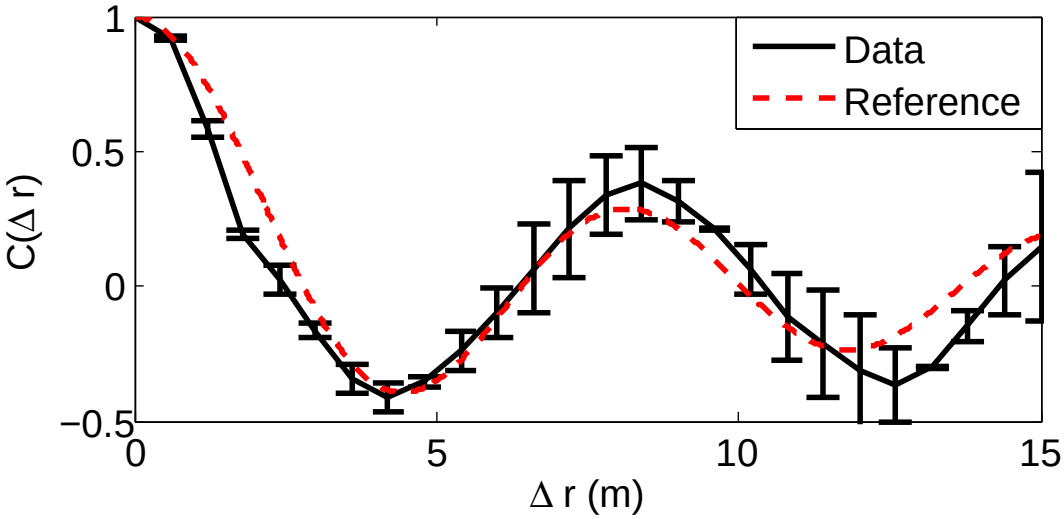

Figure 4.4: Field correlation. The zero passage reveals a wavelength of about 7 m. The field correlation can only be fitted for the first oscillations.

4.3.4 First phase derivative distribution

As we cannot determine the phase derivative analytically from our data, we use a finite-difference approach in space ($P(\Phi') \approx P(\Delta\Phi)/\delta$). We can use both, the wrapped and the unwrapped phase, to estimate the spatial derivative of the phase from the simple finite-difference formula $\Phi' \approx \Delta\Phi/\delta$ and $\Phi'_u \approx \Delta\Phi_u/\delta$, respectively. $\Delta\Phi$ and $\Delta\Phi_u$ are the differences of the phases between two seismometers that are separated by a distance δ. We recall that the theoretical formulation for the phase difference distribution is given in Eq. 4.14.

In Fig. 4.5 we show the wrapped and unwrapped phase finite-difference-distributions, together with the theoretical phase difference distribution $P(\Delta\Phi)$ (Eq. 4.14), and the analytical derivative distribution $P(\Phi')$ (Eq. 4.15). The distributions $P(\Delta\Phi)$ and $P(\Delta\Phi_u)$ are symmetric and therefore just represented for positive values in a logarithmic scale. We note that the analytical derivative is followed longer by the wrapped phase. We use the fitting parameters $g = 0.93$ (obtained from the field correlation), and $Q \approx \frac{2\pi^2}{\lambda^2} = 0.3$ m^{-2} with $\lambda = 8$ m (from field correlation, preliminary seismic refraction experiment). The agreement of the theoretical distributions and the data is excellent and we can conclude that our field satisfies 2-point Circular Gaussian Statistics with good accuracy.

4.3.5 Phase derivative correlations

To compute the phase difference correlation, we work with the spatially unwrapped phase Φ_u, as the wrapped phase is dominated by 2π jumps of geometrical and not physical origin. We compute the correlations between all possible receiver combinations,

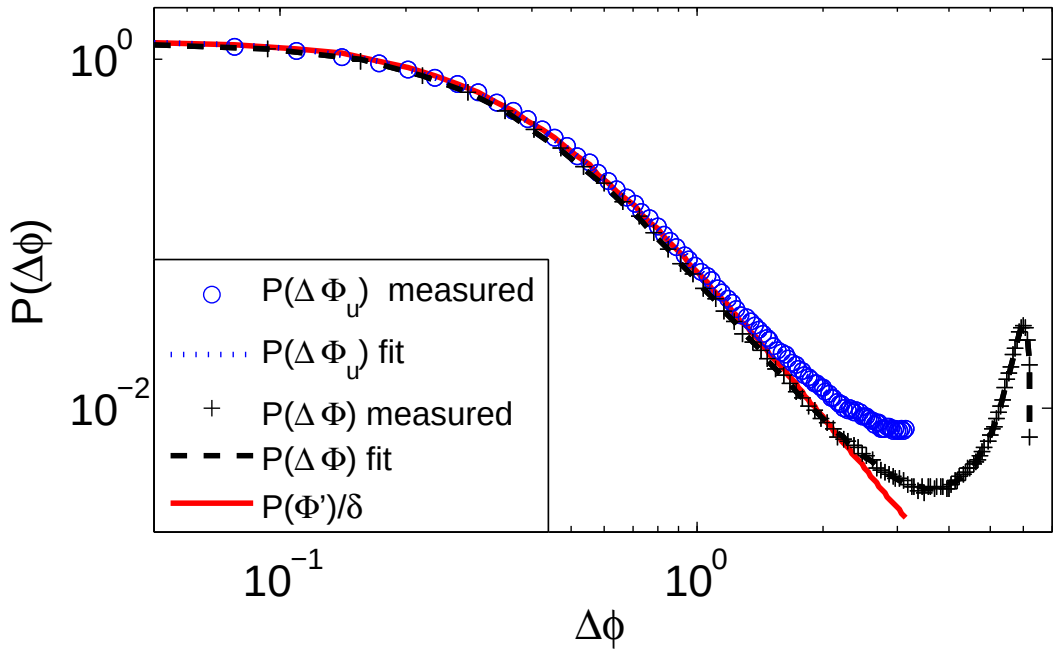

Figure 4.5: Unwrapped and wrapped phase difference distribution plotted together with the theoretical distribution and the theoretical phase derivative

separately for each shot, and then average correlations from the same receiver distances. Anache-Ménier et al. (2009) have shown with numerical simulations, that the asymptotic exponential regime is already reached for $r > \lambda/5$. As the aperture of our experimental network is several wavelength in size, we can in principle measure the scattering mean free path directly from the slope $(-1/\ell)$ of the phase derivative decay as a function of distance in logarithmic scale. However, since the fluctuations of our measurements are very large, we do not attempt to determine exactly the value of ℓ, but instead try to provide an estimate of its order of magnitude.

In Fig. 4.6 we plot the phase difference correlation in logarithmic scale versus the distance. We multiplied the correlation with r, so that the slope is directly proportional to $-1/\ell$. We superpose theoretical predictions (Eq. 4.18) for three scattering mean free paths (10 m, 100 m and 1000 m) on the data in Figure 4.6. In spite of the large fluctuations, we can reasonably exclude 10 m and 1000 m as possible values for ℓ. $\ell \approx$100 m seems to be a good approximation and is in agreement with previous findings by Larose et al. (2004a). A more precise determination is unfortunately not possible with the limited number of receivers and shots in our experiment.

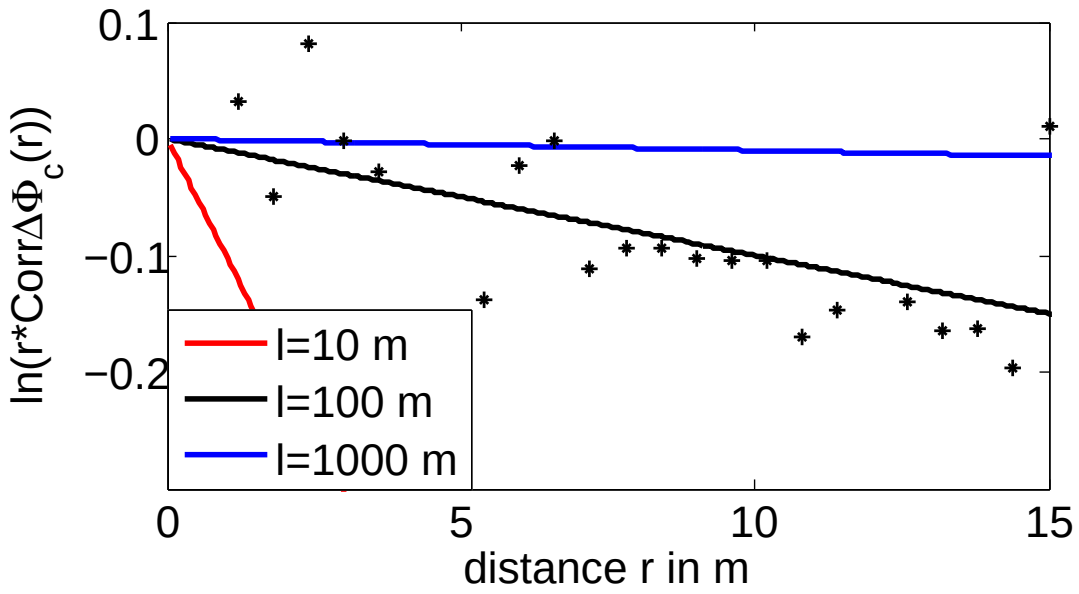

Figure 4.6: Phase difference correlation for 48 receivers with 0.6 m spacing in logarithmic representation multiplied by the distance.

4.4 Conclusion

In this paper, we demonstrate that the correlation function of the spatial derivative offers a new, promising opportunity to measure directly the scattering mean free path ℓ of a given heterogeneous medium. This measurement is independent of the absorption length and offers access to the scattering properties of the medium. In future applications, the ideal configuration should consist of a much larger number of receivers, to cover at least 10 λ. The inter-station distance of the order of $\lambda/10$ proved to be good enough to keep a high correlation between two nearby stations and to reduce systematic errors in the derivatives. Our method may find applications in various areas of seismology where the effects of scattering are prominent and a knowledge of the scattering properties is necessary to describe the propagation. As an example, an unbiased estimate of the scattering mean free path is crucial for the localization of changes in multiply scattering media, where a sensitivity kernel based on diffusion theory is used (Larose et al., 2010; Obermann et al., 2013b,a). Our experimental approach may also provide independent estimates of the scattering mean free path in volcanic areas where particularly strong scattering has been proposed, based on the fitting of energy envelopes using energy transport approaches (Wegler and Lühr, 2001; Yamamoto and Sato, 2010).

Chapter 5

Numerical simulations of the depth sensitivity of coda waves

Contents

In this part, I present the results from numerical simulations of wave propagation in heterogeneous media in 2D to study the sensitivity of coda waves to velocity perturbations at depth (Chapter 5.2). We have recently started simulations in 3D and show a first verification of the depth sensitivity with coda lapse time in Section 5.3). Before discussing the studies and their results, I briefly describe the difficulties to find an adapted simulation code and the SPECFEM package that we finally used.

5.1 Finding an adapted simulation code

We want to simulate the elastic wave propagation in an heterogeneous medium and study the sensitivity of the multiple scattered waves to weak changes in the medium. There are a couple of uncommon requirements that we need for these simulations and that made it, especially for the simulations in 3D, very difficult to find an adapted code. The heterogeneous medium shall have different elastic parameters in each cell. As we wish

to introduce changes whose extent is limited to sub-wavelength scale, we require the code to use several grid points per wavelength. To model elastic wave propagation with surface and body waves, we need well defined reflecting (for the surface) and absorbing boundaries (for the open halfspace). In general, especially the absorbing boundaries are not perfect. Therefore the model needs to be big enough to be affected as little as possible by any unwished reflections from these boundaries (we needed $\approx 50\lambda \times 50\lambda$ in 2D). Another uncommon requirement is the very long propagation time of 20-30 s to simulate multiply scattered coda waves. Most codes are unstable at such long propagation times or introduce numerical artifacts.
A major problem with the computational very expensive (many grid points) calculations in 3D is the mesh. Most codes use meshes that adapt in size to the elastic parameters, to be as cost efficient as possible. For us this is not acceptable. When we introduce a weak velocity perturbation in the medium, we do not want the cells to change their size compared to the medium without velocity perturbation. Otherwise it would be impossible to separate the effect that comes from the velocity perturbation from the effect that arises due to the different cell size.

To sum up the requirements:

- well defined reflecting and absorbing boundaries (PML)
- stable at late propagation times (20-30 s)
- different elastic parameters in each cell
- stable at high frequencies
- several grid points per wavelength

After several unsuccessful tries, we decided to use the code package SPECFEM that is available in 2D (SPECFEM2D) and 3D (SPECFEM3D basin, SPECFEM3D global) for the simulations. The simulations in 3D that are extremely costly, but thanks to Heiner Igel, we can use the SuperMUC server from the Leibniz Computation Center in Munich (LRZ).
These spectral element codes from the SPECFEM package were first developed in the nineties by Dimitri Komatitsch and Jean-Pierre Vilotte (IPGP, France) and then continued and maintained by them and their colleagues. Since 2002 the code package is available as open source from the Computational Infrastructure for Geodynamics (CIG), and has been successfully tested on a wide variety of clusters. The SPECFEM codes are entirely written in Fortran90 and allow simulations of acoustic, (an)elastic, and poroelastic seismic wave propagation. The code gives the possibility to include effects due to topography, lateral variations in wave speed, density, and/or attenuation, as well as full anisotropy. The spectral-element solver can accommodate regular and unstructured meshes, that can be generated for example with Cubit, a special meshing software. The

version of the spectral-element solver that we used (in 2D as well as in 3D), has Convolution PML absorbing layers (Martin et al., 2008) as well as higher-order time schemes (4th order Runge-Kutta and LDDRK4-6). In 2D we can run the solver in serial on our local cluster, in 3D this is not possible anymore. Depending on the scale of the simulation and on the frequency content, tens of millions of elements are required. The need of a parallel computational approach is unmistakable. The computational domain represented by the mesh needs to be decomposed using the incorporated SCOTCH software library, while the Message Passing Interface (MPI) is used to parallelize the code. As mentioned previously, the simulations in 3D were done on the SuperMUC server.

5.2 Depth sensitivity of seismic coda waves to velocity perturbations in an elastic heterogeneous medium

Depth sensitivity of seismic coda waves to velocity perturbations in an elastic heterogeneous medium

Anne Obermann, Thomas Planès, Eric Larose, Christoph Sens-Schönfelder, Michel Campillo.

Article published in *Geophysical Journal International* 2013.

Abstract: Numerous monitoring applications make use of seismic coda waves to evaluate velocity changes in the Earth. This raises the question of the spatial sensitivity of coda-wave-based measurements. Here, we investigate the depth sensitivity of coda waves to local velocity perturbations using two-dimensional numerical wave-field simulations. We calculate the impulse response at the surface before and after a slight perturbation of the velocity within a thin layer at depth is introduced. We perform a parametric analysis of the observed apparent relative velocity changes, ε^{obs}, versus the depth of the thin perturbed layer. Through the analysis of the decay of ε^{obs}, we can discriminate two different regimes: one for a shallow perturbation and the other for a deep perturbation. We interpret the first regime as the footprint of the one-dimensional depth sensitivity of the fundamental surface-wave mode. To interpret the second regime, we need to model the sensitivity of the multiply scattered body waves in the bulk. We show that the depth sensitivity of coda waves can be modeled as a combination of bulk-wave sensitivity and surface-wave sensitivity. The transition between these two regimes is governed by mode conversions due to scattering. We indicate the importance of surface waves for the sensitivity of coda waves at shallow depths and at early times in the coda. At later times, bulk waves clearly dominate the depth sensitivity and offer the possibility of monitoring changes at depths below the sensitivity of the surface waves. Based on the transition between

the two regimes, we can discriminate a change that occurs at the surface from a change that occurs at depth. This is illustrated for shallow depth perturbations through an example from lunar data.

5.2.1 Introduction

Detecting slight temporal changes in elastic properties of rocks at depth is of increasing interest for various applications (Poupinet et al., 1984, 1996; Meunier et al., 2001; Snieder and Hagerty, 2004; Niu et al., 2008). Provided that the sources and receivers are perfectly reproducible, the change in the seismic waveforms between two acquisitions performed at two distant dates can be solely attributed to changes in the propagation medium. When the medium is not too heterogeneous, locating such changes with ballistic waves is possible, although the sensitivity to weak changes is low. In contrast, in a highly heterogeneous medium, waves enter the multiple scattering regime. Heterogeneities in the medium generate late-arriving wave trains, which constitute the so-called 'coda'. These waves provide dense sampling of the medium and are very sensitive to small velocity perturbations. In optics, this sensitivity is used in diffuse wave spectroscopy (Pine et al., 1988). It is also used with elastic and acoustic waves in diffuse acoustic-wave spectroscopy (Cowan et al., 2002) and with coda seismic (Poupinet et al., 1984; Snieder et al., 2002; Snieder, 2006).

The detection of temporal changes has been successfully applied to different areas in seismology. These areas include the monitoring of oil reservoirs (Meunier et al., 2001), volcanoes (Grêt et al., 2005; Brenguier et al., 2008b), fault zones (Brenguier et al., 2008a), landslides (Mainsant et al., 2012), and even subduction zones (Rivet et al., 2011). A central question in the interpretation of the changes detected is that of the depth of the velocity variations. A recent discussion of possible causes for velocity perturbations and their depth range can be found in Sens-Schönfelder and Wegler (2011). Observations of velocity changes that occur at different depths have come from investigations using combinations of borehole and surface sensors, which have allowed the identification of changes at shallow depths (Sawazaki et al., 2009; Nakata and Snieder, 2011). With interpretations of coda-wave measurements, Rivet et al. (2011) located changes that occurred at great depth in a subduction zone. Their interpretation was based on the assumption that coda waves are dominated by Rayleigh waves that follow a two-dimensional (2D) diffusion process at the free surface. The depth sensitivity is therefore limited to the depth sensitivity of the surface waves. In contrast, Sens-Schönfelder and Wegler (2006) investigated shallow velocity changes at a volcano, which they interpreted as a response to changes in the hydrological system. Supported by the lapse-time dependence of the apparent relative velocity change, their interpretation was based on the assumption that the coda is dominated by body waves that show slower decay of the sensitivity with depth.

We know that regions that show tectonic and/or volcanic activity are highly heterogeneous (Abubakirov and Gusev, 1990; Aki and Chouet, 1975; Aki and Ferrazzini, 2000; Sato and Fehler, 1998). In particular, heterogeneities located right beneath the

free surface convert surface waves into bulk waves, and reciprocally, bulk waves into surface waves (e.g Larose et al. (2005b)). In the present study, we deal with waves that propagate in media containing vertical and horizontal heterogeneities. We investigate the following questions:

1. Is the assumption of the surface-wave diffusion process sufficient to describe the sensitivity of coda waves, or does the bulk-wave diffusion play a role in fully heterogeneous media?

2. Can changes at depth be detected if the sources and sensors are placed at the free surface?

3. If changes can be detected, what is the depth sensitivity of the coda waves in this multiple scattering regime?

4. How can we differentiate between shallow and deep velocity variations?

In this study, we will answer these questions on the basis of 2D numerical simulations. In section 5.2.2, we describe the elastic heterogeneous medium, introduce the velocity perturbation, and characterize the degree of heterogeneity. In section 5.2.3, we separately describe the depth sensitivity kernel of Rayleigh and bulk waves, and propose a linear combination of bulk and surface wave sensitivity to model the depth sensitivity of coda waves. In section 5.2.4, we compare theoretical predictions with numerical simulations. We demonstrate the accuracy of the model for weak changes located at different depths. These theoretical predictions are also tested at different times in the coda and for different degrees of heterogeneity. We emphasize the importance of bulk waves for the depth sensitivity of coda waves collected by arrays at the free surface. We obtain a model that shows the partition ratio of surface-wave and bulk-wave sensitivity at different times in the coda and for different levels of heterogeneities. In the last part, we use lunar data to demonstrate the practical relevance of our findings.

5.2.2 Numerical simulations

To study the sensitivity of coda waves to velocity perturbations at depth, we perform numerical simulations of seismic waves in a heterogeneous 2D elastic medium without intrinsic attenuation. The scattering is weakly anisotropic but the medium itself does not show any preferential direction.

To create the heterogeneous 2D elastic medium, we follow the procedure described by Frankel and Clayton (1986). The 2D velocity field has a constant background P-wave velocity v_p^0 with superimposed spatial velocity fluctuations $\delta v_p(x,z)$ that constitute the scatterers. The total P-wave velocity can be decomposed as:

$$v_p(x,z) = v_p^0 + \delta v_p(x,z). \tag{5.1}$$

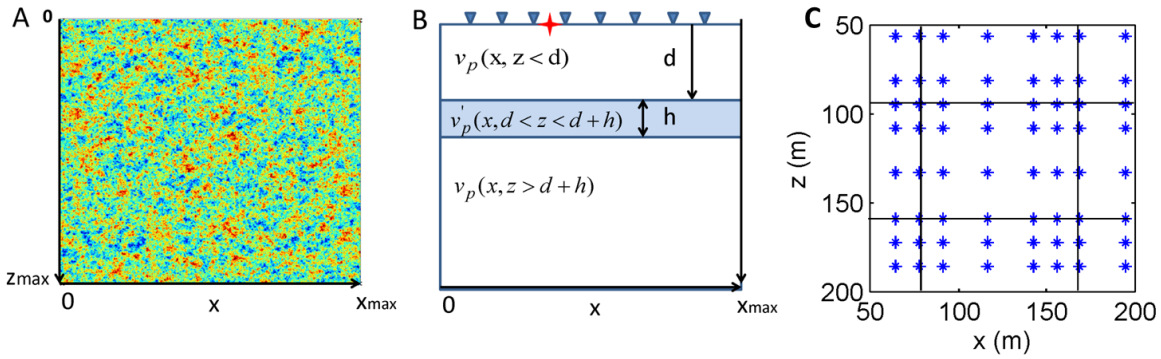

Figure 5.1: A. Medium with von-Karman correlation function. The correlation distance is $a \approx \lambda_0$. x and z are $50\lambda_0 \times 50\lambda_0$. B. Configuration for the study of depth sensitivity. A medium of dimension x, z contains a thin layer (h) with a small velocity perturbation at depth d (note that the thickness of h is exaggerated for better visualization). C. Grid element used for the simulations. The black lines limit the grid points (blue stars) of one element.

The total S-wave velocity relates to the total P-wave velocity, as $v_s = \frac{v_p}{\sqrt{3}}$, and thus undergoes the same respective velocity variations. The velocity fluctuations $\delta v_p(x, z)$ are themselves characterized by a spatial autocorrelation function. The main statistical parameters that characterize the medium are described in section 5.2.2. Figure 5.1A shows a typical realization of a random medium.

In this initial velocity model, we introduce a small velocity perturbation $\frac{dv}{v}$ in a layer of thickness h at depth d, as shown in Figure 5.1B. The perturbed velocity v_p' in the layer is proportional to the velocity v_p:

$$v_p'(x,z) = \begin{cases} v_p(x,z) \cdot (1 + \frac{dv}{v}) & \text{for} \quad d < z < d+h, \\ v_p(x,z) & \text{for} \quad z < d \text{ or } z > d+h. \end{cases} \tag{5.2}$$

We take v_p^0=6500 m/s and dv=100 m/s which corresponds to a relative velocity change of $\frac{dv}{v} = 1.54\%$.

We simulate a semi-infinite medium with a free surface by imposing three absorbing conditions at the sides and one traction-free condition at the surface. To solve the wave equation, we use the 2D spectral-element method developed by Komatitsch and Vilotte (1998) and implemented in the SPECFEM2D solver, version 6.1, by Tromp et al. (2008). An element of the discretization grid is shown within the black lines in Figure 5.1C. We place a receiver array and a source at the free surface.

For the simulations, we use a vertical force as the source mechanism, with a central frequency of f_0=20 Hz, and a frequency bandwidth of Δf=12 Hz. The corresponding wavelength for the P-wave is $\lambda_0 = \frac{v_p^0}{f_0}$=325 m. We want to note here that the perturbed layer has a thickness of only 200 m, and it is therefore thinner than λ_0. The grid size

Table 5.1: Physical parameters of the numerical simulations used in the present study.

Notation	Value	Description
L	16.8×16.8 km^2	Grid size
Δ x, Δ z	20 m	Grid spacing
	9 s	Record length
Δ t	$3{\cdot}10^{-4}$s	Time step
f_0	20 Hz	Source frequency
Δf	12 Hz	Source bandwidth
a	300 m	Correlation length
σ	5, 10, 15, 20, 30 %	Velocity fluctuations
v_p		Initial P-wave velocity field
v_p'		Perturbed P-wave velocity field
v_p^0	6500 m/s	Mean P-wave velocity
v_s^0	3750 m/s	Mean S-wave velocity
λ_0	325 m	Central P-wavelength
h	200 m	Thickness of perturbed layer
d		Depth of perturbed layer
$\frac{dv}{v}$	1.54%	Relative velocity change
ε		Apparent relative velocity change

is 16.8×16.8 km^2 ($50\lambda_0 \times 50\lambda_0$), with a 20 m spatial pitch ($\approx \lambda_0/20$). We compute the displacement $\varphi(t)$ for waves propagating in the initial medium $v_p(x,z)$, and $\varphi'(t)$ for waves propagating in the slightly perturbed medium $v_p'(x,z)$. This procedure is reproduced for different depth positions d of the layer. All the important parameters for the simulation are summarized in table 5.1. In the following sections, if not stated differently, we display results for source-receiver distances of 4 km.

Characterization of the heterogeneous medium

In this part, we characterize the level of heterogeneity of the medium. In section 5.2.2, we discuss the correlation function that we chose for the random medium in more detail. In section 5.2.2, we determine the equipartition ratio and therewith the energy velocity ratio. Then in section 5.2.2, we provide special focus on the determination of the scattering (ℓ) and transport ($\ell^\star$) mean free paths. These quantities are important for the theoretical model in section 5.2.4.

Autocorrelation function of the random medium : For the velocity model $v_p(x,z)$, we decided to work with a von-Karman type autocorrelation function, as this model is consistent with the general observations concerning rock and surface geology, which show very rough behaviors at small length scales (Frankel and Clayton, 1986; Holliger and Levander, 1992). This correlation function is defined as Tatarskiĭ (1961):

$$N(r) = \frac{1}{2^{m-1}\Gamma(m)} \left(\frac{r}{a}\right)^m K_m \left(\frac{r}{a}\right) \sigma^2, \tag{5.3}$$

where $K_m(x)$ is a modified Bessel function of order m, $\Gamma(m)$ is the gamma function, r is the offset (or spatial lag), a is the correlation distance and σ the relative standard deviation of the velocity. We consider a specific type of von Karman function, where m is 0.5. For this case, the two dimensional Fourier transform $\Phi_{\text{Karman}}(k_r)$ that represents the power spectrum of the medium fluctuations, is given by:

$$\Phi_{\text{Karman}}(k_r) = \frac{a^2}{1 + k_r^2 a^2} \sigma^2, \tag{5.4}$$

where k_r is the radial wavenumber. We chose $a \approx \lambda_0$ to allow strong interactions between waves and heterogeneities, and to enhance scattering. σ ranges from $\sigma = 5\%$ to 30%. For each configuration, we perform numerical simulations in ten different media that obey the same statistics (for averaging purposes).

Equipartition ratio : In a heterogeneous elastic medium, waves propagate both as P-waves and S-waves, and they are repeatedly converted from one state to another. The available elastic energy in the phase space at long times will be equally distributed among all of the possible states of the P-waves and S-waves (Weaver, 1982, 1985). This phenomenon is referred to as the equipartition of seismic waves (Hennino et al., 2001). In an unbounded 2D medium, the modes are plane waves with either SV or P polarization. If $v_s = \frac{v_p}{\sqrt{3}}$, the equipartition ratio in two dimensions reads:

$$\left\langle S^2 \right\rangle / \left\langle P^2 \right\rangle = 3, \tag{5.5}$$

where S and P are the amplitudes of the S-waves and P-waves respectively. To verify the equipartition ratio, we place a source close to the free surface. We then place 150 receivers in a vertical line in the middle of the medium. The top receiver is still several wavelengths away from the free surface. We calculate the energy ratio between the squared curl and the squared divergence of the wave field in a gliding time-section. We average over the time sections and 50 realizations of the random medium. The data yield a ratio of $\langle S^2 \rangle / \langle P^2 \rangle = 3.4$. Repeating the experiment and considering four reflecting boundaries yields a ratio of exactly 3. We conclude that the difference between the experiment with a free surface and three absorbing boundaries and the theory for infinite space is due to the absorbing boundary conditions and the surface. Boundaries appear to absorb P-waves more quickly than S-waves. The energy velocity c which reflects the celerity at which the seismic energy is transported, can thus be approximated according to the energy ratio:

$$\frac{1}{c} = \frac{0.77}{v_s} + \frac{0.23}{v_p}. \tag{5.6}$$

Determination of the scattering mean free path : In a regime where multiple scattering is very strong, waves traveling from a source to a receiver follow many trajectories. In this case, wave propagation can be considered as a random walk process, and can be described to a good approximation by the diffusion equation (for further information, see for example the review of Margerin and Nolet (2003)). Within this approximation, the multiply scattered waves that propagate in n dimensions are described by the energy velocity c, the transport mean free path $\ell^\star$ or the diffusion coefficient as

$$D = \frac{c\ell^\star}{n}. \tag{5.7}$$

We need the scattering mean free path ℓ and the transport mean free path $\ell^\star$ for the modeling of the depth sensitivity of coda waves. ℓ is a central quantity in radiative transfer and diffusion theory. It represents the typical length scale after which a beam with a given propagation direction has been significantly attenuated by scattering. $\ell^\star$ is the distance after which the "memory" of the initial direction of the beam is lost (Paasschens, 1997; Sato, 1993). $\ell^\star$ is related to the scattering mean free path via:

$$\ell^\star = \frac{\ell}{1 - \langle \cos\theta \rangle}, \tag{5.8}$$

where $\langle \cos\theta \rangle$ is the directional average of the cosine weighted probability of the scattering angle. When the scattering is isotropic (i.e., inhomogeneities scatter equal amounts of energy in all directions), $\ell^\star = \ell$. In our case, where the correlation length and wavelength are similar ($a \approx \lambda_0$), scattering is not completely isotropic. We would expect $\ell^\star > \ell$ according to Equation 5.8.

In the following, we determine $\ell^\star$ and ℓ numerically from the coherent and incoherent parts of the recorded signals. The coherent part of the waveform is the wave that resists averaging over different realizations of disorder. The incoherent part of the waveform is constituted by waves vanishing while averaging over disorder.

We arrange 148 receivers in a cross-shape array in the initial heterogeneous medium. The spacing between the receivers is 200 m. The source is placed in the center of the receivers. For this simulation, all four of the boundaries are reflecting. To have enough data to average, we ran 50 realizations with this configuration in media that obey the same statistics.

From the coherent part $\langle \varphi(t) \rangle$ of the waveform, we determine the scattering mean free path ℓ following Derode et al. (2001). The power spectrum of the coherent signal $|\langle H(\omega) \rangle|^2$ is linked to the scattering mean free path ℓ via:

$$|\langle H(\omega) \rangle|^2 = \exp(-\frac{x}{\ell}), \tag{5.9}$$

where x denotes the distance between source and receiver in the medium. In Figure 5.2A, we plot the logarithm of the normalized energy versus the source-receiver distance.

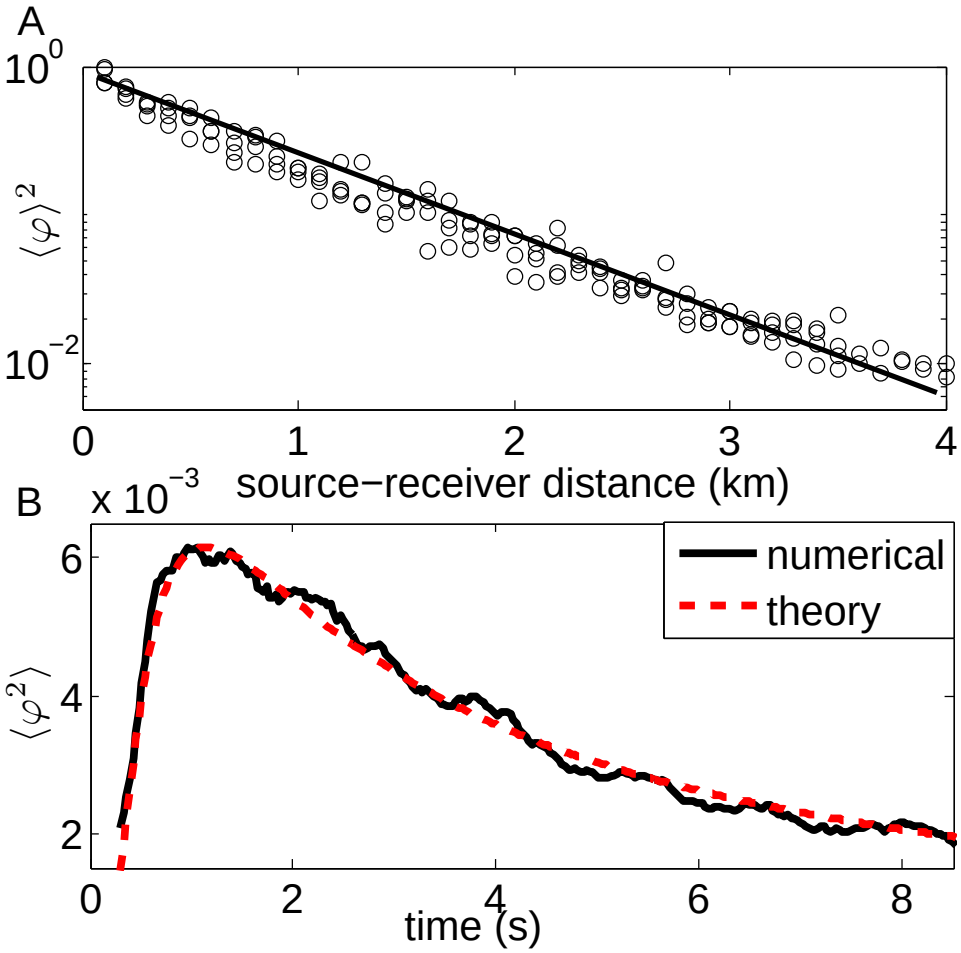

Figure 5.2: A. Logarithm of the normalized coherent Intensity $\langle\varphi\rangle^2$ versus source-receiver distance averaged over 50 simulations. After correcting the geometrical spreading, the slope is proportional to $-1/\ell$. B. Normalized incoherent intensity $\langle\varphi^2\rangle$ versus time. $\ell^\star$ is calculated from the diffusion constant of the diffusion equation that gives the best fit.

The slope of the regression line is $-1/\ell$. The results for different σ are given in Table 5.2.

From the incoherent part of the waveform, we determine the transport mean free path $\ell^\star$. We look at the energy envelope of the waveforms. We take a sliding time window of 2T=0.3 s, which corresponds to six periods, and we calculate the average intensity in this window according to:

$$I(t) = \left\langle \varphi(\tau)^2 \right\rangle_{\tau\in[t-T,t+T]} \tag{5.10}$$

We then average the intensity over 50 models that obey the same statistics. We search for the diffusion constant D that gives the best fit with the diffusion Equation and we calculate $\ell^\star$, as in Equation (5.7). In Figure 5.2B we illustrate the intensity for a model with σ=20% and its fit with the diffusion equation.

Table 5.2: Scattering mean free path and transport mean free path calculated experimentally for models with different amounts of heterogeneity.

Model	Scattering mean free path (ℓ) $\pm 5\%$	Transport mean free path ($\ell^\star$) $\pm 10\%$
σ=5 %	10000 m	13000 m
σ=10%	2200 m	2700 m
σ=15%	1200 m	1500 m
σ=20%	900 m	940 m
σ=30%	500 m	450 m

Table 5.2 gives the results for the scattering mean free paths that were obtained from numerical calculations for media with different degrees of heterogeneity σ. We note that ℓ and $\ell^\star$ have close values, which indicates only weakly anisotropic scattering ($\ell \approx \ell^\star$). The uncertainties for the measures are the standard deviations that we obtained by averaging over 50 models.

Determination of the apparent relative velocity changes with the stretching technique

We now use the numerical simulation with one free surface and three absorbing boundaries. We run a first experiment with an initial model v_p, and then a second with a perturbed velocity v_p' in a layer. Figure 5.3 shows the seismograms for an initial (blue) and a perturbed (red) medium for a receiver 2 km away from the source. The disturbance occurs at 50 m in depth in a medium with velocity fluctuations of $\sigma = 20\%$. By zooming into the coda of the seismograms, we can see that the perturbed seismogram lags behind in time with respect to the unperturbed seismogram, while the shape of the wave train remains largely unchanged.

We use the stretching technique to analyze these apparent relative velocity changes in the coda of the perturbed seismograms (Lobkis and Weaver, 2003; Sens-Schönfelder and Wegler, 2006). We assume that the perturbation of the signal can be measured as the effect of a slight change of its global velocity $\delta V/V$. It has been stretched or compressed in time in comparison to the unperturbed signal by a factor $t(1-\varepsilon)$, where $\varepsilon = \delta V/V$. To obtain the optimal value for $\delta V/V$, we test systematically various values of ε. For each ε we calculate the correlation coefficient CC of the perturbed stretched signal φ' and the unperturbed signal φ:

$$CC(\varepsilon) = \frac{\int_{t_1}^{t_2} \varphi'\left[t(1-\varepsilon)\right] \varphi\left[t\right] dt}{\sqrt{\int_{t_1}^{t_2} \varphi'^2\left[t(1-\varepsilon)\right] dt \int_{t_1}^{t_2} \varphi^2\left[t\right] dt}}, \tag{5.11}$$

where t_1 and t_2 are the beginning and end of the time window used. The value of ε, that maximizes the cross-correlation coefficient between the perturbed and the unperturbed signals at a given time corresponds to the observed value (ε^{obs}) of the apparent relative

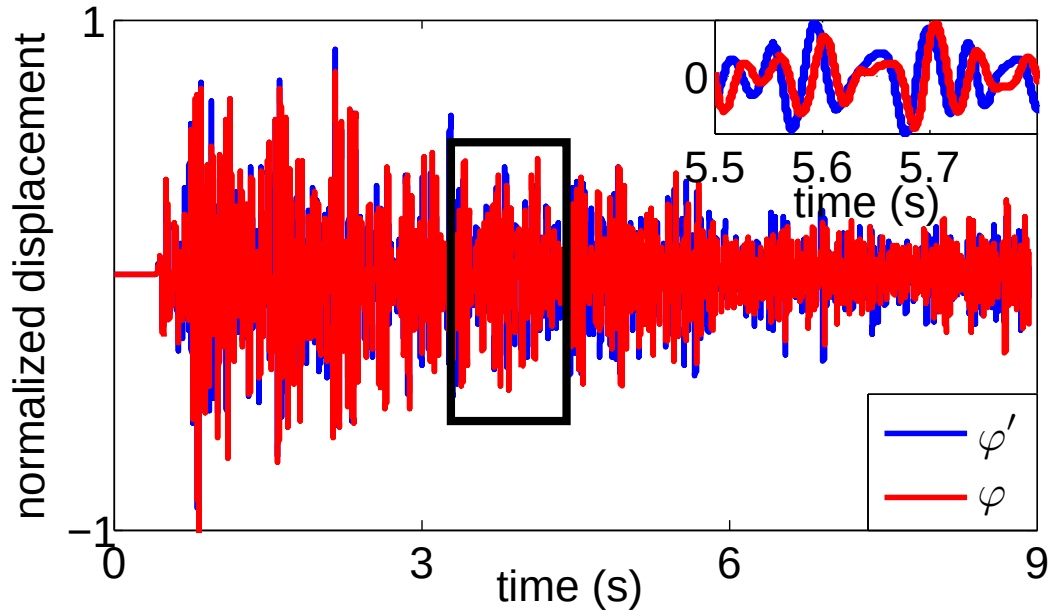

Figure 5.3: Synthetic seismograms recorded with (blue) and without (red) perturbed layer at 50 m in depth. The black box indicates the a time window for the stretching around 3.6 s. Inset: zoom in on the unperturbed and perturbed seismograms.

velocity change. For more detailed information, the reader should refer to Hadziioannou et al. (2009), for example. We apply this procedure to calculate the apparent relative velocity changes for all of the depth positions of the perturbed layer. The length of the time window is 1.5 s, and it is centered at different times in the coda.

Results for the apparent relative velocity changes with depth

When analyzing the apparent relative velocity changes ε^{obs} versus the depth of the perturbed layer in Figure 5.4, we observe a decrease of ε^{obs} with depth, which testifies to reduced sensitivity of our measurements to changes at greater depths. We can discriminate two different regimes of sensitivity: for shallow and deep perturbed layers. Their separation is marked in figure 5.4 with the dash-dotted line. In the first regime, which concerns the early part of the slope, the sensitivity of ε^{obs} decays rapidly with depth, until a depth of approximately half the central wavelength λ_0. In the second regime, which concerns the later part of the slope, the slower decay results in a deeper sensitivity.

We interpret the rapid decay (shallow perturbed layers) as the footprint of the vertical depth sensitivity of the fundamental mode of the surface waves. For perturbations at greater depths (deep perturbed layers), we propose a model based on 2D diffusion of body waves. We will show in the following sections that we can model the apparent relative velocity changes $\varepsilon^{\text{Bulk}}$ and $\varepsilon^{\text{Surf}}$, computed for the bulk and surface wave sensitivities according to:

$$\varepsilon^{\text{theo}}(d,t) = \alpha(t)\varepsilon^{\text{Surf}}(d) + (1-\alpha(t))\varepsilon^{\text{Bulk}}(d,t), \tag{5.12}$$

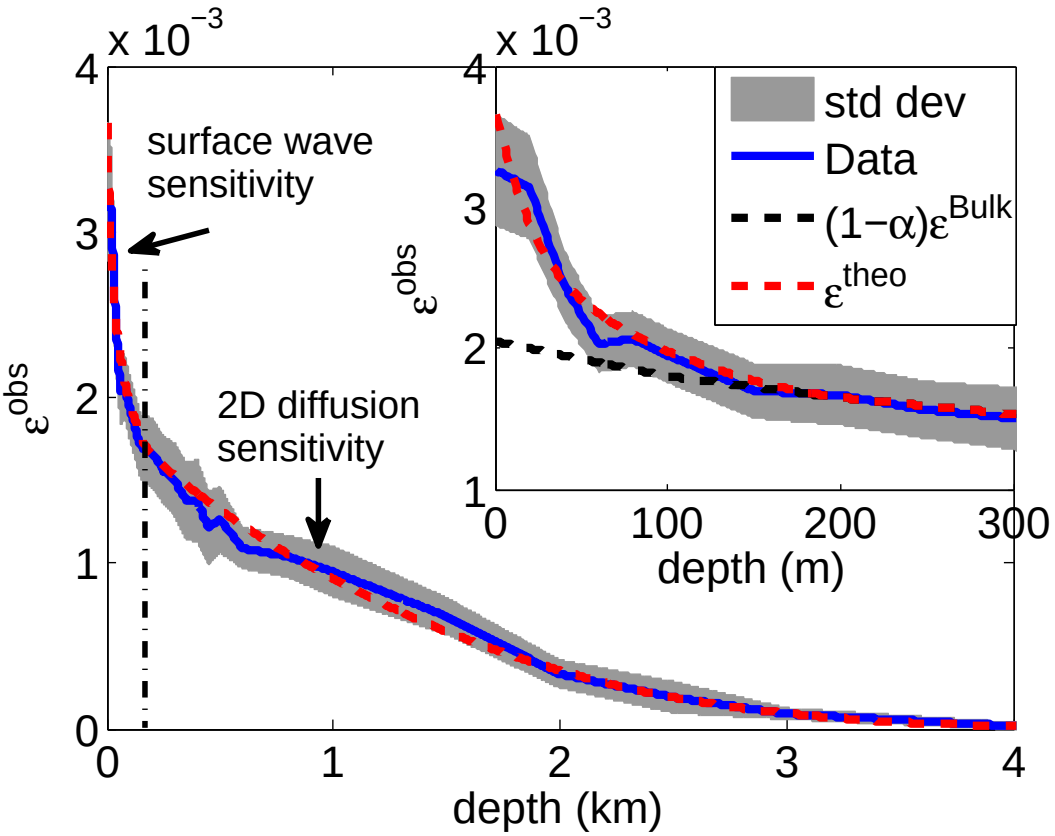

Figure 5.4: Apparent relative velocity changes with depth of the perturbed layer averaged over ten realizations ($\sigma = 20\%$). We can discriminate two different regimes of sensitivity for a shallow and a deep perturbed layer marked by the black chain line. The modeled data (red) $\varepsilon^{\text{theo}}(d, t = 3.6\text{ s})$ for the depth sensitivity of coda waves fit the observations very well. Inset: importance of the surface waves to describe the depth sensitivity, as the bulk regime $(1-\alpha)\varepsilon^{\text{Bulk}}$ alone cannot account for the steep slope at short times.

where $\varepsilon^{\text{theo}}(d, t)$ is the modeled relative velocity change and α the fitting parameter, or the partition coefficient. Note that this partition coefficient is different from the equipartition ratio, as it integrates the time spent in each state of the wave (bulk or surface). In section 5.2.3, we study the computation of the relative velocity changes $\varepsilon^{\text{Bulk}}$ and $\varepsilon^{\text{Surf}}$ in the bulk and surface wave sensitivity regime independently.

5.2.3 Modeling the two sensitivity kernels

In this section we describe the 1D surface wave regime and the 2D diffusion regime, which we use to model the depth sensitivity of the coda waves. For the bulk waves, we will compare an approach based on the diffusion solution to an approach based on the radiative transfer solution.

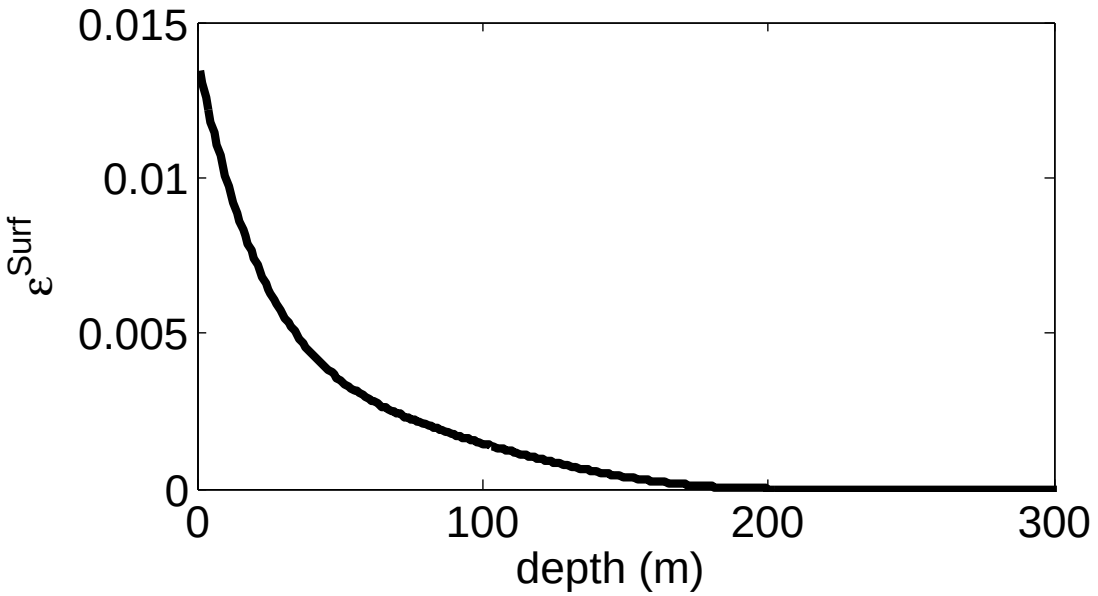

Figure 5.5: Apparent relative velocity changes $\varepsilon^{\mathrm{Surf}}(d)$ for the 1D surface-wave sensitivity regime as a function of the depth of the perturbed layer.

Surface-wave sensitivity

To study the depth penetration of surface-wave energy independent of bulk waves, we propagate a pulse in a homogeneous medium (constant velocity, no fluctuations). This medium does not allow conversion scattering into bulk waves. Similar to the previous numerical simulations, we introduce a thin layer with a slightly different velocity ($\frac{dv}{v} = 1.54\%$). Figure 5.5 shows the apparent relative velocity changes $\varepsilon^{\mathrm{Surf}}(d)$ versus the depth of the layers that were measured from the direct arrivals. As can be seen, the surface wave sensitivity decays very rapidly with depth and disappears entirely after 2/3 of the central wavelength λ_0.

Bulk sensitivity: the diffusive kernel approach

As we have seen previously, the apparent relative velocity changes of the seismograms can be quantified by a stretching factor $\varepsilon^{\mathrm{obs}}$. The theoretical bulk contribution $\varepsilon^{\mathrm{Bulk}}$ can be related to a local velocity perturbation using the sensitivity kernel introduced by Pacheco and Snieder (2005) :

$$K(\boldsymbol{S}, \boldsymbol{R}, \boldsymbol{r}_0, t) = \frac{\int_0^t p(\boldsymbol{S}, \boldsymbol{r}_0, u) p(\boldsymbol{r}_0, \boldsymbol{R}, t-u) du}{p(\boldsymbol{S}, \boldsymbol{R}, t)} \tag{5.13}$$

where $\boldsymbol{S}$ and $\boldsymbol{R}$ are the positions of the source and the receiver, $\boldsymbol{r}_0$ is the position of the local velocity variation, and t is the center of the time interval in the coda where the stretching is evaluated. $p(\boldsymbol{a}, \boldsymbol{b}, t)$ is the intensity of the wave field from $\boldsymbol{a}$ to $\boldsymbol{b}$ at time t.

An example of the sensitivity kernel is shown in Figure 5.6 at t=3.6 s in the coda for a source and receiver inside the medium.

This sensitivity kernel is relevant in the multiple scattering regime, and it can be interpreted as the volumetric density of time that the scattered waves spend at $\boldsymbol{r}_0$. It can be noted that the total time t spent in the medium is retrieved by integrating the kernel over the volume of the studied medium:

$$\begin{aligned} t &= \int_{\text{medium}} K(\boldsymbol{S},\boldsymbol{R},\boldsymbol{r},t)d\boldsymbol{r} \\ &= \int_{x=0}^{x_{\max}}\int_{z=0}^{z_{\max}} K(\boldsymbol{S},\boldsymbol{R},x,z,t)dxdz, \end{aligned} \tag{5.14}$$

where $\boldsymbol{r} = x\boldsymbol{e_x} + z\boldsymbol{e_z}$. $(\boldsymbol{e_x},\boldsymbol{e_z})$ are cartesian unit vectors. This kernel can also relate the scattering cross section of a defect appearing in a multiple scattering medium to a correlation coefficient extracted from the coda (Larose et al., 2010; Rossetto et al., 2011).

For a local velocity variation $\frac{dv}{v}$ in an elementary volume ΔV centered on $\boldsymbol{r}_0$, the stretching coefficient $\varepsilon^{\text{Bulk}}(\boldsymbol{r}_0,t)$ for signals emitted in $\boldsymbol{S}$ and received in $\boldsymbol{R}$ reads:

$$\varepsilon^{\text{Bulk}}(\boldsymbol{r}_0,t) = \frac{K(\boldsymbol{S},\boldsymbol{R},\boldsymbol{r}_0,t)}{t}\frac{dv}{v}\Delta V. \tag{5.15}$$

In our numerical experiment, the velocity variation is applied to a layer of thickness h located at a depth d. As the velocity variation is weak, the measured stretching coefficient can be expressed as the spatial integral of the kernel on the medium, weighted by the applied velocity change:

$$\begin{aligned} \varepsilon^{\text{Bulk}}(d,t) &= \int_{\text{medium}} \frac{K(\boldsymbol{S},\boldsymbol{R},\boldsymbol{r},t)}{t}\frac{dv}{v}(\boldsymbol{r})d\boldsymbol{r} \\ &= \int_{x=0}^{x_{\max}}\int_{z=d}^{z=d+h} \frac{K(\boldsymbol{S},\boldsymbol{R},x,z,t)}{t}\frac{dv}{v}dxdz, \end{aligned} \tag{5.16}$$

with the velocity change $\frac{dv}{v}(\boldsymbol{r}) = \frac{dv}{v}$ in the layer and $\frac{dv}{v}(\boldsymbol{r}) = 0$ elsewhere.

Intensity propagator in the diffusion approximation : As a first approximation, we describe the intensity propagator in Equation (5.13) with the diffusion equation solution:

$$p(\boldsymbol{S},\boldsymbol{R},t) = \frac{1}{4\pi Dt}e^{\frac{-\|\boldsymbol{S}-\boldsymbol{R}\|^2}{4Dt}} \tag{5.17}$$

where D is the diffusion constant that depends on the medium heterogeneity. Equation (5.17) stands for 2D infinite media. To take the free surface into account, a semi-infinite space has to be considered. In this case, the solution is found in terms of the sum of

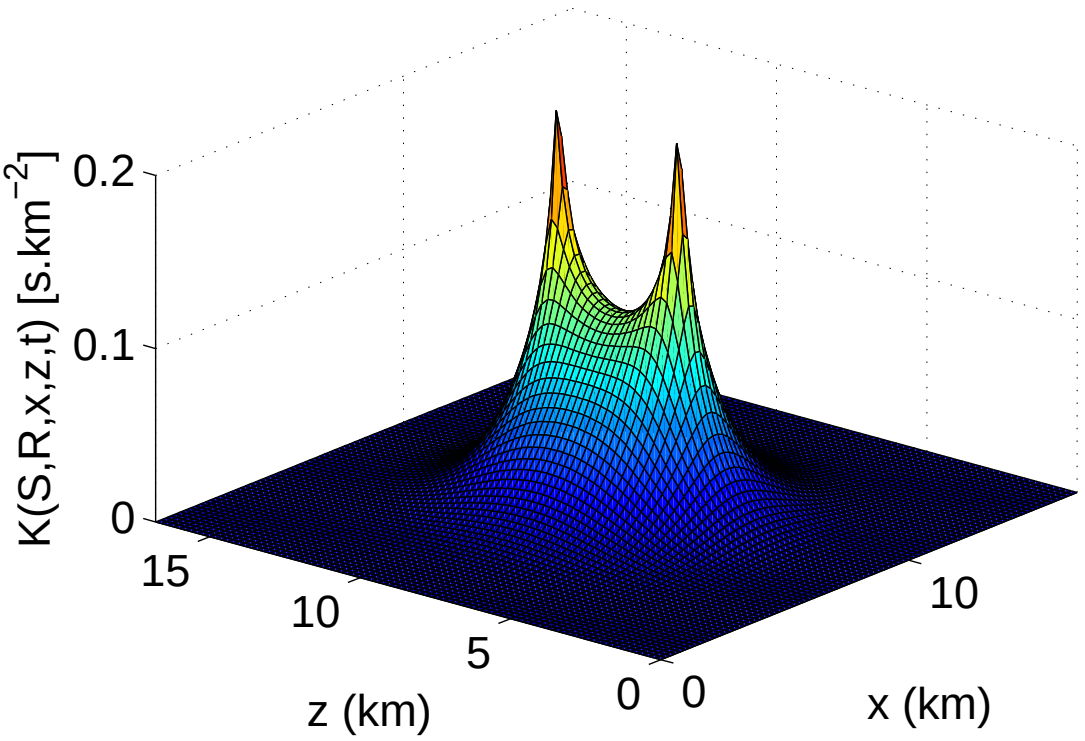

Figure 5.6: Spatial representation of sensitivity kernel K(S,R,x,z,t) in the diffusion approximation at t=3.6 s. The two peaks correspond to the positions of the source and receiver.

the infinite medium solution and its mirror image from the free surface. This solution can be easily computed and gives an analytical solution of the kernel (Equation (5.13)). Nevertheless, this kernel is only accurate when the diffusion approximation is valid: at times much greater than the transport mean free time $t >> t^\star$, where $t^\star = \ell^\star/c$, and for velocity variations located far away from the sensors.

Intensity propagator for a radiative transfer approximation : The radiative transfer equation allows for a more general representation of wave intensities in scattering media. In our case of weakly anisotropic scattering ($\ell^* \approx \ell$), we assume that we can use the following exact solution (Sato, 1993; Paasschens, 1997), valid for 2D isotropic scattering:

$$\begin{aligned} p(r,t) &= \frac{e^{-ct/\ell}}{2\pi r}\delta(ct-r) \\ &+ \frac{1}{2\pi\ell ct}(1-\frac{r^2}{c^2t^2})^{-\frac{1}{2}} e^{[\ell^{-1}(\sqrt{c^2t^2-r^2}-ct]}\Theta(ct-r), \end{aligned} \tag{5.18}$$

where c is the energy velocity, r is the distance between source and receiver, ℓ is the scattering mean free path and $\Theta(x)$ is the Heaviside (or step) function. The first term

describes the coherent part of the intensity that decreases exponentially with the distance relative to the scattering mean free path. The second term describes the diffuse intensity. We note that the diffusion solution is reached when $t >> r/c$.

Bulk sensitivity kernel in an infinite medium : As the next step, we want to see how well the diffusion or radiative transfer approach models the bulk sensitivity of our data. For this purpose, we study the bulk waves without influence of the surface waves. Therefore we slightly change the configuration of our numerical simulations. We place the source and the horizontal receiver array within the medium at a depth of 8.8 km, and take absorbing conditions at all four boundaries. With this configuration, we would not expect any surface waves to appear on our record, and so the apparent relative velocity changes should only be governed by the 2D propagation of bulk waves.

The resulting apparent relative velocity changes $\varepsilon^{\text{obs}}(d, t = 3.6\text{ s})$ are shown in blue in Figure 5.7, versus the depth of the perturbed layer for a heterogeneity of $\sigma = 20\%$. The error bars indicate the standard deviation over 10 models. We also plot $\varepsilon^{\text{Bulk}}$ from the diffusion-based kernel in black and from the radiative-transfer-based kernel in red (Figure 5.7). As expected, the main difference between the diffusion and radiative transfer approach is visible for small offsets to the source; i.e., when the time until visiting the layer is small. For long distances, the difference between the two approaches is negligible: both of the approaches fit the data very well at large distances from the source. For distances smaller than one scattering mean free path, the diffusion equation is not valid yet, and it underestimates the expected apparent relative velocity changes. This problem is solved by the radiative transfer approach, which is accurate at short times. We will therefore take the radiative transfer approach to model the depth sensitivity. We emphasize that $\varepsilon^{\text{Bulk}}$ from the radiative transfer in Figure 5.7 directly fits the data (no free parameters). The small discrepancies between the observation and model might be a result of the effective diffusivity that we used in the model, as we cannot measure the scattering mean free path for P-waves and S-waves separately (Turner, 1998).

5.2.4 Model for the depth sensitivity

To obtain a theoretical model $\varepsilon^{\text{theo}}(d, t)$ that describes the coda-wave sensitivity at depths, according to Equation (5.12), we now combine the surface wave part and the bulk part. For the bulk regime, we apply the radiative transfer approach. Figure 5.4 shows the depth sensitivity averaged over 10 models with $\sigma = 20\%$ velocity fluctuations. The source and receivers are placed at the free surface. The time window in the coda was centered around 3.6 s. With the minimum mean-square error criterion, we search the partition coefficients α for the surface waves and $1 - \alpha$ for the bulk waves, that optimize the fit of the depth sensitivity from the numerical simulations. In this case, the best fit to the experimental slope is obtained with a partition ratio of 1/4 for surface to bulk waves (α=0.25). The ratio between the coefficients implies that the waves spent more time as bulk-waves than as surface waves. As we can see in Figure 5.4, the proposed model gives an excellent fit. The zoom at small distances indicates the need to consider

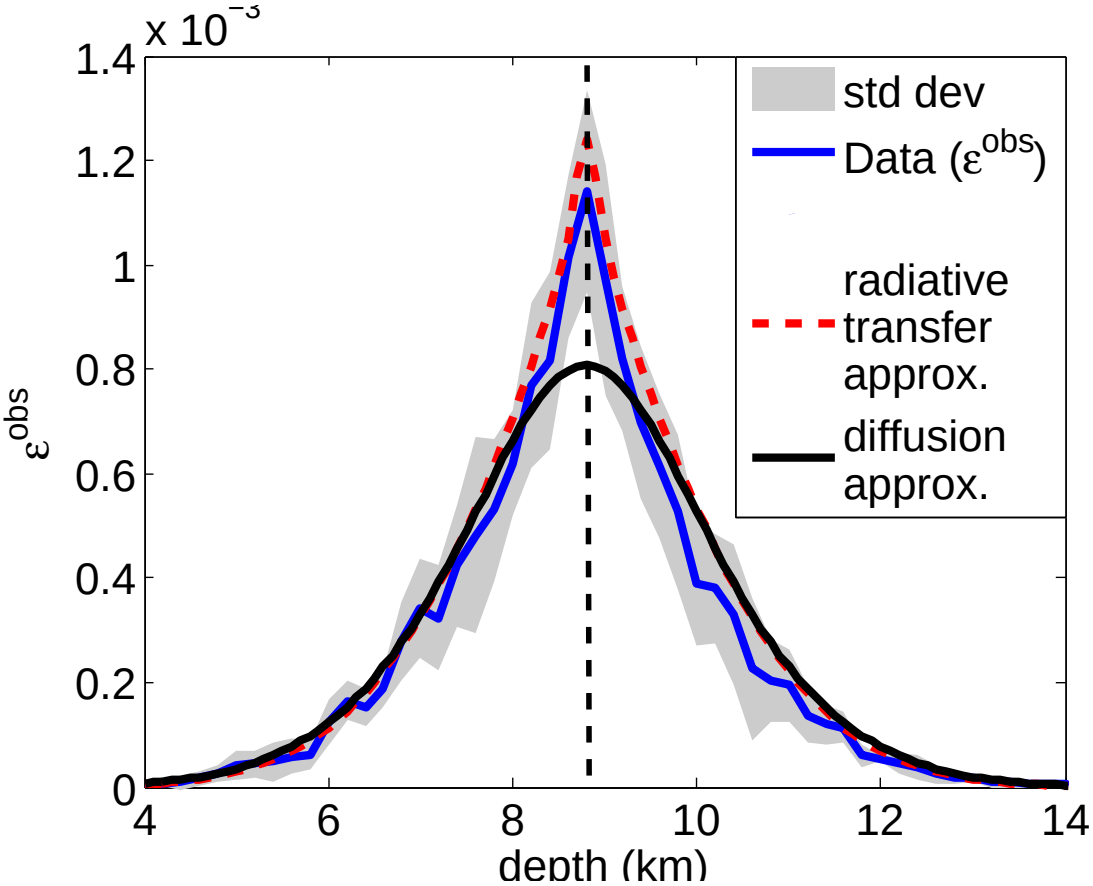

Figure 5.7: Apparent relative velocity changes $\varepsilon^{\text{obs}}(d, t = 3.6 \text{ s})$ versus depth of the perturbed layer for bulk waves in an infinite medium with $\sigma = 20\%$. The black line shows $\varepsilon^{\text{Bulk}}$ in the diffusion approximation and the dashed red line shows $\varepsilon^{\text{Bulk}}$ in the radiative transfer approximation. The vertical broken black line marks the positions of the source and the receivers.

surface waves in the model. In black, we see the fit using the sensitivity of bulk waves only (Figure 5.4). The steep slope over short distances is due to the rapidly vanishing sensitivity of the surface waves versus the depth.

According to Equation (5.15), which is written for weak velocity changes, the observed apparent relative velocity changes ε^{obs} depend linearly on the velocity changes $\frac{dv}{v}$ introduced in the perturbed layer. This is shown in Figure 5.8, where the apparent relative velocity changes at a receiver at close distance from the source are computed. The perturbed layer is at 500 m in depth, and its velocity is successively increased by 1%, 2%, 4% and 8%.

In the following, we now look at the behavior of the depth sensitivity and the evolution of the partition coefficient α by considering:

- different levels of heterogeneity (σ) in the model, in section 5.2.4.

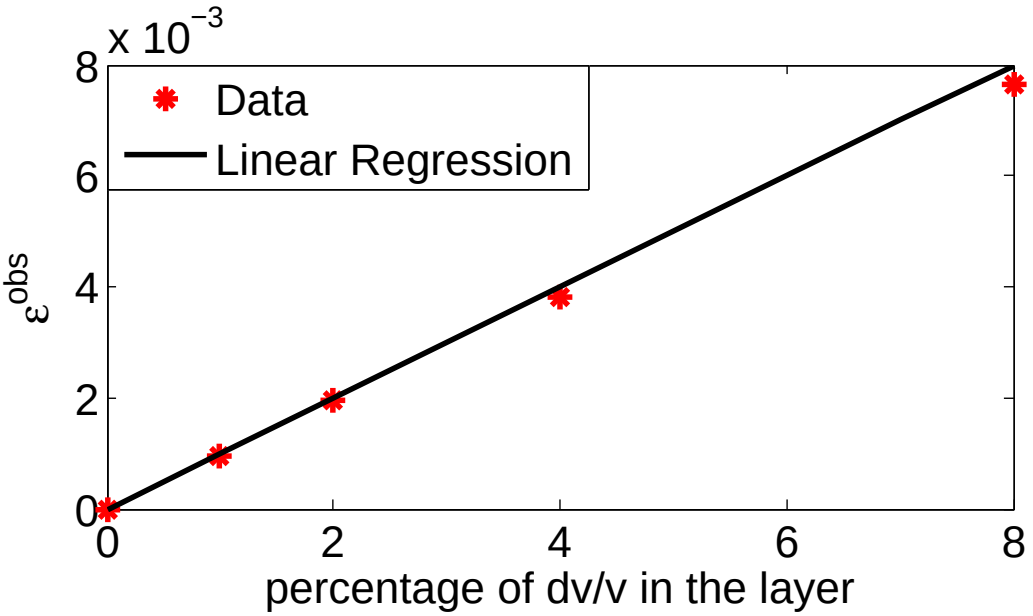

Figure 5.8: Apparent relative velocity changes $\varepsilon^{\text{obs}}(d, t = 3.6 \text{ s})$ versus the degree of perturbation in the layer. The layer is at 500 m in depth, and the receiver in the immediate vicinity of the source.

- different time windows in the coda, in section 5.2.4.

Different degrees of heterogeneity

In this section, we report on the results of the simulations with different levels of heterogeneity. To that end, we repeat the same types of simulations as described in section 5.2.2, using a free surface and three absorbing boundary conditions. We use velocity fluctuations of σ=5%, 10%, 15%, 20% and 30% for the random elastic medium. In Figure 5.9, we look at the apparent relative velocity changes $\varepsilon^{\text{obs}}(d, t = 3.6 \text{ s})$ averaged over ten models versus the degree of heterogeneity for three depth positions of the layer (200, 1000, 2000 m). We see clearly that waves traveling in media with little heterogeneity ($\sigma = 5\%$) are hardly sensitive to perturbations at depth, even to perturbations at 200 m depth only. The medium is not heterogeneous enough to cause significant conversion from Rayleigh to bulk waves, and vice versa. Therefore, the depth sensitivity is dominated by surface waves and limited to their penetration depth. When the medium becomes more heterogeneous ($\geq$ 10%), the bulk waves start to have an important role, and the coda waves become sensitive to changes at greater depths. This is even more emphasized in very heterogeneous medium (20%-30%), where an important apparent relative velocity change ε^{obs} is obtained for changes at greater depth. Such heterogeneous regimes are dominated by bulk waves.

This behavior can also be seen in Figure 5.10, where we report on the evolution of the partition coefficient α for surface waves and $1 - \alpha$ for bulk waves with time in the coda,

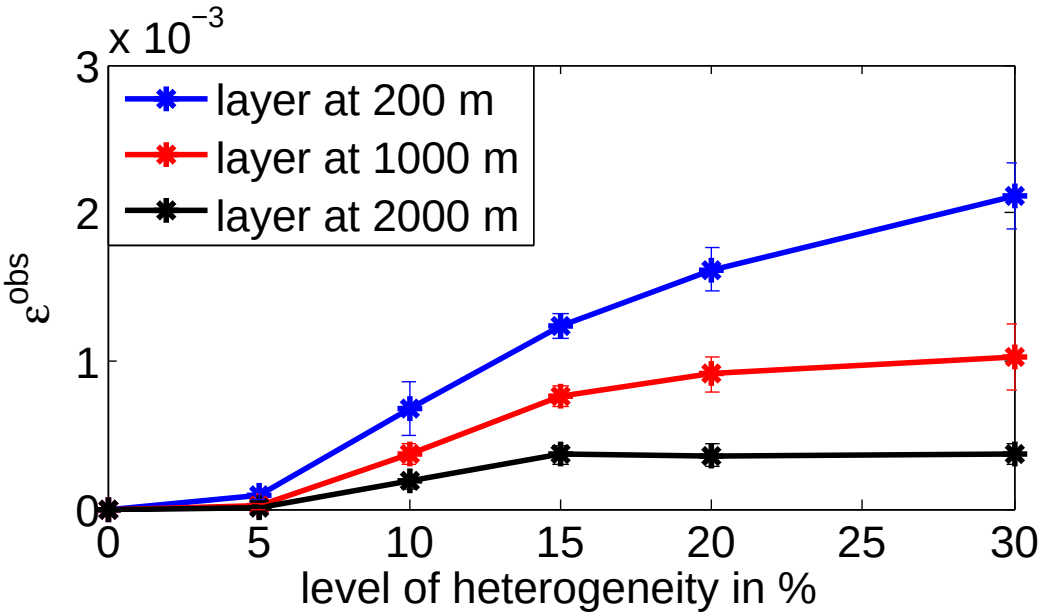

Figure 5.9: Depth sensitivity $\varepsilon^{\text{obs}}(d, t = 3.6 \text{ s})$ computed for different levels of heterogeneity towards changes occurring at 200, 1000 and 2000 m in depth.

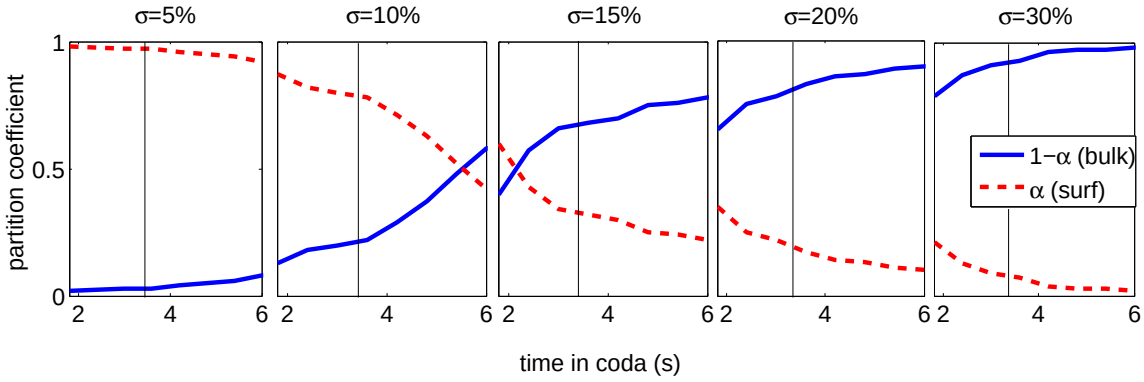

Figure 5.10: Evolution of the partition coefficients with time in the coda for models with degrees of heterogeneity ranging from 5% to 30%. In dashed red, the partition coefficient α for the surface-wave sensitivity, and in blue, $1 - \alpha$ for the bulk-wave sensitivity. The black vertical lines mark the processed times at t=3.6 s.

for models with degrees of heterogeneity ranging from 5% to 30%. At the moment, we focus only on values at 3.6 s, marked by black vertical lines in Figure 5.10, and discuss the time dependence in section 5.2.4. Consistent with the previous observations, in media with heterogeneities of only 5%, the partition coefficient for surface waves is at α=0.97. In media with heterogeneities of 10%, $\alpha = 0.8$. In media with $\sigma = 15\%$, we observe that $\alpha = 0.32$. For strongly heterogeneous media, bulk waves clearly dominate over surface waves with $\alpha = 0.17$ for $\sigma = 20\%$ and $\alpha = 0.1$ for $\sigma = 30\%$.

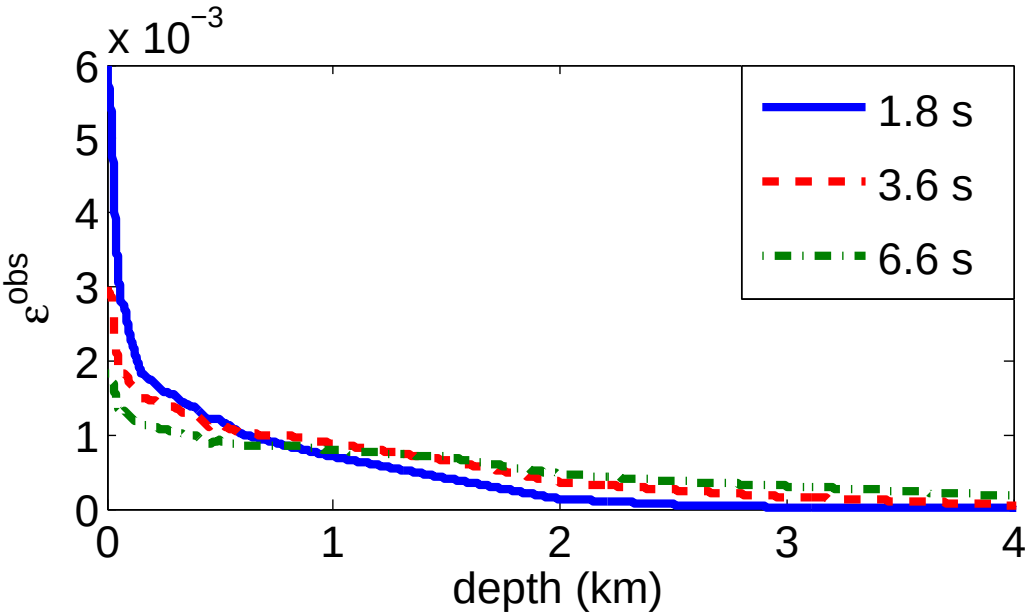

Figure 5.11: Depth sensitivity computed at different times in the coda for $\sigma = 20\%$. Note the importance of the surface-wave sensitivity for early times in the coda.

At this lapse time (t=3.6 s), the depth sensitivity is limited to the penetration depth of surface waves for weakly heterogeneous media, while in media with an increased amount of heterogeneity body waves play an prominent role.

Different times in the coda

In this section, we study the depth sensitivity at different times in the coda. To this end, we calculate the apparent relative velocity changes in different time windows in the coda, scanning a range from 1.8 s to 6.6 s. Figure 5.11 shows the results for a model with velocity variations of $\sigma = 20\%$ at three different times (1.8, 3.6 and 6.6 s). The importance of surface waves at shallow depths for early times in the coda is seen clearly. At later times in the coda, the bulk waves become increasingly important.

To have a more quantitative approach, we can study the evolution of the partition coefficients with time in the coda, as shown in Figure 5.10 for different heterogeneities. For media with heterogeneities of $\sigma = 5\%$, surface waves dominate bulk waves at all times in the coda. For media with heterogeneities of $\sigma = 10\%$, there is a crossing of α and $1 - \alpha$ at 5.4 s. Afterwards the sensitivity of the bulk waves is greater than that of the surface waves. Media with heterogeneities of $\sigma = 15\%$ also show the crossing from surface-wave dominance to bulk-wave dominance, although much earlier, at about 2.1 s, which indicates that due to the increased amount of scattering there have been much more surface wave to bulk wave conversions at an early time in the coda. At later times, α appears to stabilize. For strongly heterogeneous media with $\sigma = 20\%$, and $\sigma = 30\%$, bulk waves dominate surface waves at all times in the coda. We observe a continuous

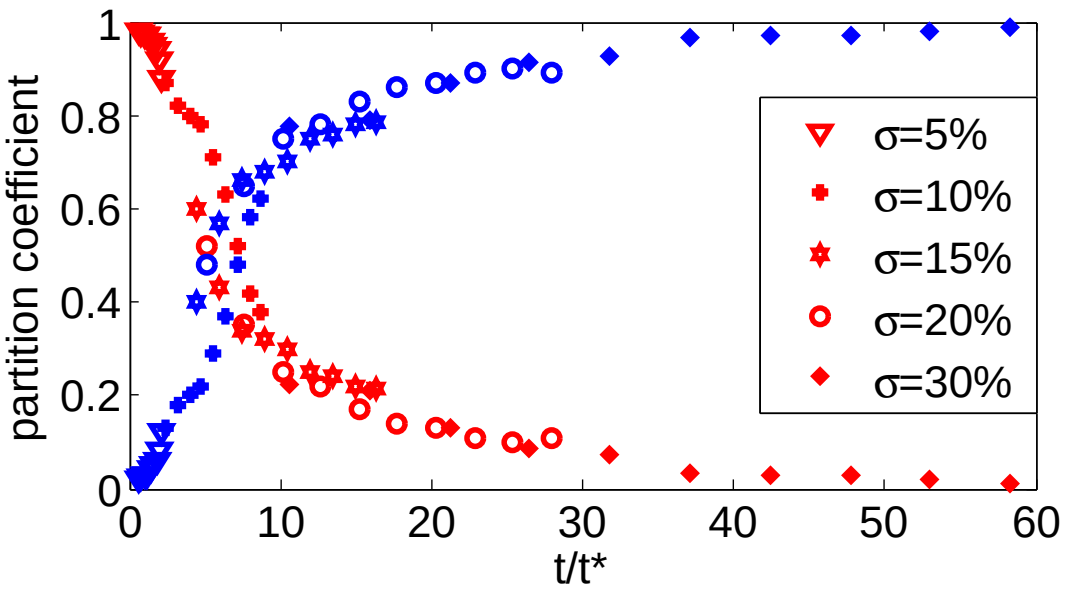

Figure 5.12: Evolution of the partition coefficients for different degrees of heterogeneity in the medium ranging from 5% to 30%. The time axis has been normalized by the transport mean free time $t^\star = \ell^\star/c$. In red the partition coefficients α for the surface-wave sensitivity, and in blue $1-\alpha$ for the bulk-wave sensitivity. The surface waves dominate for the first six mean free times.

slow decrease for α in the case of $\sigma = 20\%$ and for early times in $\sigma = 30\%$. For times after 4 s in the case of $\sigma = 30\%$, the bulk wave to surface wave contribution is stabilized with a marginal contribution of surface waves.

Looking at the ensemble of subplots in Figure 5.10, the evolution of the partition coefficients for different heterogeneities appears to be complementary. To prove this, we normalize the time axis by the transport mean free time $t^{\star=}\ell^\star/c$ and plot the partition coefficients against the new, dimensionless axis $t/t^\star$. The result is shown in Figure 5.12 for all heterogeneities. The crossing point of the partition coefficients for surface waves and bulk waves coincides quite well for all of the different heterogeneities. The surface waves dominate the depth sensitivity for about six mean free times. For later times, the bulk waves dominate.

A very interesting aspect that emerges from the time dependence in the coda is that we can discriminate a change that occurs at the surface from a change that occurs at depth by only looking at the shape of the apparent relative velocity changes ε^{obs} only. Figure 5.13 shows ε^{obs} versus the time in the coda: A) for very shallow positions of the perturbed layer (20 m), and B) for profound depths (1500 m) of the layer. For perturbations at shallow depth, the surface waves have an important role in the depth sensitivity of the coda waves. Their contribution is high at early times in the coda and decreases at later times. This is what we see as a decay in ε^{obs} on Figure 5.13A. For perturbations at greater depth, the contribution of the surface waves to the depth

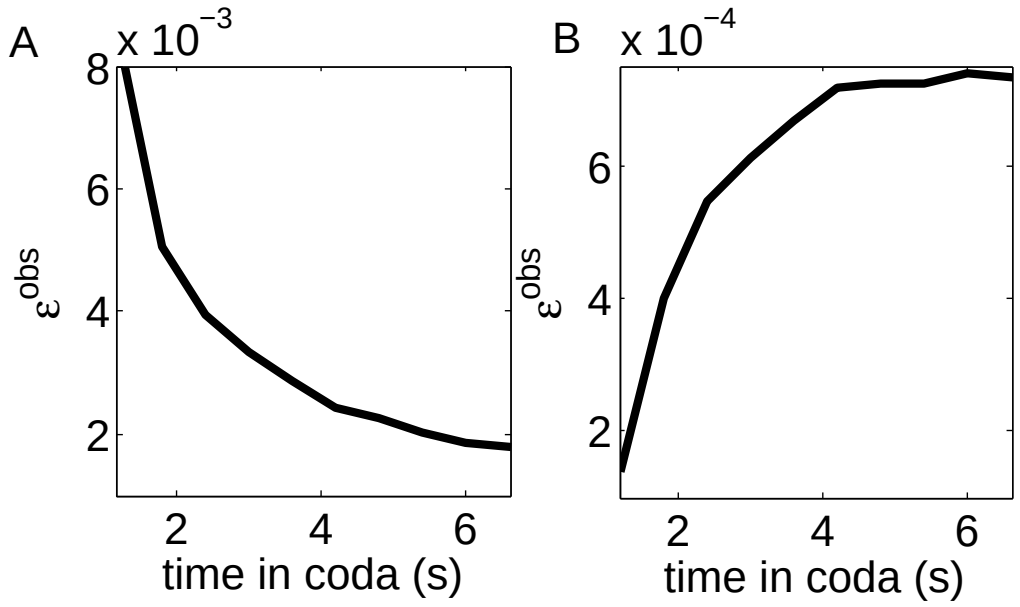

Figure 5.13: Apparent relative velocity changes ε^{obs} versus time in the coda. A. for a layer at shallow depth (20 m) and B. for a layer at great depth (1500 m).

sensitivity of the coda waves is negligible. Bulk waves have an important role here. At late times in the coda, the time increases that bulk waves have spent on average at greater depth, sampling the area more densely. The depth sensitivity consequently increases with time in the coda. This is why there is an increase in the apparent relative velocity changes ε^{obs} in Figure 5.13B.

Practical application for shallow depth

To demonstrate the practical relevance of the findings in this study, we re-visit the investigations of Sens-Schönfelder and Larose (2008, 2010), who analyzed the data from the Lunar Passive Seismic Experiment of the Apollo 17 mission. Similar to many datasets on Earth the ambient noise recorded during the Apollo era has been analyzed with the principles of seismic interferometry to obtain Green's functions between stations by correlation of the ambient noise field. Though the lunar seismic noise has different origin and the subsurface structure differs notably from Earth, the Green's functions exhibit a surface wave part that was used by Larose et al. (2005a) to image the subsurface. The coda part of the Green's functions was investigated by Sens-Schönfelder and Larose (2008) to measure the apparent velocity variation in the lunar subsurface over a period of eight day-night cycles on the Moon (about eight months).

The Green's functions obtained from the Apollo data thus have similar properties as their counterparts on Earth and the signals in the numerical simulation in this study. Interestingly the environmental conditions on the Moon affecting the subsurface velocities are much better known than on Earth because of absent tectonics and atmosphere.

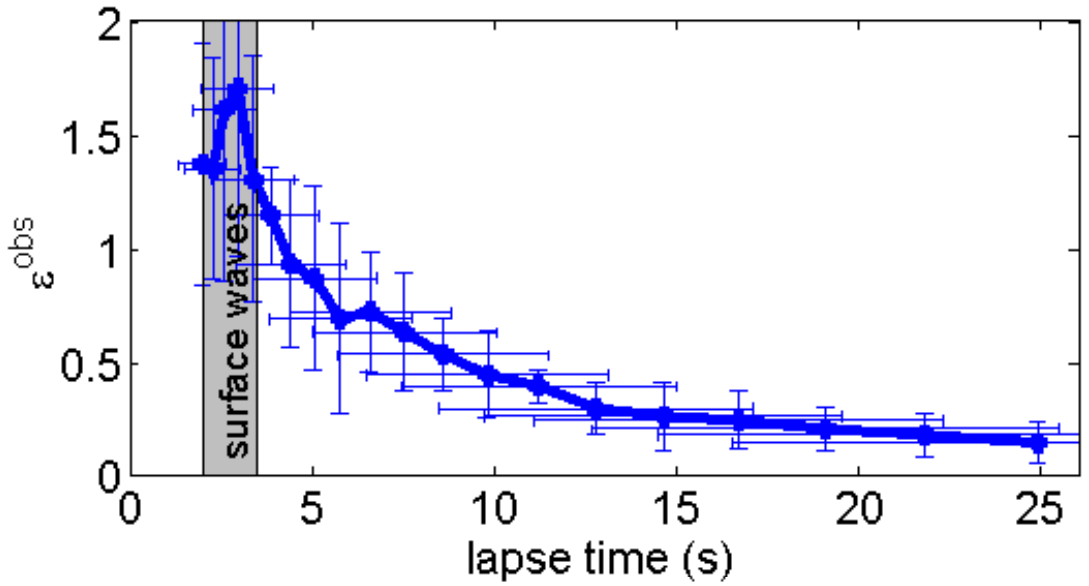

Figure 5.14: Relative amplitude of the apparent relative velocity changes computed for the lunar data. Velocity changes at the moon are limited to the shallow subsurface and verify the prediction about the decrease in the lapse with time, as illustrated in Figure 5.13 for the apparent relative velocity changes at shallow depths.

This renders the dataset ideal to illustrate the concepts developed in this article.

We construct daily cross correlation functions (CCF) between the six possible sensor pairs by correlating all available 24 hours segments of lunar noise. Apparent relative velocity changes were estimated in different time windows of the CCFs with the stretching technique (section 5.2.2) in comparison to a reference trace obtained by averaging all daily CCFs for each pair. Velocity variations show a periodicity of one month and were modeled as the consequence of temperature variations induced by the solar irradiation with its day and night cycle.

Thanks to this well controlled surface process that limits velocity changes to the shallow subsurface we can verify the predictions about the lapse time dependence of the apparent velocity change illustrated in Figure 5.13 with real seismic data. Measured in different time windows the apparent velocity curves are merely identical and differ only in their amplitude. Figure 5.14 shows the lapse time dependent factor that scales the amplitudes of the apparent relative velocity variations obtained from different lapse times windows. After the passage of the ballistic surface wave train associated with the maximum of the apparent velocity change we observe a decrease with increasing lapse time. This is exactly the predicted behavior for a near surface velocity perturbation because of the transition from surface wave sensitivity at early times to bulk wave sensitivity at later times as illustrated in Figure 5.13.

5.2.5 Conclusion

In this study, we investigated the depth sensitivity of coda waves to velocity perturbations at depth. We have presented the results from numerical wave-field simulations in media with different degrees of heterogeneity that contain a layer with perturbed velocities. We measured the apparent relative velocity changes due to the velocity perturbations at different depths. Analyses were conducted for different degrees of heterogeneity in the model, different percentages of velocity change within the layer, and different times in the coda:

1. we can relate the depth sensitivity of coda waves to a combination of bulk-wave sensitivity and surface-wave sensitivity as described in Equation (5.12).

2. changes at depth can be detected even if the sources and sensors are placed at the free surface, due to the scattering phenomena that mix surface waves and bulk waves, given a sufficiently heterogeneous medium.

3. from the time dependence of the relative velocity change in the coda, we can discriminate a change that occurs at the surface from a change that occurs at depth (Figure 5.13).

4. as illustrated in Figure 5.8, the apparent relative velocity changes increase linearly with the amplitude of the perturbation.

5. in Figures 5.10 and 5.12, we demonstrate the universal behavior of the partition ratio versus the time in the coda normalized by the scattering mean free time.

We have seen that the depth sensitivity of the coda waves depends on:

- the level of heterogeneity in the model,
- the lapse time in the coda,
- the degree of velocity perturbation,
- the depth position of the change.
- the source-receiver distance

The sensitivity kernel depends on the offset between source and receiver, nevertheless, in our geometry the sensitivity towards offsets is weak and has therefore not been addressed in more detail.

Frequency plays a crucial role in the value of the mean free time and therefore in the partition ratio of surface and bulk waves. Depending on the frequency band considered, the interpretation of velocity change measurements can be interpreted as the sensitivity of either body waves (Sens-Schönfelder and Wegler (2006), working at 0.5 Hz and above)

or sensitivity of surface waves (Rivet et al. (2011), working at 0.2 Hz and below and at very early times in the coda).

An interesting observation is the importance of surface waves for shallow depth and at early times in the coda. After six mean free times, the bulk waves clearly dominate the depth sensitivity. As a general framework, we can say that at early times, the waves most probably propagate as surface waves, and are sensitive to shallow changes. Later on the coda, scattering and mode conversions have occured and the waves sensed at the surface have spent more time in the bulk, they are therefore more sensitive to changes at depth. In any case, the observed apparent velocity change ε^{obs} is weaker than the actual local velocity change $\frac{dv}{v}$.

These results are of interest to improve future monitoring techniques using coda waves. The results will be used, for instance, to improve the inversion schemes on real data, including the imaging and locating of small changes that occur in fault zones or volcanic areas.

5.3 Numerical verifications in 3D

In the previous section we have shown that we can discriminate a change that occurs at the surface from a change that occurs at depth by only looking at the shape of the apparent relative velocity changes with time in the coda. We here demonstrate that this behavior is equally valid for waves propagating in all three dimensions.
We construct the 3D model similar to the 2D model. The model size is $10 \times 10 \times\ 6\ km^3$ in the x-, y- and z-direction respectively. The grid spacing is $\delta x = \delta y = \delta z = 50$ m. The record length is 16 s with a time step of 10^{-4} s. We use a van-Karman distribution for the heterogeneous medium and allow 20% of velocity fluctuations around a background P-wave velocity of v_P=6500 m/s. The S-wave depends on the P-wave velocity with $v_S = v_P/\sqrt{3}$. An exmeplary model is shown in Fig. 5.15.

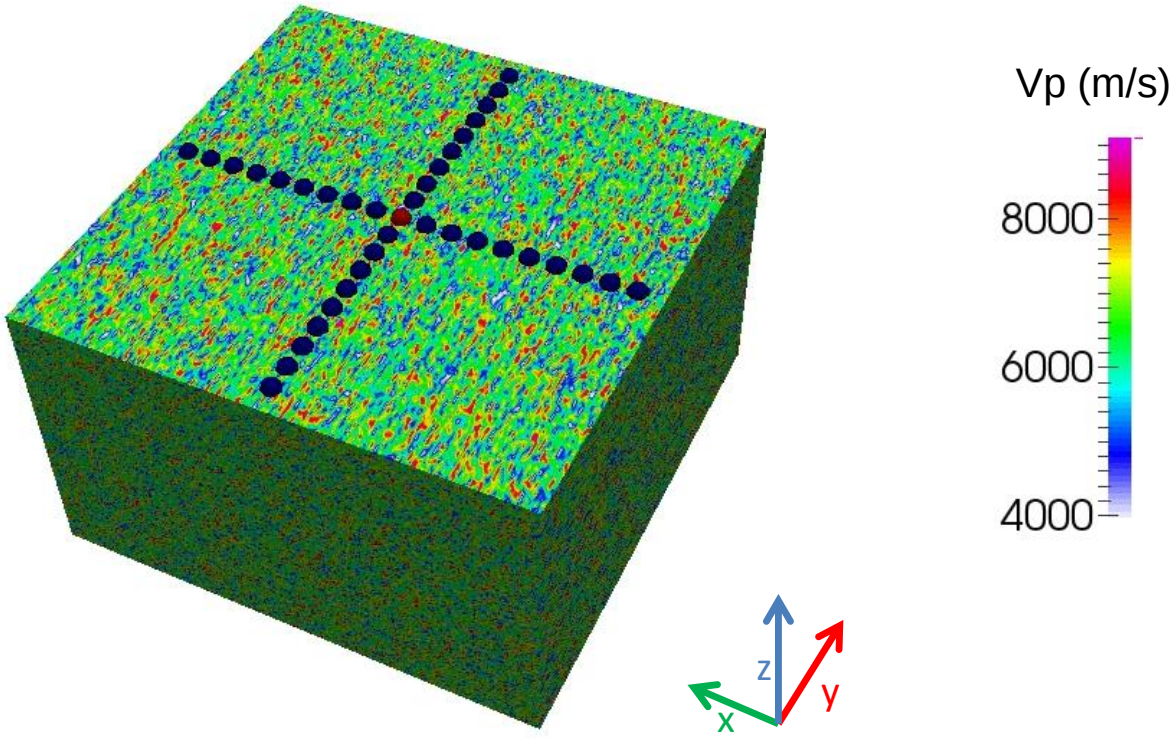

Figure 5.15: Heterogeneous model x,y=10 km, z=6 km. The red half-sphere marks the source position and the blue half-spheres mark the receiver positions.

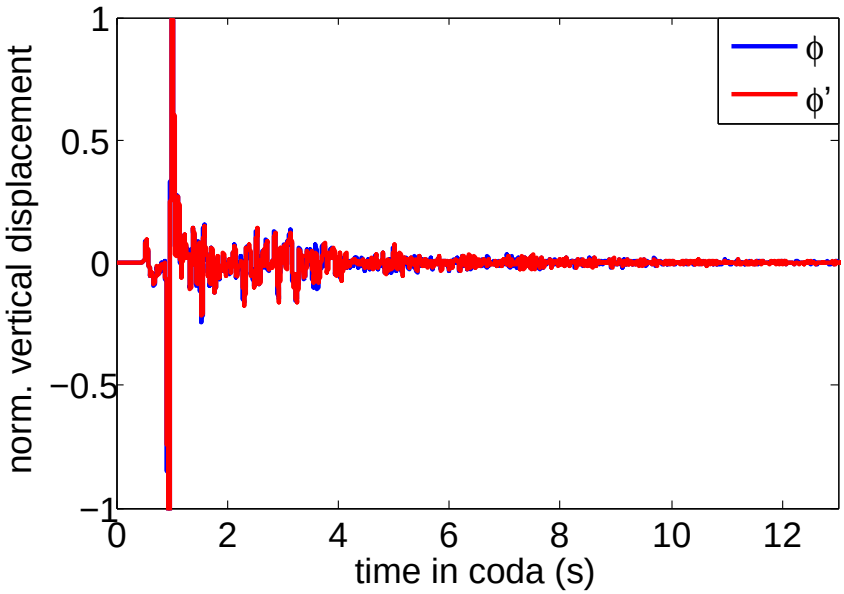

Figure 5.16: Synthetic seismograms recorded without (ϕ, blue) and with perturbed layer (ϕ', red) at the surface.

A source with a central frequency of 20 Hz is placed in the center of the medium in the first grid point below the surface (x, y=5000 m, z=50 m). We place a cross of receivers with 500 m spacing at the surface of the medium centered around the source. We run three simulations: A first one in the heterogeneous model as described above (background state), a second one in the medium above after introducing a thin layer (100 m) with a velocity reduction of $\frac{dv}{v} = 1.54\%$ at the surface (shallow perturbation) and third one after introducing this layer at 1500 m depth (deep perturbation). In Fig. 5.16 we show an exemplary synthetic seismogram at 3 km distance from the source with (red) and without (blue) the thin perturbed layer at the surface.

With the stretching technique we then determine the apparent velocity changes introduced by the layer in 1 s long time windows in the coda. As the source-receiver distances are small even for the receiver the furthest away from the source (4500 m), we average the results over all receivers. The results for the shallow and deep perturbation are shown in Fig. 5.17. We can clearly confirm the importance of surface waves to the depth sensitivity of coda waves for perturbations at shallow depths, as well as the important role that bulk waves play to sample the medium at more profound depth at later times in the coda.

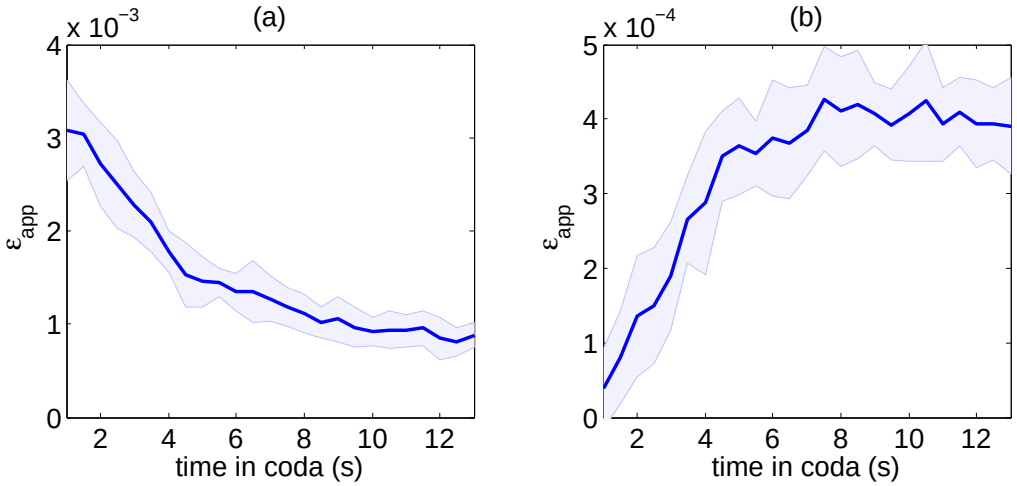

Figure 5.17: Apparent relative velocity changes ε^{obs} from the 3D simulations versus time in the coda. a) For a layer at the surface and b) for a layer at greater depth (1500 m).

Part III

Locating changes in multiple scattering media

Chapter 6

Locating changes on a volcano

Contents

At present there are about 500 to 600 active volcanoes around the world out of which approximately 50 erupt each year. Volcanoes claimed about 200,000 fatalities over the last 200 years (Bourseiller and Durieux, 2001) with an increasing risk, as many of these hazardeous areas have very fertile soils and are hence densely populated (e.g. 2 million. people around Merapi, 4 million around Popocatepetl and 3 million close to Vesuv). It is of great importance to better understand the dynamics at work in volcanoes to eventually precisely predict eruptions and save lives. Here, we focus on the use of ambient seismic noise correlations to locate underground changes associated with potential eruptions at Piton de la Fournaise volcano on La Réunion Island.

6.1 Why study the Piton de la Fournaise Volcano?

In the following, I give an overview of the geological context and the monitoring network at Piton de la Fournais (PdF), La Réunion Island, that make this volcano a fantastic natural laboratory. I then give brief summary of previous works that motivated us.

6.1.1 Geological context

PdF is on the corner of the hot spot track that extends from India to La Réunion Island in the South-Western part of the Indian Ocean (Fig. 6.1a). Courtillot et al. (1986) have shown that at the end of the Cretaceous (65 Ma) India was above the hot spot and great volumes of basaltic lava erupted to produce India's immense Deccan traps. The plate continued to move northeast over the hot spot and formed more volcanic centers: the Maldives (55−60 Ma), the Chagos Ridge (48−60 Ma), the Mascarene Plateau (35 Ma), the Mauritius Islands (7−1 Ma) and La Réunion Island (5-0 Ma). La Réunion Island is formed by the extinct volcano Piton des Neiges (3069 m, 5 Ma) (Deniel et al., 1992) in the west and the active volcano Piton de la Fournaise (2631 m, 0.530 Ma) in the East (Fig. 6.1b). Piton de la Fournaise (PdF) is at the position once occupied by the ancient Les Alizés volcano.

PdF is a basaltic shield volcano that became active around 0.5 Ma ago (Gillot and Nativel, 1989). In its actual form, PdF consists of the Plaine des Sables and an U-shaped structure composed of the Enclos depression (4.5 ka) and the Grand Brûlé slope down to the ocean (Fig. 6.1c). The volcanic activity of PdF is mainly restricted to the caldera. There are only few eruptions along the NE and SE rift zones, the Plaine des Sables and the Rivière des Remparts (Bachelèry, 1981). In April 2007 a large eruption cut the summit of the active cone (Michon et al., 2007) and formed a new caldera. These events were recorded by the monitoring network of the PdF Volcano Observatory.
At present day, PdF is one of the most active volcanoes in the world. From 1980 to 2010 PdF has erupted 60 times, twice per year on average (Peltier et al., 2009). These events can be sorted into three categories based on the location of their eruptive fissures: summital, proximal and distal eruptions. Summital eruptions occur in the summit craters of the volcano (Dolomieu and Bory), proximal eruptions take place on the volcanic cone and distal eruptions further afield. As mentioned previously, most eruptions occur in the summit area (Fig. 6.1c).

Magma storage and transport at PdF
The magma storage and transport at PdF is well studied and has been illustrated in form of a conceptual model by Famin et al. (2009) (Fig. 6.2). The magma reservoir beneath PdF is at 7.5 km or more. According to Famin et al. (2009), we can distinguish three main magma differentiation stages that yield summital or distal eruptions (Fig. 6.2):

1. The parental magma (in blue) may rise directly from the deep reservoir. In this

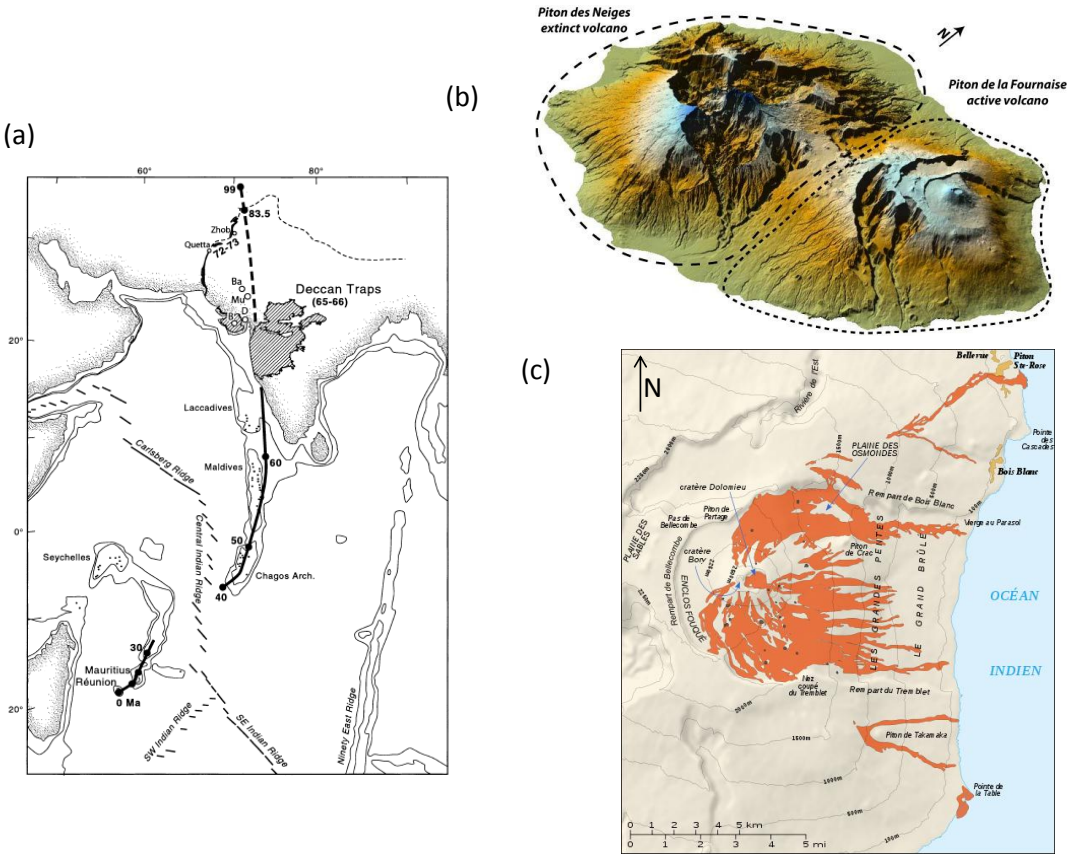

Figure 6.1: (a) The heavy line indicates the model track (0−65 Ma) of the La Réunion hotspot (Duncan, 1990; Mahoney et al., 2002). (b) La Réunion Island (*www.geosciencesreunion.fr*). (c) Map of the recent eruptions (1972 to 2000) of the Piton de la Fournaise shield volcano (*Institut de Physique du Globe de Paris*).

case, magmas undergo differentiation by plagioclase and clinopyroxene fractionation (yellow) during their ascent, yielding melts of the "Abnormal Group" that normally are found with eruptions at the distal flanks of the edifice.

2. However, most of the parental magma, episodically rises through a shallower reservoir at 2−2.5 km depth (or a complex of connected reservoirs) in which it undergoes differentiation by olivine fractionation. Between episodic refills, this reservoir becomes vertically chemically zoned by differentiation with steady state basalts (red) at the top and picrites (green) at the bottom. Dykes originating at the top of this storage complex yield summit eruptions, while dykes originating at the base of the reservoir yield lateral eruptions, as shown by GPS data and earthquake depths determination (Longpré et al., 2007; Peltier et al., 2005a).

3. Crystallization of plagioclase and clinopyroxene microlithes during magma ascent produces differentiated residual matrix glasses (in yellow) within, steady state

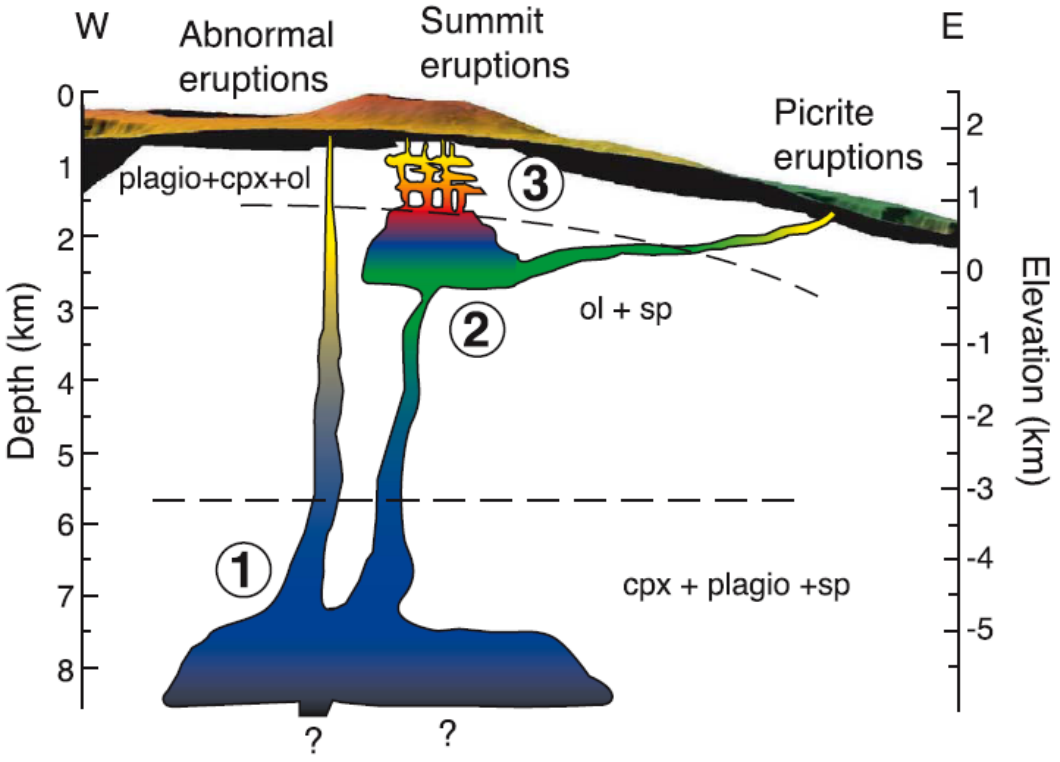

Figure 6.2: Conceptual model of magma storage and transport beneath PdF volcano (Famin et al., 2009). (1) Parental magmas (in blue) may occasionally rise directly from a deep reservoir at 7.5 km depth or more. (2) Most of the parental magma, rises through a shallower reservoir at 2−2.5 km depth. Dykes originating at the top of this storage complex yield summit eruptions, while dykes originating at the base of the reservoir yield lateral eruptions. (3) Occasionally, some very shallow pockets of magma may become disconnected from the main storage complex and evolve for longer time, yielding small differentiated eruptions.

basalts, picrites and abnormal basalts at shallow level (<600 m depth). Occasionally, some very shallow pockets of magma may become disconnected from the main storage complex and evolve for longer time, yielding small differentiated eruptions.

These internal magma transportation processes have an influence on the volcanic cone. Rising magma below the cone in form of a dyke intrusion or sills, is expressed as a slight deformation/dilatation of the cone (Fig. 6.3a). These deformations are transmitted to the surface as slight changes in the slope of the cone, fissure openings or distance changes between two reference points. The swelling of the cone normally disappears with the onset of the eruption itself (Fig. 6.3b). These changes are very small, local and invisible but they can be measured and monitored with GPS, extensometers and

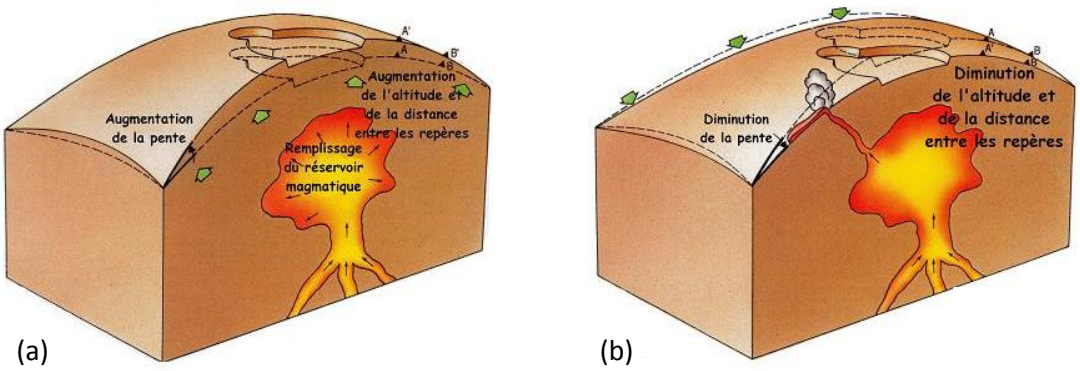

Figure 6.3: Schematic model of the deformations introduced by the swelling of the volcanic cone due to the filling of a magma reservoir (a) and after the eruption (b). (Source: *Institut de Physique du Globe de Paris*).

with coda wave interferometry, as the swelling of the volcano introduces small pressure changes and hence small changes in the seismic velocities.

6.1.2 Monitoring network at PdF

Since the establishment of the "Piton de la Fournaise volcanic observatory" (OVPF/IPGP) in 1980, a permanent and telemetered instrumentation of the volcano began. The OVPF maintained since then a permanent seismic and deformation network with a varying amount of stations, and also since 2008 a three miniDOAS network that permanently measure the SO_2 output around PdF. At the moment, the deformation network is composed of sixteen permanent GPS stations, seven tiltmeters and three extensometer stations (Staudacher et al., 2009). The seismic network has continuously recorded data from about ten short-period 1 Hz seismometers and six broad-band stations since 1999. Since 2009, fifteen additional broad-band high-resolution seismic stations have been installed in the framework of the UnderVolc (Understanding Volcanic Processes, http://undervolc.fr) research project (Brenguier et al., 2012).
This unique surveillance network is used to cover different research topics. Among others: processes of dike injection (Taisne et al., 2011), dike-induced deformation (Peltier et al., 2011), microseismicity relocation (Got et al., 2008), shear-wave splitting monitoring (Gerst and Savage, 2004), long-period event source inversion (De Barros et al., 2011), flank instability/rock fall processes (Hibert et al., 2011), and predictability of volcanic eruptions (Grasso and Zaliapin, 2004). Of highest interest for us is certainly the development of high-precision seismic velocity monitoring from seismic noise (Brenguier et al., 2008b).

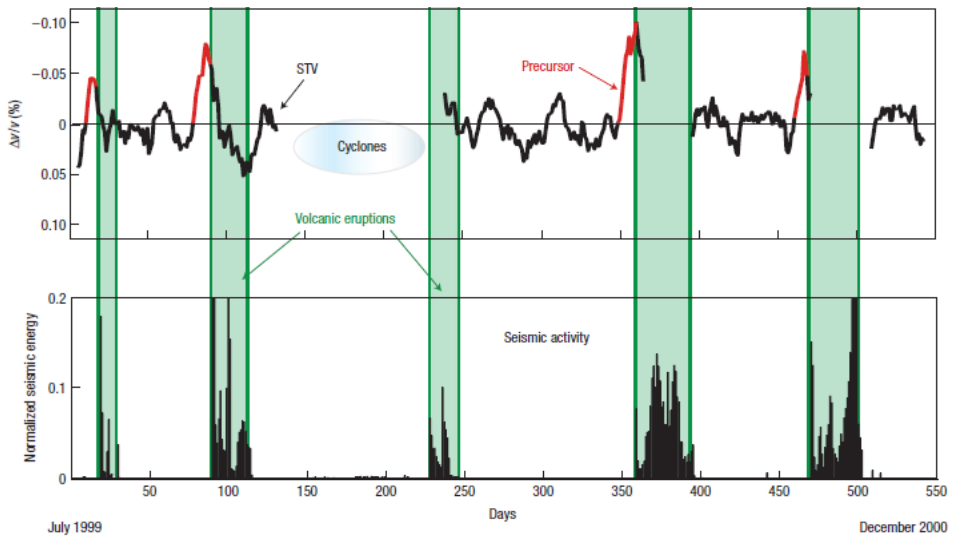

Figure 6.4: Evolution of relative velocity changes at PdF. The lower panel shows the daily seismic energy measured at a sensor located near Dolomieu crater. (Source: Brenguier et al. (2008b)).

6.1.3 Previous studies and motivation

Since the nineties, observations of temporal variations in coda waves have been linked to volcanic processes. Fehler et al. (1988) interpreted variations of the intrinsic attenuation of the seismic coda before and after the Mount St. Helens eruption in 1981 as the opening and closing of microfractures. Aki and Ferrazzini (2000) studied quantitative seismic events at long period to estimate the magma transport in real time at PdF. In the last decade, with the upcoming of ambient seismic noise cross-correlations, very interesting advances in forecasting volcanic eruptions have been made. Sens-Schönfelder and Wegler (2006); Brenguier et al. (2008b) have shown that the apparent relative velocity changes act as precursors of volcanic eruptions (Fig. 6.4).

Duputel et al. (2009) have identified two major processes at the origin of the apparent relative velocity changes. They could identify processes accompanied by velocity drops as summit inflations and processes accompanied by velocity increases as edifice deflations These last ones follow for instance the opening of eruptive fissures.

Not only forecasting volcanic eruptions in time but also their location (summit, flank, etc) is of first importance for risk management. As the strength of the coda variation depends on the position of the station pair relative to the change and the size of the change itself, this property has been used by Brenguier et al. (2008b) and Duputel et al. (2009) to regionalize velocity changes at PdF. They determined relative velocity changes

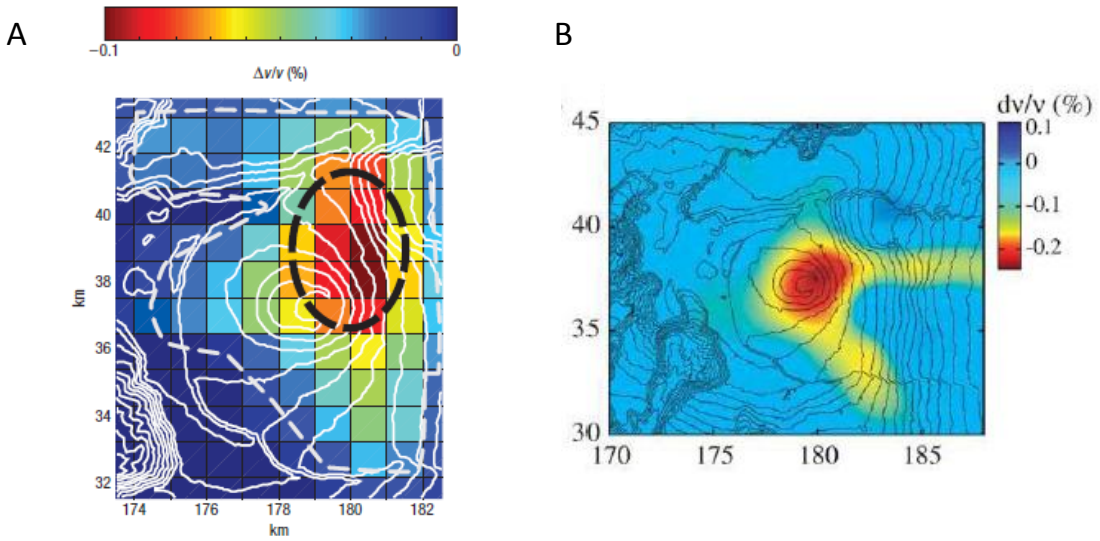

Figure 6.5: Geometrical regionalisation of velocity changes at PdF by Brenguier et al. (2008b) (A) and Duputel et al. (2009) (B).

separately for different receiver-couples and then considered ellipses of single scattering around the direct trajectory. In case of ellipses that cross each other, the velocity changes are averaged and attributed to the concerned grid cells. As a result they obtained a 2D map with a rough estimation of the spatial distribution of the velocity changes (Fig. 6.5). To optimize this procedure, which is necessary in case of dense receiver networks, a probabilistic approach is necessary. The use of more realistic sensitivity kernels of the coda time shifts should help to image localized velocity perturbations.

The new installation of 15 additional broadband seismic stations at PdF in 2009 (Brenguier et al., 2012) makes it possible to try these more challenging localization methods. Based on recent developments in wave physics in multiple-scattering media (Larose et al., 2010; Rossetto et al., 2011; Froment, 2011; Planès, 2013; Planès et al., 2013), we develop an imaging procedure that benefits from the high sensitivity of scattered waves to weak changes in the media, and that allows a spatial location of mechanical changes in the edifice.

6.2 Imaging pre- and co-eruptive structural and mechanical changes of a volcano with ambient seismic noise

Imaging pre- and co-eruptive structural and mechanical changes of a volcano with ambient seismic noise

Anne Obermann, Thomas Planès, Eric Larose, Michel Campillo.

Article published in *Journal of Geophysical Research* 2013.

Abstract:

Forecasting the location of an eruption is of primary importance for risk management in volcanic regions. Locating the underground structural changes associated with a potential eruption is also a key issue to better understand the dynamics at work in a volcano. Using recent results in wave physics, we develop an imaging procedure that is based on the sensitivity of multiply scattered waves to weak changes in heterogeneous media. This procedure allows to locate changes in both mechanical and scattering properties of the studied medium.

We study ambient seismic noise from 19 broadband stations at the active volcano Piton de la Fournaise on Reunion Island, recorded from June to December 2010. During this period, two volcanic eruptions occurred at two different locations. We calculate the noise cross-correlations and study two types of changes in the coda: apparent velocity variations related to changes in the elastic properties of the medium; and, waveform decoherence associated with variations in the scattering, and thus the geological structures. We observe that the temporal variations of both of these parameters provide potential precursors of volcanic eruptions at Piton de la Fournaise. The locations determined from the pre- and co-eruptive changes in both parameters are in good agreement with the actual eruptive activities. These data demonstrate that the coda of ambient noise correlations contains deterministic information on the locations of the eruptive processes in an active volcano. Our analysis offers an original and significant constraint for the localization of forthcoming volcanic eruptions.

6.2.1 Introduction

Estimating the location of potential eruptive fissures (e.g., summit area, flank of the volcanic cone, or further afield) is of essential importance for risk management in volcanic areas. Localization of the underground structural changes associated with a pending eruption is also a key issue, for the better understanding of the dynamics of a volcano.

Nevertheless, these scientific challenges are not always correctly addressed by the existing seismic, geodetic, and geochemical techniques. Patanè et al. (2006) reported that an increase in the pressure of volcanic fluids (e.g., magma, water) or gases is often accompanied by dyke intrusions prior to volcanic eruptions at Mount Etna. This activity induces perturbations to the elastic properties that can result in subtle changes in the volcanic edifice. These changes can be detected by geodetic methods, such as the use of tilt- and strain- meters (Peltier et al., 2005b) and satellites (Massonnet et al., 2001). These methods are limited by their sensitivity, as they can only monitor changes that occur at the near surface. Information about short-term (i.e., from seconds to days) magma migration at depth can be obtained from the precise localization of volcanic seismicity (Chouet, 1996, 2003; Battaglia et al., 2005). However, the analysis of volcanic seismicity cannot be used to detect the aseismic magma pressurization that precedes fracturing and magma migration.
Observation and interpretation of modifications of seismic waveforms in late arriving coda waves provide a potential method to detect fracturation and magma migration. Coda waves result from multiple scattering of seismic vibrations by the heterogeneities that compose a complex medium. As coda waves propagate much farther than direct waves, they can sample the medium more densely and are sensitive to small perturbations in its mechanical properties. This feature led to the development of the coda-wave interferometry (CWI) technique (Poupinet et al., 1984; Roberts, 1991; Roberts et al., 1992; Snieder et al., 2002; Snieder, 2006), which can detect small velocity changes in a heterogeneous medium. The detection of temporal changes with coda waves has been successfully applied in different areas in seismology. This includes the monitoring of volcanoes (Ratdomopurbo and Poupinet, 1995; Brenguier et al., 2008b, 2011; Haney et al., 2009), fault zones (Wegler and Sens-Schönfelder, 2007; Brenguier et al., 2008a), landslides (Mainsant et al., 2012), subduction zones (Rivet et al., 2011) and seasonal changes (Meier et al., 2010; Sens-Schönfelder and Wegler, 2011). Here, we monitor the mechanical changes associated with two eruptions of Piton de la Fournaise (PdF) on Reunion Island in 2010. PdF is currently one of the most active volcanoes on Earth, with three eruptions per year on average (Brenguier et al., 2011). With intense eruptive activity but weak tectonic activity, this volcano is very well suited for the study of innovative monitoring techniques.

Since the 1990s, seismic noise has been recorded constantly at PdF using a varying number of seismic stations. Brenguier et al. (2008b) used the apparent relative velocity changes obtained from seismic noise cross-correlations between the different stations at PdF as precursors of volcanic eruptions. Duputel et al. (2009) identified two major processes at the origin of the apparent relative velocity changes. They identified processes that were accompanied by velocity drops as summit inflations, and processes that were accompanied by velocity increases as edifice deflations, which follow, for instance, the opening of eruptive fissures.

Existing techniques allow the detection of apparent relative velocity changes prior

to an eruption, although the locating of these changes is only possible with limited resolution. Variations in the cross-correlation coda properties depend on the position of a station pair relative to the location and magnitude of the medium perturbation. Brenguier et al. (2008b) and Duputel et al. (2009) used CWI measurements to regionalize velocity changes at PdF, and Takagi et al. (2012) used the direct waves of the cross-correlation functions to regionalize velocity changes that are associated with an earthquake. In such geometrical regionalizations, influences from cross-correlation pairs are only considered along ellipses around the direct trajectory within the single scattering regime. A better resolution requires the multiple scattered path to be taken into account.

In 2009, 15 additional broadband seismic stations were installed at PdF (Brenguier et al., 2012). The new density of the broadband stations allows the investigation and application of more sophisticated localization methods. Based on recent results in wave physics (Larose et al., 2010; Rossetto et al., 2011; Froment, 2011; Planès, 2013; Planès et al., 2013), we develop here an imaging procedure that is based on the sensitivity of the scattered waves to weak changes in the multiple scattering media, and that allows spatial localization of the changes of structural and mechanical properties in the edifice.

In section 6.2.2, we describe the seismic and geodetic data that we use in this study, and we explain how we compute the cross-correlations from ambient seismic noise, and how we determine the estimates of the apparent relative velocity changes and waveform decoherence. We emphasize that the apparent relative velocity changes and the waveform decoherence act as precursors of volcanic eruptions. In section 6.2.3, we describe the linear least-squares inversion that can be used to locate the medium changes, and we show the inversion results for the apparent relative velocity changes. We image pre- and co-eruptive elastic changes for the major eruption at PdF. In section 6.2.4, we adapt the inversion scheme to the decoherence data. The results from the corresponding inversion provide an image of the pre- and co-eruptive structural changes of the volcanic edifice for both eruptions.

6.2.2 Seismic and geodetic data and data processing

We analyze continuous seismic records from 19 broadband stations on PdF from June to December 2010 (Fig. 6.6). During the 7 month period of interest, a major eruption occurred between October 14 (Julian day 287) and October 31 (Julian day 304), and a minor eruption occurred between December 9 (Julian day 343) and December 10 (Julian day 344). The October eruption was southeast of the Dolomieu crater, and the December eruption was northwest of the crater (Fig. 6.6, black stars).

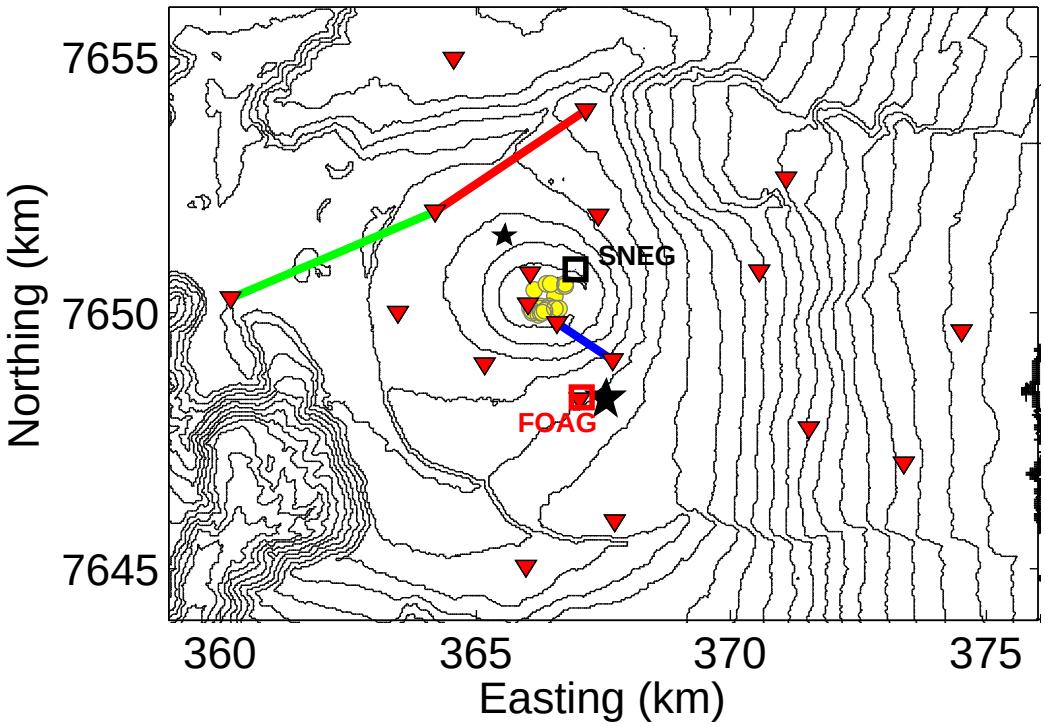

Figure 6.6: Topography map of PdF showing the location of the broadband seismic stations (inverted triangles). The larger star marks the volcanic eruption in October 2010, southeast of the Dolomieu crater, and the smaller star marks the volcanic eruption in December 2010, northwest of the crater. The axes are in UTM zone 40S coordinates. The yellow circles represent the locations of major seismic events that occurred prior to the eruption. The colored lines correspond to the station pairs discussed in section 5.2.2. The squares indicate the locations of the GPS stations FOAG (red) and SNEG (black).

Cross-correlation of ambient seismic noise

The data processing follows Brenguier et al. (2008b). We down-sample the continuously recorded seismic noise from 100 Hz to 20 Hz, and apply a spectral whitening filter in the 0.1 Hz to 1.0 Hz spectral band. Cross-correlation functions in this period range consist mainly of Rayleigh waves, which are sensitive to about 2 km below the edifice surface (Brenguier et al., 2007). We apply one-bit amplitude normalization (Larose et al., 2004a), and cross-correlate the vertical component of the seismic noise between all of the stations. We correlate 2 h segments, remove segments with earthquakes, and stack daily correlation functions. A daily stack is rejected if <8 segments are available. We obtain a total of 171 cross-correlation functions (φ^i) that are associated with all of the possible station pair combinations i. In Fig. 6.7, we show an example of 7 months of cross-correlation functions for the receiver pair UV05 and UV12 (Fig. 6.6, blue).

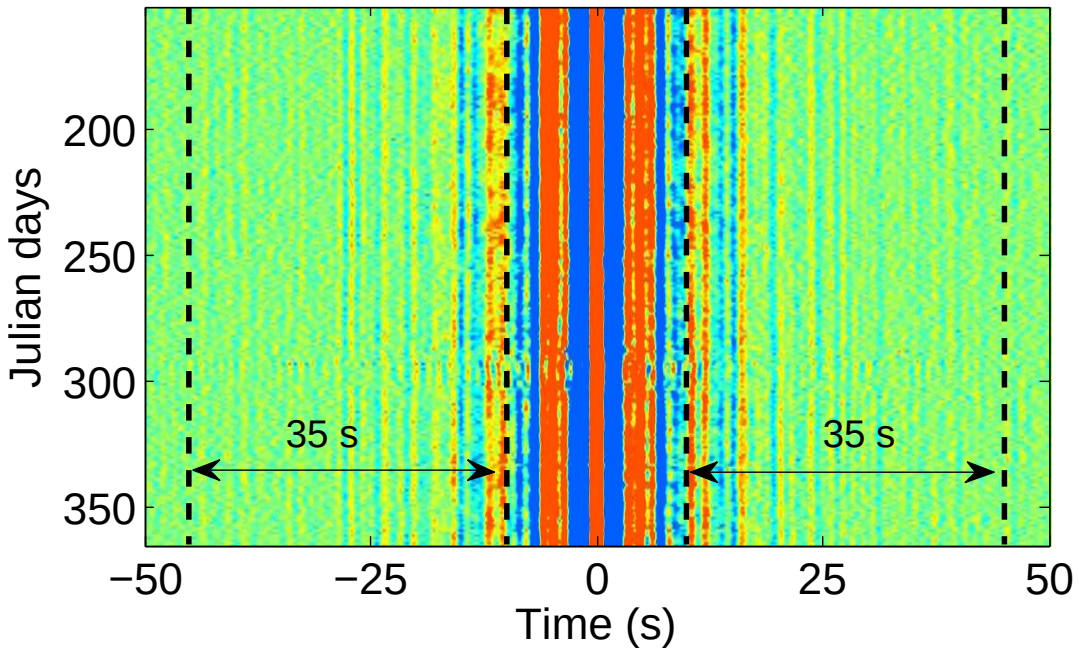

Figure 6.7: Cross-correlation function between the receiver pair UV05 and UV12 for the 7 months of interest.

The cross-correlation functions are stable over the observed time period, although slight daily fluctuations occur. These random fluctuations are due to changes in the noise sources. The correlations have thus not fully converged to the Green's function. An estimate of these fluctuations can be found in Weaver et al. (2011). For the present study, we are interested in the coda between 10 s and 45 s.

Apparent velocity variations in the coda of the cross-correlations

From June to August 2010, there was no volcanic activity at PdF. We stack these 90 daily cross-correlations, to construct a set of stable reference cross-correlation functions $\varphi_i^{\text{ref}} = \langle \varphi_i^{1:90} \rangle$ for all of the receiver pairs i. The temporal evolution is then tracked by comparing this reference φ_i^{ref} with the 'current' correlation $\varphi_i^{\text{curr}} = \left\langle \varphi_i^{j-1:j+1} \right\rangle$ around day j. A current correlation thus consists of a 3-day-long stack. We use the stretching technique (Lobkis and Weaver, 2003; Sens-Schönfelder and Wegler, 2006) to quantify the temporal evolution of the seismic velocity. Each waveform φ_i^{curr} is stretched or compressed in time by a factor $t \to t(1-\varepsilon)$ and compared to the reference waveforms φ_{ref}^i. For each ε, we calculate the correlation coefficient CC between the current stretched signal φ_i^{curr} and the reference signal φ_i^{ref} (Hadziioannou et al., 2009):

$$CC(\varepsilon) = \frac{\int_{t_1}^{t_2} \varphi^{\mathrm{curr}}\left[t(1-\varepsilon)\right] \varphi^{\mathrm{ref}}\left[t\right] dt}{\sqrt{\int_{t_1}^{t_2} (\varphi^{\mathrm{curr}})^2\left[t(1-\varepsilon)\right] dt \int_{t_1}^{t_2} (\varphi^{\mathrm{ref}})^2\left[t\right] dt}}, \tag{6.1}$$

where t_1 and t_2 are the beginning and the end of the time window used (Fig. 6.7, dashed lines). In our case, the length of the time window is 35 s and it starts after the surface-wave arrivals. The value of ε that maximizes the cross-correlation coefficient between the reference and the current signals corresponds to the apparent relative velocity change $\varepsilon_i^{\mathrm{app}}$ observed for each pair of stations i. If we assume a global homogeneous velocity change $\frac{dv}{v}$ in the volume of the edifice, the apparent velocity change $\varepsilon_i^{\mathrm{app}}$ measured in the coda corresponds to the actual velocity change: $\varepsilon^{\mathrm{app}} = \frac{dv}{v}$. In general the assumption of a global change provides simplification, as the velocity changes are confined to limited regions. In this case, the apparent velocity change $\varepsilon_i^{\mathrm{app}}$ depends on the coda lapse time, on the position x_0 of the change relative to the couple of the receivers i, and on the amplitude of the local change $\frac{dv}{v}(x_0)$; thus, in general: $\varepsilon_i^{\mathrm{app}} < \frac{dv}{v}(x_0)$.
As the computed cross-correlation functions are asymmetric, due to the anisotropy of noise propagation directions (Stehly et al., 2007), we stretch the causal and acausal parts of the signal independently and average the results. As a quality criterion, we only keep correlations from station pairs that were recorded continuously and show coherence greater than 0.8 on average during the eventless period from June to August. We are hence left with 104 station pairs for the October eruption, and 89 station pairs for the December eruption.

In Fig. 6.9a, we show the measured apparent velocity changes from June to December 2010 for the three cross-correlation pairs indicated in Fig. 6.6. The shaded zones mark the time periods of the two eruptions. For a station pair southeast of the cone and in the vicinity of the October eruption site, we observe a decay of $\varepsilon^{\mathrm{app}}$ (up to 0.6%) prior and during the October eruption (Fig. 6.9a, blue). After the eruption, the $\varepsilon^{\mathrm{app}}$-value increases slowly, although it does not reach its initial value by the end of the year. We interpret the observed decreases in the seismic velocities as an effect of dilation of part of the volcano edifice, which results from magma pressurization within the volcano plumbing system (Brenguier et al., 2008b). The recovery of the $\varepsilon^{\mathrm{app}}$-value after the eruption is consistent with deflation caused by depressurization of the magma during its extrusion to the surface. The December eruption that was located northwest of the cone cannot be clearly identified from this pair of stations, as it is probably too far away to have an influence. For a station pair situated northeast of the crater, and therefore close to the minor December eruption site, we observe a decrease in the $\varepsilon^{\mathrm{app}}$-value prior to the October eruption, an increase during the October eruption, and a return to the initial value, which is followed by an increase for the December eruption (Fig. 6.9a, red). We interpret the observed decrease in the seismic velocities as an inflation of the volcanic edifice prior to the eruption. The stresses (pressure increase) then localize beneath the main crater, which induces a decrease of velocity in the caldera (Fig. **??**b), but also a soil compaction, and hence increase of velocity, outside the caldera. For a station pair located at the western rim of the volcano at a significant distance from both of the

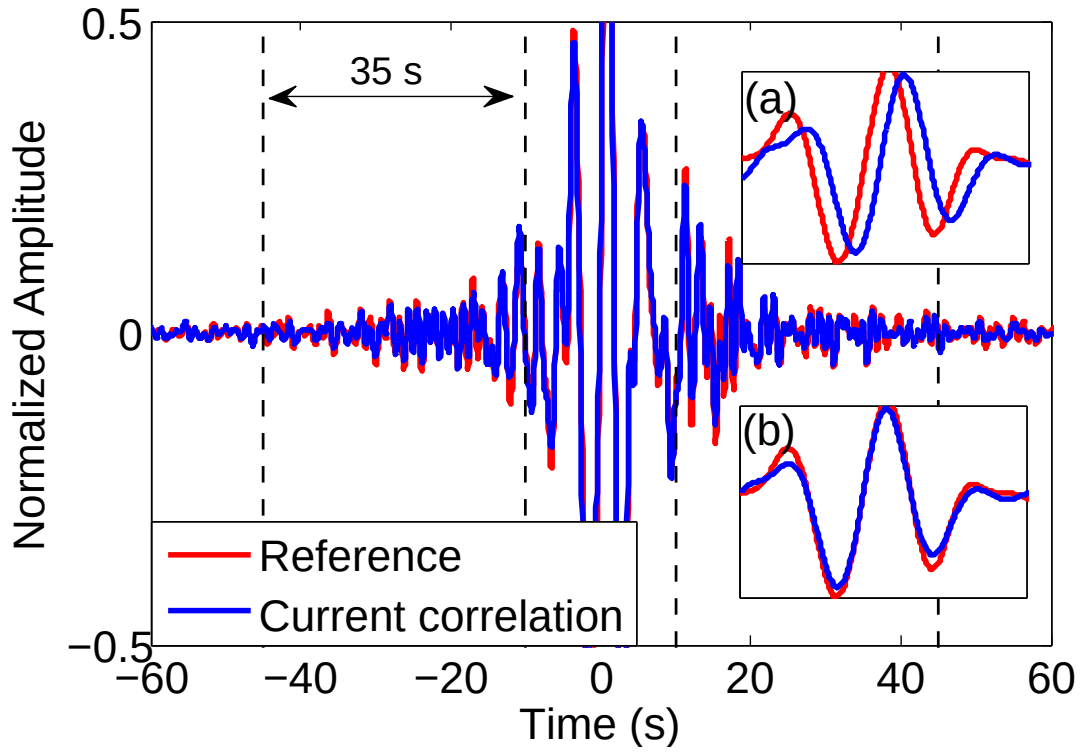

Figure 6.8: Reference correlation function (red) and 'current' correlation function (blue). Inset (a) shows the time delay of the 'current' correlation function in the coda centered at about 30 s. Inset (b) shows the 'current' correlation function after it has been corrected for its time delay. We observe waveform decoherence.

eruptions, the coda were not affected by any of the eruptions (Fig. 6.9a, green).

Waveform decoherence in the coda of the cross-correlations

To explain waveform decoherence, let us focus on Fig. 6.8. If we consider a wave that encounters a local velocity perturbation (e.g., a mechanical change in the medium), the change will show its signature on the current record (Fig. 6.8, blue) in the form of a time shift of the late-arriving waves, when compared to a reference (Fig. 6.8, Inset a; initial state in red). As described in the previous section, we can quantify the temporal change with the stretching technique and correct for this by stretching the current record with $\varepsilon_i^{\text{app}}$ (Eq. 6.1).
As well as a time shift, we often observe small changes in the waveform (Fig. 6.8, Inset b). This signature results from small changes in the scattering properties of the medium (e.g., structural changes in the medium) that are responsible for residual distortion or decorrelation of the coda waveforms. This waveform decoherence has been used in acoustics in laboratory experiments with aluminum plates (Michaels and Michaels, 2005) and for concrete (Larose et al., 2010; Rossetto et al., 2011; Planès, 2013), to quantify defects

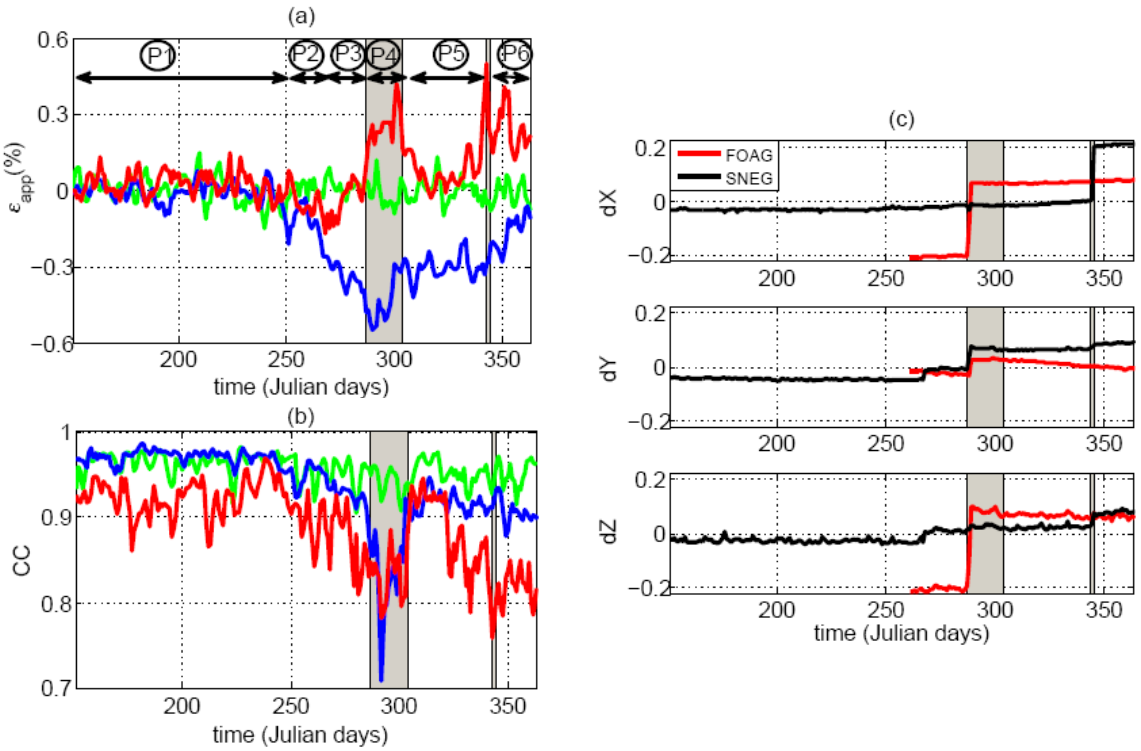

Figure 6.9: (a) Apparent velocity variations ε^{app} for three exemplary cross-correlation pairs that are marked in Figure 6.6. The shaded zones mark the time span for the 17-day-long October eruption (onset Julian day 287) and the 2-day-long December eruption (onset Julian day 343). The pairs are affected differently by the eruptions, according to their locations. We study the data separately for the six periods marked at the top. P1: eventless period, or reference state of the volcanic edifice; P2: intrusion; P3: period prior to the eruption; P4: period during the October eruption; P5: period between the two eruptions; P6: period after the December eruption. (b) The coherence values that correspond to the displayed receiver pairs from June to December. Again, the pairs are affected differently by the eruptions, according to their locations. (c) GPS data from the FOAG and SNEG stations, as marked in Figure 6.6. An increase in the value indicates a displacement towards the East (dX), the North (dY), or vertical (dZ). The GPS data do not show any precursor of the displacements.

that are much smaller than a wavelength in materials. We measure here the average coherence CC with the stretching technique for a time window from 10 s to 45 s in the coda (see section 6.7). The decoherence is then the difference in the coherence from one date to the other.

In Fig. 6.9b), we show the coherence values CC that correspond to the three station

pairs indicated in Fig. 6.6. For the station pair in the vicinity of the eruption site in October (Fig. 6.9b, blue), we observe significant decoherence prior to and during the October eruption. After the eruption, the coherence values recover, although they remain about 5% below the initial value. The December eruption does not have a significant effect on this station pair. For the station pair in the vicinity of the December eruption (Fig. 6.9b, red), we also observe a significant decrease prior to and during the October eruption, with recovery of the coherence value almost to its initial state, and a significant decrease (10%) associated with the December eruption. The coherence value for this station pair did not recover until the end of the observation period. The coherence value for the furthest station pair situated on the rim remains unaffected for both eruptions (Fig. 6.9b, green).
We interpret the permanent decrease in coherence as a structural modification of the medium that is irreversible, whereas the recoverable loss of coherence could be associated with reversible displacements of scatterers or opening and closing of pre-existing cracks. Also, we cannot exclude that changes in the local noise sources contribute to the decoherence due to the onset of the volcanic activity. However, it can be noted that as we use a frequency band from 0.1 Hz to 1 Hz, our analysis is not sensitive to tremors associated with the eruptions, which have dominant frequencies that usually range between 2 Hz and 4 Hz. We have seen that the origin of the noise sources is also relatively stable over the period of interest (Fig. 6.7), and this induces less than the few percent of decoherence that is similar for all receivers. We conclude that the decoherence is mainly due to physical changes of the volcanic edifice that are directly associated with the volcanic activity, and are not due to instrumental or data-processing artifacts.

From these observations we can clearly see that the measured apparent velocity variations and the coherence values depend on the position of the stations relative to the change in the medium.

Geodetic data from GPS measurements

We compare our observations with the displacements measured by two global positioning system (GPS) stations (FOAG and SNEG) of the PdF Volcano Observatory (see Fig. 6.6 for their locations), to obtain a model for the underlying dynamic mechanisms of the eruptions. In Fig. 6.9c, we show the displacements measured by these two GPS stations towards the East (dX) and the North (dY), and the vertical displacement (dZ), for the period of interest. The FOAG station, was installed in September 2010 (Julian day 259) and is located south of the cone, close to the October eruption. With the onset of the October eruption (Julian day 287), FOAG station registers strong displacement eastwards, a small displacement to the north, and a vertical displacement. SNEG station is located on the northern rim of the cone, and 25 days prior to the October eruption, it registers a northward and vertical displacement, while with the onset of the October eruption, there is a northward movement. With the onset of the December eruption (Julian day 343), SNEG station also registers a northward and vertical movement. At

PdF, the eruptions are mainly triggered by magma overpressure within a reservoir that is located below the crater, at approximately sea level (Nercessian et al., 1996; Peltier et al., 2005b). The event that caused the displacement at station SNEG on the September 24 (Julian day 267) was characterized by Roult et al. (2012) as a major magma intrusion. Therefore, we believe that the apparent velocity changes and the decoherence of the wavefield that we observe for this time period are not yet related to the October eruption. We divide the total observation time into six periods of interest (top Fig. 6.9a). For each period, we average the CC_i and $\varepsilon_i^{\text{app}}$ values.

- P1 comprises the quiet/ event-less period from June to August, and it defines the reference state of the volcanic edifice that we use to calculate the reference correlations (Julian days 152 to 250).
- P2 comprises 21 days (Julian days 256 to 276) that include the intrusion on September 24 (Julian day 267), as observed from geodetic measurements.
- P3 is the time prior to the October eruption where the data associated with station pairs close to the forthcoming eruption indicate precursors. P3 is 12 days long (Julian days 273 to 284), and does not include the onset of the major eruption (Julian day 287).
- P4 comprises the 18 days during the October eruption (Julian days 287 to 304).
- P5 is the time between the October and December eruptions. We leave several days to the October and December eruption and average over 21 days. (Julian days 311 to 331).
- P6 is 18 days long, and it is after the December eruption until the end of the year (Julian days 348 to 365).

6.2.3 Localization with inversion of apparent velocity changes

In section 6.2.2, we observed that the coda of correlations associated with station pairs located close to the eruption show significant changes in their apparent relative velocity. The coda of correlations associated with station pairs that are further away from the eruption are less, if at all, affected. We use this property to locate the medium changes. We compute sensitivity kernels between the stations and apply a linear least-squares inversion scheme (Tarantola and Valette, 1982; Froment, 2011), to obtain the horizontal distribution of the apparent relative velocity changes.

Sensitivity kernel

In section 6.2.2, we quantified the apparent relative velocity changes with the stretching factor $\varepsilon_i^{\text{app}}$. We now relate $\varepsilon_i^{\text{app}}$ to a local velocity perturbation $\frac{dv}{v}(x_0)$ using the sensitivity

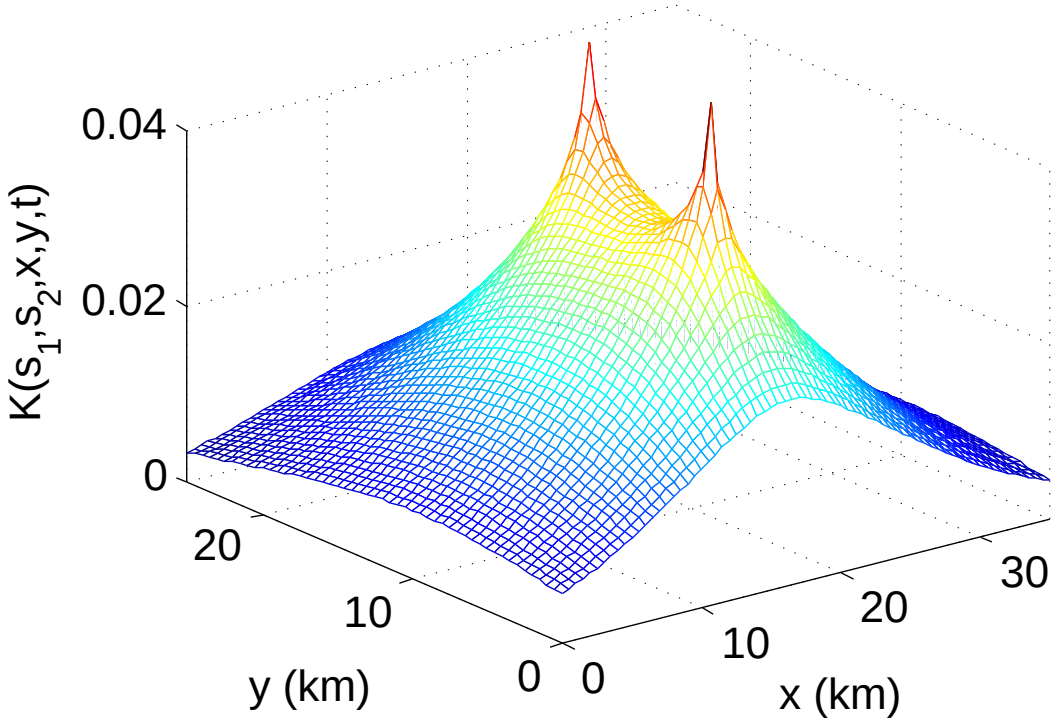

Figure 6.10: Spatial representation of the sensitivity kernel that describes the statistical time spent in each area. The two peaks indicate the position of the station pair. The time statistically spent in a region decreases with its distance to the stations.

kernel introduced by Pacheco and Snieder (2005); Larose et al. (2010); Planès et al. (2013):

$$K(\boldsymbol{s_1}, \boldsymbol{s_2}, \boldsymbol{x}_0, t) = \frac{\int_0^t p(\boldsymbol{s_1}, \boldsymbol{x}_0, u) p(\boldsymbol{x}_0, \boldsymbol{s_2}, t-u) du}{p(\boldsymbol{s_1}, \boldsymbol{s_2}, t)} \tag{6.2}$$

where $\boldsymbol{s_1}$ and $\boldsymbol{s_2}$ are the positions of the stations, $\boldsymbol{x}_0$ is the position of the local velocity variation, and t is the center of the time interval in the coda where the stretching is evaluated. The sensitivity kernel is a statistical measure of the time spent in each part of the region under test. $p(\boldsymbol{s_1}, \boldsymbol{s_2}, t)$ is the probability that the wave has traveled from $\boldsymbol{s_1}$ to $\boldsymbol{s_2}$ during time t, which can be approximated by the intensity of the wavefield from $\boldsymbol{s_1}$ to $\boldsymbol{s_2}$ at time t. Since surface waves are the dominant wave type, we use the analytic two-dimensional solution of the radiative transfer for isotropic scattering for the intensity propagator (Shang and Gao, 1988; Sato, 1993; Paasschens, 1997):

$$\begin{aligned} p \quad (\boldsymbol{r}, t) &= \frac{e^{-ct/\ell}}{2\pi r} \delta(ct - r) \\ + \quad & \frac{1}{2\pi \ell ct} \left(1 - \frac{r^2}{c^2 t^2}\right)^{-\frac{1}{2}} \exp^{[\ell^{-1}(\sqrt{c^2t^2 - r^2} - ct)]} \Theta(ct - r), \end{aligned} \tag{6.3}$$

where c is the wave speed, r is the distance between source and receiver, ℓ is the transport mean free path, and $\Theta(x)$ is the Heaviside (or step) function. The first term describes the coherent part of the intensity that decreases exponentially with the distance relative to the transport mean free path. The second term describes the diffusion intensity. We note that the diffusion solution is reached when $t \gg r/c$. An example of the sensitivity kernel is shown in Figure 6.10.

Velocity variations with time in the coda and the mean free path

For the computation of the sensitivity kernel, we need the transport mean free path ℓ or the scattering attenuation $Q_s = 2\pi f\ell/c$ which are both unknown for PdF. The first input comes from a comparison with attenuation studies of other volcanoes. Del Pezzo et al. (2001) determined $Q_s = 105$ for Mt. Etna at 1.0 Hz, which yields $\ell \approx 40$ km. Mayeda et al. (1992) determined $Q_s = 53$ for Hawaii at 1.5 Hz, and Aki and Ferrazzini (2000) reported $Q = 40 - 60$ for PdF at 3 Hz.

The second input comes from the evolution of the velocity variations with time in the coda which gives access to a rough estimate of the transport mean free path between 20 km and 60 km, and will be describe in more detail. Considering the standard case of a noise source at the surface, based on scattering and mode conversion arguments, it can be shown that surface waves statistically dominate the early part of the seismic record, whereas bulk waves statistically dominate the later part (Obermann et al., 2013b). Hence medium changes result in lapse-time-dependent amplitudes of the apparent velocity changes. Changes at shallow depth result in a large amplitude apparent velocity change at early lapse times and then decrease in amplitude with later lapse times. On the contrary, for changes at depths greater than the wavelength, the apparent velocity change will increase from a negligible value at early times to a significant contribution at later times.

Fig. 6.11 shows the average apparent velocity changes for the 15 station pairs that lie within a region of 4 km around the October eruption (Fig. 6.12d), at different coda lapse times for the periods P1 (blue, quiet), P3 (black, prior to the October eruption) and P4 (red, during the October eruption). For P3, the apparent velocity changes are present at all times, and they have their highest amplitudes at early times in the coda. For P4, the apparent velocity changes have an even higher amplitude at early times in the coda than during P3, and again the amplitude decreases with time but remains present at all times in the coda. This allows us to conclude that the changes for the stations studied occur mainly at shallow depth, in addition to a possible smaller change at greater depth. In our case, an inversion at different times does not provide further information, and therefore this is not shown in the results.

In numerical studies (Obermann et al., 2013b), the transition from surface sensitivity to bulk sensitivity in the coda occurs at about $6 \times t/t^\star$, with $t^\star = \ell/c$ as the mean free

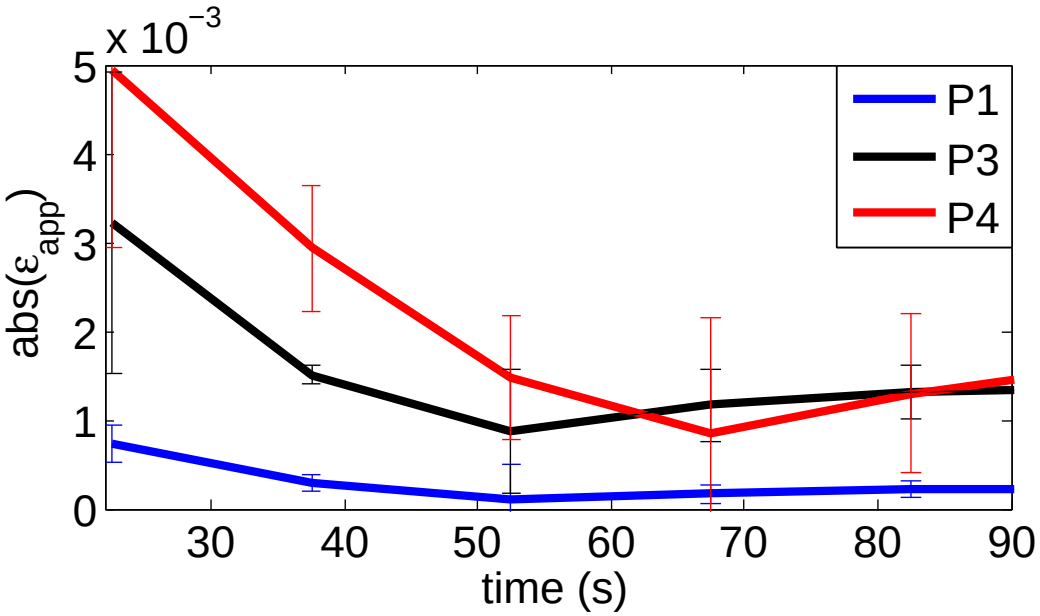

Figure 6.11: Evolution of the velocity variations with time in the coda for the event-less period (P1), prior to the eruption (P3), and during the eruption (P4). The sensitivity behavior indicates shallow changes.

time. In Fig. 6.11, this transition occurs between 60 s and 80 s. This information and a wave speed of 2.4 km/s (Brenguier et al., 2007) favor the very rough estimation of the transport mean free path between 20 km and 60 km, which is the same order of magnitude as the values determined by the studies mentioned above.

In the present study, we arbitrarily fix the value of the transport mean free path at 50 km, which is in the range discussed above. In the Supplementary Materials, we test the sensitivity of our results toward different values of ℓ and observe that the choice of ℓ has an influence on the size of the affected area, but not on the location of the affected area.

Linear least-squares inversion

The apparent relative velocity variation that results from the spatial (2D) distribution of relative velocity change can be expressed according to:

$$\boldsymbol{\varepsilon}^{\mathbf{app}} = \boldsymbol{G}\boldsymbol{m}, \tag{6.4}$$

where $\boldsymbol{\varepsilon}^{\mathbf{app}}$ is a vector, for which each component $\varepsilon_i^{\mathrm{app}}(i = 1...n)$ corresponds to the apparent velocity change that we measure between station pair n with the stretching technique. $\boldsymbol{G}$ is the matrix, for which each component $G_{ij} = \frac{\Delta s}{t} K_{ij}$ corresponds to the sensitivity kernel K for station pair i in cell j, weighted by the area of the cells Δs

over time t in the coda. And $\boldsymbol{m}$ is a vector that contains the actual velocity changes that we wish to estimate for each pixel j. As the data that we invert represent local velocity changes, there is no constraint concerning the sign of $\boldsymbol{m}$. We can use for instance the formulation of the minimum square method for linear problems to determine $\boldsymbol{m}$, as proposed by Tarantola and Valette (1982):

$$\boldsymbol{m} = \boldsymbol{m_0} + \boldsymbol{C_m G^t}(\boldsymbol{G C_m G^t} + \boldsymbol{C_d})^{-1}(\boldsymbol{\varepsilon^{app}} - \boldsymbol{G m_0}), \tag{6.5}$$

where $\boldsymbol{m_0}$ is the initial model, with a zero vector in our case, as we do not have any a-priori information about the expected changes. $\boldsymbol{C_d}$ is the diagnoal covariance matrix for the data, and it contains the variances of the data $\sigma^2_{d,i}$. $\boldsymbol{C_m}$ is the covariance matrix for the model. To estimate the standard deviation $\sigma_{d,i}$ of the data, we use the theoretical formulation proposed by Weaver et al. (2011):

$$\sigma_{d,i} = \frac{\sqrt{1 - CC_i^2}}{2CC_i}\sqrt{\frac{6\sqrt{\frac{\pi}{2}}T}{\omega_c^2(t_2^3 - t_1^3)}}, \tag{6.6}$$

where T is the inverse of the frequency bandwidth, t_1 and t_2 are the beginning and end of the processed time window in the coda, $\omega_c = 2\pi f$ is the central frequency, and $CC_i = CC(\varepsilon_i^{\mathrm{app}})$ is the coherence value of the respective station pair i (Eq. 6.1).

Our inversion covers an area that extends from 350 km to 385 km Easting and from 7640 km to 7665 km Northing, (UTM zone 40 S coordinates), which represents approximately 35 km × 25 km around the PdF caldera. We divide this area into 35×25 = 875 cells with $\Delta s = 1$ km^2. We do not consider the topography in the inversion. As we use 104 station pairs, the inverse problem is under-determined. To limit the number of independent parameters, we introduce spatial smoothing obtained from correlations of neighboring cells. A detailed discussion concerning the smoothing method as well as quality tests for the inversion is provided in the Supplementary Materials.

The inversion models for the apparent velocity variations associated with the six different time periods (Fig. 6.9a) are shown in Fig. 6.12. As expected, there are no velocity fluctuations during the quiet period (Fig. 6.12a). During the intrusion (Fig. 6.12b) there is a weak velocity change that covers the summit area. Prior to the October eruption (Fig. 6.12c), there is a velocity decrease that has its highest intensity north-east of the final eruption location (Fig. 6.12, larger star). This velocity decrease could be associated with an increase in the tensile stresses at depth induced by over-pressurization of the magma in the dykes that dilate the volcanic edifice at the free surface. During the October eruption (Fig. 6.12d), there is a strong velocity decrease that is centered around the actual eruption location. This velocity decrease can be associated with the continued inflation of the edifice that causes the opening of microcracks; and the change of material with the ejected magma. Between the October and December eruptions (Fig. 6.12e), the velocity increases again without reaching its background level (Fig. 6.9a, blue), and the affected region becomes smaller. This tendency continues after the

December eruption (Fig. 6.12f). With the eruption itself, the magma over-pressurization that appears to have an important role in the velocity decrease, is released. It is likely that the magma intrusion in September 2010 had already filled the existing dyke system, so that there was no major magma movement prior to the December eruption (Roult et al., 2012). The two-day-long December eruption can be seen as a residual eruption of the major October eruption, and is not visible on the velocity variation measurements.

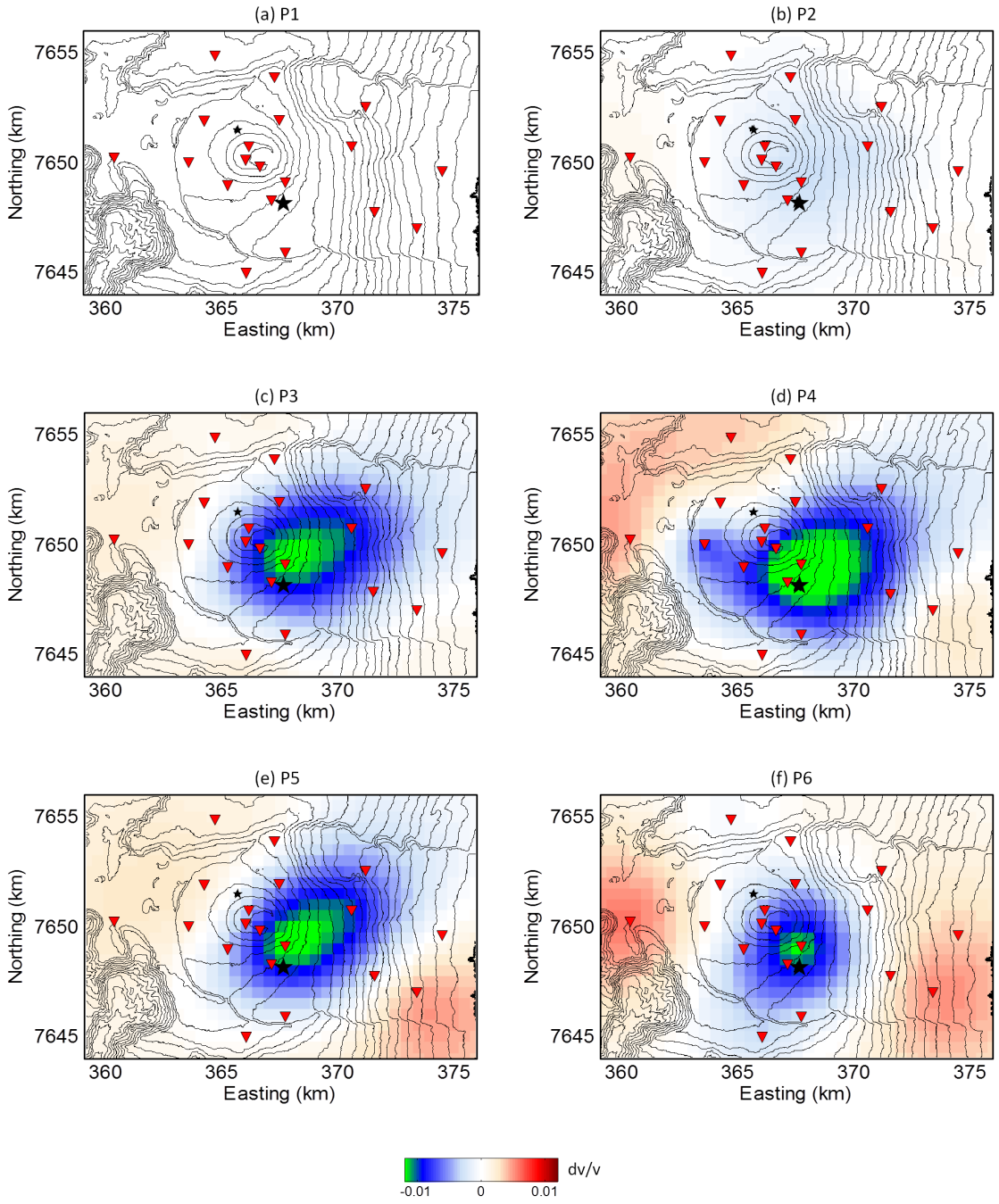

Figure 6.12: Least-squares inversion of the apparent velocity changes. (a) Time prior to the eruption with no volcanic activity (P1). (b) During the intrusion (P2). (c) Precursor prior to the eruption (P3). (d) During the October eruption (P4). (e) After the October eruption (P5). (f) After the December eruption (P6).

6.2.4 Localization with inversion of decoherence values

Complementary to the study of relative velocity changes, we study the waveform decorrelations that are due to structural changes in the scattering medium. In this case, the model that we obtain is a scattering cross-section density map of the changes. The cross-section of the change corresponds to the size and the strength of the change, as probed by seismic waves.

Decorrelation

With the stretching technique, we calculate coherence values for all of the station pairs for the study period from June to December 2010. Consistent with the procedure applied to the velocity changes, we calculate the average of the coherence values for each of the six periods. These average values are referred to as the average coherence value AC_i for that period. To quantify the amount of decorrelation DC_i from one period to another, we subtract the AC^i-values of interest (P2,...,P6) from the 'reference'-values AC_i^{ref} (P1 or P5):

$$DC_i = AC_i^{\text{ref}} - AC_i. \tag{6.7}$$

We can compute a theoretical waveform decorrelation DC_i^{th} induced by a change that appeared in $\boldsymbol{x_0}$ (Rossetto et al. 2011, Planès et al. 2013):

$$DC_i^{th}(\boldsymbol{s_1}, \boldsymbol{s_2}, \boldsymbol{x_0}, t) = \frac{c\sigma}{2} K(\boldsymbol{s_1}, \boldsymbol{s_2}, \boldsymbol{x_0}, t), \tag{6.8}$$

where $\boldsymbol{s_1}$, $\boldsymbol{s_2}$ are the positions of the stations, K is the sensitivity kernel from Equation 6.2 and σ is the scattering cross-section associated with the strength and size of the change.

Linear least-squares inversion with positivity constraint

Following Planès (2013), we adapt the least-squares inversion described in section 6.2.3 to the decoherence measurements:

$$\boldsymbol{DC} = \boldsymbol{Gm}, \tag{6.9}$$

where $\boldsymbol{DC}$ is a vector, for which each component $DC_i (i = 1...n)$ corresponds to the additional decorrelation that we measure between station pair n with the stretching technique. $\boldsymbol{G}$ is the matrix, for which each component $G_{ij} = \frac{c\Delta s}{2} K_{ij}$ corresponds to the sensitivity kernel K for station pair i in cell j, weighted by the surface area of the cells Δs and the Rayleigh wave group velocity $c/2$. And $\boldsymbol{m}$ is a vector that contains the scattering cross-section density changes that we wish to estimate for each pixel j. The scattering cross-section densities that we obtain are necessarily positive, and we therefore use an iterative procedure to impose a positivity constraint. The initial model

Table 6.1: Scattering cross-sections for the different periods (intrusion, October eruption, December eruption), and ejected magma volume (Roult et al. 2012) for both of the eruptions.

Period	σ	Ejected volume
P1-P3	120 m	
P1-P4	180 m	$3 \cdot 10^6 \mathrm{m}^3$
P5-P6	45 m	$0.5 \cdot 10^6 \mathrm{m}^3$

m_0 is again zero everywhere. Then, at each iteration step, we keep positive values only and use this model as the new input model. Eight iterations are needed to obtain the scattering cross-section maps in Fig. 6.13 for the different periods.
Thirty days prior to the eruption (P2; Fig. 6.13a), we locate structural changes at or below the Dolomieu crater. We interpret this observation as the magma that rose via the main feeding channel below the summit. This is in good agreement with the localization of pre-eruptive micro-seisms below the summit, as illustrated with the yellow circles in Fig. 6.6. Ten days prior to the eruption (P3; Fig. 6.13b) there are structural changes in the southeast, close to the future eruption site. We believe that this follows here the magma movement and its transfer towards the future eruption location. During the eruption (P4; Fig. 6.13c) there are strong changes located southeast of the cone in an area that includes the eruption zone. At the same time, we note changes of minor intensity northwest of the cone, outside the Dolomieu crater. This last northwest change can be viewed as a precursor signal of the small forthcoming December eruption. For the changes that occur after the small December eruption with respect to the time after the October eruption (P6-P5; Fig. 6.13d), there are two regions where there is decorrelation, which includes both of the eruptive zones. This time the intensity is greater for the region northwest of the cone (the December eruption). We believe that the changes that we observe to the northwest of the cone reflect the fissure opening due to the December eruption, as well as the magma ejection. The region of change that includes the October eruption is linked to the cooling of the magma. The results in Figs. 6.13b,c,d) are in good agreement with the InSAR-derived co-eruptive displacements (Fig. 6.13e).

In Table 6.1, we report the scattering cross-sections that we obtained from the tests for the different periods, and compare the values with the ejected magma during the eruptions (Roult et al., 2012). It is difficult to conclude that there is a direct relationship between the scattering cross-section σ and the ejected volume, but we observe that a larger scattering cross-section corresponds to greater magma volume, and that the volume of the ejected magma appears to be of the order of the cubic value of the scattering cross-section. This feature is not well explained yet, and it will be the subject of further investigations.

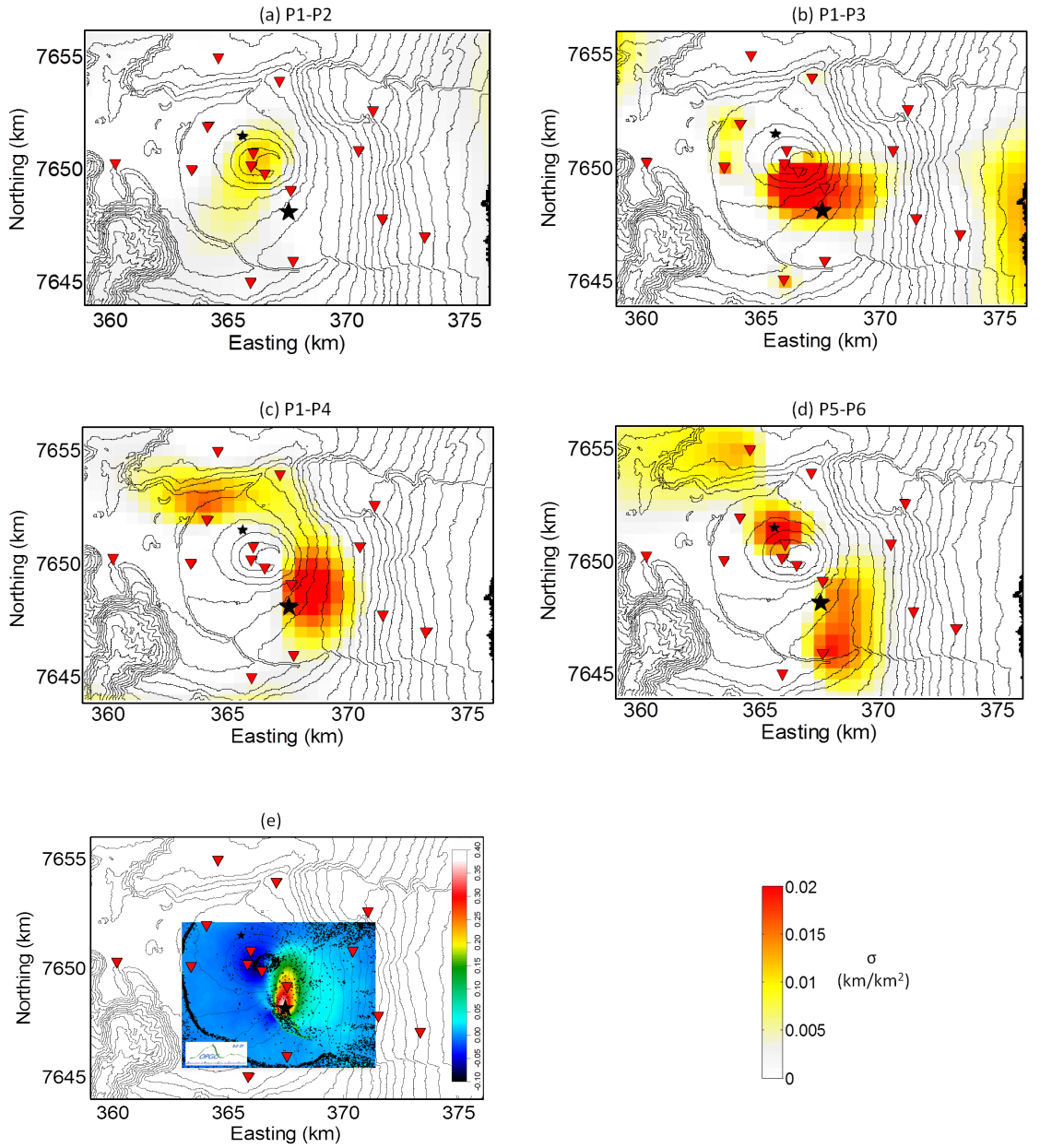

Figure 6.13: Scattering cross-section density maps. (a) During the intrusion (P2). (b) Prior to the eruption (P3). (c) During the October eruption (P4). (d) Changes caused by the December eruption (P5-P6). (e) InSAR-derived co-eruptive displacements for the period from September to October 2010, displayed is the East-West component, in meters. *Courtesy of Jean-Luc Froger from the OPGC, Clermont Ferrand.*

6.2.5 Conclusion

In our study, we have analyzed continuous ambient seismic noise records from the active volcano PdF on La Reunion Island, from June to December 2010. Two volcanic eruptions occurred during the observation period, which were at different locations. When looking at the variations in the coda of the correlations, we can distinguish two types of measurements associated to two types of changes: apparent relative velocity variations associated with changes in macroscopic elastic properties of the medium; and waveform decoherence caused by changes in the geological structures, and hence the scattering properties of the medium. We observe that the temporal variations of both of the parameters are good potential precursors of volcanic eruptions at PdF.
To locate the sources corresponding to these changes, we used an imaging technique derived from wave physics in complex media and based on probabilistic approaches. We computed sensitivity kernels between the stations using a radiative transfer approach for the intensity propagation of the seismic wavefield. Then we applied a linear least-squares inversion to compute the horizontal distribution of the relative velocity changes, and the horizontal distribution of the scattering cross-section density changes.
Using the velocity variations that were observed prior to the major October eruption, we located a region with a significant velocity decrease (up to 0.6%) at the forthcoming eruption site. During the October eruption, we observed a strong velocity decrease centered around the actual eruption location. After the October eruption, the affected area underwent a slow recovery until the end of the observed period. The velocity variations are not sensitive to the minor December eruption on the northwestern flank of the volcano.
Using the waveform decoherence, we resolved a magma intrusion below the cone 30 days prior to the October eruption. Then, 10 days prior to the October eruption, we located a clear precursor signal at the forthcoming eruption site. During the October eruption we located strong changes southeast of the cone, in an area that includes the eruption zone. Of particular interest, at the same time we noted minor intensity changes northwest of the cone, which indicated the forthcoming December eruption. Using waveform decoherence, we precisely located this second eruption. The cross-sections that we obtained appear to be related to the magma volume.
These data demonstrate that the coda of ambient noise correlations can be used to extract deterministic information on the positions of eruptive processes in an active volcano. They also offer an original and significant constraint on the locating of forthcoming volcanic eruptions.
The combined monitoring of apparent velocity changes and decoherence provides insights into the on-going processes in the volcanic edifice. The observables used in this study are sensitive to different properties. Relative velocity changes are characteristic of macroscopic elastic properties of the medium, while decoherence results from structural changes. Their association increases the efficiency of ambient noise monitoring in a volcanological context.

6.3 Supplementary Material

6.3.1 Spatial smoothing

The inverse problem is under-determined with 104 datasets and 875 model parameters. To limit the number of independent parameters, we introduce spatial smoothing obtained from correlations of the neighboring cells. This spatial smoothing is introduced in the covariance matrix of the model $\boldsymbol{C_m}$ via an exponential function. The elements (i, j) of the otherwise diagonal matrix are given by:

$$C_m(i,j) = (\sigma_m \frac{\lambda_0}{\lambda})^2 \exp(-\frac{d(i,j)}{\lambda}), \tag{6.10}$$

where $d(i,j)$ is the distance between two cells i and j. The matrix is weighted by $(\sigma_m \frac{\lambda_0}{\lambda})^2$, where λ_0 is a scaling factor that was taken here to be equal to the cell length (1 km), and λ is the correlation length that defines the length over which the parameters are correlated. The larger we chose λ, the fewer independent parameters we have. σ_m is the a-priori standard deviation of the model. To select the optimal smoothing parameters λ and σ_m, we use the L-curve criterion (Hansen, 1992). This criterion corresponds to the best agreement between: 1) the stability of the model for the velocity variations; and 2) the minimized difference between the model predictions $\boldsymbol{\varepsilon_i^m}$ and the data $\boldsymbol{\varepsilon_i^{app}}$. According to equation (6.11) the normalized residual (res) between n measured and modeled apparent velocity variations ($\boldsymbol{\varepsilon_i^{app}}$ and $\boldsymbol{\varepsilon_i^m}$ respectively) is used to quantify the agreement between the model and the data:

$$res = \sqrt{\frac{1}{N}\sum_{i=1}^{N} \frac{(\boldsymbol{\varepsilon_i^m} - \boldsymbol{\varepsilon_i^{app}})^2}{(\boldsymbol{\sigma_i^d})^2}}. \tag{6.11}$$

In Fig. 6.14, the normalized residuals (res) are plotted as a function of maximal velocity fluctuations in the model, for different values of σ_m and λ. The optimal smoothing is found by minimizing the values on both axes, which corresponds to maximal bending of the curve. With the gray shading in Fig. 6.14, we indicate three different smoothing regimes. Within the light gray zone, very strong velocity variations are allowed in the final model, and the smoothing has not been efficient enough for these combinations of parameters. The dark gray zone, on the other hand, shows too strong smoothing. The velocity variations are weak, but the agreement with the data is also weak. The optimum is for the smoothing parameter pairs that fall into the maximal curvature zone (gray). We chose σ_m=0.032 km/km^2 and λ=2 km.

6.3.2 Quality tests of the inversion model

To confirm the validity of the inversion model, we perform four quality tests. An important point is the model resolution, which gives us information about the region of

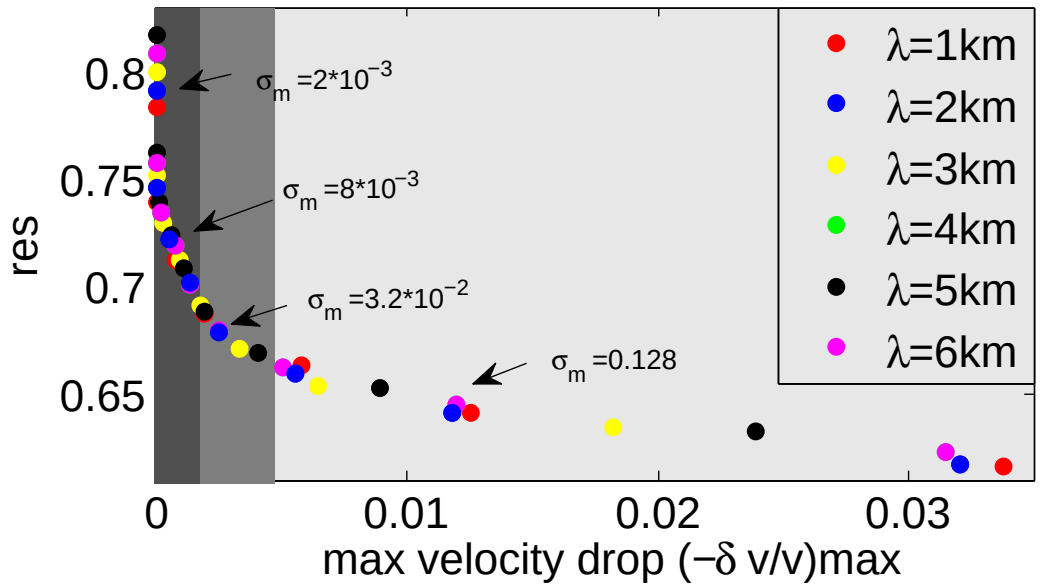

Figure 6.14: Normalized residuals as a function of the maximal velocity drop for the different smoothing parameters σ_m and λ. We differentiate three different smoothing zones. In the zone in dark gray, the smoothing is too strong, allowing only very weak velocity variations. In the gray zone, where the curve has its maximum flexion point, the optimal smoothing is found for minimized values on both axes. In the light gray zone, the smoothing is too weak which results in very strong velocity variations.

interpretability of our model. According to Tarantola and Valette (1982), the resolution matrix R is given by:

$$\boldsymbol{R} = \boldsymbol{C_m G^t} (\boldsymbol{G C_m G^t} + \boldsymbol{C_d})^{-1} \boldsymbol{G}. \tag{6.12}$$

The diagonal elements of this matrix indicate whether the apparent velocity variations of a particular cell have been recovered by the inversion result. As we introduced smoothing in the form of the model covariance matrix $\boldsymbol{C_m}$, neighboring cells should reflect these apparent velocity variations. Hence, the j^{th} line of the matrix R indicates how well the velocity variations of the j^{th} cell have been projected on the entity of cells. The sum over the elements of the j^{th} line of the resolution matrix shows if the velocity variations in this cell have been completely recovered by the contribution of the cell ensemble. In this case, the restitution index is ≈ 1. If the velocity variation cannot be recovered by the inversion, the restitution index is < 1. Fig. 6.15a shows the restitution matrix for the entire region that we used to invert our data. Please note that the region of interest is much smaller, and is well described with a restitution index of ≈ 1 for the entire region.

In Fig. 6.15b, we represent the resolution of a particular cell j (i.e., the j^{th} line of the matrix R). The chosen cell is marked with an empty circle, and it is well situated in the zone were the model predicts the maximal velocity variations. Fig. 6.15b shows the spatial smoothing that has been applied (λ=2 km).

It is important to make sure that the inversion result is not governed by the spatial distribution of the stations. Therefore, in Fig. 6.15c we look at the contributions of each station to the ensemble of data. The circles indicate the station location, and their size is proportional to the number or occurrences (n) of this station in the ensemble of the data considered ($1< n <19$). Comparing the weight of the stations with the amplitude of the velocity variations in the background, we do not observe any correlation. So we can conclude that the model is not biased by the spatial distribution of the data.

In Fig. 6.15d, we show the distribution of the standard deviation between the measured ε^i_{app} and modeled ε^i_{mod} velocity variations normalized with the characteristic error of the data. These are well fitted with a Gaussian distribution (Fig. 6.15d, red curve), as required by the theory.

6.3.3 Sensitivity towards the transport mean free path

In this section, we test the sensitivity of our model towards the transport mean free path ℓ. In Fig. 6.16, we compare the inversion result at period P3 for ℓ=1 km (a), ℓ=50 km (b) and ℓ=100 km (c). Please note that in the case of ℓ=1 km, $\ell < \lambda$ and we would be in the regime of strong localization. The main characteristics of the inversion result do not change with the different choices of the transport mean free path. However, we see clearly that the area that is affected by the change in our inversion result increases with the increasing length of the transport mean free path.

6.4 Maximum Likelihood method - χ^2 test

If we expect a change to occur at one location only, we can alternatively use a simpler maximum-likelihood method, also called χ^2-test or *Locadiff*, to locate the region of maximal physical change (Larose et al., 2010; Planès, 2013). This method uses the same sensitivity kernels as described previously and is applied for comparison to the same data set from PdF.
We are now looking for the couple $\{x_0, \sigma_0\}$ that minimizes the misfit between the measured decorrelations DC^i and the theoretical decorrelations DC^i_{th} (Eq. 6.8). Using the maximum likelihood method based on the value of χ^2, we can write:

$$\chi^2(x,\sigma) = \frac{\sum_{i=1}^{N}(DC^i_{th}(x) - DC^i)^2}{N\delta^2} \tag{6.13}$$

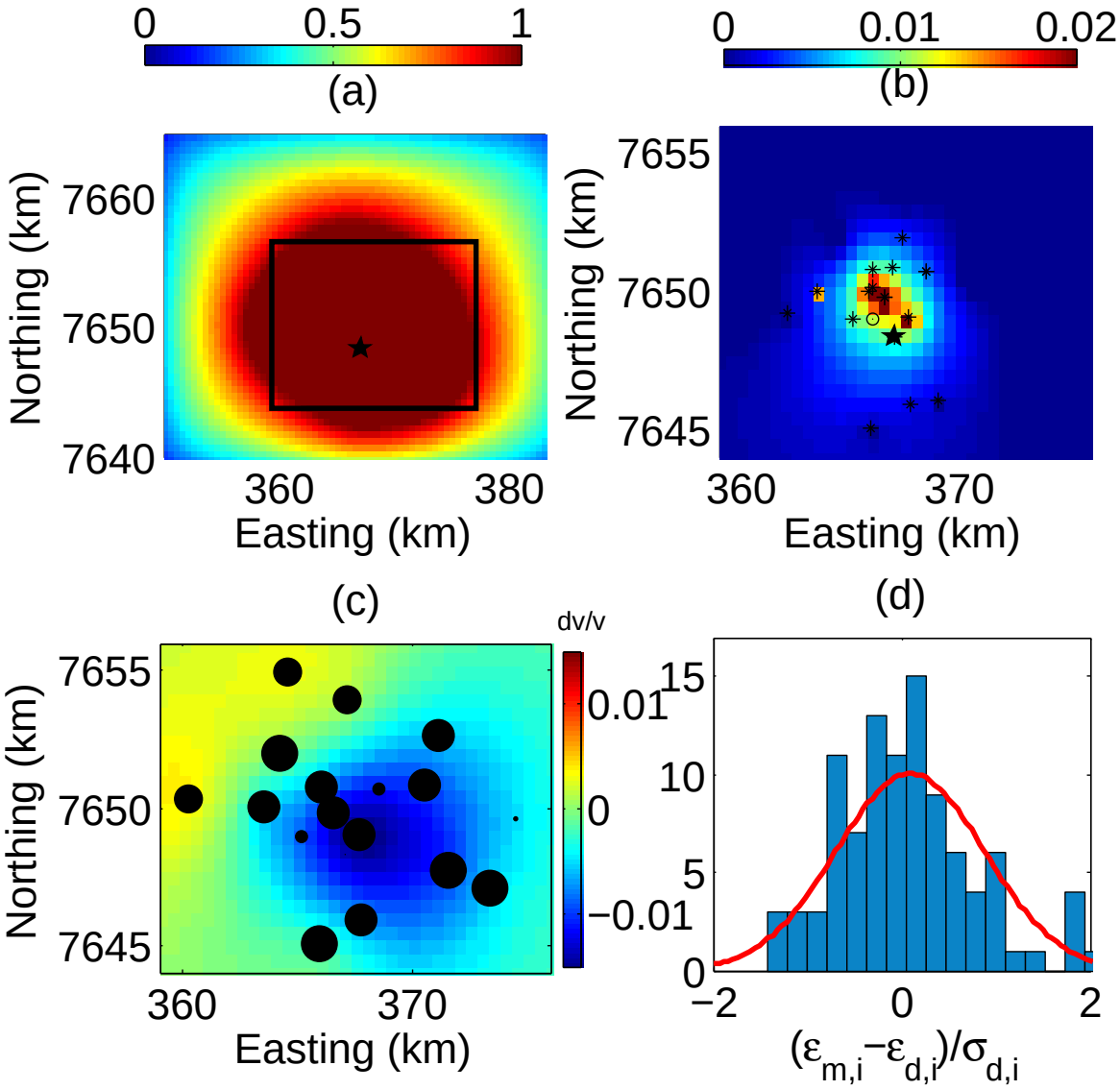

Figure 6.15: (a) Model resolution. The black box indicates the area that we interpret. (b) Resolution for the cell indicated with an open circle. The locations of the stations around are indicated with black crosses. (c) Model obtained from the inversion and the weight of each station for its construction. The sizes of the black points correspond to the number n of occurrences in the used measures (1<n<19). (d) Distribution of the standard deviation between the modeled (ε_i^m) and measured $\varepsilon_i^{\text{app}}$ apparent velocity variations. The red curve corresponds to a Gaussian distribution, and indicates that the residuals are well described by a normal distribution.

$$= \frac{\sum_{i=1}^{N}(\frac{c\sigma}{2}K_i(x) - DC^i)^2}{N\delta^2},$$

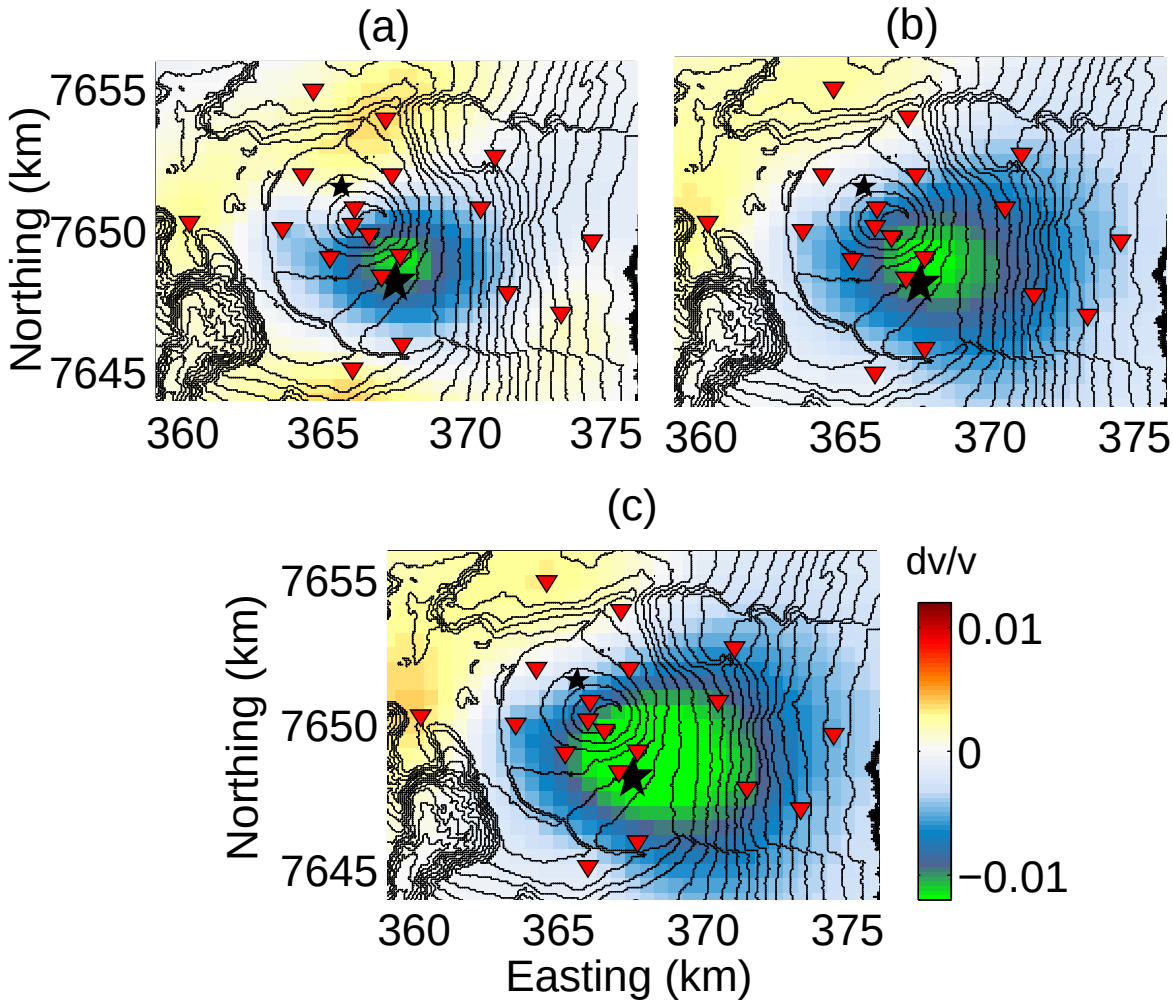

Figure 6.16: Inversion result for period P3, for different transport mean free paths a) ℓ=1 km b) ℓ=50 km c) ℓ=100 km.

where N is the number of station pairs and δ the estimated error of the measurements of DC. At the moment, Eq. 6.13 depends on two unknowns $\{x, \sigma\}$. The dependence on σ can be rendered implicit. For this purpose we consider the hypothetical cross-section $\sigma^{Hyp}(x)$ of a change in x. The value that corresponds to $\sigma^{Hyp}(x)$ is found when the function χ^2 is minimized in the point x. Taking $\frac{\partial \chi^2(x)}{\partial \sigma} = 0$ yields:

$$\sigma^{Hyp}(x) = \frac{2}{c} \frac{\sum_{i=1}^{N} K_i(x) DC^i i}{\sum_{i=1}^{N} K_i(x)^2}, \tag{6.14}$$

we notice that χ^2 is expressed as second degree polynomial in σ.

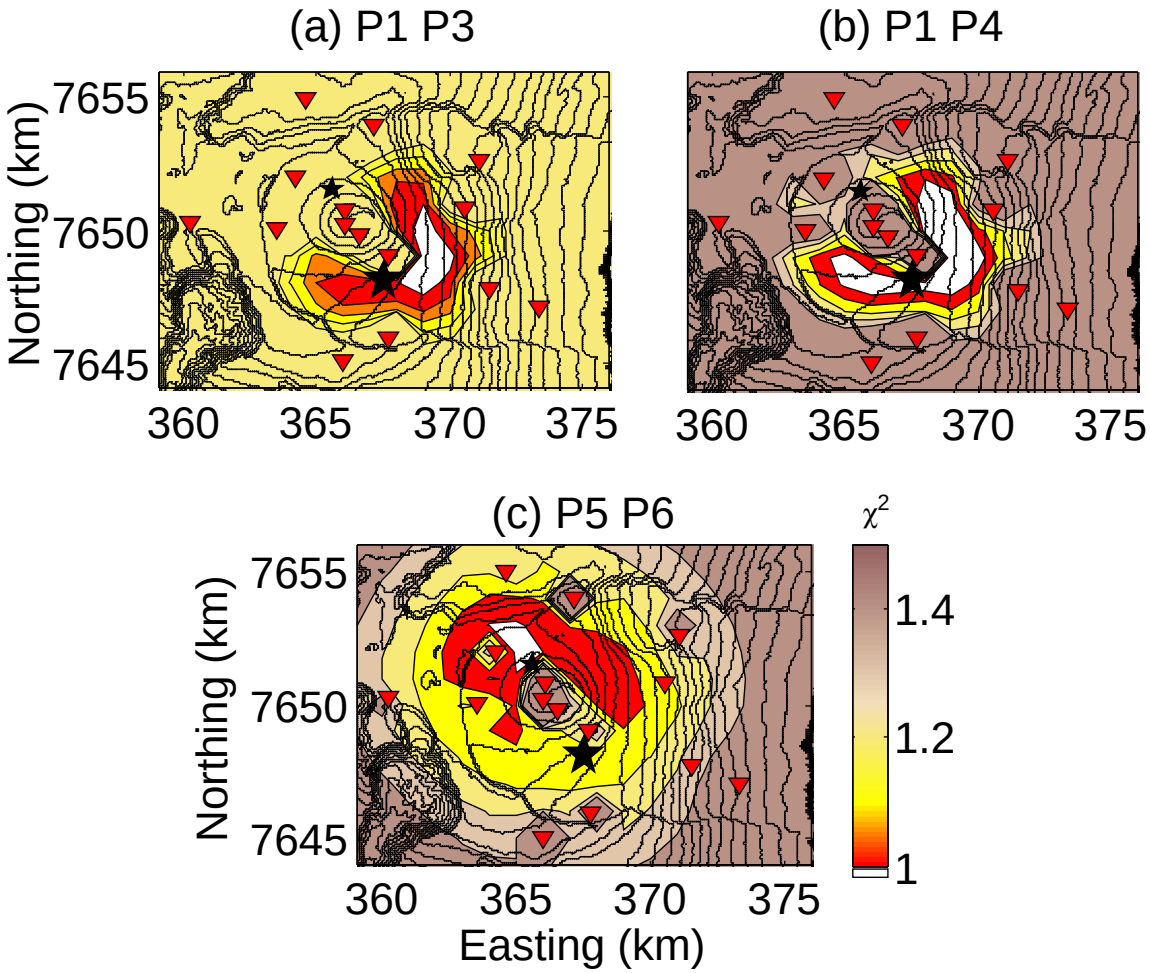

Figure 6.17: Model for the decorrelation. Normalized residual error χ^2 after the inversion. The changes are highly likely within the white areas ($\chi^2 < 1$). (a) Prior to the October eruption (P3). (b) During the October eruption (P4). (c) Changes caused by the December eruption (P6-P5).

χ^2 can now be expressed in dependence of the position of the change only:

$$\chi^2(x) = \sum_{i=1}^{N} \frac{(\frac{2}{c}\sigma^{Hyp}(x)K_i(x) - DC^i)^2}{N\epsilon^2}, \tag{6.15}$$

$\chi^2 < 1$ when the misfit between theory and data is reasonably limited, corresponding to the position where the change is very likely. In the areas where the misfit is large, $\chi^2 \geq 1$, the change is unlikely. In Fig. 6.17a), we plot the normalized residual error χ^2 for the time prior to the October eruption (P3). The changes are highly likely within white areas where χ^2 <1. We identify the region of maximal physical change as being North-East of the later eruption fissure. In Figure 6.17b), we plot χ^2 for the time during the October eruption (P4). The region of maximal physical change that we locate

includes the eruption zone. The L-shape is likely due to an artifact connected to the distribution of stations, and should not be paid attention to. In Figure 6.17c), we plot χ^2 for the changes that occurred due to the December eruption (P6). We hereby take the average coherence values AC^i of P5 as reference coherence values (AC^i_{ref}) and only evaluate the decorrelation that occurred relative to P5. We notice, that also in this case, the region of maximal physical change includes the eruption zone and the magma flow. From the way the maximum likelihood method is constructed, the cross-section of the change will not lay below a station. This explains the L-shape of the region of maximal physical change in Figure 6.17b).

In Table 6.2 we report the scattering cross-sections that we obtained from the tests for the different periods and compare the values to the ejected magma during the eruptions (Roult et al., 2012) and to the values that we obtained from the Tarantola-Valette inversion. It is difficult to conclude whether a direct relation exists between the scattering cross-section σ and the ejected volume, but we do notice that a larger scattering cross-section corresponds to a greater magma volume and that the values from the different inversion methods are in the same order of magnitude.

Table 6.2: Scattering cross-section determined from the Maximum-Likelihood method (χ^2-test) and the Tarantola-Valette inversion (TV) and the ejected magma volume for the different periods (Roult et al., 2012).

Period	σ from χ^2	σ from TV	Ejected volume
P3	200 m	120 m	
P4	300 m	180 m	$3 \cdot 10^6 \text{m}^3$
P6	100 m	45 m	$0.5 \cdot 10^6 \text{m}^3$

Chapter 7

Locating changes occurring with earthquakes

Contents

7.1 Why study the Sichuan region in China?

7.1.1 Tectonical context

Central-Southern China has a high seismic potential that is related to the collision between the Indian and the Eurasian plates about 50 Ma ago and Indias' continuous northward movement into the Eurasian continent since then (Molnar and Tapponnier, 1975; Tapponnier et al., 1982) (Fig. 7.1). In the Western Sichuan Plateau (Eastern Tibetan Plateau), this collision generated several seismically active fault systems, like the Longmen Shan fault system (Densmore et al., 2007; Robert et al., 2009), where the hypocenter of the 12 May 2008 Mw 7.9 Wenchuan earthquake was located (Fig. 7.2a).

The Longmen Shan range is characterized by a particularly steep topographical transition from the Sichuan Basin (500-600 m) to the Tibetan plateau (5000 m) over a lateral distance of less than 50 km (Fig. 7.2b). In contrast with the Himalayas, prior to the May 2008 Wenchuan earthquake there has been no important shortening ascertained across the Longmen Shan range (King et al., 1997; Chen et al., 2000; Godard et al., 2009). These extremely low shortening rates cause debates within the scientific community regarding the tectonic processes along this margin and the possible interaction with strong denudation processes. There are two contradictory models to explain the steep topographical gradient in the area:

1. The uplift is caused by localized shear between coherent lithospheric blocks that leads to crustal faulting. Particularly reverse faulting events are a primary driver of uplift (e.g. Tapponnier et al. (2001); Hubbard and Shaw (2009)) (Fig. 7.3a).

2. An eastward flow of ductile middle and lower crust below the entire plateau encounters the old and resistant lithosphere below the Sichuan basin. (e.g. Royden et al. (1997); Burchfiel et al. (2008)). This results in continuous crustal thickening by inflation, inflicting strong vertical movement but no horizontal shortening (Fig. 7.3b).

The main distinction between these two models concerns the deformation processes in the deep crust: ductile versus brittle.

7.1.2 The Wenchuan earthquake (Mw 7.9, May 12th 2008)

On 12 May 2008, a Mw 7.9 earthquake struck the Longmen Shan region, China, along the Eastern margin of the Tibetan Plateau. This earthquake caused over 80,000 fatalities and enormous material damage in the densely populated counties of Wenchuan,

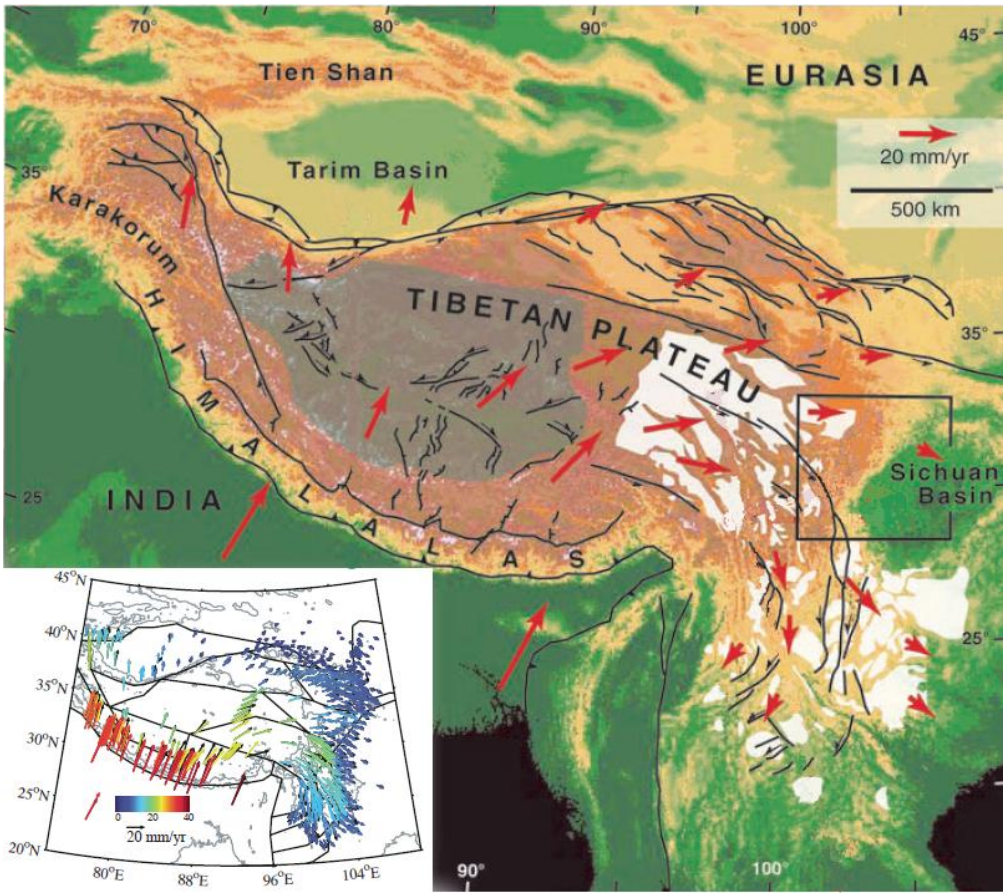

Figure 7.1: Topography map for the Tibetan region. The red arrows are generalized GPS measurements (Royden et al., 2008). The black box indicates the region around the Longmen Shan where the seismic network is placed. The inset shows detailed GPS measurements for the region (Meade, 2007). The movement is relative to the Eurasian plate. (Source: Froment (2011)).

Beichuan and Qingchuan. Earth scientists did not anticipate an event of this magnitude in this region. As discussed previously, although the Western margin of the Sichuan basin is known to be seismically active, the slip rates across the Longmen Shan fault zone are very slow (<2-3 mm/yr) (e.g. King et al. (1997); Chen et al. (2000); Burchfiel et al. (2008); Densmore et al. (2007)), which indicates relatively modest strain accumulation and therefore a slowly accumulating seismic hazard (Zhang et al., 2010). The most devastating, great reverse- or thrust-faulting historic earthquakes (Chile 1960, Alaska 1964, Sumatra 2004) commonly rupture gently dipping thrust faults along which slip occurs rapidly (>50 mm/yr at the oceanic subduction zones and >15 mm/yr along the Himalaya collision zone) and not high-angle reverse faults (Zhang et al., 2010). However, the 2008 Wenchuan earthquake occurred on such a high angle-dipping listric-reverse fault with a slip rate of less than 2-3 mm/yr within the continental interior (Densmore et al., 2007; Zhou et al., 2007).

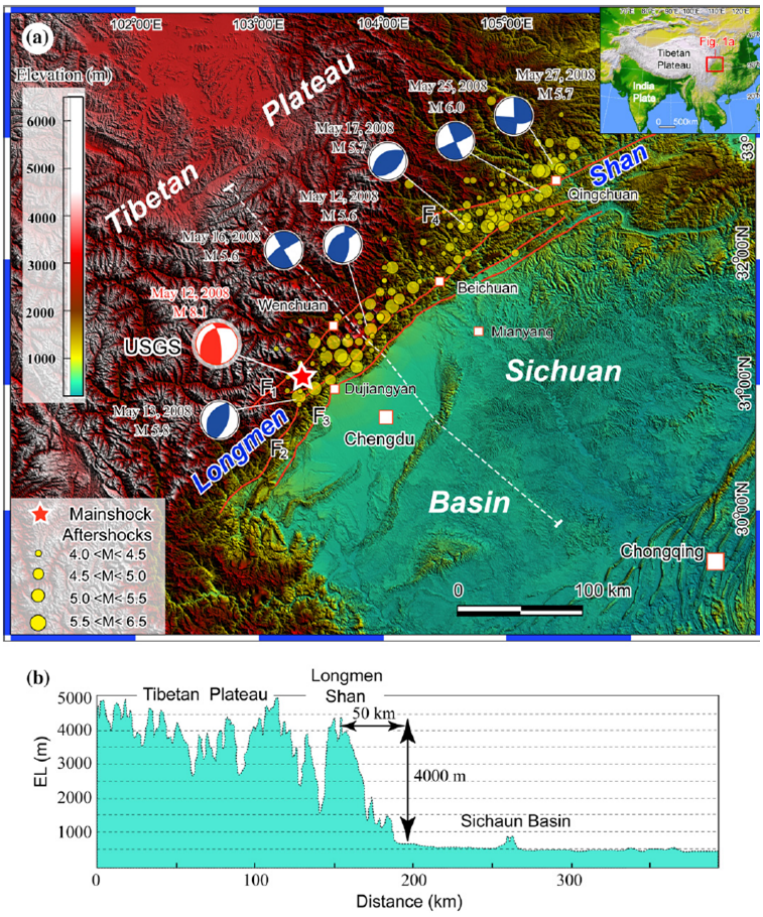

Figure 7.2: (a)Shaded-relief topographic map of the Longmen Shan region showing the epicenters of the 12 May 2008 Wenchuan earthquake and strong aftershocks (>M 4.0). (b) topographic profile across the Longmen Shan and Sichuan Basin, following the dashed line shown in Fig. 7.2a. (Source: Fu et al. (2011)).

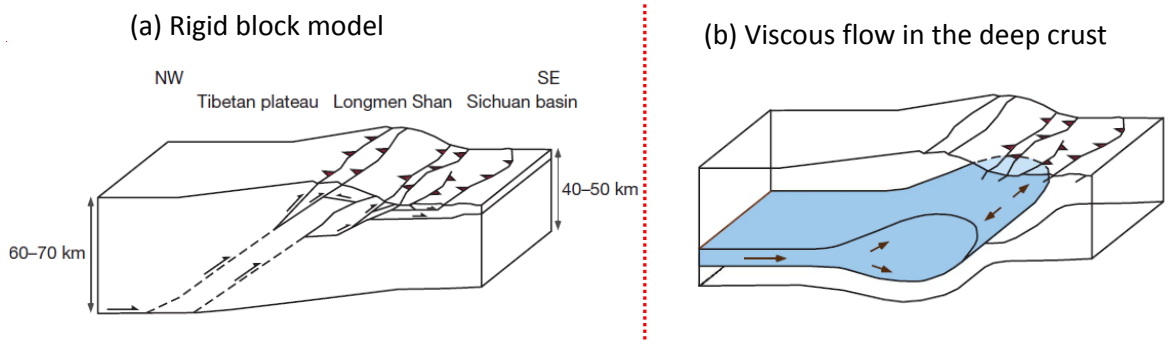

Figure 7.3: The two debated models to explain the formation of the Longmen Shan range. (a) Rigid block model. (b) Viscous flow model. (Source: Hubbard and Shaw (2009), modified after Froment (2011))

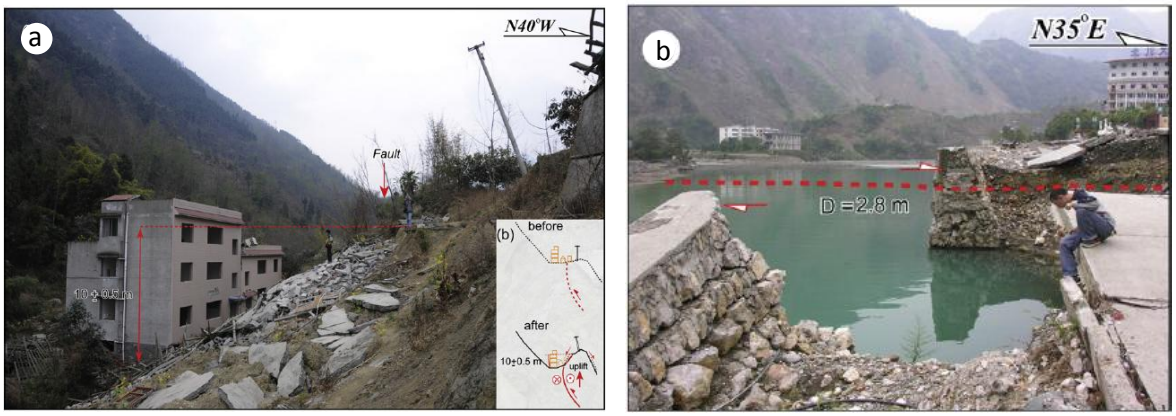

Figure 7.4: Surface deformation produced by the Wenchuan earthquake: (a) a fault scarp of 10±0.5 m in height; (b) Riverbed displacement by 2.8 m across the surface rupture.(Source: Fu et al. (2011)).

Seismological data show that the rupture initiated in the southern Longmen Shan (LMS) and propagated unilaterally northeastward on a northwest dipping fault for more than 320 km (Ji and Hayes, 2008). Several hundred strong aftershocks (M≥4.5) followed the mainshock (yellow circles in Fig. 7.2a) along the rupture zone (Fu et al., 2011). Aftershock relocation results (Chen et al., 2009) show that the dipping angle of the fault zone is 70°∼80° near the surface and is 30°∼60° near the hypocenter (at 10∼20 km depth according to USGS data). The total crustal shortening caused by this earthquake was up to 8.5 m, accompanied by a vertical uplift of up to 10 m (Fu et al., 2011) (Fig. 7.4).

As I think it is very interesting debate, I want to mention, that there is an intense scientific discussion on whether the several hundred million tons of water behind Sichuan's Zipingpu Dam may have triggered this devastating earthquake. The Zipingpu dam is just 500 m from the fault that failed and 5.5 km from the epicenter of the earthquake. Since its inaugauration in December 2004, the reservoir has seen dramatic rates of filling and draw−down, that certainly had an influence on the stresses on the fault (Kerr and Stone, 2009). To the interested reader, I suggest the Probe International study by Xiao and the Regional Geological Survey Team (2012) from the Sichuan Geology and Mineral Bureau, Chengdu, China, that also gives a dozen of references to scientific articles that have investigated the relationship between the Zipingpu reservoir and the Wenchuan earthquake.

7.1.3 The seismic network and the noise data

In October 2006, the State Key Laboratory of Earthquake Dynamics, Institute of Geology, China Earthquake Administration (under the responsibility of Qi Yuan and Jiu Hui Chen) deployed 297 broad-band seismic stations in the Western Sichuan province

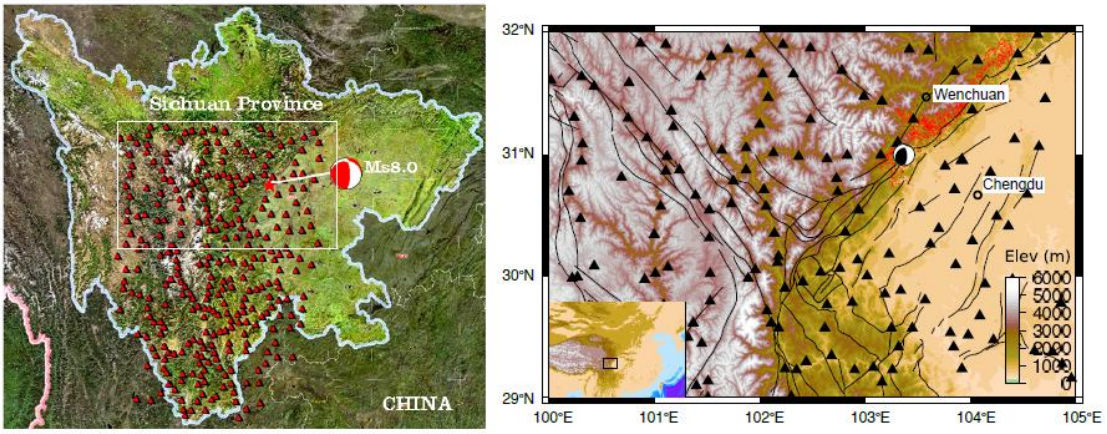

(a) (b)

Figure 7.5: (a) Map of the Sichuan province and the 297 seismic stations from the WSSA array. The white square corresponds to the region that we used in our study and to the region shown in Fig. 7.5b. (b) Stations used in our study. The beachball indicates the epicenter and the red dots the aftershock locations. The black lines correspond to the major faults in the region. (Source: Froment (2011)).

(Fig. 7.5a). This network covers 2/3 of the fault system activated during the Wenchuan earthquake in 2008. This Western Sichuan Seismic Array (WSSA) was operational since its installation until the end of 2008. In a collaboration agreement, the pre-processed data from January 2007 until the end of December 2008 have been made available to our group in Grenoble. It should be mentioned that the pre-processing steps that are requested by the Chinese authorities when taking the data abroad (amplitude normalization and stacking of the raw data over ten days) are very unfortunate and limit our analysis in terms of time resolution.
The area that we study, comprises the northern part of the WSSA (29° to 32°N and 100° to 105°E). In this area are 156 stations, with average station spacing of 20 to 30 km (Fig. 7.5b). The closest station is within 20 km of the epicenter of the Wenchuan earthquake. During and after the main shock, several stations suffered power failure. A considerable effort was made to recover these stations after at most 15 days.

7.1.4 Previous studies and motivation

Of particular interest for us are the studies of Chen et al. (2010) and Froment et al. (2013) who used the WSSA array data to investigate the changes of seismic velocity associated with the Wenchuan earthquake at a regional scale. For both studies, they had at their disposal the same data set as we do, from January 2007 until December 2008.

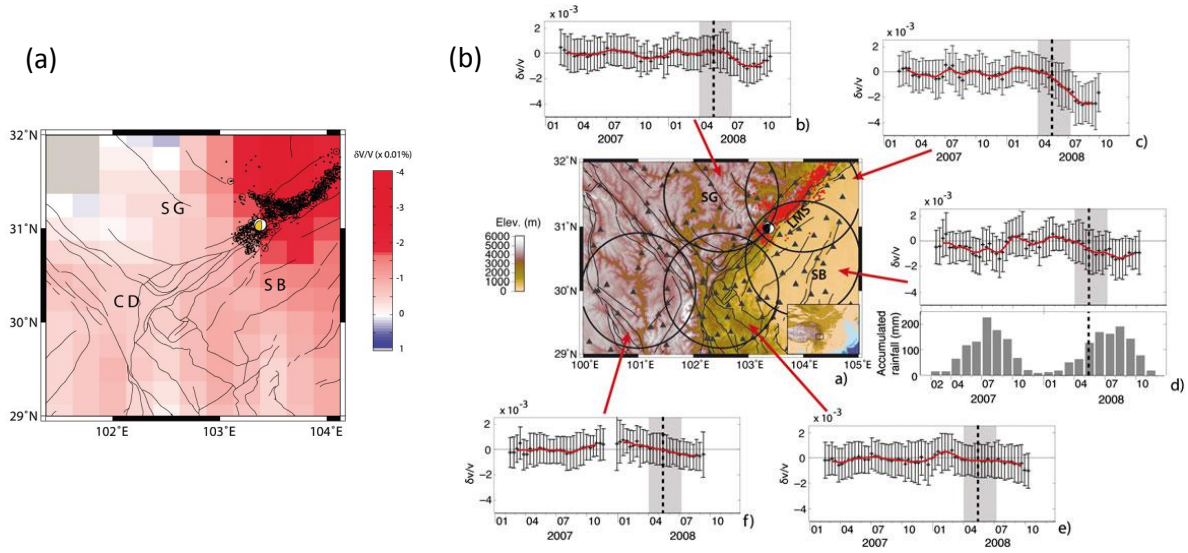

Figure 7.6: (a) Regionalisation in the 1-3 s period band (Source: Chen et al. (2010)). (b) Velocity variations in sub-arrays in the 12-20 s period band (Source: Froment et al. (2013)).

Chen et al. (2010) used continuous seismic recordings from this network to track the temporal changes of the seismic wave speed associated with the Wenchuan earthquake in the 1-3 s period band, corresponding to the shallow crust. They applied a doublet analysis to the codas of seismic noise cross-correlation functions and found clear evidence that the seismic velocity dropped by up to 0.08% in the fault region just after the earthquake. They interpolated their results to obtain a spatial distribution of the co-seismic velocity changes (Fig. 7.6a). They found that "this distribution is consistent with the volumetric strain change during the Wenchuan earthquake and shows that the co-seismic velocity change is not controlled by the response of the sediments in the Sichuan basin".

Froment et al. (2013) investigated the temporal changes of the seismic wave speed at depth. They used the 12-20 s period band which has its maximum sensitivity for $\approx 10-20$ km depth (Fig. 7.7). By comparison with measurements in the 1-3 s period band they showed that the seismic velocity changes cannot be explained by a shallow perturbation but are related to deformation at depth in the crust. Froment et al. (2013) then study the velocity variations in sub-arrays. Their results suggest a different behavior of the crust beneath Tibet and the Sichuan basin in response to the earthquake (Fig. 7.6b).

We study the velocity variations and the decorrelation in both period bands (1-3 s and 12-20 s) and use the inversion procedure described in section 6.2 to locate the changes. We add a new dimension to the inversion by studying the velocity variations and the decorrelation at different times in the coda that we then invert jointly. This

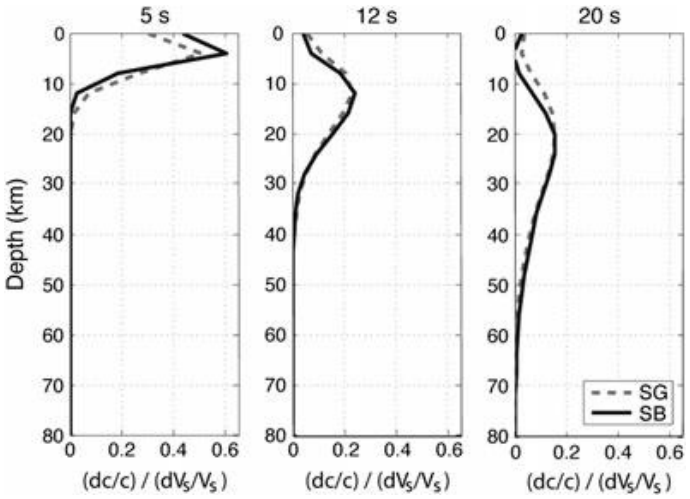

Figure 7.7: Sensitivity of the Rayleigh phase velocity c to a shear velocity perturbation dV_s for different periods: 5 s (left), 12 s (middle) and 20 s (right). (Source: Froment et al. (2013)).

procedure has the advantage that the sensitivity kernels describe the wave propagation at a specific time instead of averaging the propagation over a long time window. An additional advantage is that we have much more data to constrain the inversion.

7.2 Seismic noise correlations to image structural and mechanical changes associated with the Mw7.9 2008 Wenchuan earthquake

Imaging structural changes in the lower and middle crust associated with the Wenchuan earthquake by inverting measurements at different times in the coda

Anne Obermann, Bérénice Froment, Eric Larose, Michel Campillo, Thomas PlanÃ¨s, Bernard Valette, Jiuhui Chen and Qiyuan Liu.

Article submitted to *Journal of Geophysical Research* 2013.

Abstract: We locate temporal changes of seismic wave speed and seismic waveforms associated with the 2008 Mw 7.9 Wenchuan earthquake. To that end, we analyze ambient seismic noise records from 2007 until the end of 2008 in the 1-to-3 s period band and in the 12-to-20 s period band from a region that covers the southern two-thirds of the fault activated during the earthquake. To locate the changes, we use a refined imaging procedure based on the sensitivity of scattered waves to weak perturbations. This inverse

method uses the radiative transfer approximation to describe the intensity of the noise correlation coda.
Our results show that the largest structural changes are observed northeast of the Wenchuan epicenter, around the fault zone where aftershocks are distributed. The spatial and temporal characteristics of the behavior of the crust at depth around the Wenchuan earthquake suggest a post-seismic and geology-dependent signature of the middle crust. We also observe a clear seasonal signature within the Sichuan Basin at depth, that we relate to the heavy rainfalls during the monsoon season. This seasonality can also be observed at the surface in form of a waveform decoherence due to strong impedance contrasts. Our study highlights that seismic velocity changes and waveform decoherence are independent measurements, that are sensitive to different parameters and can thus give complementary information. In our study we also point out the interest of studying the evolution of the changes at different times in the coda.

7.2.1 Introduction

On 12 May 2008, a Mw 7.9 earthquake struck the Longmen Shan region, China along the Eastern margin of the Tibetan Plateau (Burchfiel et al., 2008; Zhang et al., 2010). This earthquake caused over 80,000 fatalities and enormous material damage in the surrounding counties. Surface geological surveys indicate a 240 km long rupture zone (Xu et al., 2009). Nearly 300 strong aftershocks followed the main shock along the rupture zone (Chen et al., 2009; Fu et al., 2011) (red dots in Fig. 7.8). The hypocenter was located at 14-19 km depth (Chen et al., 2009).
In October 2006, the Institute of Geology of the China Earthquake Administration deployed about 300 broad-band seismic stations in the Western Sichuan province. This Sichuan Seismic Array (WSSA) covers 2/3 of the fault system activated during the Wenchuan earthquake in 2008. The network was operated continuously from the initial installation until the end of 2008 and provides unique recordings before, during and after the Wenchuan quake. A collaboration agreement gave us access to the pre-treated data (amplitude normalization, stack over 10 days) from January 2007 until December 2008 from the Northern half part of the array (Fig. 7.8).

The physical processes that accompany earthquakes, such as co-seismic stress changes, the migration of fluids and the formation of damage zones in the shallow layers, are likely to cause changes in mechanical properties of nearby crustal material. The sensitivity of the multiply scattered coda of ambient seismic noise cross-correlations is in general high enough to detect relative changes in the order of 10^{-4}. With the approximation that the sensitivity of coda waves at early times in the coda is dominated by surface waves, we can study the noise correlations in different frequency bands, that are sensitive to different depths. In previous works, Chen et al. (2010) used this same data set and showed that they could track the temporal change of the seismic wave speed in the 1-3 s period band

(sensitive to the upper crust) at a regional scale. They found clear evidences that the seismic velocity dropped by up to 0.08% in the fault region just after the earthquake with fluctuations within 0.02% prior to the earthquake. They split the area of interest in different sub-arrays and compared the measurements of these arrays to obtain a spatial distribution of the velocity changes. They found the distribution to be consistent with the volumetric strain change during the Wenchuan earthquake and could show that the co-seismic velocity changes are not controlled by the response of the sediments.

Still using the same data subset, Froment et al. (2013) investigated the temporal changes of the seismic wave speed at larger depth. To do that, they used the 12-20 s period band, which has its maximum sensitivity for 20-30 km depth. Besides a velocity drop associated with the earthquake, they also detected apparent seasonal variations of the seismic velocity in the Sichuan basin. By comparison with measurements in the 1-3 s period band they show that the seismic velocity changes in the 12-20 s period band cannot be explained by a shallow perturbation but are related to deformation at depth in the crust. They used these variations to characterize the middle crust behavior around the Wenchuan earthquake. Their results suggest that the deformation in the middle crust is different beneath Tibet and the Sichuan basin.

In the present paper we study the temporal changes of seismic wavespeed and the distortion of the seismic waveform (waveform decoherence) due to structural changes in the medium in both the 1-3 s and 12-20 s period bands. Based on recent results in wave physics (Larose et al., 2010; Rossetto et al., 2011; Froment, 2011; Planès, 2013; Planès et al., 2013), we then use an imaging procedure (Obermann et al., 2013a) that is based on the sensitivity of scattered waves to weak changes in the multi-scattering media, and that allows spatial localization of scattering properties. With this method we can successfully image the lateral distribution of the velocity variations and the waveform decoherence associated with the 2008 Wenchuan earthquake and the heavy rainfalls in the monsoon season in summer 2007. As Obermann et al. (2013b) pointed out the different informations that are contained at different times in the coda, we further develop the inversion technique to jointly invert for different times in the coda.

In section 7.2.2, we describe the seismic data that we use in this study and we briefly explain the computation of the cross-correlation functions and the determination of the relative velocity changes and the decoherence with the stretching technique. As the use of the decoherence in seismology is new, we give a short description of this measure. In section 7.2.3, we explain the linear least square inversion that we use to locate the medium changes. In section 7.2.4 we show and discuss the inversion results for the velocity changes and the waveform decoherence in the shallow and middle crust. We particularly emphasize that the apparent velocity changes and the waveform decoherence show different behavior at different times in the coda. We use this time evolution to improve the resolution on the horizontal plane and to obtain qualitative information at depth.

7.2.2 Seismic data and data processing

The study area comprises the northern part of the WSSA (29° to 32°N and 100° to 105°E). In this area are 156 stations, with an average station spacing of 20 to 30 km. We remove stations with instrumental timing errors using a time symmetry argument for noise cross correlations as introduced by Stehly et al. (2007). The remaining 114 stations are distributed over different geological units in this area (Fig. 7.8): the Prehimalaya with the Songpan-Ganzi (SG) and Chuan-Dian (CD) blocks, the Longmen Shan mountain range (LMS) and the sedimentary Sichuan Basin (SB). Some stations near the epicenter of the earthquake (beachball in Fig.7.8) suffered power failure during the main shock, most of them were recovered in the weeks after the quake. Nevertheless, within the small time windows that we study, the data quality degrades increasingly towards the end of 2008.

We obtained the seismic records from our Chinese collaborators in stacks of 10 days and with normalized amplitudes. We analyze the vertical component and apply the following further processing steps: (1) re-sampling of the data to a sampling frequency of 5 Hz; (2) filtering and whitening in the period band of 1 s to 3 s and 12 s to 20 s respectively; (3) application of one-bit normalization; and (4) computation of the 10-day noise correlations for all of the station pairs with a spacing of <350 km; (5) stacking of the correlations to obtain a stable cross-correlation function. A difficulty that we face here is, that the longer the period of the signal, the slower its convergence towards a stable correlation function. We need to stack 50 days in the 1-3 s period band and 100 days in the 12-20 s period band to obtain a stable function, which will limit the temporal resolution of our results. We then track the temporal variations in the coda by comparing the 50-day/100-day correlation function at each date to a reference correlation function that is the average over the whole two-year period (Fig. 7.10). The seismic velocity variations $\delta v/v$ and the waveform coherence CC are computed with the *stretching technique* (Lobkis and Weaver, 2003; Sens-Schönfelder and Wegler, 2006). This method is based on the concept, that a spatially homogeneous velocity variation in the medium will result in stretching or compression of the waveform (Fig. 7.10, Inset a). The stretching method then determines the relative velocity variation $\delta v/v = -\delta t/t$ as the factor ϵ by which the time axis of the current trace has to be stretched or compressed to obtain the best correlation CC with the reference trace. In case of local medium perturbations, we do not expect a linearly increasing velocity change with increasing time in the coda (Obermann et al., 2013b). We hence apply the stretching technique to different time windows in the coda (Fig. 7.9). In the 1-3 s period band we use 50 s long windows centered around 30, 50, 70 and 90 s. In the 12-20 s period band we use 90 s long windows (more than two periods) centered around 50, 70 and 90 s in the coda. We exclude autocorrelations and only work with station pairs that have a coherency value above 0.75 during the background period (neither rainfall, nor earthquake disturbances) that is defined in Fig. 7.8e.

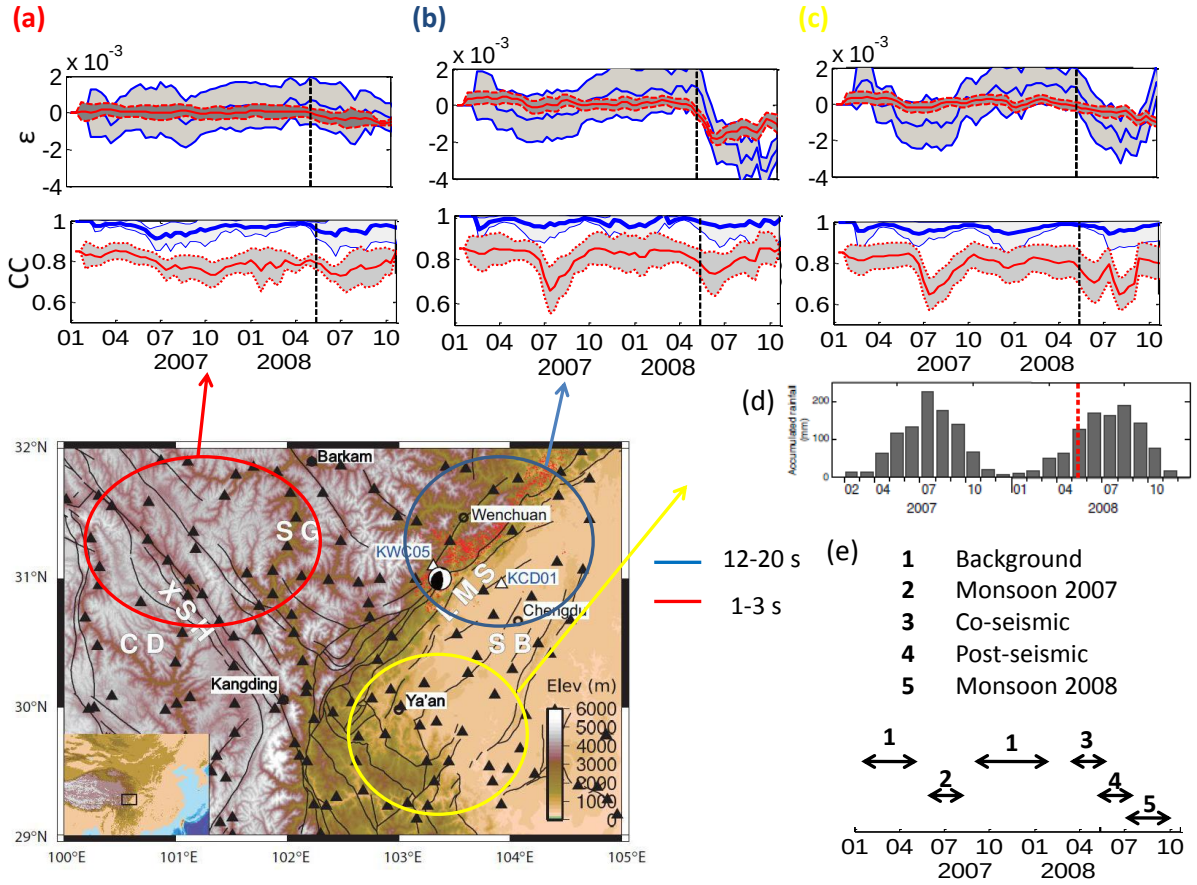

Figure 7.8: Location map of the stations used in the present study (black triangles). The beach ball indicates the epicenter of the Wenchuan earthquake, and the red dots represent the aftershocks (Chen et al., 2009). The black lines show the major faults in the region. SB, SG and LMS indicate the main geological units to which this study refers: the Sichuan sedimentary basin, the Songpan-Ganzi block, and the Longmen Shan fault zone, respectively. The colored circles indicate the subregions for which we show the velocity variations and the coherence for the time of interest at 50 s in the coda: The Pre-Himalaya (red, a), the Longmen-Shan region where the earthquake took place (blue, b) and the southern Sichuan basin (yellow, c). d) shows the accumulated rainfall in the Sichuan basin and e) indicates the time spans that we used to average the different states (background, rain, coseismic and postseismic).(Figure inspired by Froment et al. (2013).)

If the wave did not only encounter a velocity perturbation in the medium, but also a structural change of the medium, we observe additional small residual distortions of the waveforms (Fig. 7.10, Inset b). To quantify the decorrelation or waveform decoherence that has been introduced by the change in the medium, we subtract the current correlation value CC_i^{Curr} of a station pair i from the reference correlation value CC_i^{Ref} that

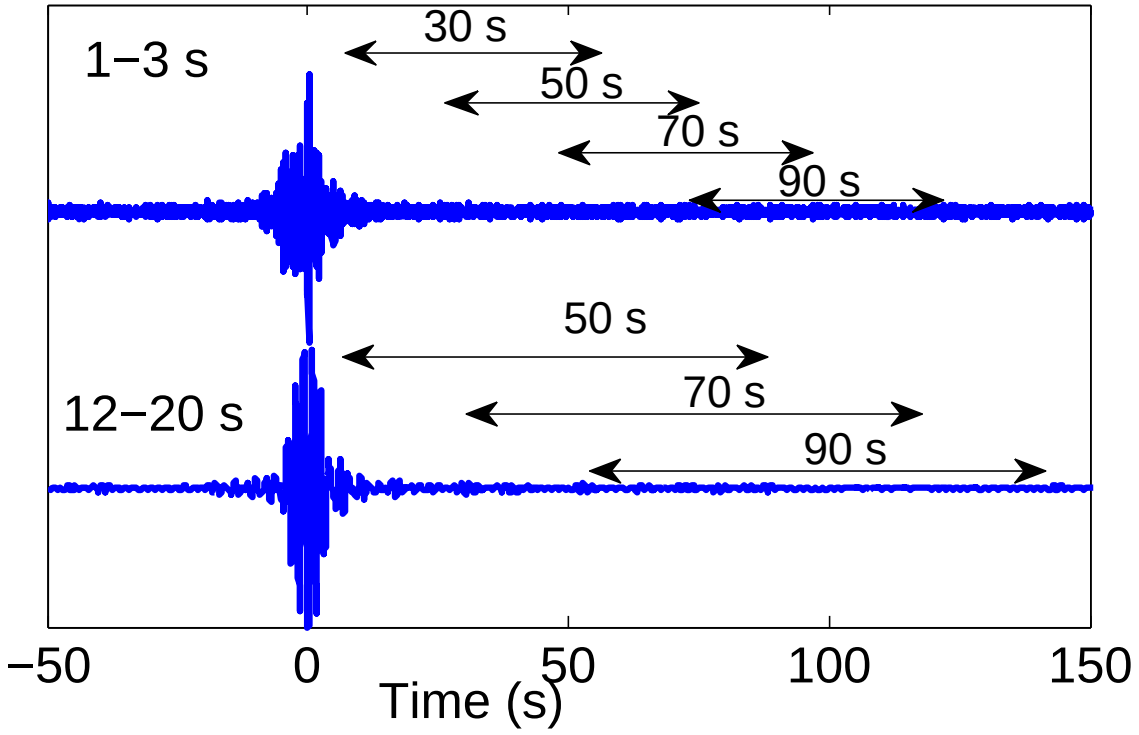

Figure 7.9: Illustration of a reference correlation function for a station pair ≈ 40 km apart in the 1-3 s and 12-20 s period range. We sketch the coda time windows that we use for the inversion. For the 1-3 s period band we use four 50 s long windows centered around 30, 50, 70 and 90 s. In the 12-20 s period band we use 90 s long windows centered around 50, 70 and 90 s.

was calculated as the average over the background period (Fig. 7.8e):

$$DC_i = CC_i^{\mathrm{Ref}} - CC_i^{\mathrm{Curr}}. \tag{7.1}$$

This waveform decoherence has been used in acoustics on laboratory experiments with aluminum plates (Michaels and Michaels, 2005) and on concrete (Larose et al., 2010; Rossetto et al., 2011; Planès, 2013) to quantify defects in materials that are much smaller than one wavelength (*Locadiff technique*). Obermann et al. (2013a) used the waveform decoherence successfully to locate pre-and co-eruptive changes on a volcano with high spatial resolution using ambient seismic noise measurement.

In Fig. 7.8a,b,c) we show the velocity variations and the waveform coherence from early 2007 until late 2008 at 50 s in the coda for both frequency bands. We here averaged the measurements from the cross-correlations in three subregions: the Pre-Himalaya (red, a), the Longmen-Shan region where the earthquake took place (blue, b) and the southern Sichuan basin (yellow, c). The black dotted line in Fig. 7.8a,b,c) marks the date of the earthquake. We note that there are no velocity changes or waveform decoherence during

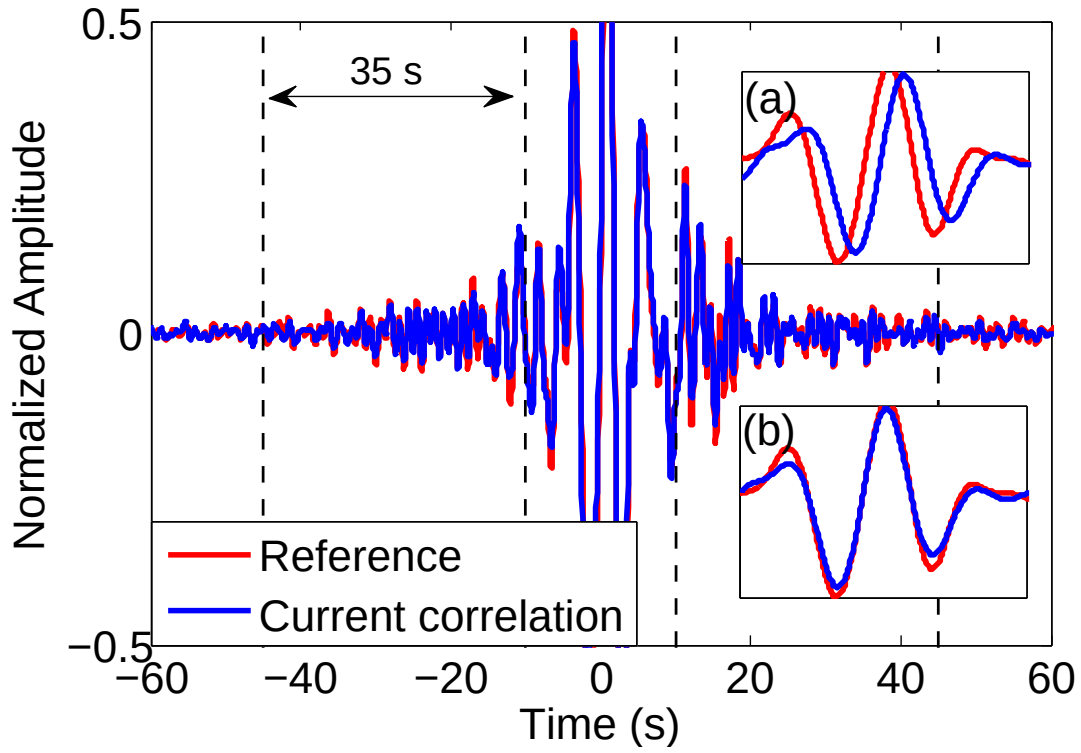

Figure 7.10: Illustration of a reference correlation function (blue) and "current" correlation function (red). Inset (a) shows the time delay of the "current" correlation function in the coda. Inset (b): the "current" correlation function has been corrected for its time delay. We observe waveform distortion that is due to a change in the scattering properties of the medium. This is what we refer to as waveform decoherence. (Source: Obermann et al. (2013a).

the period of interest in the Pre-Himalayan region (a). In the Longmen-Shan region (b), we observe a clear velocity drop in the two period bands with onset of the earthquake that reaches its maximum after the earthquake in both frequency bands. In the 12-20 s period band we can further observe a small velocity drop between May and August 2007 that seems to correlate with the accumulated rainfalls during monsoon season in this area (Fig. 7.8d). In the southern Sichuan basin (c), the velocity drop from May to August 2007 is even more pronounced in the 12-20 s period band. In the southern Sichuan basin, we do not observe any significant velocity variations in the 1-3 s period band for the entire period of interest. The coherence in the 12-20 s band remains high (0.95 on average) with only small fluctuations for all three subregions. In the 1-3 s period band, we note a very pronounced decorrelation (20%) in July/August 2007 in the Sichuan basin and the Longmen-Shan region (b,c). In these regions we also observe a decorrelation of about 10% with the onset of the earthquake. The coherence in the 12-20 s period band does not seem to be significantly affected in any region. For the inversion, we define four time periods that we want to study independently and over which we will average the

velocity variations and the waveform decoherence measurements for each station pair respectively (Fig. 7.8e). We identify the background state, that comprises the parts of the years 2007 and 2008 that are neither affected by the monsoon nor the earthquake; the peak of the monsoon period from June to July 2007, the co-seismic period around May 2008 and the post-seismic period from June-August 2008.

The observations that we made for the velocity variations are in general consistent with the observations of Chen et al. (2010) and Froment et al. (2013). The slight differences that are there arise mainly from a different selection of station pairs for the subregions. Here, we see one of the main interests of the inversion procedure, that takes into account the information from all station pairs without averaging them spatially.

Seasonal noise source changes in the ocean have been suggested to be at the origin of velocity changes observed in this region (Liu et al., 2010). As these changes should affect the entire region in the same way, which is not the case, we exclude seasonal noise source changes as origin of observed waveform decoherence and velocity variations, and relate them solely to changes in the ground.

7.2.3 Joint inversion at different times in the coda

The velocity changes measured on noise correlations are representative of a set of scattering paths between two stations. This measure can be viewed as a linear sum of contributions from each space element in the medium. Note that we consider here a two-dimensional medium, as the use of surface waves in a limited period band makes it possible to assume as a first approximation that we are investigating the medium at a specific depth. We hence attempt to locate the velocity changes and the waveform decoherence measurements in the $x-y$ plane in the shallow and middle crust. We have velocity change (ε_i) and decoherence measurements $DC_i = CC_i^{\mathrm{ref}} - CC_i^{\mathrm{curr}}$, that correspond to a pair of seismic stations i. As these measurements are performed on multiply scattered coda waves that follow very complex paths between the two stations, it is not possible to associate a specific arrival time in the seismograms to a specific trajectory in the medium. The challenge is thus to relate a measurement corresponding to a station pair to every space element of the medium sampled by the coda waves. To do that, it is relevant to describe the wave propagation with probabilities (random walk). We can then compute sensitivity kernels between the stations and apply a linear least-square inversion scheme to locate the changes in the $x-y$ plane. Obermann et al. (2013a) used this inversion scheme with sensitivity kernels in the radiative transfer approximation to locate changes on a volcano. While they use one large time window in the coda for their analysis, we here take several short windows at different times in the coda and invert them simultaneously. By doing so, we expect an increase in resolution and additional information about the depth of the changes (Obermann et al., 2013b).

7.2.3.1 Sensitivity kernel

The probabilistic wave propagation in the multiple scattering regime is calculated using the solution to the radiative transfer equation (Boltzmann transport equation). In 2D for isotropic scattering, the solution reads (Shang and Gao, 1988; Sato, 1993; Paasschens, 1997):

$$p(\boldsymbol{r},t) = \frac{e^{-ct/\ell}}{2\pi r}\delta(ct-r) \tag{7.2}$$
$$+\frac{1}{2\pi\ell ct}\left(1-\frac{r^2}{c^2t^2}\right)^{-\frac{1}{2}}\exp\quad^{[\ell^{-1}(\sqrt{c^2t^2-r^2}-ct)]}\Theta(ct-r),$$

where c is the wave speed, r is the distance between source and receiver, ℓ is the transport mean free path and $\Theta(x)$ is the Heaviside (or step) function. The first term describes the coherent part of the intensity that decreases exponentially with the distance relative to the transport mean free path. The second term describes the diffuse intensity. We note that the diffusion solution is reached when $t \gg r/c$. With this intensity propagator, we can describe the probability that the wave has traveled between two points in the medium during time t. We can now relate the measured velocity changes ε^i or decoherence measurements CC_i to a local medium perturbation in x_0 using the sensitivity kernel introduced by Pacheco and Snieder (2005); Larose et al. (2010); Planès et al. (2013):

$$K(\boldsymbol{s_1},\boldsymbol{s_2},\boldsymbol{x}_0,t) = \frac{\int_0^t p(\boldsymbol{s_1},\boldsymbol{x}_0,u)p(\boldsymbol{x}_0,\boldsymbol{s_2},t-u)du}{p(\boldsymbol{s_1},\boldsymbol{s_2},t)} \tag{7.3}$$

where $\boldsymbol{s_1}$ and $\boldsymbol{s_2}$ are the positions of the stations, $\boldsymbol{x}_0$ is the position of the local medium perturbation (velocity perturbation or structural change) and t is the center of the time interval in the coda where the stretching is evaluated. $p(\boldsymbol{s_1},\boldsymbol{s_2},t)$ is the intensity propagator in the radiative transfer solution (Eq. 7.2). The sensitivity kernel is herewith a measure of the statistical time spent in each part of the region at test. An example of the sensitivity kernel K is shown in Fig. 7.11.

The diffusivity D is computed for a velocity v=3 km/s (Rayleigh-wave group velocity measured in the 1-3 s period range) and v=5 km/s in the 12-20 s period range. The value of the transport mean free path ℓ is difficult to estimate. Obermann et al. (2013a) tested the sensitivity of the inversion toward different values of ℓ and observed that ℓ has an influence on the size of the affected area but not on the location itself. The results presented in the main body of the text correspond to a transport mean free path ℓ of 60 km in the 1-3 s period range and 500 km in the 12-20 s period range.

7.2.3.2 Linear least-square inversion at different times in the coda

To estimate the horizontal distribution of the changes in the study area, we pose the direct problem in form of a system of linear equations in matrix form according to:

$$\boldsymbol{d} = G\boldsymbol{m}, \tag{7.4}$$

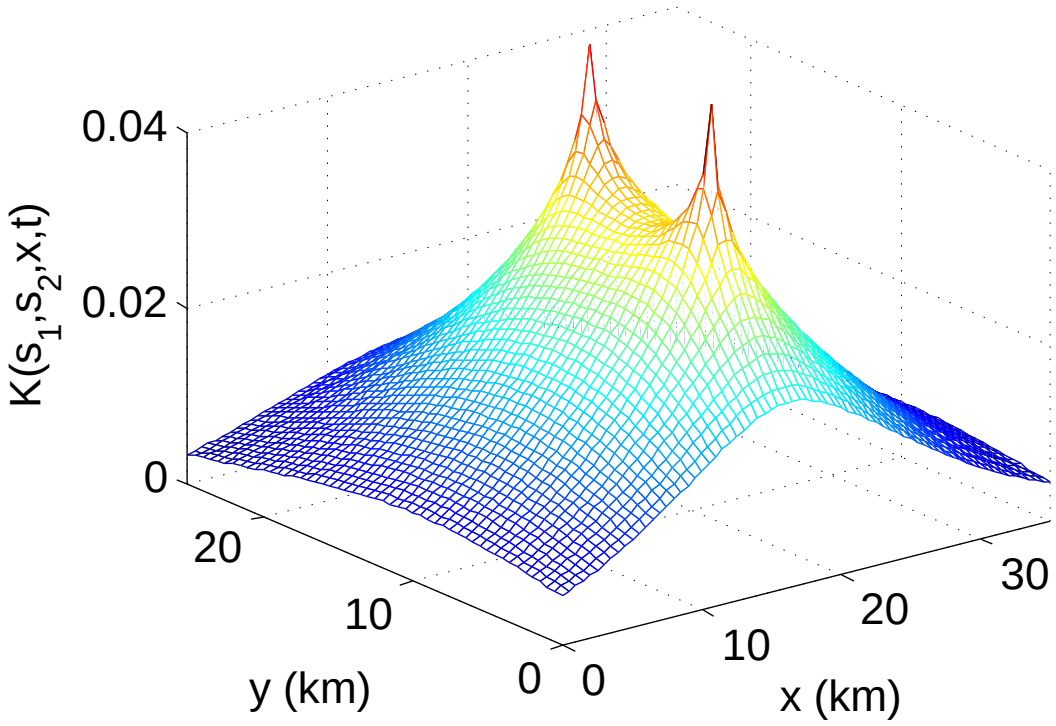

Figure 7.11: Spatial representation of the sensitivity kernel K (Eq.7.3). The values along the vertical axis can be interpreted as the sensitivity toward a perturbation in the medium located in (x, y).

where $\boldsymbol{d}$ is a vector, for which each component $d_i (i = 1...n)$ corresponds to the apparent velocity change or decorrelation that we measured between n station pairs with the stretching technique. $\boldsymbol{G}$ is a matrix, for which each component G_{ij} corresponds to the sensitivity kernel K for station pair i in cell j evaluated at time t in the coda and weighted by the surface of the cells Δs and either the lapse time t in the coda (velocity changes), or the Rayleigh wave group velocity c (decorrelation measurements). $\boldsymbol{m}$ is a vector, for which each component m_j contains the actual velocity changes that we estimate for each pixel j (without units) or the scattering cross-section density (km/km^2):

$$d = \varepsilon, \quad G_{ij} = \frac{\Delta s}{t} K_{ij}, \quad m = \frac{\delta v}{v}. \tag{7.5}$$

$$d = DC, \quad G_{ij} = \frac{c\Delta s}{2} K_{ij}, \quad m = \sigma. \tag{7.6}$$

When the data that we invert represent local velocity changes, there is no constraint concerning the sign of $\boldsymbol{m}$. We can thus directly use the formulation of the linear least-square method as proposed by Tarantola and Valette (1982) to determine $\boldsymbol{m}$:

$$\boldsymbol{m} = \boldsymbol{m_0} + \boldsymbol{C_m G^t} (\boldsymbol{G C_m G^t} + \boldsymbol{C_d})^{-1} (\boldsymbol{\varepsilon} - \boldsymbol{G m_0}), \tag{7.7}$$

where $\boldsymbol{m_0}$ is the initial model, a zero vector in our case, as we do not possess any a priori information about the expected changes. $\boldsymbol{C_d}$ is the diagonal covariance matrix for the data and contains the variances of the data $\sigma^2_{d,i}$. $\boldsymbol{C_m}$ is the covariance matrix for the model. To estimate the standard deviation $\sigma_{d,i}$ of the data, we use the theoretical formulation proposed by Weaver et al. (2011):

$$\sigma_{d,i} = \frac{\sqrt{1 - CC_i^2}}{2CC_i} \sqrt{\frac{6\sqrt{\frac{\pi}{2}}T}{\omega_c^2(t_2^3 - t_1^3)}}. \tag{7.8}$$

T is the inverse of the frequency bandwidth, t_1 and t_2 are the begin and end of the processed time-window in the coda, $\omega_c = 2\pi f$ is the central frequency and $CC_i = CC(\varepsilon_i)$ is the coherence value of the respective station couple i.

When we study the decorrelation, the scattering cross-section density that we obtain is necessarily positive and we need to impose a positivity constraint during the inversion. We herefore use an iterative procedure. The initial model m_0 is again zero everywhere and then at each iteration step, we only keep positive values and use this model as a new input model. We use eight iterations to obtain the scattering cross-section maps shown in Fig. 7.13.
We compute the kernels at different lapse times in the coda and then jointly invert the data. This increases the amount of data and the horizontal resolution.

We study an area from 100 E to 105 E and from 29 N to 32 N (Fig. 7.8), which covers a region of about 480 km × 340 km. To minimize model-edge effects across the region of interest, we model the velocity variations in a larger zone. In view of the spreading of the sensitivity kernels used, we have decided to consider the region of interest extended by 250 km in each direction. We finally investigate the changes in 51×42=2193 cells of 20 km × 20 km (ΔS = 400 km^2).
In this monitoring context, the data are available for 65 10-day periods between January 2007 and October 2008. We focus on five specific periods as shown in Fig. 7.8e. Within each of these periods we average the measured velocity changes and decoherence values. As mentioned previously, we apply a quality criterion and invert only the measurements from station pairs with average correlation coefficients above 0.75 in the background state. This leaves us with about 600 station-pair measurements that cover the entire area. Note that this inverse problem is under-determined (≈ 600 data and ≈ 2200 model parameters). To decrease the number of independent parameters, we introduce a spatial smoothing in the inversion process, which is obtained by correlating nearby parameters (Hansen, 1992). A detailed discussion concerning the smoothing method as well as quality tests for the inversion is provided in the Supplementary Material.

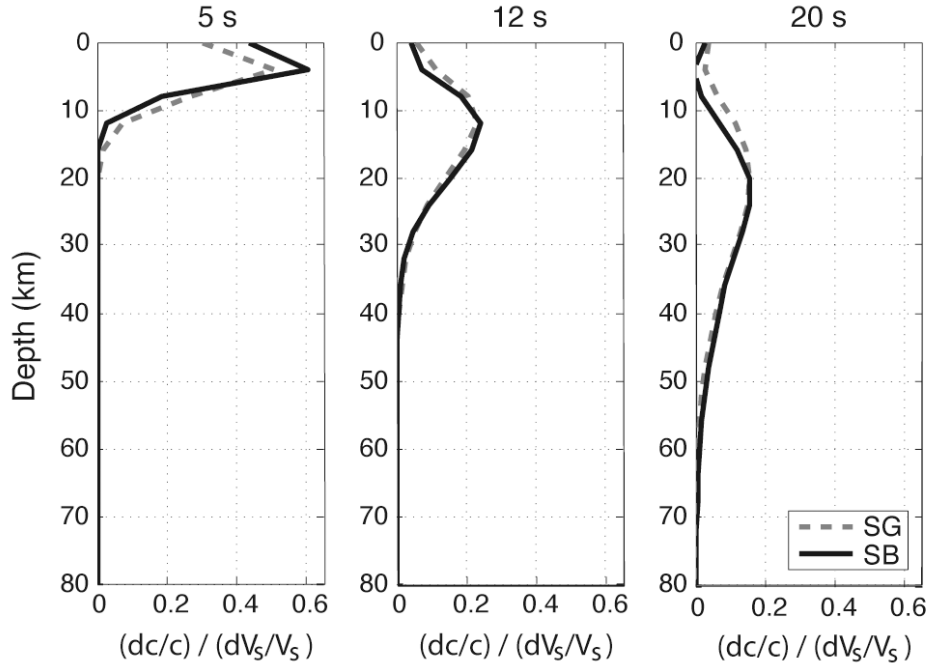

Figure 7.12: Depth sensitivity of the Rayleigh phase velocity c to a shear wave velocity perturbation dV_s at 5, 12 and 20 s computed in the region of interest (Figure from Froment et al. (2013)). SG (grey dashed line) corresponds to an analysis in the Songpan Ganzi block and SB (black line) to the Sichuan basin.

7.2.4 Inversion results in the 1-3 s and 12-20 s period band

In this section we discuss the inversion results for the velocity variations and the waveform decoherences in both frequency bands and at different times in the coda. To have a better idea of the depth we are talking about in the different period bands, we show in Fig. 7.12 the depth sensitivity of the Rayleigh phase velocity to a velocity perturbation at 5, 12 and 20 s (Figure from Froment et al. (2013)). We conclude that the depth sensitivity for the 1-3 s period is limited to the upper 10 km, while for the 12-20 s period band, the sensitivity is the highest between 10 and 30 km.

In Fig. 7.13 we display the images of the velocity variations based on the inversion of the relative delays in the coda and the images of the structural changes (scattering cross-section of the change) based on the inversion of the decoherence values in the coda (second line for the 1-3 s period band and fourth line for the 12-20 s period band). The images are the joint inversion results for different times in the coda as indicated in Fig. 7.9. We display in each column from left to right the averages for: the peak of the monsoon season in 2007 (July-August 2007), the co-seismic period (May 2008), the post-seismic period (June-beginning of July 2008) and the peak of the monsoon season in 2008 (July-August 2008). We recall that velocity drops indicate mechanical weakening of the material, while a decorrelation indicates structural changes that result from

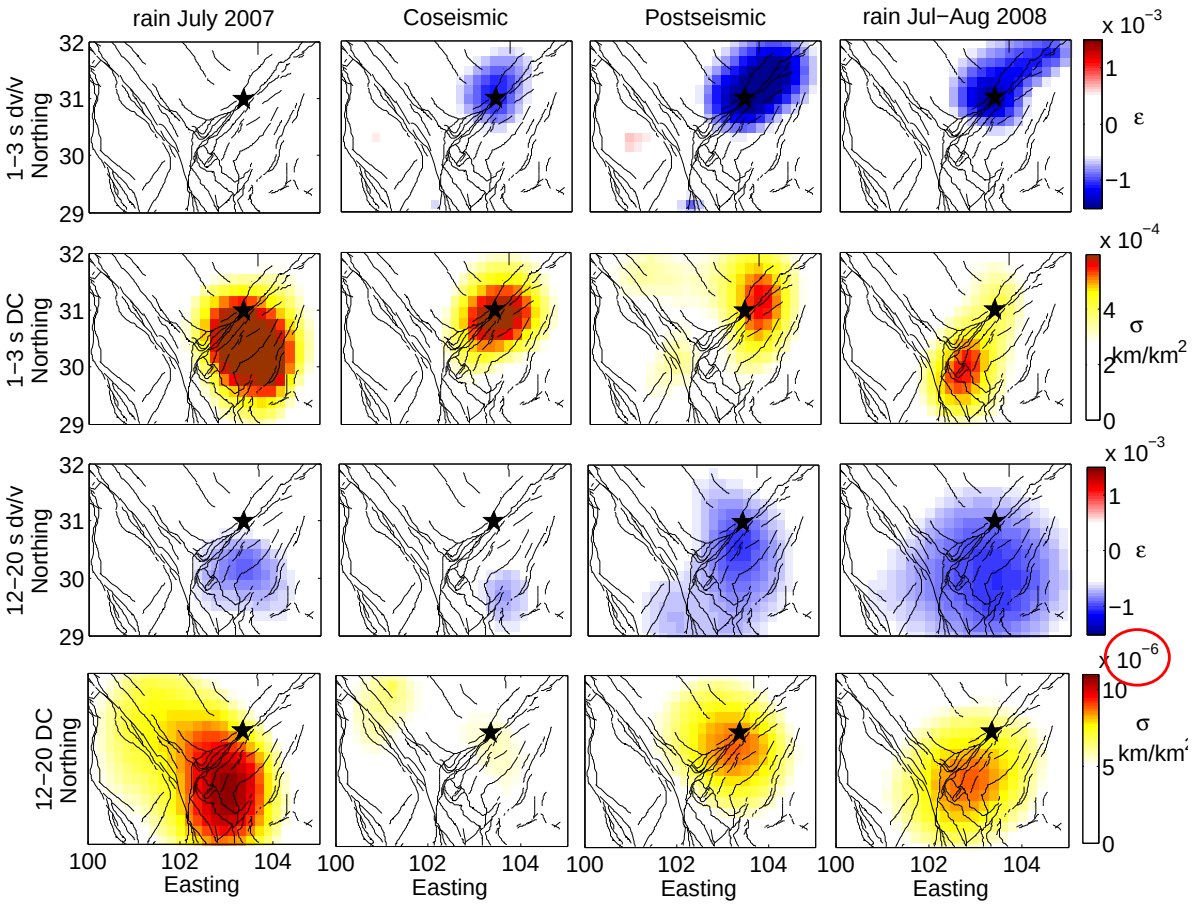

Figure 7.13: Least square inversion of the relative velocity changes (dv/v) and the decoherence values (DC) in the 1-3 s (jointly for 30, 50, 70 and 90 s in the coda) and in the 12-20 s period band (jointly for 50, 70 and 90 s in the coda). In the columns we show the results for the peak of the monsoon period in 2007, the co-seismic period (May 2008), the post-seismic period (June-July 2008) and the peak of the monsoon period in 2008.

changes of the scattering properties of the medium.

The 2D horizontal maps with the velocity variations in the 1-3 s period band (Fig. 7.13, first line) show no velocity variation during the monsoon season in 2007. Whereas we observe a co-seismic velocity drop (-0.8%) at the earthquake location and a strong post-seismic signature (-2%) over a large area that includes the aftershocks along the fault zone (red dots in Fig. 7.8). In the monsoon period 2008 we still observe a velocity drop at the earthquake location and along the fault zone.

When studying the 2D horizontal maps with the scattering cross-section densities (Fig. 7.13, second line), we observe a strong decorrelation in the Sichuan basin during the monsoon season 2007. We further observe a co-seismic decorrelation that affects the

area around the earthquake. The post-seismic signature is weaker and extends toward the North of the hypocenter, along the fault zone with the aftershocks. In the monsoon period 2008 we observe a small decorrelation at the earthquake location and a strong, localized decorrelation in the Sichuan basin.

When studying the velocity variations in the 12-20 s period band (Fig. 7.13 third line), we observe a velocity drop in the Sichuan basin during the monsoon period 2007. We observe a very local, low amplitude, velocity drop in the Sichuan basin during the co-seismic period but no visible velocity variations at the earthquake location. In the post-seismic period, we observe velocity drops in the entire Sichuan basin including the earthquake zone and extending in the Songpan Ganzi. During the monsoon period in 2008, we observe an extended velocity drop in the Sichuan basin extending in the Songpan Ganzi.

When studying the decoherence in the 12-20 s period band (Fig. 7.13 fourth line), we observe a decorrelation in the Sichuan basin during the monsoon periods of 2007. There is hardly any decorrelation in the co-seismic period. In the post-seismic period we see a decorrelation at the earthquake location. During the monsoon in 2008 we observe a decorrelation again in the Sichuan basin, including the earthquake location. Please note that the decorrelation in the 12-20 s period band is one order of magnitude below the decorrelation in the 1-3 s period band and hence rather insignificant.

These observations lead us to propose interpretations concerning the effect of the rain and of the earthquake on the velocity variations and the waveform decoherence. Let us start with the observations during the monsoon periods of 2007 and 2008. The changes of the water table in the Sichuan basin during the monsoon (Fig.7.8) can be seen in form of a decorrelation in the 1-3 s period band and as a velocity drop in the 12-20 s period band, whereas we do not observe a significant velocity drop in the 1-3 s period band. The hydrological conditions at the surface (1-3 s) do not significantly modify the elastic parameters of the Sichuan basin that is saturated all year long, but they change the scattering properties at the surface (river load etc). That water saturation can induce decoherence as shown in laboratory experiments on concrete (Planès, 2013). At depth (12-20 s), we follow the interpretation from Froment et al. (2013) that the loading due to the rain induces significant deformation at depth, the water saturation does not. The loading can significantly increase the pore pressure and hences cause a velocity diminution (Dvorkin et al., 1999; Carcione and Tinivella, 2001). Another strong lead in this direction is the remarkable synchrony of the rain and the velocity drop. This excludes that fluid transport at depth could be at its origin, as the hydrological diffusion time would delay the response. It indicates more instantaneous mechanical effects that go in hand with the interpretation of the velocity drop as a consequence of the loading. The absence of the signal in the 1-3 s period band excludes seasonal thermo-elastic effects that should be strong close to the surface.

Let us now interpret the co-and post-seismic observations. The co-seismic signature (velocity drop and decoherence) in the 1-3 s period band around the earthquake hypocenter can be directly related to the strong damages caused by the earthquake at the surface and in the fault zone itself (240 km long rupture zone, up to 10 m vertical offset, landslides). The strong post-seismic velocity drop along the fault zone is occurring in the region where most of the aftershocks occurred. It is possible that it is associated with the non-linear dynamic response of the shallow layers to the numerous aftershocks. The non linear response of shallow layers to strong motion has been observed to have a rapid recovery (Sawazaki et al., 2006; Karabulut and Bouchon, 2007; Rubinstein et al., 2007). In the 12-20 s period band, we do not observe a significant co-seismic signature. This could indicate that the nonlinear effects due to the strong motions are limited to the surface. Instead we observe a significant post-seismic change at the earthquake location. As a cause of these post-seismic changes, both poro-elastic relaxation or post-seismic slip at depth (Froment et al., 2013) could explain our observations. Please note that since our measurements correspond to both, a space and time average, the overall amplitude of the changes should not be analyzed with too much attention.

In Fig. 7.14 we focus on the evolution of the changes with lapse time in the coda during the post-seismic period in both frequency bands. We here invert the velocity variations and the waveform decoherences at each time in the coda separately, instead of doing a joint inversion with different times in the coda. Obermann et al. (2013b) have shown based on scattering and mode conversion arguments, that surface waves statistically dominate the early part of a seismic record, whereas bulk waves statistically dominate the later part. As a consequence, changes at shallow depth (compared to the wavelength) result in a large amplitude velocity change (or decoherence) at early lapse times and then decrease in amplitude later. On the contrary, for changes at depths greater than the wavelength, the velocity change will increase from a negligible value at early times to a significant contribution at later times. With this analysis we hence expect to obtain some additional information about the nature of the changes. We notice that the velocity drop in the 1-3 s period band is stronger at early times in the coda (30 s) than at later times (50, 70 s). The decorrelation in this period band shows the opposite behavior, there is no decorrelation at early times, while it grows larger at later times in the coda. We hence conclude that the mechanical changes occurred within one wavelength from the surface, while the structural changes took place further at depth.

In the 12-20 s period we observe a velocity drop in the Sichuan basin at early times in the coda (50 s), whereas the sensitivity shifts toward the earthquake location at later times (70, 90 s). The decorrelation in the 12-20 s period band is the strongest at 70 s in the coda. We do not put much attention to the observations of the decorrelation in this frequency band, as the amplitude of the changes is insignificant. We conclude that the monsoon that we observe at early times in the coda has an effect down to about 30 km. The effect of the earthquake can only be seen at later lapse times and we hence attribute this to a change of the mechanical parameters below 30 km, which is also below

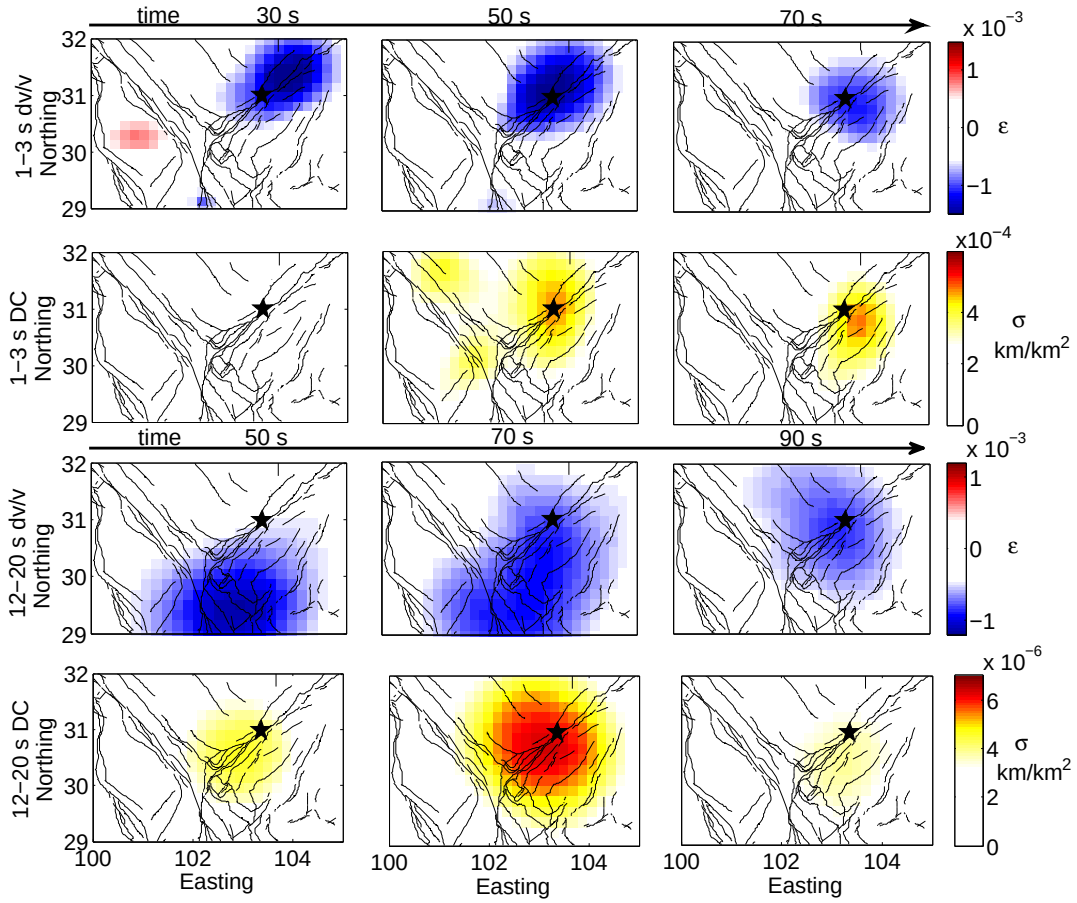

Figure 7.14: Evolution of the post-seismic changes with time in the coda for the velocity variations dv/v and the decoherence DC in the 1-3 s period band at 30, 50 and 70 s in the coda and dv/v and DC in the 12-20 s period band at 50, 70 and 90 s in the coda.

the earthquake hypocenter.

7.2.5 Conclusion

In the present study, we investigated the temporal evolution of elastic and scattering parameters in the crust at different depth ranging from 0 to 40 km over two years including the May 12, 2008 M_w 7.9 Wenchuan earthquake. We monitored the temporal evolution by measuring seismic velocity changes and also waveform decoherence in the coda part of the noise correlation functions. We could detect co- and post-seismic changes, as well as changes associated with the monsoon seasons. We studied the spatial distribution of these temporal changes with a refined localization method that is based on the inversion of the velocity change/waveform decoherence measurements at different times in the coda. With both measurements, we could locate the damage around the earth-

quake hypocenter and along the rupture zone. We also observed that the crust below the hypocenter suffered from significant post-seismic changes in its elastic parameters that could be due to slow transfer of the load caused by the earthquake (poro-elastic relaxation).

We could further see a significant loading effect from the rain during the monsoon season on the middle crust in form of a velocity drop. This hydrological change is also visible close to the surface in form of a waveform decoherence introduced by the changes in scattering properties probably due to river activity/level. We observed that the two observables, apparent velocity change (phase of the seismic signal) and waveform decoherence (waveform of the seismic signal) are not sensitive to the same physical parameters. They must have different physical origins. Apparent velocity are associated with changes in the poro-elasticity of the medium, while waveform decoherence is associated with changes in the scattering properties of the medium (structural changes). We emphasize the importance of simultaneously studying velocity variations and waveform decoherence to obtain additional information.

7.3 Supplementary material

7.3.1 Spatial smoothing

The inverse problem is under-determined with approximately 600 datasets and 2200 model parameters. To limit the number of independent parameters we introduce a spatial smoothing obtained from correlations of neighboring cells. This spatial smoothing is introduced in the covariance matrix of the model $\boldsymbol{C_m}$ via an exponential function. The elements $(i,\, j)$ of the else-wise diagonal matrix are given by:

$$C_m(i,j) = (\sigma_m \frac{\lambda_0}{\lambda})^2 \exp(-\frac{d(i,j)}{\lambda}), \tag{7.9}$$

where $d(i,j)$ is the distance between two cells i and j. The matrix is weighted by $(\sigma_m \frac{\lambda_0}{\lambda})^2$ where λ_0 is a scaling factor that was taken here equal to the cell length (20 km) and λ is the correlation length that defines the length over which the parameters are correlated. The larger we chose λ the fewer independent parameters we have. σ_m is the a priori standard deviation of the model. To select the optimal smoothing parameters λ and σ_m, we use the L-curve criterion (Hansen, 1992). This criterion corresponds to the best agreement between: 1) the stability of the model for the velocity variations and 2) the minimized difference between the model predictions $\boldsymbol{\delta v/v}$ and the data $\boldsymbol{\varepsilon}$. According to equation (7.10) the normalized residual (res) between n measured and modeled apparent velocity variations is used to quantify the agreement between model and data:

$$res = \sqrt{\frac{1}{N}\sum_{i=1}^{N}\frac{(\frac{\boldsymbol{\delta v}}{\boldsymbol{v}} - \boldsymbol{\varepsilon})^2}{(\boldsymbol{\sigma_d})^2}}. \tag{7.10}$$

In Fig. 7.15 the normalized residuals (res) are plotted as a function of maximal velocity fluctuations in the model, for different values of σ_m and λ for both frequency bands. The optimal smoothing is found for minimized values on both axes, which corresponds to a maximal bending of the curve. With the gray shadings we indicate three different smoothing regimes. Within the light gray zone, very strong velocity variations are allowed in the final model, the smoothing has not been efficient enough for these combinations of parameters. The dark gray zone on the other hand shows a too strong smoothing. The velocity variations are weak, but the agreement with the data is also weak. The optimum is found for smoothing parameter pairs that fall into the maximal curvature zone (gray). We chose $\sigma_m = 5 \times 10^{-3} km/km^2$ and λ=50km.

7.3.2 Quality tests of the inversion model

To confirm the validity of the inversion model we perform a couple of quality tests. An important point is the model resolution, which gives us information about the region of interpretability of our model. According to Tarantola and Valette (1982), the resolution matrix R is given by:

$$\boldsymbol{R} = \boldsymbol{C_m G^t}(\boldsymbol{G C_m G^t} + \boldsymbol{C_d})^{-1}\boldsymbol{G}. \tag{7.11}$$

The diagonal elements of this matrix indicate whether the apparent velocity variations of a particular cell have been recovered by the inversion result. As we introduced a smoothing in form of the model covariance matrix C_m, neighboring cells should reflect these apparent velocity variations. Hence, the j^{th} line of the matrix R indicates how well the velocity variations of the j^{th} cell have been projected on the entity of cells. The sum over the elements of the j^{th} line of the resolution matrix shows if the velocity variations in this cell have been completely recovered by the contribution of the cell ensemble. In this case the restitution index is ≈ 1. If the velocity variation could not be recovered by the inversion, the restitution index is < 1. Fig. 7.16a) shows the resolution matrix for the entire region that we used to invert our data. Please note, that the region of interest is well described with a restitution index of > 0.8 for the entire region.

In Fig. 7.16b) we represent the resolution of a particular cell j (i.e. the j^{th} line of the matrix $\boldsymbol{R}$). The chosen cell is marked with an empty circle and well situated in the zone were the model predicts the maximal velocity variations. The figure shows the spatial smoothing that has been applied (λ=50 km).

In Fig. 7.16c) we show the distribution of the standard deviation between the measured $\boldsymbol{\varepsilon}$ and modeled $\boldsymbol{\delta v/v}$ velocity variations normalized with the characteristic error of the data. They are well fitted with a Gaussian distribution (red curve), as required for the theory.

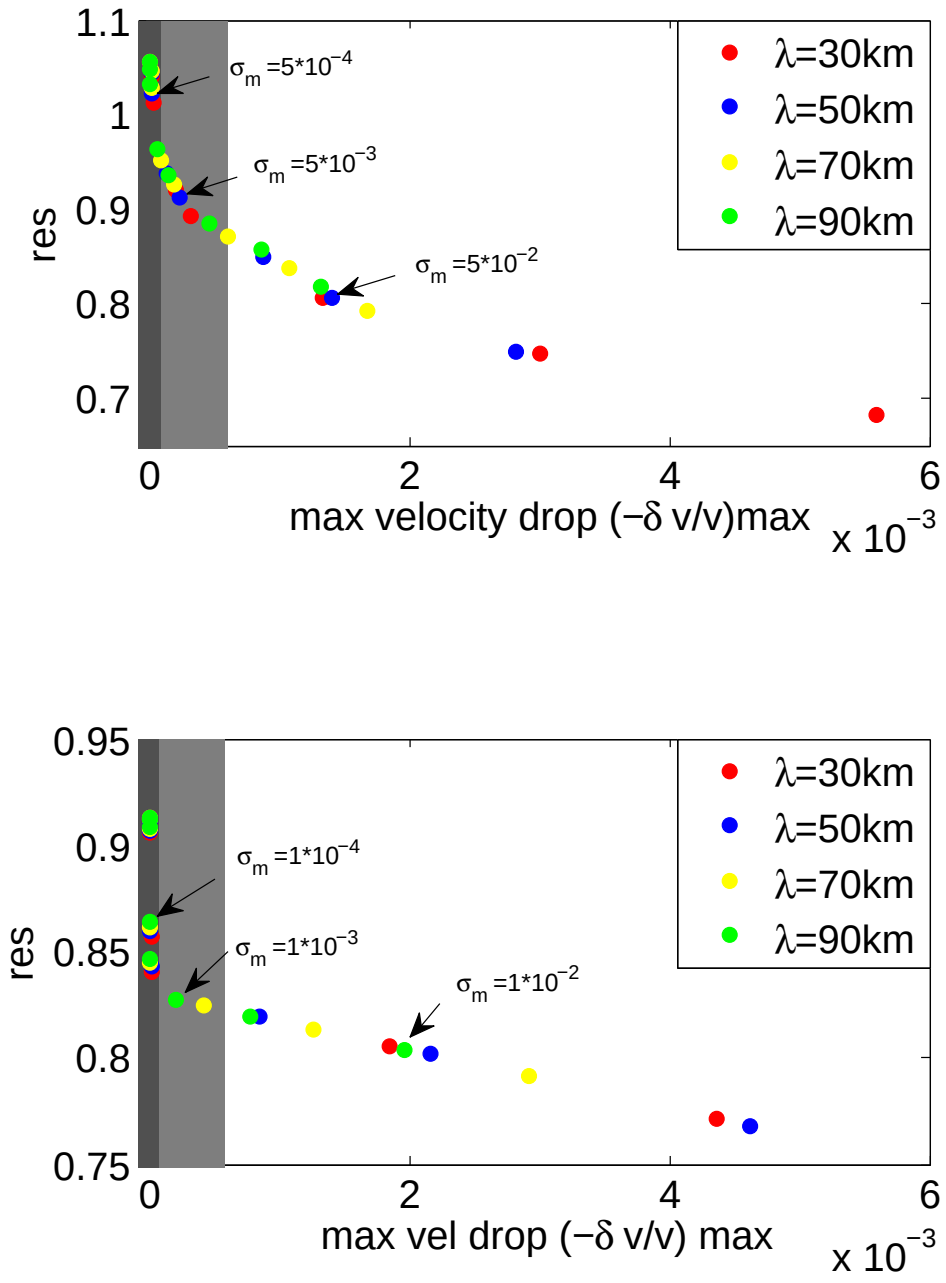

Figure 7.15: L-curve in the 1-3 s period band (a) and in the 12-20 s period band (b). The normalized residuals are plotted as a function of maximal velocity fluctuations in the model for different values of the smoothing parameters σ_m and λ. The background shadings indicate different smoothing regimes. The optimal smoothing parameters are found in the region with maximal bending of the curve (light grey).

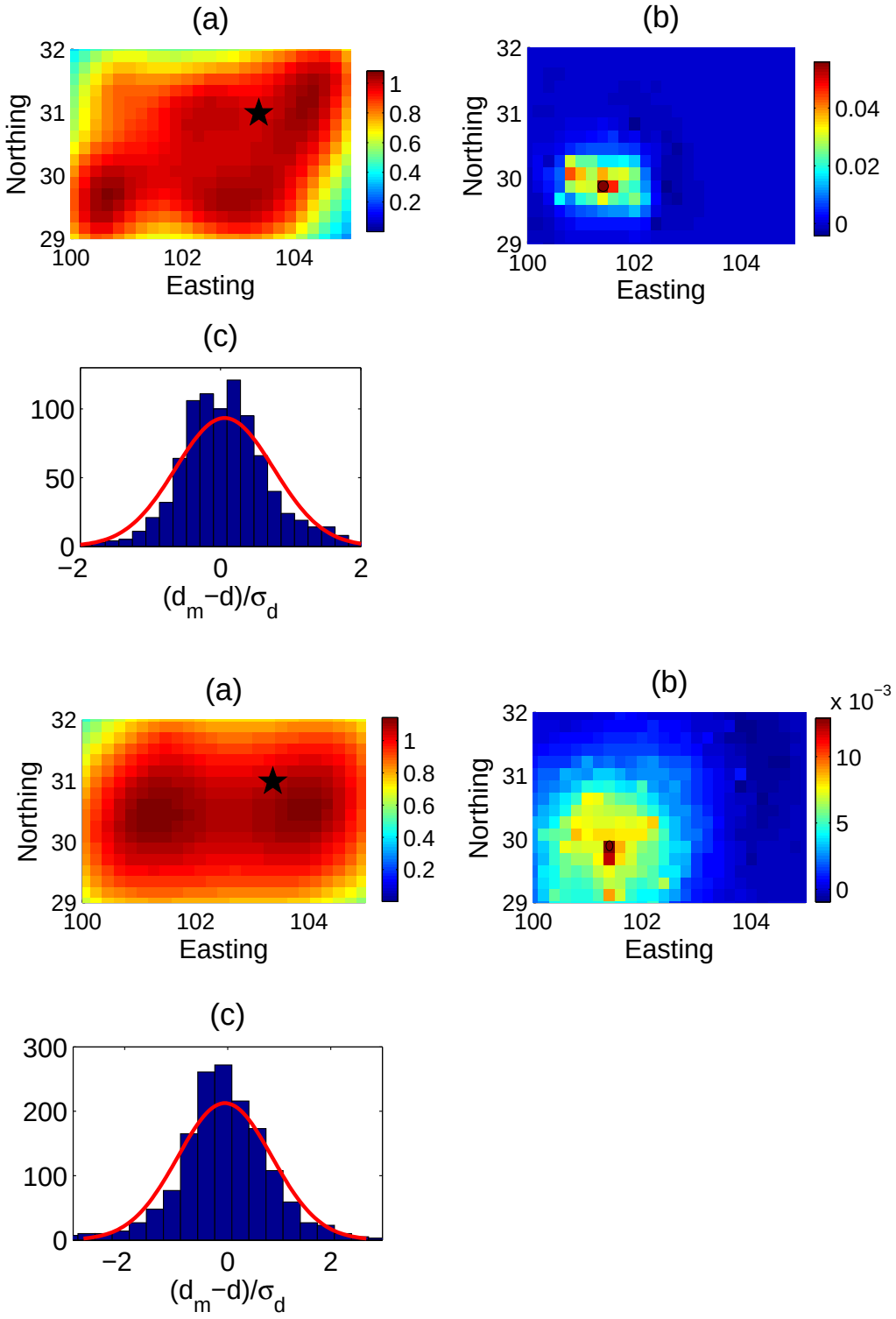

Figure 7.16: Quality tests above for the 1-3 s period band, below for the 12-20 s period band. a) Model resolution. b) Resolution for the cell indicated with an open circle. The location of the stations around is indicated with black crosses. c) Distribution of the standard deviation between the modeled and measured apparent velocity variations. The red curve corresponds to a Gaussian distribution and indicates that the residuals are well described by a normal distribution.

Chapter 8

Crack detection in concrete using a 3D inversion procedure

Contents

In an extensive laboratory experiment Eric Larose and collaborators [1] exposed four concrete blocks with and without pre-existing cracks to increased tension. The tension caused further fracturing of the blocks and led to failure in two cases. At each pressure step ultrasonic data from various sources and receivers was acquired. Student intern Angela Digulescu started to treat the data and I supervised her in implementing a 3D inversion procedure, similar to the ones used in Chapter 6 and 7. The inversion algorithm involves a 3D sensitivity kernel provided by Thomas Planès. After her internship I then continued the work to monitor the crack propagation in the different concrete blocks in the horizontal and vertical plane by inverting the decorrelation measurements. It also seems to be possible to relate the effective cross-section to the actual fissure size. A publication on this experiment is currently under preparation that is most likely intended for JASA.

[1] The experiment was performed by Eric Larose, Jean-François Chaix and G. Moreau at LMA-Marseille with the financial support of the EDF.

8.1 Context of the work

Tests made upon concrete structures aim to evaluate their structural integrity and adequacy. Intrusive methods present the disadvantage that they can raise high costs or lead to an insufficient number of tests, thereby giving misleading conclusions. An interesting approach is therefore the non-destructive testing using ultrasounds. However, classical imaging methods based on direct or singly scattered waves are limited in resolution and penetration depth because of the multiple scattering of ultrasound in concrete (Planès and Larose, 2013). In previous works, Larose et al. (2010) successfully used diffuse ultrasonic measurements and a maximum likelihood method (χ^2-test) described in section 6.4 to locate small changes ($<\lambda$) in a concrete block. The objective here is to implement the more stable (and precise) least-squares inversion scheme used in Chapters 6 and 7 to monitor the crack propagation in the concrete blocks under tension. To be able to follow the crack in all three dimensions, we use a 3D sensitivity kernel (Planès, 2013) that we implement in the inversion scheme. Besides the localization, a big challenge is to quantitatively know the size of the crack/damage in the structure. We attempt this by relating the effective cross-section that we obtain from the inversion to the size of the crack.

8.2 Experimental Setup

8.2.1 Sample preparation

Four concrete samples of size 120 mm×120 mm×600 mm were prepared several weeks before the test. The concrete formulation is given in Tab. 8.1 and is a typical formulation used in civil engineering. On each concrete block, a 1 cm deep notch was created at 300 mm at the edge of the block (Fig. 8.1) to initiate the future cracking processes. Then, three samples underwent a first fracturation process to produce an additional crack with a controlled length. For this process a three-point flexure system was used. This is a common test in mechanical engineering, where the concrete block is placed on two bearing points on each end and a force is applied to the middle of the block. The stress will be maximal at the midpoint (where the notch is located) and reduced elsewhere. Sufficient stress then causes the notch to open further. The flexure tests were stopped for different openings on the three blocks. The crack lengths and depths were then measured with a microscope (of magnification x60) and a simple ruler. The final cracks ranged from 0 mm (intact) to 23 mm, 30 mm and 50 mm (please note that the notch is not counted here).

Component	Mass (kg/m^3)
Cement CEM I 52.5 N	370
Sand 0/4 mm	774
Aggregate SR 4/14 mm	1069
Water (w/c = 0.57)	212

Table 8.1: Concrete composition used for the concrete blocks. This is a typical formulation in civil engineering.

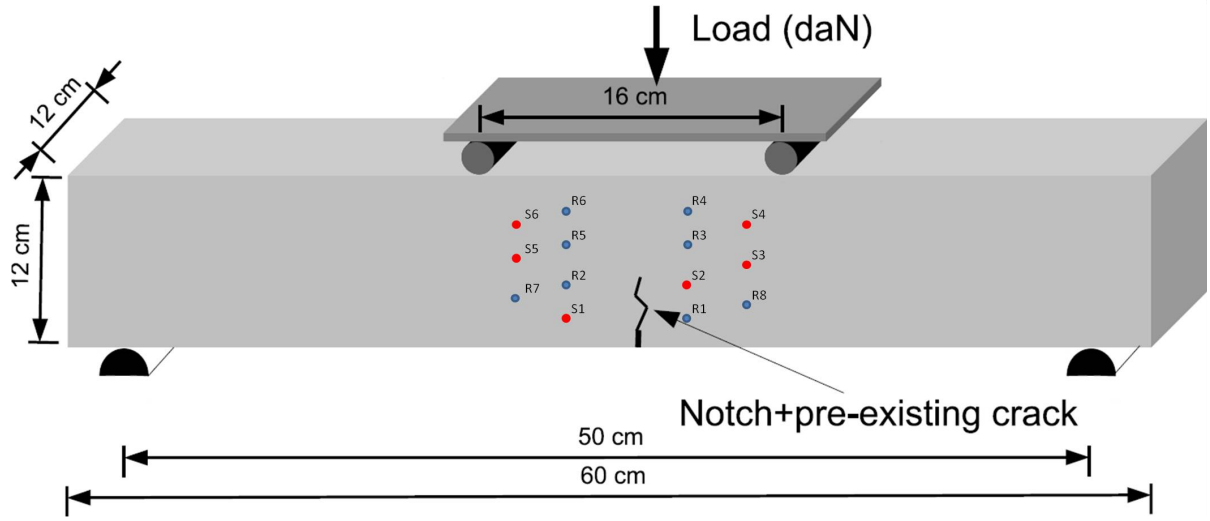

Figure 8.1: Experimental setup for the four-point flexure test and the position of the sources (red circles) and receivers (blue circles).

8.2.2 The four-point flexure test

A four-point flexure test was performed on each concrete block. In this test the force is not applied to the middle of the block only, but to an extended region (Fig. 8.1). With this test, which is also a standard test in mechanical engineering, a large part of the specimen is exposed to the stress and defects and flaws can be more easily detected. The two lower bearing points are fixed at the table and the two upper move along the vertical direction. Each bearing point is cylindrical and adapts to the specimen by small rotation movements according to the European norm for the test (NF EN 12390-5). The mechanical loading is performed by controlling step by step the vertical displacement of the two upper fulcrums. The samples are equipped with a displacement sensor to follow the opening of the crack. They are also equipped with six ultrasonic sources and eight receivers, distributed on one side of the block around the central part of the specimens were the crack is expected to be re-activated (Fig. 8.1). The load is increased from 0 daN to about 1000 daN by increments of about 100 daN, and then released. After each load the ultrasonic data is acquired. At the very end of the test, the slight increase of the crack depth is measured with the microscope (see Tab. 8.2).

Sample n°	Initial crack length	Final crack length	Crack length from σ
1	notch only	notch only	8 mm
2	23 mm	25 mm	14 mm
3	30 mm	37 mm	28 mm
4	50 mm	60 mm	40 mm

Table 8.2: Measured crack depth (with surface microscope) before and after the bending test and the crack depth as determined with the cross-section from the inversion.

8.2.3 Ultrasonic (US) data acquisition

Each source S_i is excited by a chirp $c(t)$ of frequencies ranging linearly from 500 kHz to 900 kHz and an amplitude of $\pm$ 2 V. The waveforms recorded at receivers j are noted $r_{ij}(t)$. The excitation is reproduced 200 times and records are stacked accordingly. The waveforms are simultaneously recorded on all the available receivers j and are further correlated with the source function to reconstruct the impulse response in the working frequency band:

$$h_{ij}(t) = r_{ij}(t) \times c(t). \tag{8.1}$$

In Fig. 8.2a we display an example of the impulse response, showing the main characteristic of multiply scattered waves: the direct wave is strongly attenuated, and followed by a long lasting coda whose average amplitude (the envelope) is well described by the solution of the diffusion equation:

$$\partial_t I(r,t) - D\Delta I(r,t) - 1/\tau_{abs} I(r,t) = \text{source}(t). \tag{8.2}$$

The fitting parameters are the diffusivity D = 12 $mm^2/\mu s$ and the absorption time τ_{abs} of 25 μs. As the imaging procedure does not require the absorption time, but only a rough estimate of the diffusion constant, we do not pay too much attention to a precise evaluation of these quantities. What is important is that the diffusion solution is evaluated taking into account all reflections on the sides of the sample.

The US impulse response h_{ij} represents the US fingerprint of the medium. If anything changes in the material, even far away from the source-receiver segment, the US fingerprint will potentially evolve, and cause waveform decoherence as illustrated in Fig. 8.2b.

8.3 Data Processing

The initial level of the applied force is considered to be the reference level. During the experiment, two physical phenomena may lead to a slight increase of the US velocities: the change of temperature and the change of stress (acousto-elasticity). To try to correct the waveforms from these effects, we interpolate the waveforms with various stretching

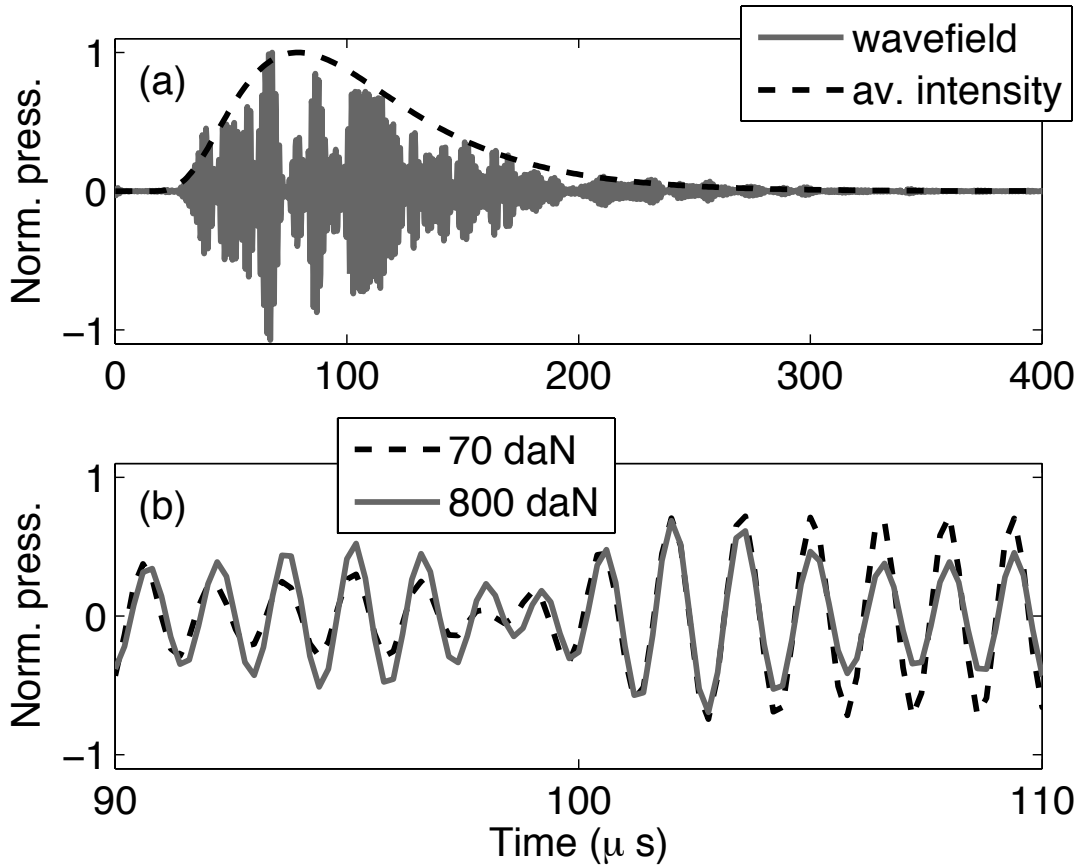

Figure 8.2: Example of ultrasonic impulse responses acquired in the concrete sample in the 500-900 kHz frequency range between source 6 and receiver 8 with the 23 mm pre-cracked sample. (a) The diffuse regime is characterized by the attenuation of the direct wave, and by the onset of the late and long-lasting ultrasonic coda. (b) Zoom into the coda. The two waveforms are acquired with fixed source and receiver but with a different mechanical load. The decorrelation is mainly due to the opening of the crack during the loading.

factors ε: $h_{ij}(t) \rightarrow h_{ij}(t(1+\varepsilon))$, and find the stretching factor that makes the current impulse response (h^k) best resemble the reference impulse response (h^{ref}). In practice, the actual relative velocity change $\varepsilon = dV/V$ is the stretching factor that maximizes the following cross-correlation coefficient:

$$CC_{ij}(\varepsilon, k, t) = \frac{\int_{t-\frac{T}{2}}^{t+\frac{T}{2}} h_{ij}^{\text{ref}}(\tau) h_{ij}^{k}(\tau(1+\varepsilon))d\tau}{\sqrt{\int_{t-\frac{T}{2}}^{t+\frac{T}{2}} h_{ij}^{\text{ref}}(\tau)^2 d\tau \int_{t-\frac{T}{2}}^{t+\frac{T}{2}} h_{ij}^{k}(\tau(1+\varepsilon))^2 d\tau}} \tag{8.3}$$

where T is the time window centered on time t in the coda. In practice, we chose a time window of duration T=50 μs centered at different times t=50, 100, 150, 200 μs. Then, for each load step k we compute the experimental decorrelation between the reference

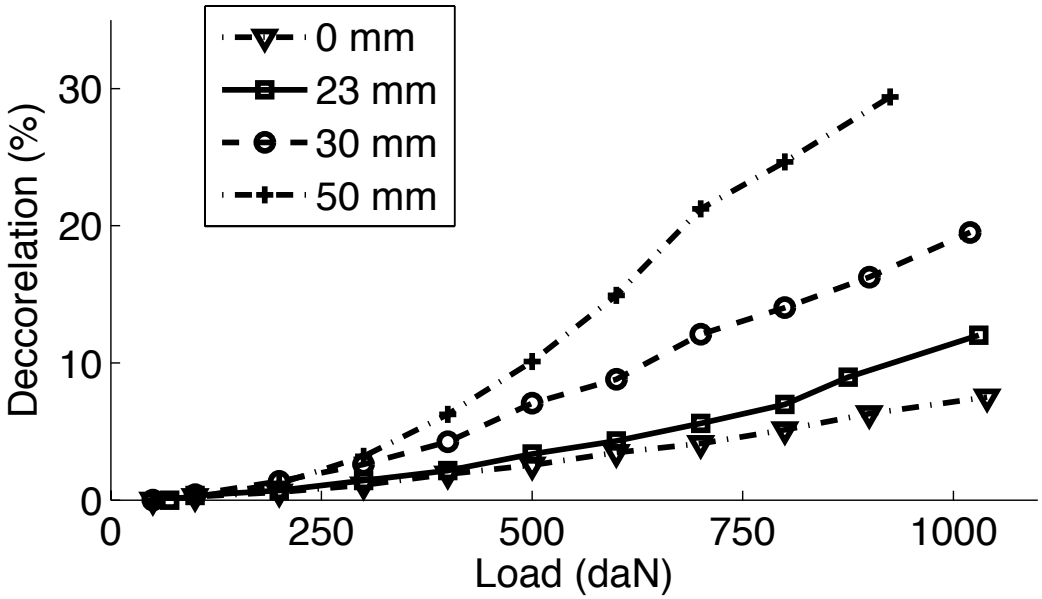

Figure 8.3: Decorrelation of ultrasonic coda waves obtained for various size of the initial crack, and for various load. The larger the pre-existing crack, the larger the decorrelation.

impulse response $h_{ij}^{\text{ref}}(t)$ and the corrected current impulse response $h_{ij}^{k}(t(1+\varepsilon_{max}))$:

$$DC_{ij}(k,t) = 1 - CC(\varepsilon_{max}, k, t). \tag{8.4}$$

This experimental decorrelation is plotted in Fig. 8.3 for each load step k and for the four specimen averaging on all source-receiver pairs. We observe an increase in decorrelation with increasing load, but also with increasing size of the pre-existing crack.

Following previous theoretical and numerical works (Rossetto et al., 2011; Planès et al., 2013), a theoretical estimation of the decorrelation can be evaluated, assuming a punctual change at position x with a cross-section σ:

$$DC_{ij}^{Th}(x,t) = \frac{c\sigma}{2} K_{ij}(x,t), \tag{8.5}$$

where c is the transport velocity of the US intensity (the shear wave speed in first approximation), and $K_{ij}(x,t)$ the sensitivity kernel. This sensitivity kernel represents the probability for a wave packet launched at the source i at time 0 and received at time t at receiver j to have passed by the location x and have interacted with the anomaly. So far, we have used a sensitivity kernel in 2D, either in the diffusion or radiative transfer approximation. Here, we use a sensitivity kernel in 3D in the diffusion approximation that takes into account the reflection conditions at the sides of the samples (Planès, 2013), assuming a perfect reflection condition.

8.4 Data Inversion

The direct problem consists in estimating the decorrelation induced by a volumetric distribution of change:

$$\boldsymbol{DC} = \frac{c\delta V}{2}\boldsymbol{K}\boldsymbol{\sigma}, \tag{8.6}$$

where $\boldsymbol{DC}$ is a vector whose component DC_i corresponds to the decorrelation measurements for each pair i. $\boldsymbol{K}$ is the matrix of the 3D sensitivity kernels whose elements K_{ij}^t for all pairs i at voxel j are evaluated at time t. $\boldsymbol{\sigma}$ is the vector whose elements σ_j are scattering cross-section density of the changes for each voxel j of the medium. δV is the volume of each voxel.
To solve the inverse problem, which consists in evaluating $\boldsymbol{\sigma}$, we use the least-squares inversion algorithm proposed by Tarantola and Valette (1982):

$$\boldsymbol{\sigma} = \boldsymbol{\sigma_0} + \boldsymbol{C_m}\boldsymbol{K^t}(\boldsymbol{G}\boldsymbol{C_m}\boldsymbol{K^t} + \boldsymbol{C_d})^{-1}(\boldsymbol{DC_i} - \boldsymbol{K^t}\boldsymbol{\sigma_0}), \tag{8.7}$$

where $\boldsymbol{\sigma_0}$ is the initial model: a zero vector in our case since we have no apriori information about the position, size and number of cracks. C_d represents the covariance matrix for the data and C_m the covariance matrix for the model. C_d contains the coherence of the data in the initial state in its diagonal. As the scattering cross-section is necessarily positive, an iterative procedure is introduced that imposes a positivity constraint (Planès, 2013; Obermann et al., 2013a). Therefore, at each iteration step, only positive values are kept and used as the new input model. In this study, we perform ten iterations.

For the inversion we consider a region of 200 mm in the x direction, centered around the crack, and 120 mm in the y and z direction. We use a grid size of 10 mm in all directions. As the problem is under-determined with 48 measurements and roughly 3500 model cells, we use the L-curve criterion by Hansen (1992) to introduce a spatial smoothing between neighboring cells. We calculated the L-curves for all different concrete samples at various loads. As the choice of the smoothing parameters can introduce slight shifts in model amplitudes, we decided to keep the same parameters for all samples and loads and chose the smoothing parameters λ=30 mm and σ_L=0.3 as the best compromise (please see Section 6.3.1 for more details on these parameters). An example of an L-curve is shown in Fig. 8.4.

An example of the inversion from the concrete block with the 50 mm pre-existing crack evaluated at 100 μs in the coda is shown in Fig. 8.5 at various loads. The first two rows show the horizontal xy-plane that containes the sources and receivers and the third and fourth row display a cross-section of the vertical xz-plane for the same loads. We observe that the location of the crack at 300 mm is well achieved in both planes. Furthermore, the cross-section (σ) increases with increasing load.

We determine the resolution of the models in the xy and xz plane following Tarantola and Valette (1982) (as in the previous chapters):

$$\boldsymbol{R} = \boldsymbol{C_m}\boldsymbol{G^t}(\boldsymbol{G}\boldsymbol{C_m}\boldsymbol{G^t} + \boldsymbol{C_d})^{-1}\boldsymbol{G}. \tag{8.8}$$

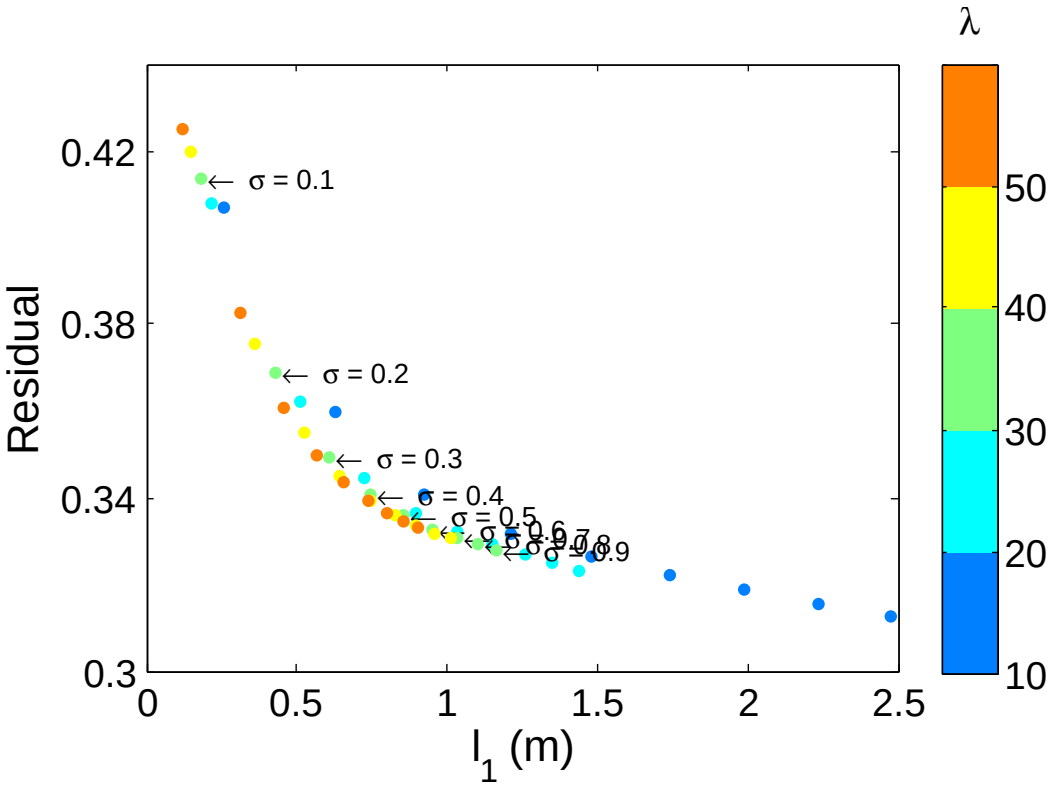

Figure 8.4: Exemplary L-curve for the sample with no pre-existing crack at 700 dN. Plotted is the residual against the norm.

The results are displayed in Fig. 8.6. We notice that we have an excellent model restitution on the horizontal plane that only degrades towards the edges. In the vertical plane we have a very good model restitution until a depth of about 50 mm only. If we wanted to go deeper, a possibility would be to study the decorrelation at much later times in the coda or at lower frequencies where D is larger.

Hence in order to determine the size of the fissure, we integrate the effective cross-sections in the well resolved volume only. The σ_{tot} values for the different concrete blocks and loads are shown in Fig. 8.7. As could have been expected from the decorrelation, we observe that the total cross-section increases with the size of the pre-existing crack. We use the horizontal cross-section of the final loading step to approximate the size of the fissure. The results are given in Table 8.2. We note that the order of magnitude of the calculated crack size corresponds to the measured crack size. Apart from the sample with notch only, the values seem to be one third smaller than the actual values.

8.5 Tests at different times in the coda

We have seen in Chapter 6 that the cross-section gives us a very rough estimate of the emitted magma volume that corresponds to the same order of magnitude of the

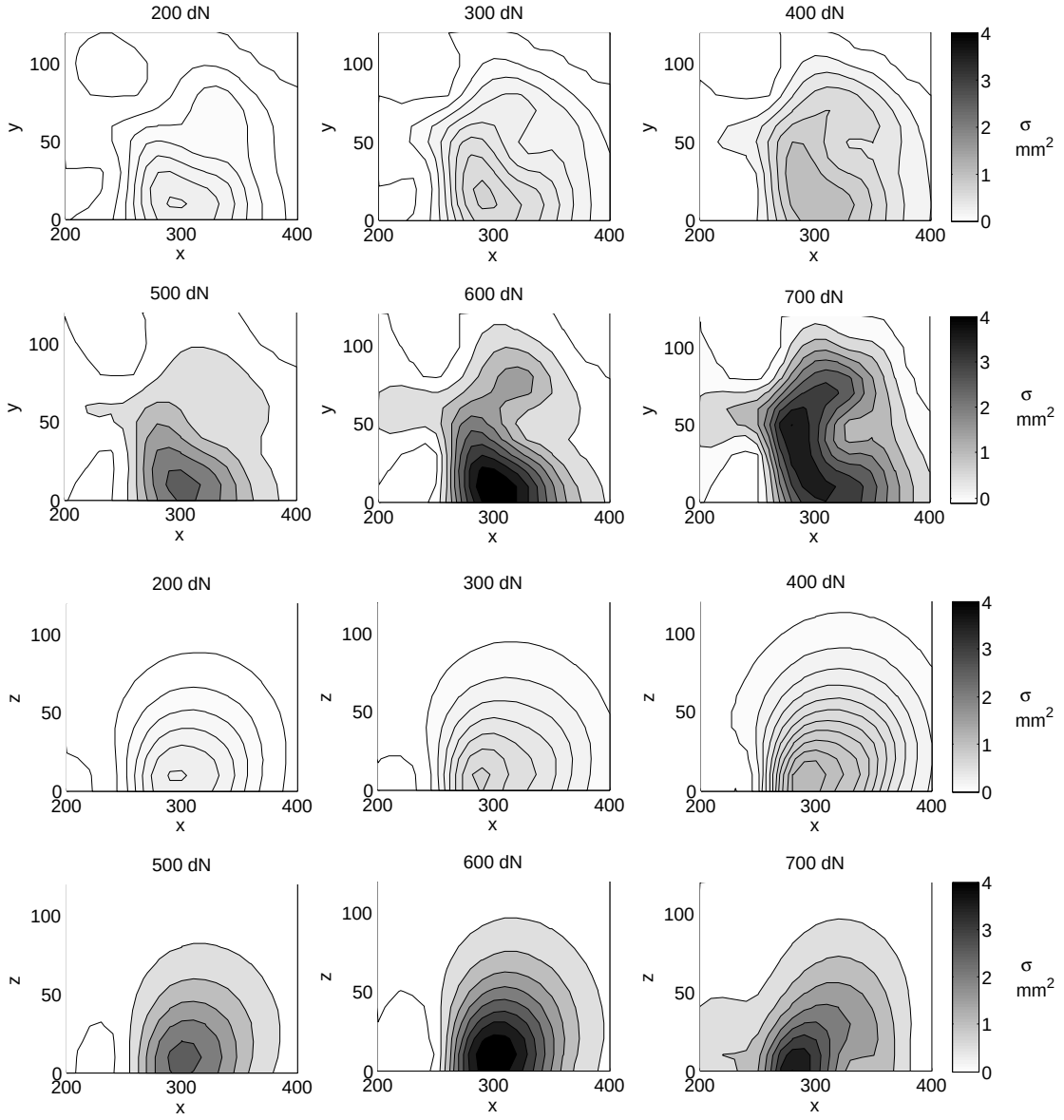

Figure 8.5: Inversion results for different loads in the xy plane and a cut in the xz plane (depth) for the concrete block with a pre-existing crack of 50 mm evaluated at 100 μs in the coda.

actual emitted magma volume. In this section we can see that on a much smaller scale with concrete we obtain from the scattering cross-section a crack length that is in the same order of magnitude as the actual measured crack. This raises the question, what precision in terms of sizing can be obtained from the cross-section with this method. I do not answer this question at this point but open the discussion with a look at Fig. 8.8 where I present the normalized σ_{tot} values at different times in the coda (50, 100, 150 and 200 μs) for all the concrete blocks. What we observe is that the σ_{tot} values vary significantly with time in the coda for the small cracks (larger σ_{tot} at later times). With

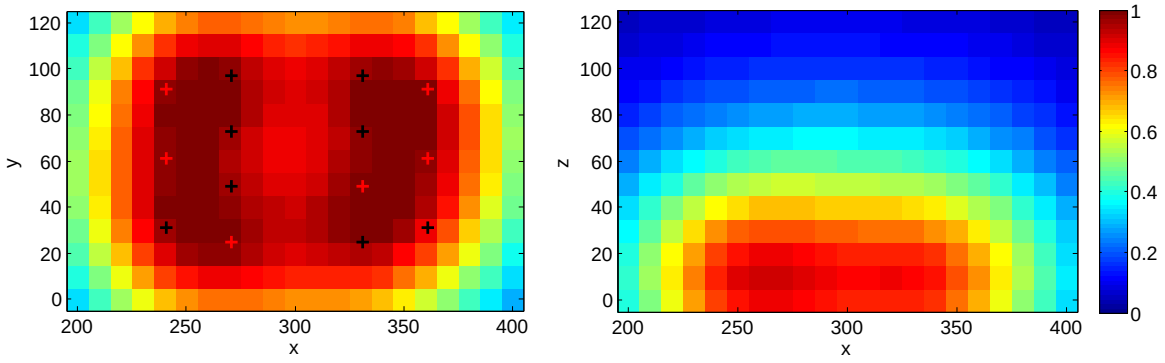

Figure 8.6: Resolution in xy and xz (depth) direction. Values close to 1 indicate an excellent model restitution.

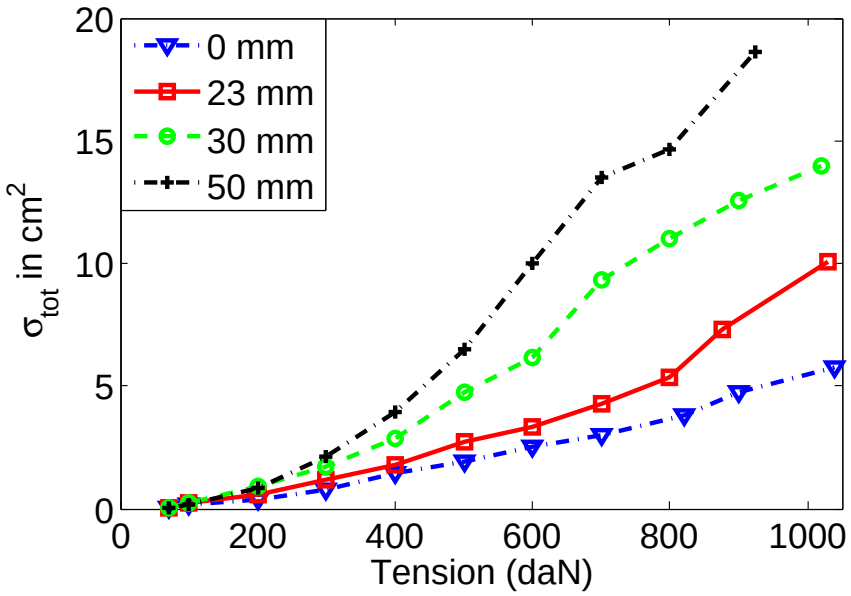

Figure 8.7: Integrated σ_{tot} values for the different concrete blocks at 100 μs in the coda.

increasing initial crack size the lapse time dependence becomes less important. For the time at 50 *mus* we could think that this effect is due to the small diffusive halo, that might not cover the entire area of integration. However, I think that the discrepancy for later lapse times is due to the lower signal to noise ratio at these times that introduces an additional decorrelation, which is significant compared to the decorrelation from small initial cracks, but small compared to the decorrelation from larger initial cracks. It seems hence important to think of a procedure to correct for this effect.

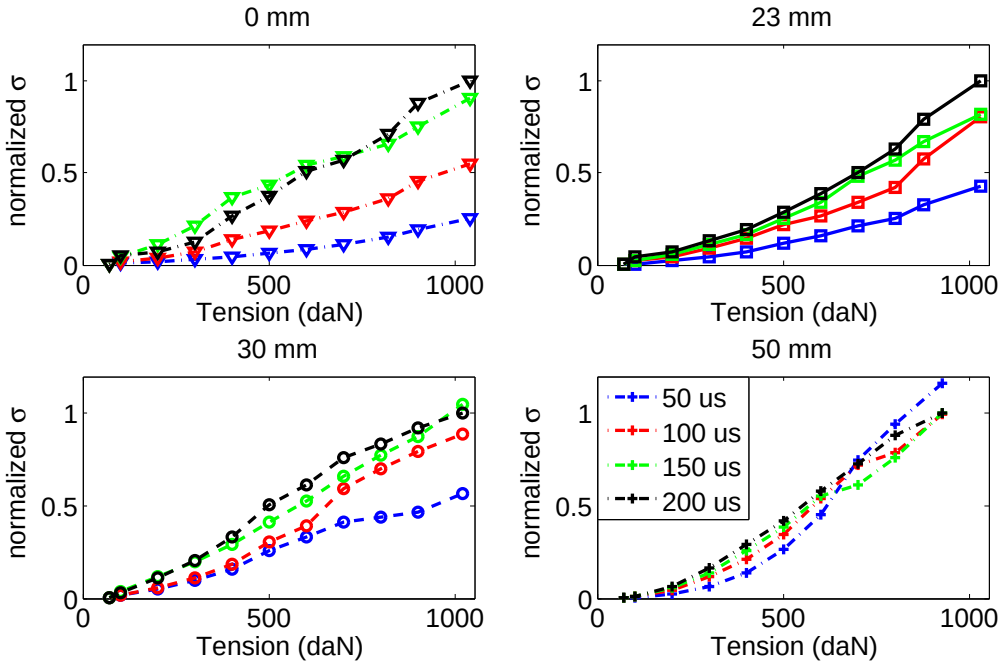

Figure 8.8: σ_{tot} values for the different concrete blocks at various times in the coda (50, 100, 150 and 200 μs). The values have been normalized by the maximum value at 200 μs.

8.6 Conclusion

We monitored the crack propagation in four concrete blocks with different initial crack lengths under increased tension. We implemented a 3D sensitivity kernel in the inversion procedure and were able to successfully locate the crack in the horizontal and vertical plane. We also observed that the decorrelation, as well as the cross-section determined with the inversion, are proportional to the actual crack size for all four concrete blocks and at all loading steps.
At the moment, the sizing of the crack should still be examined with caution, as the level of additional decorrelation due to noise artifacts at different coda lapse times needs a closer investigation.

Conclusions and perspectives

The results that I present in my dissertation deal with different aspects of monitoring the elastic properties of the crust. For this purpose, I use both numerical analysis and applications with ambient seismic noise.

After a general introduction of the methods and concepts behind wave propagation in complex media and coda wave interferometry, Part II of my thesis deals with a more theoretical analysis of the properties of coda waves. In a first study, with a temporary field experiment, we demonstrate that the correlation function of the spatial phase derivative offers a promising opportunity to measure directly the scattering mean free path of a given heterogeneous medium. An unbiased estimate of the scattering mean free path is can improve the localization of changes in multiply scattering media, where a sensitivity kernel based on the diffusion theory is used (Part III of my dissertation). In a second numerical study in 2D heterogeneous media, we analyzed the depth sensitivity of coda waves to velocity perturbations at depth. We could see that the depth sensitivity of coda waves is related to a combination of bulk- and surface-wave sensitivity. We then studied the time dependence of the apparent relative velocity change in the coda and showed that this property can be used to discriminate a change that occurs at the surface from a change that occurs at depth. Furthermore, the partition ratio between bulk- and surface-wave sensitivity versus time in the coda in different media shows a universal behavior when normalized by the scattering mean free time.
Recent 3D simulations in heterogeneous media confirm that we can quantitatively discriminate a change at the surface from a change at depth by studying the time evolution of the relative velocity change with time in the coda.

In Part III we present a least-squares inversion method that is used to obtain information about the spatial distribution of changes in the medium from scattered waves. We apply this technique and further develop it with three different data sets. Besides studying relative velocity changes, we introduce the waveform decoherence as a monitoring quantity in the seismological context.
In the first study, we used ambient seismic noise correlations from Piton de La Fournaise. We could successfully locate pre-and co-eruptive changes associated with two eruptions on different sides of the volcanic cone in 2010. These results point out the possibility to locate forthcoming eruptions.

In a second study, we used ambient seismic noise correlations from the Mw7.9 2008 Wenchuan earthquake. We were able to image structural and mechanical changes associated with this earthquake and with seasonal hydrological changes. Instead of averaging the velocity changes and the decoherence over a long part of the coda, we analyzed the changes in short time windows and inverted the measurements jointly. As the sensitivity kernels are always evaluated at a precise time, this procedure yields the advantage of better attributing the diffusion halo to the measurements at different coda lapse-times. Additionally, by jointly inverting the measurements at different lapse times, we have an increased amount of data to constraint the inversion. In this study we can clearly see that the velocity changes are related to mechanical changes in the medium, while waveform decoherence is caused by structural changes of the medium. We hence emphasize the importance of studying both observables to obtain complementary information.
In an additional study, we tested 3D localisations with data from an ultrasonic experiment on concrete. The concrete samples were exposed to increased tension and we could successfully monitor the crack propagation with waveform decoherence. We integrate the scattering cross-section over the volume of interest and found that the total scattering cross-section is a good indicator for the crack size and evolution.

As future perspectives of the work presented, we would like to point out that the localization method is currently being applied to a dataset from a geothermal injection project in Basel (Gregor Hillers), as well as to a dataset from the Colima volcano in Mexico (Philippe Lesage). With the increasing installation of dense seismic networks, many geological or tectonic active areas are (or will be) suitable to this kind of processing in the near future. It is desirable to increase the data quality ("signal" to noise ratio) in order to increase the temporal resolution of the monitoring.
Further work should also be done on the localization method itself. The influence of the different parameters of the inversion (smoothing parameters, scattering mean free path, length of the time window in the coda, covariance matrix) should be systematically evaluated to quantify their influence on the model. The tests that I did during my dissertation suggest that there is not much of an influence on the spatial localization, but that there is an ambiguity concerning the absolute value of the velocity variation or cross-section in the final model that depends on these parameters. Solving this issue is of particular interest if we wish to infer the exact size of the change (volume of magma, precise size of the crack, etc) from the inversion of the decoherence measurements.
In order to equip new regions with seismic stations for similar studies, it could also be of interest to do a systematic evaluation of how many stations/ station density we need to obtain a stable inversion result.
Apart from the last study on concrete, we have only studied the horizontal distribution of changes. With the assumption that we mainly deal with surface waves, our only way to access the depth dimension was by using different frequency bands. In such cases, the 3D kernel might offer a possibility to obtain more information about the depth of the changes.

Yet, another more challenging issue concerns the sensitivity kernels themselves. The intensity propagator that we use in the sensitivity kernels in 2D as well as in 3D uses the solution of the radiative transfer (or the diffusion) equation in the acoustic approximation. This means that only one mode of propagation is taken into account. As we have seen in Obermann et al. (2013b), the surface/bulk wave conversions play an important role. It could be interesting to build a kernel based on intensity propagators that take into account S, P and surface wave modes and their conversions.

We are currently working with simulations in 3D to address some of these issues.

Bibliography

Abubakirov, I.R.. and Gusev, A.A.. (1990). Estimation of scattering properties of lithosphere of Kamchatka based on Monte-Carlo simulation of record envelope of a near earthquake. *Phys. Earth planet. Int.*, 64(1):52–67.

Aki, K. (1957). Space and time spectra of stationary stochastic waves, with special reference to microtremors. *Bull. Earthq. Res. Inst.*, 35:415–456.

Aki, K. (1969). Analysis of seismic coda of local earthquake as scattered waves. *J. Geophys. Res*, 74(2):615–631.

Aki, K. and Chouet, B. (1975). Origin of coda waves: source, attenuation and scattering effects. *J. Geophys. Res*, 80(23):3322–3342.

Aki, K. and Ferrazzini, V. (2000). Seismic monitoring and modeling of an active volcano for prediction. *J. Geophys. Res.*, 105(B7):16617–16640.

Anache-Ménier, D., van Tiggelen, B.A.., and Margerin, L. (2009). Phase statistics of seismic coda waves. *Phys. Rev. Lett.*, 102(248501).

Anderson, P.W.. (1958). Absence of diffusion in certain random lattices. *Phys. Rev. Lett.*, 100(1492).

Arroucau, P., Rawlinson, N., and Sambridge, M. (2010). New insight into Cainozoic sedimentary basins and Palaeozoic suture zones in southeast Australia from ambient noise surface wave tomography. *Geophys. Res. Lett.*, 37(L07303).

Bachelèry, P. (1981). *Le Piton de la Fournaise (Ile de la Rúnion). Etude volcanologique, structurale et pétrologique*. PhD thesis, Université de Clermont-Ferrand.

Backus, M., Burg, J., Baldwin, D., and Bryan, E. (1964). Wide band extraction of mantle p waves from ambient noise. *Geophysics*, 29:672–692.

Barabanenkov, Y. N. and Ozrin, V. (1991). Asymptotic solution of the bethe-salpeter equation and the green-kubo formula for the diffusion constant for wave propagation in random media. *Physics Letters A*, 154(1):38–42.

Barabanenkov, Yu.N.. and Orzin, V.D.. (1995). Diffusion asymptotics of the Bethe-Salpeter equation for electromagnetic waves in discrete random media. *Phys. Lett. A.*, 206:116–122.

Battaglia, J., Ferrazzini, V., Staudacher, T., Aki, K., and Cheminée, J.L.. (2005). Pre-eruptive migration of earthquakes at the Piton de la Fournaise volcano (Réunion Island). *Geophys. J. Int.*, 161:549–558.

Bensen, G.D.., Ritzwoller, M.H.., and Shapiro, N.M.. (2008). Broadband ambient noise surface wave tomography across the United States. *J. Geophys. Res.*, 113(B5):1239–1260.

Bonnefoy-Claudet, S., Cotton, F., and Bard, P. (2006). The nature of noise wavefield and its applications for site effects studies: A literature review. *Earth-Science Reviews*, 79(3–4):205–227.

Boué, P., Poli, P., Campillo, M., Pedersen, H., Briad, X., and Roux, P. (2013). Teleseismic correlations of ambient seismic noise for deep global imaging of the Earth. *Geophys. J. Int.*, 194(2):844–848.

Bourseiller, P. and Durieux, J. (2001). *Des volcans et des hommes*. Editions La Martinière.

Brenguier, F., Campillo, M., Hadziioannou, C., Shapiro, N.M.., Nadeau, R.M.., and Larose, E. (2008a). Postseismic relaxation along the San Andreas Fault at Parkfield from continuous seismological observations. *Science*, 321:1478–1481.

Brenguier, F., Clarke, D., Aoki, Y., Shapiro, N.M.., Campillo, M., and Ferrazzini, V. (2011). Monitoring volcanoes using seismic noise correlations. *Comptes Rend. Geosci.*, 343:633–638.

Brenguier, F., Kowalski, P., Staudacher, T., Ferrazzini, V., Lauret, F., Boissier, P., Catherine, P., Lemarchand, A., Pequegnat, C., Meric, O., Pardo, C., Peltier, A., Tait, S., Shapiro, N.M.., Campillo, M., and Di Muro, A. (2012). First results from the UnderVolc high resolution seismic and GPS network deployed on Piton de la Fournaise volcano. *Seismo. Res. Lett.*, 81(1).

Brenguier, F., Shapiro, N.M.., Campillo, M., Ferrazzini, V., Duputel, Z., Coutant, O., and Nercessian, A. (2008b). Towards forecasting volcanic eruptions using seismic noise. *Nature Geoscience*, 1:126–130.

Brenguier, F., Shapiro, N.M.., Campillo, M., Nercessian, A., and Ferrazzini, V. (2007). 3-D surface wave tomography of the Piton de la Fournaise volcano using seismic noise correlations. *Geophys. Res. Lett.*, 34(L02305).

Bromirski, P.D.. and Duennebier, F.K.. (2002). The near-coastal microseism spectrum: Spatial and temporal wave climate relationships. *J. Geophys. Res.*, 107(B8).

Burchfiel, B.C.., Royden, L.H.., van der Hilst, R.D.., Chen, Z., King, R.W.., Li, C., Lu, J., Yao, H., and Kirby, E. (2008). A geological and geophysical context for the Wenchuan earthquake of 12 May 2008, Sichuan, People's Republic of China. *GSA Today*, 18(7).

Campillo, M. and Paul, A. (2003). Long-range correlations in the diffuse seismic coda. *Science*, 299:547–549.

Campillo, M., Sato, H., Shapiro, N.M.., and van der Hilst, R.B.. (2011). New developments on imaging and monitoring with seismic noise. *Comptes Rendus Géosciences*, 343(8–9):487–495.

Carcione, J.M.. and Tinivella, U. (2001). The seismic response to overpressure: a modelling study based on laboratory, well and seismic data. *Geophysical Prospecting*, 49:523–539.

Carcolé, E. and Sato, H. (2010). Spatial distribution of scattering loss and intrinsic absorption of short-period S-waves in the lithosphere of Japan on the basis of the Multiple Lapse Time Window Analysis of Hi-net data. *J. Geophys. Res.*, 180(1):268–290.

Cessaro, R.K.. (1994). Sources of primary and secondary microseisms. *Bull. Seismol. Soc. Am.*, 84:142–148.

Chen, J.H.., Froment, B., Liu, Q.Y.., and Campillo, M. (2010). Distribution of seismic wave speed changes associated with the 12 May 2008 Mw 7.9 Wenchuan earthquake. *Geophys. Res. Lett.*, 37(L18302):1–4.

Chen, J.H.., Liu, Q.Y.., Li, S.C.., Guo, B., Wang, J., and Qi, S.H.. (2009). Seismotectonic study by relocation of the Wenchuan M(S)8.0 earthquake sequence. *Chinese Journal of Geophysics-Chinese Edition*, 52(2):390–397.

Chen, Z., Burchfield, B.C.., Liu, Y., King, R.W.., Royden, L.H.., Tang, W., Wang, E., Zhao, J., and Zhang, X. (2000). Global Positioning System measurements from eastern Tibet and their implications for India/Eurasia intercontinental deformation. *J. Geophys. Res.*, 105(B7):16215–16227.

Chevrot, S., Sylvander, M., Benahmed, S., Ponsolles, C., Lefvre, J.M.., and Paradis, D. (2007). Source locations of secondary microseisms in western Europe: Evidence for both coastal and pelagic sources. *J. Geophys. Res*, 112(B11301).

Chouet, B. (1996). Long-period volcano seismicity: Its source and use in eruption forecasting. *Nature*, 380:309–316.

Chouet, B. (2003). Volcano seismology. *Pure Appl. Geophys.*, 160:739–788.

Clarke, D., Zaccarelli, L., Shapiro, N.M.., and Brenguier, F. (2011). Assessment of resolution and accuracy of the Moving Window Cross Spectral technique for monitoring crustal temporal variations using ambient seismic noise. *Geophys. J. Int.*, 186:867–882.

Courtillot, V., Besse, J., Vandamme, D., Montigny, R., Jaeger, J., and Cappetta, H. (1986). Deccan flood basalts at the Cretaceous/Tertiary boundary? *Earth Planet. Sci. Lett.*, 80:361–374.

Cowan, M.L.., Jones, I.P.., Page, J.H.., and Weitz, D.A.. (2002). Diffusing acoustic wave spectroscopy. *Phys. Rev. E.*, 65:1–11.

De Barros, L., Lokmer, I., Bean, C.J.., O'Brien, G.S.., Saccorotti, G., Metaxian, J.P.., Zuccarello, L., and Patane, D. (2011). Source mechanism of long-period events recorded by a high-density seismic network during the 2008 eruption on Mount Etna. *J. Geophys. Res.*, 116(B01304).

Del Pezzo, E. and Bianco, F. (2010). Two-layer earth model corrections to the MLTWA estimates of intrinsic-and scattering-attenuation obtained in a uniform half-space. *Geophys. J. Int.*, 182(2):949–955.

Del Pezzo, E., Bianco, F., and Saccorotti, G. (2001). Separation of intrinsic and scattering Q for volcanic tremor: an application to Etna and Masaya volcanoes. *Geophys. Res. Lett.*, 28:3083–3086.

Deniel, C., Kieffer, G., and Lecoindre, J. (1992). Th^{230}, U^{238} and C^{14} age determinations from Piton des Neiges volcano, Réunion a revised chronology for the differentiated series. *J. Volcanol. Geotherm. Res.*, 51:253–267.

Densmore, A.L.., Ellis, M.A.., Li, Y., Zhou, R., Hancock, G.S.., and Richardson, N. (2007). Active tectonics of the Beichuan and Pengguan faults at the eastern margin of the Tibetan Plateau, Tectonics. *Tectonics*, 26(4):253–267.

Derode, A., Larose, E., Campillo, M., and Fink, M. (2003a). How to estimate the Green's function of a heterogeneous medium between two passive sensors? Application to acoustic waves. *Applied Physics Letters*, 83(15):3054–3056.

Derode, A., Larose, E., Tanter, M., de Rosny, J., Tourin, A., Campillo, M., and Fink, M. (2003b). Recovering the Green's function from field-field correlations in an open scattering medium. *The Journal of the Acoustical Society of America*, 113(6):2973–2976.

Derode, A., Tourin, A., and Fink, M. (2001). Random multiple scattering of ultrasound. I. Coherent and ballistic waves. *Phys. Rev. E*, 64(3):036605.

Duncan, R.A.. (1990). The volcanic record of the Réunion hotspot. *Proceedings of the Ocean Drilling Program, Scientific Results*, 115:1–10.

Duputel, Z., Ferrazzini, V., Brenguier, F., Shapiro, N.M.., Campillo, M., and Nercessian, A. (2009). Real time monitoring of relative velocity changes using ambient seismic noise at the Piton de la Fournaise volcano (La Réunion) from January 2006 to June 2007. *J. Volcanol.Geotherm. Res.*, 184(1):164–173.

Dvorkin, J., Mavko, G., and Nur, A. (1999). Overpressure detection from compressional- and shear-wave data. *Geophys. Res. Lett.*, 26(22):3417–3420.

Ekström, G., Abers, G.A.., and Webb, S.C.. (2009). Determination of surface-wave phase velocities across USArray from noise and Aki's spectral formulation. *Geophys. Res. Lett.*, 36(L18301).

Famin, V., Welsch, B., Okumura, S., P., B., and Nakashima, S. (2009). Three differentiation stages of a single magma at Piton de la Fournaise (Reunion hotspot). *G-Cubed*, 10(1).

Fehler, M., Roberts, P., and Fairbanks, T. (1988). A temporal change in coda wave attenuation observed during an eruption of Mount St. Helens. *J. Geophys. Res.*, 93.

Fink, M. (1992). Time reversal of ultrasonic fields, Part I: Basic principles. *IEEE Transactions on Ultrasonics, Ferroelectrics, and Frequency Control*, 39(5):555–566.

Frankel, A. and Clayton, R.W.. (1986). Finite difference simulations of seismic scattering: Implications for the propagation of short-period seismic waves in the crust and models of crustal heterogeneity. *Journal of Geophysical Research*, 91:6465–6489.

Friedrich, A., Kruger, F., and Klinge, K. (1998). Ocean-generated microseismic noise located with the Grafenberg array. *J. Seismol*, 2:47–64.

Froment, B. (2011). *Utilisation du bruit sismique ambiant dans le suivi temporel de structures géologiques*. PhD thesis, Université de Grenoble.

Froment, B., Campillo, M., Chen, J.H.., and Liu, Q.Y.. (2013). Deformation at depth associated with the May 12, 2008 Mw 7.9 Wenchuan earthquake from seismic ambient noise monitoring. *Geophys. Res. Lett.*, 40:78–82.

Froment, B., Campillo, M., Roux, P., Gouédard, P., Verdel, A., and Weaver, R.L.. (2010). Estimation of the effect of nonisotropically distributed energy on the apparent arrival time in correlations. *Geophysics*, 75(5).

Fu, B., Shi, P., Guo, H., Okuyama, S., Ninomiya, Y., and Wright, S. (2011). Surface deformation related to the 2008 Wenchuan earthquake, and mountain building of the Longmen Shan, eastern Tibetan Plateau. *Journal of Asian Earth Sciences*, 40:805–824.

Gerst, A. and Savage, M.K.. (2004). Seismic anisotropy beneath Ruapehu Volcano: A possible eruption forecasting tool. *Science*, 306(1):543–547.

Gerstoft, P., Fehler, M.C.., and Sabra, K.G.. (2006). When Katrina hit California. *Geophys. Res. Lett.*, 33(L1730).

Gerstoft, P., Shearer, P.M.., Harmon, N., and Zhang, J. (2008). Global P, PP, and PKP wave microseisms observed from distant storms. *Geophys. Res. Lett.*, 35(L23306).

Ghysels, A. (2005). *Propagation des ondes sismiques: Analyse de la phase aléatoire*. PhD thesis, Universitde Grenoble.

Gillot, P. and Nativel, P. (1989). Eruptive history of the Piton de la Fournaise volcano, Réunion island, Indian Ocean. *Journal of volcanology and geothermal research*, 36:53–65.

Godard, V., Pik, R., Lave, J., Cattin, R., Tibari, B., de Sigoyer, J., Pubellier, M., and Zhu, J. (2009). Late Cenozoic evolution of the central LongmenShan, eastern Tibet: Insight from (U-Th)/Hethermochronometry. *Tectonics*, 28(TC5009):1–17.

Goodman, J.W.. (1985). *Statistical optics*. Wiley series in pure and applied optics.

Got, J.L.., Monteiller, V., Monteux, J., Hassani, R., and Okubo, P. (2008). Deformation and rupture of the oceanic crust may control growth of Hawaiian volcanoes. *Nature*, 451:453–456.

Gouédard, P. (2008). *Techniques de corrélations: aspects méthodologiques et applications á la sub-surface*. PhD thesis, Universitde Grenoble.

Grasso, J.R.. and Zaliapin, I. (2004). Predictability of volcanic eruption: Lessons from basaltic volcanoes. *Geophys. Res. Lett.*, 31(L05602).

Grêt, A., Snieder, R., Aster, R.C.., and Kyle, P.R.. (2005). Monitoring rapid temporal change in a volcano with coda wave interferometry. *Geophys. Res. Lett.*, 32(6):L06304.

Gudmundsson, O., Khan, A., and Voss, P. (2007). Rayleigh-wave group-velocity of the Icelandic crust from correlation of ambient seismic noise. *Geophys. Res. Lett.*, 34(14).

Gutenberg, B. (1936). On microseisms. *Bull. Seismol. Soc. Am.*, 26(2).

Hadziioannou, C. (2011). *Ondes sismiques en milieu complexe: Mesure des variations temporelles des vitesses*. PhD thesis, Université de Grenoble.

Hadziioannou, C., Larose, E., Coutant, O., Roux, P., and Campillo, M. (2009). Stability of monitoring weak changes in multiply scattering media with ambient noise correlation: Laboratory experiments. *J. Acoust. Soc. Am.*, 125(6):3688–3695.

Haney, M.M., van Wijk, K., Preston, L.A.., and Aldridge, D.F.. (2009). Observation and modeling of source effects in coda wave interferometry at Pavlof volcano. *The Leading Edge*, 28:554–560.

Hansen, P.C.. (1992). Analysis of discrete ill-posed problems by means of the L-curve. *SIAM Rev.*, 34(4):561–580.

Hennino, R., Tregoures, N., Shapiro, N.M.., Margerin, L., Campillo, M., van Tiggelen, B.A.., and Weaver, R.L.. (2001). Observation of equipartition of seismic waves. *Phys. Rev. Lett.*, 86(15):3447–3450.

Herraiz, M. and Espinoza, A.F.. (1997). Coda waves: A review. *Pure Appl. Geophys.*, 125(4):499–577.

Hibert, C., Mangeney, A., Grandjean, G., and Shapiro, N.M.. (2011). Slopes instabilities in the Dolomieu crater, la Réunion island: From the seismic signal to the rockfalls characteristics. *J. Geophys. Res.*, 116(F04032):1–18.

Holliger, K. and Levander, A.R.. (1992). A stochastic view of lower crustal fabric based on evidence from the Ivrea zone. *Geophys. Res. Lett.*, 19(11):1153–1156.

Hoshiba, M. (1993). Separation of scattering attenuation and intrinsic absorption in japan using the multiple lapse time window analysis of full seismogram envelope. *J. Geophys. Res.*, 98:809–824.

Hoshiba, M. (1997). Seismic coda wave envelope in depth-dependent S wave velocity structure. *Phys. Earth Planet. Inter.*, 104:15–22.

Hubbard, J. and Shaw, J.H.. (2009). Uplift of the Longmen Shan and Tibetan plateau and the 2008 Wenchuan (M=7.9) earthquake. *Nature*, 458(7235):194–197.

Iyer, H.M.. and Healy, J.H.. (1972). Evidence for the existence of locally generated body waves in the short!period noise at the large aperture seismic array. *Bull. Seismol. Soc. Am.*, 62:13–29.

Ji, C. and Hayes, G. (2008). Preliminary result of the May 12, 2008 Mw7.9 Eastern Sichuan, China earthquake. *http://earthquake.usgs.gov/eqcenter/eqinthenews /2008/us2008ryan/.*

Jin, A. and Aki, K. (1988). Spatial and temporal correlation between coda Q and seismicity in China. *Bull. Seism. Soc. Am.*, 78:741–769.

Kang, T.S.. and Shin, J.S.. (2006). Surface-wave tomography from ambient seismic noise of accelerograph networks in southern Korea. *Geophys. Res. Lett.*, 33(L17303).

Karabulut, H. and Bouchon, H. (2007). Spatial variability and non-linearity of strong ground motion near a fault. *Geophys. J. Int..*, 170:262–274.

Kaveh, M. (1991). *Analogies in Optics and Micro-Electronics.* Kluwer Academic.

Kerr, R.A.. and Stone, R. (2009). A human trigger for the great quake of Sichuan? *Science*, 323:322.

King, R.W.., Shen, F., Burchfiel, B.C.., Royden, L.H.., Wang, E., Chen, Z., Liu, Y., Zhang, X.Y.., Zhao, J.X.., and Li, Y. (1997). Geodetic measurements of crustal motion in southwest China. *Geology*, 25:179–182.

Komatitsch, D. and Vilotte, J.P.. (1998). The spectral element method: An efficient tool to simulate the seismic response of 2D and 3D geological structures. *Bulletin of the Seismological Society of America*, 88(2):368–392.

Landès, M. (2009). *Utilisation des corrélations du bruit en sismologie: tomographie passive et étude de distributions de sources de bruit*. PhD thesis, Institut de Physique du Globe de Paris.

Landès, M., Hubans, F., Shapiro, N.M.., Paul, A., and Campillo, M. (2010). Origin of deep ocean microseisms by using teleseismic body waves. *Geophys. J. Res.*, 115(B05302):1–14.

Larose, E., Campillo, M., Khan, A., Nakamura, Y., et al. (2005a). Lunar subsurface investigated from correlation of seismic noise. *Geophys. Res. Lett.*, 32.

Larose, E., Derode, A., Campillo, M., and Fink, M. (2004a). Imaging from one-bit correlations of wide-band diffuse wavefields. *J. Appl. Phys.*, 95(12):8393–8399.

Larose, E., Derode, A., Clorennec, D., Margerin, L., and Campillo, M. (2005b). Passive retrieval of rayleigh waves in disordered elastic media. *Phys. Rev. E*, 72(4):046607.

Larose, E., Margerin, L., van Tiggelen, B.A.., and Campillo, M. (2004b). Weak Localization of seismic waves. *Phys. Rev. Lett.*, 93(4):1–4.

Larose, E., Planès, T., Rossetto, V., and Margerin, L. (2010). Locating a small change in a multiple scattering environment. *Appl. Phys. Lett.*, 96(204101):1–3.

Li, H.Y.., Su, W., Wang, C.Y.., and Huang, Z.X.. (2009). Ambient noise Rayleigh wave tomography in western Sichuan and eastern Tibet. *Earth Planet. Sci. Lett.*, 282(1-4):201–211.

Lin, F., Ritzwoller, M.H.., Townend, J., Savage, M., and Bannister, S. (2007). Ambient noise Rayleigh wave tomography of New Zealand. *Geophys. J. Int.*, 170(2):649–666.

Lin, F.C.., Tsai, V.C.., Schmandt, B., Duputel, Z., and Zhan, Z. (2013). Extracting seismic core phases with array interferometry. *Geophys. Res. Lett.*, 40(6):1049–1053.

Liu, Z.K.., Huang, J.L.., and Li, J.J.. (2010). Comparison of four techniques for estimating temporal change of seismic velocity with passive image interferometry. *Earthq. Sci.*, 23:511–518.

Lobkis, O.I.. and Weaver, R.L.. (2003). Coda-wave interferometry in finite solids: Recovery of P-to-S conversion rates in an elastodynamic billiard. *Phys. Rev. Lett.*, 90(254302):1–4.

Longpré, M.A.., Staudacher, T., and Stix, J. (2007). The November 2002 eruption at Piton de la Fournaise volcano, La Réunion Island: Ground deformation, seismicity, and pit crater collapse. *Bull. Volcanol.*, 69:511–525.

Longuet-Higgins, M.S.. (1950). A theory of the origin of microseisms. *Philos. Trans. R. Soc. London, Ser. A*, 243:1–35.

Mahoney, J.J.., Duncan, R.A.., Khan, W., Gnos, E., and McCormick, G.R.. (2002). Cretaceous volcanic rocks of the South Tethyan suture zone, Pakistan: Implications for the Réunion hotspot and Deccan Traps. *Earth and Planet. Sci. Lett.*, 203:295–310.

Mainsant, G., Larose, E., Brönnimann, C., Jongmans, D., Michoud, C., and Jaboyedoff, M. (2012). Ambient seismic noise monitoring of a clay landslide: Toward failure prediction. *J. Geophys. Res.*, 117(F01030).

Margerin, L. (2013). Diffusion approximation with polarization and resonance effects for the modelling of seismic waves in strongly scattering small-scale media. *Geophysical Journal International*, 192(1):326–345.

Margerin, L., Campillo, M., Shapiro, N.M.., and van Tiggelen, B. (1999). Residence time of diffuse waves in the crust and the physical interpretation of coda Q. Application to seismograms recorded in Mexico. *Geophys. J. Int.*, 138:343–352.

Margerin, L. and Nolet, G. (2003). Multiple scattering of high-frequency seismic waves in the deep Earth: Modeling and numerical examples. *J. Geophys. Res*, 108(B5):2234.

Martin, R., Komatitsch, D., and Gedney, S.D.. (2008). A variational formulation of a stabilized unsplit convolutional perfectly matched layer for the isotropic or anisotropic seismic wave equation. *Comput. Model. Eng. Sci.*, 37(3):274–304.

Massonnet, D., Briole, P., and Arnaud, A. (2001). Deflation of Mount Etna monitored by spaceborne radar interferometry. *Nature*, 375:567–570.

Mayeda, K., Koyanagi, S., Hoshiba, M., Aki, K., and Zeng, Y. (1992). A comparative study of scattering, intrinsic, and coda $Q^{-}1$ for Hawaii, Long Valley, and central California between 1.5 and 15.0 Hz. *J. Geophys. Res.*, 97:6643–6659.

Meade, B.J.. (2007). Present-day kinematics at the India-Asia collision zone. *Geology*, 35(1):81–84.

Meier, U., Shapiro, N.M.., and Brenguier, F. (2010). Detecting seasonal variations in seismic velocities within Los Angeles basin from correlations of ambient seismic noise. *Geophys. J. Int.*, 181:985–996.

Meunier, J., Huguet, F., and Meynier, P. (2001). Reservoir monitoring using permanent sources and vertical receiver antennae The Céré-la-Ronde case study. *The Leading Edge*, 20(6):622–629.

Michaels, J.E.. and Michaels, T.E.. (2005). Detection of structural damage from the local temporal coherence of diffuse ultrasonic signals. *Ultrasonics, ferroelectrics and frequency Control, IEEE Transactions on*, 52(10):1769–1782.

Michon, L., Staudacher, T., Ferrazzini, V., Bachèlery, P., and Marti, J. (2007). April 2007 collapse of Piton de la Fournaise: a new example of caldera formation. *Geophys. Res. Lett.*, 34(L21301).

Molnar, P. and Tapponnier, P. (1975). Cenozoic tectonics of Asia: effects of a continental collision. *Science*, 189:419–426.

Moschetti, M.P.., Ritzwoller, M.H.., and Shapiro, N.M.. (2007). Surface wave tomography of the western United States from ambient seismic noise: Rayleigh wave group velocity maps. *Geochem. Geophys. Geosys.*, 8(Q08010).

Nakahara, H. (2012). Formulation of the spatial autocorrelation (SPAC) method in dissipative media. *Geophys. J. Int.*, 190(3):1777–1783.

Nakahara, H. and Carcolé, E. (2010). Maximum-likelihood method for estimating coda q and the nakagami-m parameter. *Bulletin of the Seismological Society of America*, 100(6):3174–3182.

Nakata, N. and Snieder, R. (2011). Near-surface weakening in Japan after the 2011 Tohoku-Oki earthquake. *Geophys. Res. Lett.*, 38(17):L17302.

Nercessian, A., Hirn, A., Lépine, J.C.., and Sapin, M. (1996). Internal structure of Piton de la Fournaise volcano from seismic wave propagation and earthquake distribution. *J. Volcanol. Geotherm. Res.*, 70:123–143.

Nishida, K., Kobayashi, N., and Fukao, Y. (2002). Origin of Earth's ground noise from 2 to 20 mHz. *Geophys. Res. Lett.*, 28(10).

Niu, F., Silver, P.G.., Daley, T.M.., Cheng, X., and Majer, E.L.. (2008). Preseismic velocity changes observed from active source monitoring at the Parkfield SAFOD drill site. *Nature*, 454(7201):204–208.

Obermann, A., Planès, T., Larose, E., and Campillo, M. (2013a). Imaging pre- and co-eruptive structural and mechanical changes on a volcano with ambient seismic noise. *J. Geophys. Res.*, 118:1–10.

Obermann, A., Planès, T., Larose, E., Sens-Schönfelder, C., and Campillo, M. (2013b). Depth sensitivity of seismic coda waves to velocity perturbations in an elastic heterogeneous medium. *Geophys. J. Int.*, 194(1):372–382.

Paasschens, J.C.J.. (1997). Solution of the time-dependent Boltzmann equation. *Phys. Rev. E*, 56(1):1135.

Pacheco, C. and Snieder, R. (2005). Time-lapse travel time change of multiply scattered acoustic waves. *J. Acoust. Soc. Am.*, 118:1300–1310.

Patanè, D., Barberi, G., Cocina, O., De Cori, P., and Chiarabba, C. (2006). Time-resolved seismic tomography detects magma intrusions at Mount Etna. *Science*, 313(5788):821–823.

Paul, A., Campillo, M., Margerin, L., Larose, E., and Derode, A. (2005). Empirical synthesis of time-asymmetrical green functions from the correlation of coda waves. *Journal of Geophysical research*, 110(B8):B08302.

Peltier, A., Bachèlery, P., and Staudacher, T. (2009). Magma transport and storage at Piton de La Fournaise (La Réunion) between 1972 and 2007: A review of geophysical and geochemical data. *J. Volcanol. Geortherm. Res.*, 184(1–2):93–108.

Peltier, A., Bachèlery, P., and Staudacher, T. (2011). Early detection of large eruptions at Piton de La Fournaise volcano (La Rúnion Island): Contribution of a distant tiltmeter station. *J. Volcanol. Geortherm. Res.*, 199:96–104.

Peltier, A., Famin, V., Bachèlery, P., Cayol, V., Fukushima, Y., and Staudacher, T. (2005a). Cyclic magma transports at Piton de La Fournaise volcano (La Reéunion hotspot) inferred from deformation and geochemical data. *Earth Planet. Sci. Lett.*, 270(3–4):180–188.

Peltier, A., Ferrazzini, V., Staudacher, T., and Bachèlery, P. (2005b). Imaging the dynamics of dyke propagation prior to the 2000−2003 flank eruptions at Piton de La Fournaise, Réunion Island. *Geophys. Res. Lett.*, 32(L22303).

Pine, D.J.., Weitz, D.A.., Chaikin, P., and Herbolzheimer, E. (1988). Diffusing wave spectroscopy. *Phys. Rev. Lett.*, 60(12):1134–1137.

Planès, T. (2013). *Imagerie de changements locaux en régime de diffusion multiple*. PhD thesis, Université de Grenoble.

Planès, T. and Larose, E. (2013). A review of ultrasonic codawave interferometry in concrete. *Cement and Concrete Research*, 53:248–255.

Planès, T., Larose, E., Margerin, L., Rossetto, V., and Sens-Schönfelder, C. (2013). Distortion and stretching of coda waves induced by local changes: multiple scattering approach and numerical validation. *submitted*.

Planès, T., Larose, E., Rossetto, V., and Margerin, L. (2012). LOCADIFF: Locating a weak change with diffuse ultrasound. *AIP Conf. Proc.*, 1511:405–411.

Poli, P., Campillo, M., Pedersen, H.A.., and working group, P. L. (2012a). Body-wave imaging of Earth's mantle discontinuities from ambient seismic noise. *Science*, 338(6110):1063–1065.

Poli, P., Pedersen, H.A.., Campillo, M., and working group, P. L. (2012b). Emergence of body waves from cross-correlation of seismic noise. *Geophys. J. Int.*, 188(B7):549–558.

Poupinet, G., Ellsworth, W.L.., and Frechet, J. (1984). Monitoring velocity variations in the crust using earthquake doublets: an application to the Calaveras fault, California. *J. Geophys. Res.*, 89(B7):5719–5731.

Poupinet, G., Ratdomopurbo, A., and Coutant, O. (1996). On the use of earthquake multiplets to study fractures and the temporal evolution of an active volcano. *Ann. Geophys.*, 39:253–264.

Prieto, G.A.., Lawrence, J.F.., and Beroza, G.C.. (2009). Anelastic Earth structure from the coherency of the ambient seismic field. *J. Geophys. Res.*, 114(B7).

Ratdomopurbo, A. and Poupinet, G. (1995). Monitoring a temporal change of seismic velocity in a volcano: Application to the 1992 eruption of Mt. Merapi (Indonesia). *Geophys. Res. Lett.*, 22(7):775–778.

Ritzwoller, M., Lin, F., and Shen, W. (2011). Ambient noise tomography with a large seismic array. *C.R. Geoscience*, 343(8):558–570.

Rivet, D. (2008). *Suivi Temporel de la Zone de Subduction d'Amérique Centrale et Imagerie de la Vallé de Mexico*. PhD thesis, Universitde Grenoble.

Rivet, D., Campillo, M., Shapiro, N.M.., Cruz-Atienza, V., Radiguet, M., Cotte, N., and Kostoglodov, V. (2011). Seismic evidence of nonlinear crustal deformation during a large slow slip event in Mexico. *Geophys. Res. Lett.*, 38(L08308).

Robert, A., Zhu, J., Vergne, J., Cattin, R., Chan, L., Wittlinger, G., Herquel, G., de Sigoyer, J., Pubellier, M., and Zhu, L.D.. (2009). Crustal structures in the area of the 2008 Sichuan earthquake from seismologic and gravimetric data. *Tectonophysics*.

Roberts, P.M.. (1991). Development of the active doublet method for monitoring small changes in crustal properties. *Seismol. Res. Lett.*, 62(36).

Roberts, P.M.., Phillips, W.S.., and Fehler, M. (1992). Development of the active doublet method for measuring small velocity and attenuation changes in solids. *J. Acoust. Soc. Am.*, 91(3291).

Rossetto, V., Margerin, L., Planès, T., and Larose, E. (2011). Locating a weak change using diffuse waves: Theoretical approach and inversion procedure. *J. Appl. Phys.*, 109(034903):1–11.

Roult, G., Peltier, A., Taisne, B., Staudacher, T., Ferrazzini, V., Di Muro, A., and the OVPF team (2012). A new comprehensive classification of the Piton de la Fournaise activity spanning the 1985−2010 period. Search and analysis of short-term precursors from a broad-band seismological station. *J. Volcanol. Geotherm. Res.*, 241-242:78–104.

Roux, P., Sabra, K.G.., Gerstoft, P., and Kuperman, W.A.. (2005). P-waves from cross-correlation of seismic noise. *Geophys. Res. Lett.*, 32(L19303).

Royden, L.H.., Burchfiel, B.C.., King, R., Wang, E., Chen, Z., Shen, F., and Liu, Y. (1997). Surface deformation and lower crustal flow in eastern Tibet. *Science*, 276(5313):788–790.

Royden, L.H.., Burchfiel, B.C.., and van der Hilst, R.D.. (2008). The geological evolution of the Tibetan plateau. *Science*, 321(5892):1054–1058.

Rubinstein, J.L.., Uchida, N., and Beroza, G.C.. (2007). Seismic velocity reductions caused by the 2003 Tokachi-Oki earthquake. *J. Geophys. Res.*, 112(B5).

Ruigrok, E., Campman, X., and Wapenaar, K. (2011). Extraction of P-wave reflections from microseisms. *C. R. Geoscience*, 343:512–525.

Sabra, K.G.., Gerstoft, P., Roux, P., Kuperman, W.A.., and Fehler, M. (2005). Extracting time domain Green's function estimates from ambient seismic noise. *Geophys. Res. Lett.*, 32(L03310).

Sato, H. (1977). Energy propagation including scattering effects, single isotropic scattering approximation. *J. Phys. Earth*, 25:27–41.

Sato, H. (1993). Energy transportation in one- and two-dimensional scattering media: analytic solutions of the multiple isotropic scattering model. *Geophys. J. Int.*, 112:141–146.

Sato, H. and Fehler, M. (1998). *Seismic Wave Propagation and Scattering in the Heterogeneous Earth*. Springer-Verlag.

Sawazaki, K., Sato, H., Nakahara, H., and Nishimura, T. (2006). Temporal change in site response caused by earthquake strong motion as revealed from coda spectral ratio measurement. *Geophys. Res. Lett.*, 33(L21303).

Sawazaki, K., Sato, H., Nakahara, H., and Nishimura, T. (2009). Time-lapse changes of seismic velocity in the shallow ground caused by strong ground motion shock of the 2000 Western-Tottori earthquake, Japan, as revealed from coda deconvolution analysis. *Bull. seism. Soc. Am.*, 99(1):352–366.

Saygin, E. and Kennett, B. (2010). Ambient seismic noise tomography of Australian continent. *Tectonophysics*, 481:116–125.

Schaff, D.P.. and Beroza, G.C.. (2004). Coseismic and postseismic velocity changes measured by repeating earthquakes. *J. Geophys. Res.*, 109(B10302).

Sens-Schönfelder, C. and Larose, E. (2008). Temporal changes in the lunar soil from correlation of diffuse vibrations. *Phys. Rev. E.*, 78(045601):1–4.

Sens-Schönfelder, C. and Larose, E. (2010). Lunar noise correlation, imaging and monitoring. *Earthq. Sci.*, 23:519–530.

Sens-Schönfelder, C. and Wegler, U. (2006). Passive image interferometry and seasonal variations of seismic velocities at Merapi Volcano, Indonesia. *Geophys. Res. Lett.*, 33(21):L21302.

Sens-Schönfelder, C. and Wegler, U. (2011). Passive image interferometry for monitoring crustal changes with ambient seismic noise. *Comptes Rend. Geosci.*, 343(8):639–651.

Shang, T. and Gao, L. (1988). Transportation theory of multiple scattering and its application to seismic coda waves of impulsive source. *Sci. Sinica*, 31:1503–1514.

Shapiro, N.M.. and Campillo, M. (2004). Emergence of broadband Rayleigh waves from the correlations of ambient seismic noise. *Geophys. Res. Lett.*, 31(L07614).

Shapiro, N.M.., Campillo, M., Margerin, L., Singh, S.K.., Kostoglodov, V., and Pachero, J. (2000). The energy partitionning and the diffuse character of the seismic coda. *Bull. Seismol. Soc. Am.*, 90(655).

Shapiro, N.M.., Campillo, M., Stehly, L., and Ritzwoller, M.H.. (2005). High-resolution surface wave tomography from ambient seismic noise. *Science*, 307:16151618.

Shearer, P.M.. (2010). Introduction to seismology: The wave equation and body waves. *Lecture Notes: http://www.deep-earth.org/2010/Seismo-1-shearer.pdf.*

Singh, S.K.. and Hermann, R.B.. (1983). Regionalization of crustal Q in the continental United States. *J. Geophys. Res.*, 88:527–538.

Snieder, R. (2006). The theory of coda wave interferometry. *Pure Appl. Geophys.*, 163(2):455–473.

Snieder, R., Grêt, A., Douma, H., and Scales, J. (2002). Coda wave interferometry for estimating nonlinear behavior in seismic velocity. *Science*, 295(5563):2253–2255.

Snieder, R. and Hagerty, M. (2004). Monitoring change in volcanic interiors using coda wave interferometry: Application to Arenal Volcano, Costa Rica. *Geophys. Res. Lett.*, 31(9):L09608.

Staudacher, T., Boissier, P., Cathérine, P., Ferrazzini, V., Garofalo, K., Kowalski, P., Lauret, F., and Peltier, A. (2009). Multi-discipline monitoring network at Piton de la Fournaise volcano, Ile de la Réunion. *Geophysical Research Abstracts*, 11(EGU2009-1939-4):1939.

Stehly, L., Campillo, M., and Shapiro, N.M.. (2006). A study of the seismic noise from its long-range correlation properties. *J. Geophys. Res*, 111.

Stehly, L., Campillo, M., and Shapiro, N.M.. (2007). Travel-time measurements from noise correlation: stability and detection of instrumental time-shifts. *Geophys. J. Int.*, 171(1):220–230.

Taisne, B., Brenguier, F., Shapiro, N., and Ferrazzini, V. (2011). Imaging the dynamics of magma propagation using radiated seismic intensity. *Geophys. Res. Lett.*, 38(L04304).

Takagi, R., Okada, T., Nakahara, H., Umino, N., and Hasegawa, A. (2012). Coseismic velocity change in and around the focal region of the 2008 Iwate-Miyagi Nairiku earthquake. *J. Geophys. Res*, 117(B06315).

Tapponnier, P., Peltzer, G., Le Dain, A.Y.., Armijo, R., and Cobbold, P. (1982). Propagating extrusion tectonics in Asia: new insights from simple experiments with plasticine. *Geology*, 10:611–616.

Tapponnier, P., Peltzer, G., Le Dain, A.Y.., Armijo, R., and Cobbold, P. (2001). Oblique stepwise rise and growth of the Tibet Plateau. *Science*, 294:1671–1677.

Tarantola, A. and Valette, B. (1982). Generalized nonlinear inverse problems solved using the least squares criterion. *Rev. Geophys.*, 20(2):219–232.

Tatarskiĭ, V.I.. (1961). *Wave propagation in a turbulent medium.* McGraw-Hill, New York.

Tourin, A., Derode, A., Roux, P., van Tiggelen, B.A.., and Fink, M. (1997). Time-dependent coherent backscattering of acoustic waves. *Phys. Rev. Lett.*, 79(3637).

Tregourès, N.P.. and van Tiggelen, B.A.. (2002). Generalized diffusion equation for multiply scattered elastic waves. *Waves Rand. Med.*, 12(21–38).

Tromp, J., Komatitsch, D., and Liu, Q.Y.. (2008). Spectral-element and adjoint methods in seismology. *Comm. Comp. Phys.*, 3:1–32.

Tsai, V.C.. (2009). On establishing the accuracy of the noise tomography travel-time measurements in a realistic medium. *Geophys. J. Int.*, 178(3):1555–1564.

Tsai, V.C.. (2011). Understanding the amplitudes of noise correlation measurements. *J. Geophys. Res.*, 116(B09311).

Turner, J.A.. (1998). Scattering and diffusion of seismic waves. *Bull. seism. Soc. Am.*, 88(1):276–283.

van Albada, M.P.. and Lagendijk, A. (1985). Observation of weak localization of light in a random medium. *Phys. Rev. Lett.*, 55(2692).

van Rossum, M.W.C.. and Nieuwenhuizen, T.M.. (1999). Multiple scattering of classical waves: microscopy, mesoscopy and diffusion. *Rev. Mod. Phys.*, 71(313).

van Tiggelen, B., Sebbah, P., Stoytchev, M., and Genack, A. (1999). Delay-time statistics for diffuse waves. *Physical Review E*, 59:7166–7172.

van Tiggelen, B.A.., Anache-Ménier, D., and Ghyssels, A. (2006). Role of mean free path in spatial phase correlation and nodal screening. *Europhysics Lett.*, 74:999–1005.

Villaseñor, A., Yang, Y., Ritzwoller, M.H.., and Gallart, J. (2007). Ambient noise surface wave tomography of the Iberian Peninsula: Implications for shallow seismic structure. *Geophys. Res. Lett.*, 34(L11304).

Weaver, R.L.. (1982). On diffuse waves in solid media. *J. Acoust. Soc. Am.*, 71:1608–1609.

Weaver, R.L.. (1985). Diffuse elastic waves at a free surface. *J. Acoust. Soc. Am.*, 78:131–136.

Weaver, R.L.., Hadziioannou, C., Larose, E., and Campillo, M. (2011). On the precision of noise correlation interferometry. *Geophys. J. Int.*, 185(3):1384–1392.

Wegler, U. and Lühr, B.G.. (2001). Scattering behaviour at Merapi volcano (Java) revealed from an active seismic experiment. *Geophys. J. Int.*, 145(3):579–592.

Wegler, U. and Sens-Schönfelder, C. (2007). Fault zone monitoring with passive image interferometry. *Geophys. J. Int.*, 168:1029–1033.

Wolf, P. and Maret, G. (1985). Weak localization and coherent backscattering of photons in disordered media. *Phys. Rev. Lett.*, 55(2696).

Xiao, F. C. e. and the Regional Geological Survey Team (2012). Did the Zipingpu Dam trigger China's 2008 Earthquake? *A Probe International Study*, pages 1–34.

Xu, X.W.., Wen, X.Z.., Yu, G.H.., Chen, G.H.., Klinger, Y., Hubbard, J., and Shaw, J. (2009). Coseismic reverse- and oblique-slip surface faulting generated by the 2008 Mw 7.9 Wenchuan earthquake, China. *Geology*, 37(6):515–518.

Yamamoto, M. and Sato, H. (2010). Multiple scattering and mode conversion revealed by an active seismic experiment at Asama volcano, Japan. *J. Geophys. Res.*, 115(B7).

Yang, Y., Li, A., and Ritzwoller, M.H.. (2008a). Crustal and uppermost mantle structure in southern Africa revealed from ambient noise and teleseismic tomography. *Geophys. J. Int.*, 174(1):235–248.

Yang, Y. and Ritzwoller, M.H.. (2008). Characteristics of ambient seismic noise as a source for surface wave tomography. *Geochem. Geophys. Geosyst*, 9(Q02008).

Yang, Y., Ritzwoller, M.H.., Lin, F.C.., Moschetti, M.P.., and Shapiro, N.M.. (2008b). The structure of the crust and uppermost mantle beneath the Western US revealed by ambient noise and earthquake tomography. *J. Geophys. Res.*, 113(B12310).

Yang, Y.J.., Ritzwoller, M.H.., Levshin, A., and Shapiro, N.M.. (2007). Ambient noise Rayleigh wave tomography across Europe. *Geophys. J. Int.*, 168(1):259–274.

Yao, H. and van der Hilst, R.D.. (2009). Analysis of ambient noise energy distribution and phase velocity bias in ambient noise tomography, with application to SE Tibet. *Geophys. J. Int.*, 179(2):1113–1132.

Yao, H., van der Hilst, R.D.., and de Hoop, M.V.. (2006). Surface-wave array tomography in SE Tibet from ambient seismic noise and two-station analysis: Phase velocity maps. *Geophys. J. Int.*, 166:732–744.

Zhan, Z., Ni, S., Helmberger, D.V.., and Clayton, R.W.. (2010). Retrieval of Moho reflected shear wave arrivals from ambient seismic noise. *Geophys. J. Int.*, 1:408–420.

Zhang, P.Z.., Wen, X.Z.., Shen, Z.K.., and Chen, J.H.. (2010). Oblique, high-angle, listric-reverse faulting and associated development of strain: The Wenchuan earthquake of May 12, 2008, Sichuan, China. *Annual Review of Earth and Planetary Sciences*, 38:353–382.

Zheng, S.H.., Sun, X.L.., Song, X.D.., Yang, Y.J.., and Ritzwoller, M.H.. (2008). Surface wave tomography of China from ambient seismic noise correlation. *Geochem. Geophys. Geosyst.*, 9(Q05020).

Zhou, R., Li, Y., Densmore, A.L.., Ellis, M.A.., He, Y., Li, Y., and Li, X. (2007). Active tectonics of the Longmen Shan region of the eastern margin of the Tibetan plateau. *Acta Geol. Sinica*, 81:593–604.